The University Of Sheffield.

In Situ Atomic Force Microscopy Studies of the Crystallization of PE and PE Containing Block Copolymer

By

Lamiaa Ghazi Alharbe

A thesis submitted for the degree of Doctor of Philosophy Department of Physics and Astronomy

September 2017

Contents

Abstract

This study investigates the crystallization behaviour of two polymer systems, polyethylene (PE) and PE containing block copolymer *in situ*, in real time, as a function of temperature using the atomic force microscopy (AFM) tapping mode.

The orientation and crystallization of microdomains were examined in a crystalline-amorphous diblock copolymer, hydrogenated poly (high-1,4-butadiene)-b-poly(high-3,4-isoprene) (E/MB), which forms cylinders of the crystallizable block (polyethylene, E). Although randomly oriented in nature, the E/MB microdomains were successfully oriented locally using the sharp tip of an AFM in tapping mode. Better ordering of the microdomains was achieved with the AFM tip since defects were generally found to be reduced by scanning over them more than once. Using AFM, the orientation process and subsequent crystallization behaviour were investigated as a function of temperature. Fully confined crystallization was observed within the range of 25 - 50 °C, with templated and breakout crystallization observed at higher crystallization temperatures. The growth rate of templated crystallization along, and perpendicular to, the existing microdomain structure was measured, and the ratio between these rates was found to increase rapidly with decreasing temperature, from ~ 4.8 at 100 °C to ~ 8 at 97 °C. Furthermore, the growth rates fluctuated with time for each crystal, as well as between crystals at different temperatures. Two maxima in the degree of orientation of the crystallized regions were found, one at relatively small supercoolings (e.g. 95 °C), where the difference in growth rate along and across microdomain boundaries was high, and one at high supercoolings (25-50 °C) where crystallization was completely dominated by nucleation.

The AFM tip was also used as flow shear to induce oriented PE crystallization and then to investigate the subsequent growth behaviour *in situ*. During the subsequent isothermal crystallization, interesting behaviours were observed. First, some crystals were observed to force their neighbouring crystals apart in order to provide themselves with more room to grow between them. Second, some crystals were observed to deform or reorganize themselves during the isothermal crystallization in order to be in a more stable state. Third, sometimes, crystals appeared to clump together: i.e. as they grew, the gap between them reduced and even disappeared. Fourth, some crystals melted

during the isothermal crystallization while the remaining crystals continued growing. Furthermore, the height of the edge-on lamellae was measured and found to be nonlinear in relation to time. Moreover, the growth rates of individual crystals were measured under isothermal conditions at different temperatures. It was found that the average growth rates increased as the crystallization temperatures decreased, although the rates fluctuated with time for each crystal as well as between crystals. The distribution of growth rates of the individual crystals was found to be non-constant under isothermal crystallization conditions (in both systems: PE and E/MB). None of these observations are accounted for in current models of crystallization, or observed in molecular simulations of crystal growth, implying a need to reappraise the underlying processes of polymer crystallization.

Acknowledgements

First and foremost I would like to express my sincere gratitude to my supervisor, Prof. Jamie Hobbs, for his continuous support throughout this project. Jamie has provided me support, guidance and encouragement during my PhD while giving me the freedom that allows me to work independently. It was my honour to be under his supervision.

I wish to thank also my second supervisor Prof. Mark Geoghegan for his valuable suggestions and advice. I would like to express my very great appreciation to Prof. Richard Register for providing me the sample E/MB and for his valuable suggestions. I also would like to thank: Prof. Toda Akihiko, Prof. Wenbing Hu, Prof. Christopher Li, for the useful discussions about this work. I would also like to extend my thanks to the laboratory technician within the Chemistry Department at the University of Sheffield, Rob Hansen, for his help in training me on how to use DSC measurements.

My appreciations also go to people in the Physics and Astronomy Department for their help and assistance, particularly Dr. Micheal Weir and Dr. Andy Parnell. I would like to thank my friends Latifah Alfhaid, Wala Dizayee and Rania Alqurashi for their helps and supports

I would like to thank my group members (SPM group): Dr. Nic Mullin, Dr. Rebecca Savage, Dr. Rik Bailey, Dr. Sandip Kumar, Dr. Paul Chapman, Stephen Jackson, Jonathan Burns, Nick Jenkins, Raveen Kaur Tank, David Owen, Spyridon Sovatzoglou, and Laia for their help and support, and especially Dr. Nic Mullin for his valuable discussions about AFM during the development of this research work.

My thanks also go to my sponsor, Umm Al-Qura University, represented by The Ministry of Education of the Kingdom of Saudi Arabia, for funding me to complete this project in the UK.

My special thanks go to my husband, Abdulaziz Alharbi, who has provided a huge amount of help, patience, encouragement and support during my PhD journey. I am also grateful and thankful for my lovely little kids; Nawaf, Faisal and Jana, who are the pride and happiness of my life, for their patience and love.

Last, but not least, I would like to thank my family in Saudi Arabia; my parents, Ghazi and Hazah, and my sisters and brothers, for their love and support throughout my PhD journey.

Presented Works and Publications

Conferences

- Poster presentation, Microscience Microscopy Congress (mmc) incorporating EMAG, Manchester UK, 29th Jun -2nd Jul 2015.

- Poster presentation, International Chemical Congress of Pacific Basin Societies (Pacifichem), in Honolulu, Hawaii, USA, 15th -20th December 2015.

- Oral presentation, the Department Postgraduate Presentations on the 11th April 2016, The Physics and Astronomy Department at Sheffield University.

- Poster presentation, SPM Conference and Users Meeting, in Cambridge, UK, 13th -14th December 2016.

- Poster presentation, Imaging Life Launch Symposium, in Sheffield, UK. 12th - 13th January 2017.

- Poster presentation, Microscience Microscopy Congress (mmc) incorporating EMAG, Manchester UK, 3rd Jun - 6th Jul 2017.

Publications and Prize

- L. G. Alharbe, R. A. Register, and J. K. Hobbs, "Orientation Control and Crystallization in a Soft Confined Phase Separated Block Copolymer," *Macromolecules*, vol. 50, no. 3, pp. 987–996, 2017.

- Using AFM-Directed Polymer Crystallization to Measure Crystal Growth Rates in Polyethylene. Paper in preparation and title may change before submission.

- *In Situ* Observations of Motion of PE Single Crystals During Growth from the Melt. Paper in preparation and title may change before submission.

- A poster prize winner for best poster, International Chemical Congress of Pacific Basin Societies (Pacifichem), 15th -20th December 2015, Honolulu, Hawaii, USA.

Nomenclature

AFM	Atomic force microscopy
TEM	Transmission electron microscopy
STM	Scanning tunnelling microscopy
SPM	Scanning probe microscopy
F	Force
F_{ts}	Force between the tip and the sample
A_o	Free amplitude
A_{sp}	Setpoint amplitude
r_{sp}	Setpoint ratio
Q	Quality factor
k	Spring constant
K	Kelvin
DSC	Differential scanning calorimetry
T_c	Crystallization temperature
T_m	Melting temperature
T_g	Glass transition temperature
Ψ	Amplitude ratio
Δ	Phase difference
OM	Optical microscope
E/MB	Hydrogenated poly (high-1,4-butadiene)-b-poly(high-3,4-isoprene)
PE	Polyethylene
rms	Root mean square
nm	Nanometer
s	Second
V	Volt
Hz	Hertz
ºC	Degree Celsius
µm	Micrometre

ΔG	Gibbs free energy
H	Enthalpy
S	Entropy
ΔT	Supercooling
rpm	Revolutions per minute
f	Volume fraction
w	Specific work
G	Growth rate
η	Shear-rate-dependent viscosity
χ	Interaction parameter
k_B	Boltzmann constant

List of Figures

List of Tables

Part I

Introduction and Background

Chapter 1

Overview

Since they were first synthesized, polymers have become essential materials in many fields, including the medical, industrial, environmental and defence fields. Owing to their importance in everyday life, understanding the mechanical, physical and chemical properties of polymers has become a new subcategory in science: polymer science.

Materials can generally form either crystalline or amorphous structures; however, polymers exhibit a dual-phase existence. Often, both crystalline and amorphous phases coexist within the same polymer structure, in that crystallites are dispersed within an amorphous matrix. The mechanical and physical properties of these polymers are strongly influenced by the structure (size and shape) of the crystalline phase. A better understanding of polymer crystallization can therefore help scientists to control and improve the desired properties of these polymers, helping to improve existing materials and even find new applications.

In 1957 it was discovered that the long chains of polymers can fold back and forth to form single crystals whose thickness is substantially less than the extended polymer chain from which they are made [1] (unlike crystallization of a small molecule). Since this discovery, numerous studies have been performed to investigate various aspects of crystallization, such as crystallization under quiescent conditions, crystallization under flow conditions and crystallization under confinement. Many questions remain unanswered, however, and the current understanding of polymer crystallization is incomplete since certain phenomena are not fully accounted for in the current theoretical accounts of polymer crystallization. Gaining new insights into crystallization is essential in order to understand completely the mechanisms that determine

crystallization. A better understanding of these processes is significant for improving existing materials and even fabricating novel materials with known properties.

The crystallization process involves the rearrangement of polymer molecules but the final morphologies of the resulting polymer crystals depend on the processing conditions. For example, crystallization under quiescent conditions leads to the formation of spherulites (spheroidal crystals), while crystallization under flow conditions leads to so-called shish kebab crystals (crystals in the shape of a central spine with protrusions). Even though these shish kebab and spherulite outcomes are well known, along with the fact that they are composed of lamellar structures of ordered polymer chains, the exact details of the process leading to these structures are not fully understood. Thus, a detailed understanding of polymer crystallization requires *in situ* observations of the crystallization process itself, as the manner in which the molecules arrive in their final crystalline positions is important.

In order to understand the details at the required level, more sophisticated techniques are required to characterize the molecular rearrangement process at the molecular and atomic levels. There is, therefore, a need to employ advanced surface characterization techniques that offer very high resolution at the atomic level.

Among these techniques, scanning tunnelling microscopy (STM) has had a great impact on the study of the atomic/molecular details of polymer structures. STM has only limited uses: it is only appropriate for good electrical conductor or semiconductor materials because of the way the technique works (i.e. the tip–sample interaction). On the other hand, *ex situ* techniques such as transmission electron microscopy (TEM) can sometimes give misleading information when it is important to watch the crystallization process as it occurs. The development of atomic force microscopy (AFM) by Binning, Quate and Gerber [2], however, has enabled researchers to study the atomic-level features of polymer crystallization without the weaknesses of the instruments described above.

Since it became commercially available in 1989, AFM has become one of the most widely used tools for imaging and measuring the nano-level features of matter, owing to its capability to reveal structural details with superior spatial resolution. Imaging with AFM can be performed in either liquid or gas media, as well as in a vacuum. AFM has

been successfully employed to study a range of polymeric materials, such as homopolymers [3–5], block copolymers [6], polymer composites, blends [7], biopolymers and thin-film polymers [8, 9] The information revealed in these studies includes local structures and compositions, as well as mechanical properties. AFM also allows dynamic processes, such as crystallization, to be observed *in situ*, in real time, with real space information on submicron length scales without significantly damaging the sample, all of which are essential for a detailed understanding of polymer crystallization. *In situ* AFM direct observations of polymer crystallization at a relatively small scale, where individual lamellae can be monitored, represents a promising method to examine the details of the growth of polymeric materials. This in turn could make a significant contribution and improvement to knowledge in the field of polymer crystallization. Thus, *in situ* AFM observations are employed throughout this work.

The particular type of crystallization that will be examined in the thesis is confinement crystallization. This is where polymers crystallize under nanoscale confinement. One reason for exploring confinement effects is that confined systems are becoming increasingly widespread, as devices and materials are constrained due to miniaturization. Second, the fundamental understanding obtained from studies of confinement effects can extend our understanding of crystallization.

Block copolymers are a class of polymers consisting two (called diblock copolymers) or more different species of monomers that are covalently connected together. These blocks assemble themselves into a variety of ordered nano-structures, due to thermodynamic incompatibility between them. The blocks can be crystallizable or amorphous. Semicrystalline block copolymers contain at least one crystallizable block, which also called crystalline−amorphous diblock copolymer [10], is one of the most convenient and common methods used to achieve confinement at the nanoscale, due to their self-assembled microdomains. Besides their importance as a confinement system in polymer crystallization, controlling the orientation of these microdomains within a specific localized region is essential for the development of novel nanometre structures and in various applications [11], such as data storage, lithography, computer memory, and nanometre-scale templating [12].

Scope and Objectives of the Thesis

The work presented in this PhD thesis, therefore, studies the crystallization of polyethylene (PE) and PE containing block copolymer in real time, *in situ* as a function of temperature. This study aimed to follow the growth of crystals at different temperatures in order to investigate the evolution of the morphology and crystallization behaviour at surfaces by AFM. Two types of polymer were used in this study: PE and block copolymer (see Section 2.5. for an explanation of block copolymers) which was hydrogenated poly (1,4-butadiene)-b-(3,4-isoprene) (E/MB). The objectives of this study were to:

- Control the orientation of microdomains in block copolymer (E/MB) locally by the AFM tip.
- Study the effect of temperature on the degree of confinement of the formation crystals in these oriented microdomains.
- Examine the subsequent crystallization behaviour *in situ* and *ex situ* in pre-oriented microdomains as a function of temperature.
- Induce and control oriented PE crystals using the AFM tip.
- Investigate the behaviour of the subsequent growth of PE induced by AFM tip *in situ*, in real time.
- Study the growth rates and the distribution of individual PE crystals in detail under isothermal conditions at different temperatures.

Outline of the Thesis

This thesis is composed of eight themed chapters. This Chapter 1 has given an overview of the research area. Chapter 2 provides an introduction to polymers in general, their crystallization and an overview of the relevant polymer crystallization theories, and is divided into six sections. The first and second parts deal with polymers in general and their classification and properties, respectively. The third part is about polymer crystallization processes in general, including nucleation and growth. The fourth section

is about crystalline morphologies of polymers and the influence of the process conditions on these morphologies. The fifth part offers an overview of copolymers, particularly block copolymers, their phase separation and their crystallization. The last section presents the use of AFM in manipulating, controlling and mapping the polymer crystallization. Chapter 3 is concerned with the methodology used for this work including the main methods used for preparing samples, and the experimental techniques that were utilized, with a particular focus on AFM, which was the main technique used in this work due to its ability to follow the crystallization *in situ* and calibration that was produced for temperature control in this PhD work. Chapters 4, 5, 6 and 7 present and analyse the results and main findings of this research. While Chapter 4 and Chapter 5 cover the experimental results obtained on E/MB regarding controlling the orientation of microdomains and the subsequent crystallization in these pre-oriented microdomains, respectively, Chapter 6 and Chapter 7 contain the experimental results obtained for PE and the *in situ* observations of the behaviour of PE crystals induced by the AFM tip and individual crystals' growth rates as a function of time and temperature. Finally, Chapter 8 provides a brief summary of the study as a whole and some recommendations for further research work.

Chapter 2

Background Theory to Polymers and Their Crystallization

2.1. Introduction

Polymers are essential materials that play a crucial and ubiquitous role in everyday life. Polymers can be natural or synthesized: protein, DNA and cellulose are all examples of polymers in nature, while polyethylene (PE) is an example of a synthesized polymer. The term 'polymer' derives from the Greek "poly", meaning many, and "meros", meaning part; thus polymer means many parts. Polymers are also called **macromolecules** and can be defined as a very long chain made up of repeating units called **monomers** that are linked together by covalent bonding. The longest chain of linked monomers is called the backbone chain, while the smaller chains that are normally attached to the sides of this backbone are called the side or functional groups, which can be made up of any type of atom. Most polymers are organic in origin and many organic polymers are hydrocarbons (i.e. made up of carbon and hydrogen atoms) in which the main backbone chains are carbon atoms and the side groups are hydrogen, or/and any other types of atoms such as oxygen or nitrogen. The process used to produce polymers is called polymerization and the degree of the polymerization (N) is determined by the number of monomer units bound into the polymer chain.

Figure **2.1** shows two examples, where ethylene and propylene have been polymerized to produce polyethylene and polypropylene, respectively.

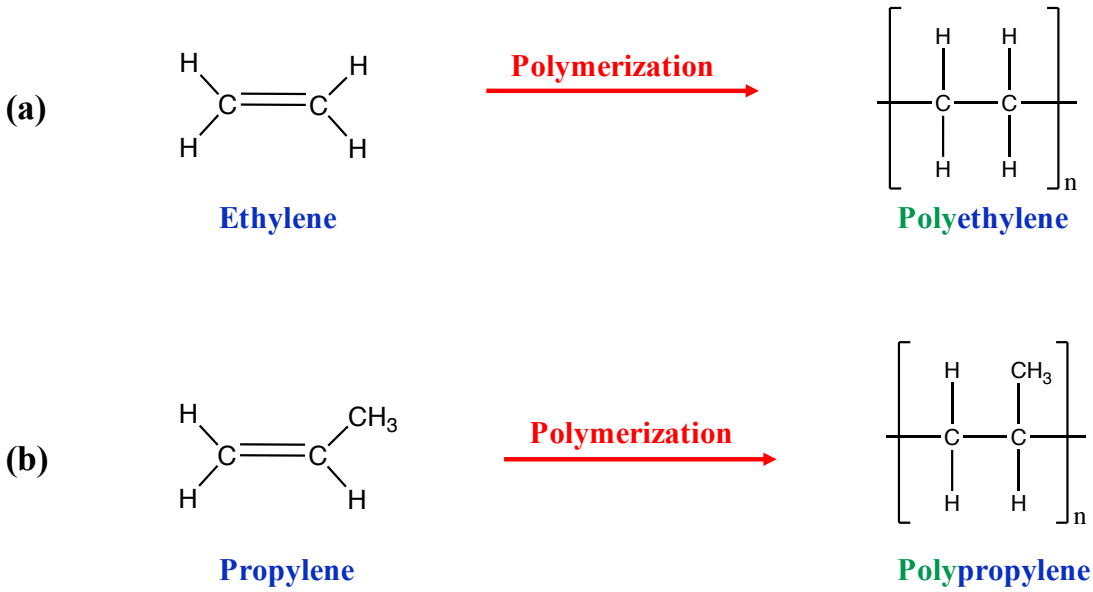

Figure 2.1: Representation of (a) ethylene and (b) propylene and their polymerization products polyethylene and polypropylene, respectively.

The remainder of this chapter explores: 1) some classifications of polymers and their properties, 2) the crystallization process, including nucleation and growth, 3) the crystalline morphology which are lamellae, spherulite and shish kebab, with an overview of the classical theoretical models for the crystallization processes of polymers, 4) AFM studies of polymer crystallization and their contribution to increasing knowledge about polymer crystallization, 5) copolymers, block copolymers, and their phase separation and crystallization.

2.2. Polymer Classification and Properties

Polymers can usually be classified into different groups depending on many factors, such as their: chemical structure, polymeric structure, arrangement of monomers,

tacticity, thermal behaviour and crystallinity (see Figure **2.2**). These factors determine the properties of polymers, as will be discussed below.

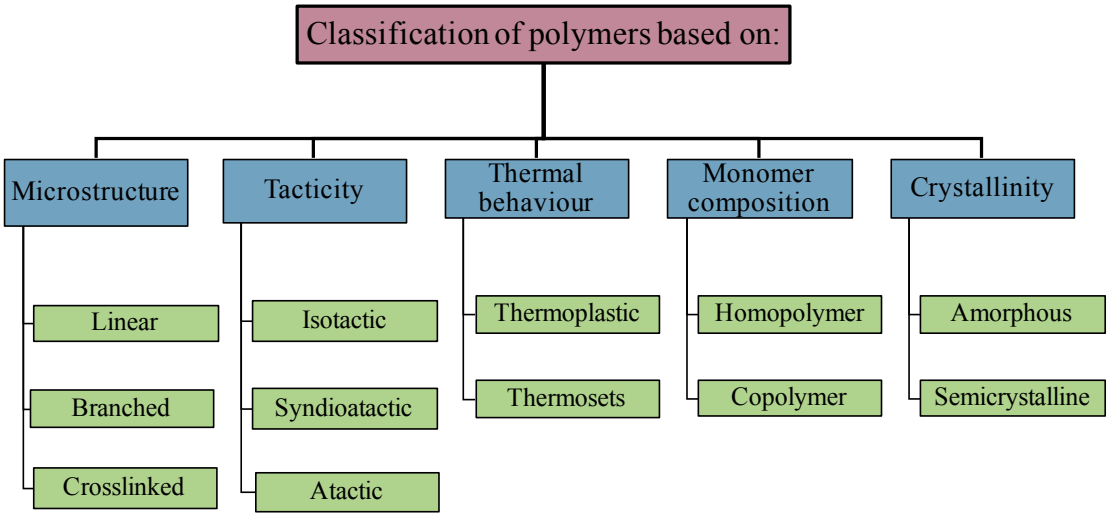

Figure 2.2: A diagram showing some of common classification of polymers based on their structure, tacticity, thermal behaviour and chemical structure.

a) Polymer Structure (Microstructure)

Polymer structure is an important determinant of the properties of polymeric materials. Structures include (a), linear polymers, which consist of long and straight chains (no branches) as shown in Figure **2.3** (a). High density polyethylene (HDPE) is a good example of this type of polymer. (b) Branched polymers, which have side-branch chains attached to the main chain, as presented in Figure **2.3** (b). An example of this type is low density polyethylene (LDPE). Finally (c), crosslinked polymers, in which there are interconnections between polymer chains, as indicated in Figure **2.3** (c). Polyacrylamide gel is an example of this type. The microstructure affects the physical properties of the polymer; for example, linear polymers are soft, melt easily and can be dissolved in certain solvents, whereas crosslinked polymers are hard and do not melt or dissolve in solvents easily due to their strong bonds between chains. The physical properties of branched polymers, meanwhile, fluctuate between those of linear and crosslinked polymers.

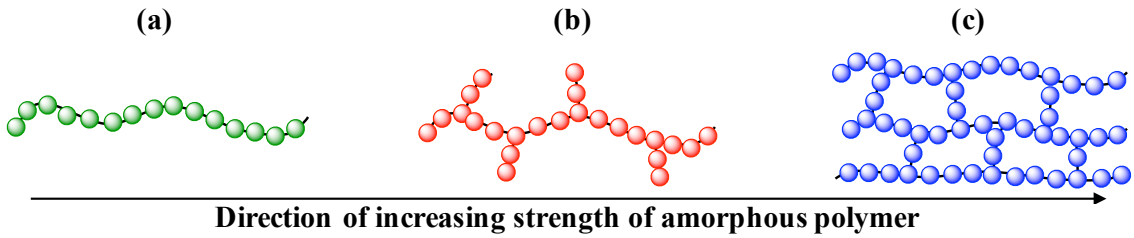

Figure 2.3: A schematic representation of: (a) linear, (b) branched and (c) crosslinked polymer structures.

b) Polymer Tacticity

The tacticity of polymers, also known as their stereochemistry, refers to the three-dimensional arrangement of the side groups or functional groups (substituents) on the main polymer backbone. Based on the arrangement of these side groups, polymers can be classified into three different types: isotactic polymers, where the side groups are regularly arranged along the polymer backbone, syndiotactic polymers, where the side groups are alternatively arranged on the sides, and atactic polymers where the side groups are arranged randomly along the polymer backbone [13] (Figure **2.4**).

In PE, for example (Figure **2.1** (a)), the side groups are all the same (hydrogen atoms). This means that there is no stereochemistry in this case, since there is only one possible manner in which these side groups can be arranged along the backbone of the polymer. In PP (Figure **2.1** (b)), however, there are two different side groups: hydrogen and CH_3 groups. This mean that polypropylene has stereochemistry and there are three different possible ways in which these side groups can arrange themselves along the backbone chain, as can be seen in Figure **2.4**.

The properties of polymers are related to their stereochemistry. For instance, isotactic and syndiotactic polymers can be crystalline due to their regular structure, whereas atactic polymer cannot be crystallized (amorphous) as it is hard for their non-regular structure to be arranged into crystals.

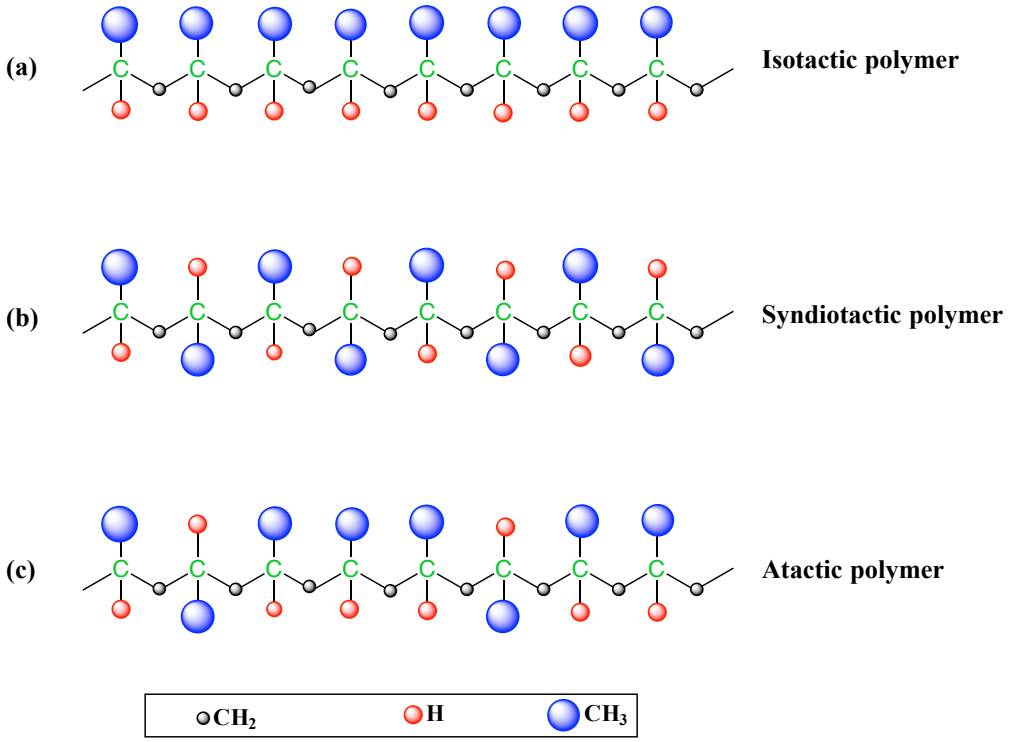

Figure 2.4: Tacticity or stereochemistry of polypropylene: isotactic, syndiotactic and atactic where the side groups are, respectively, regularly, alternately, and randomly arranged along the side of the polymer backbone.

c) Thermal Behaviour

In addition to stereochemistry, the properties of polymers can be classified based on their thermal behaviour or response to heat. Polymers that can be melted, moulded or extruded into various shapes are called thermoplastic [13], which in turn can be split into two types: semi-crystalline and amorphous polymers. On the other hand, polymers that cannot be reheated and used (i.e. that do not melt but degrade on heating) are called thermosets. Examples of thermoplastic and thermoset polymers are linear or some crosslinked polymers (e.g. PE), and massively crosslinked polymers (e.g. polyurethane).

The samples used in this study are thermoplastic semi-crystalline polymers.

d) Crystallinity

Crystallinity defines the degree of order in a polymer, and strongly influences its properties. The more crystalline a polymer, the more regularly aligned are its chains. Increasing the degree of crystallinity increases the hardness and density of the material. In term of crystallinity, polymers can be either amorphous (no crystallinity) or semicrystalline [14] (i.e. containing both amorphous and crystalline regions). Thus, there is no polymer with 100 % crystallinity. In the amorphous polymers the chains are randomly coiled and entangled in a very random structure while in the semicrystalline polymers the chain are aligned in a highly ordered structure (Figure **2.5**).

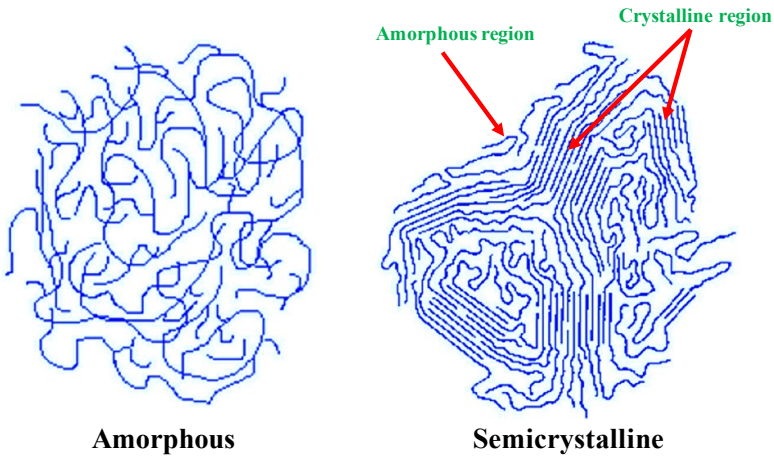

Figure 2.5: Schematic representation of amorphous and semicrystalline polymer.

There are two important temperatures affecting the amorphous and crystalline regions and in turn the properties of polymer. These temperatures are known as the "melting temperature" (T_m) and the "glass transition temperature" (T_g), as can be seen in Figure **2.6**.

The properties of these two types of polymer are affected by their temperature. The crystalline regions lose their ordered structure and become disordered melt (i.e. they melt) at a temperature termed the "melting temperature" (T_m) – this is a property only of the crystalline regions. The amorphous polymers, meanwhile, can be either rubbery (soft and flexible) or glassy (hard, rigid and brittle) depending on the temperature. The point at which they transition from a rubbery to a glassy state is called the glass

transition and the temperature is known as "glass transition temperature" (T_g) [15, 16]. Above T_g the amorphous region is rubbery (i.e. the polymer is in a rubbery state, as it becomes soft and flexible due to mobility of chains) while below T_g the amorphous region is glassy (i.e. the polymer is in a glassy state, since the polymer become brittle, rigid and hard like glass due to the decrease in the motion of chains). T_g is a property only of amorphous regions.

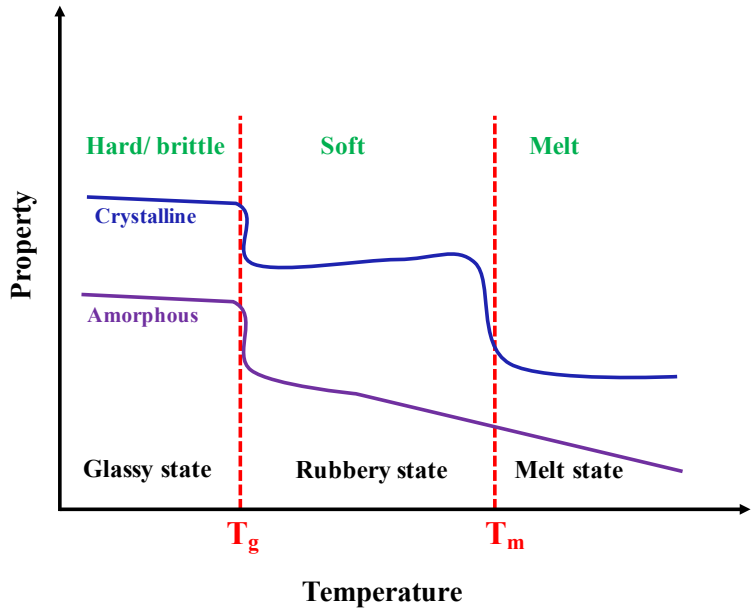

Figure 2.6: Diagram showing the properties of polymers depending on the T_g and T_m.

e) Monomer Composition

Monomer composition or chemical structure refers to the compositions within the polymer. When the polymer consists of one type of repeating unit it is called a homopolymer, whereas when the polymer consists of more than one type of repeating unit it is called a copolymer (Figure **2.2**). Copolymers and their phase separation will be discussed in more detail in Section 2.5.

2.3. Crystallization

2.3.1. General Crystallization Thermodynamics

Crystallization is a transformation from the liquid or melt phase to the crystalline phase (solid). Usually, polymer crystallization occurs in the temperature range between T_m and T_g, where the chains are sufficiently mobile and thus have the ability to organize themselves into the crystalline domain. Below T_g, the chains are frozen, while above T_m they are highly mobile (as mentioned above), although if the polymer is kept at this high temperature for a long time, it may be subject to degradation. In thermodynamic terms, a crystal will grow if the free energy of the crystalline phase is less than that needed for the formation of the liquid or melt phase at a given temperature. Thus, one condition necessary for the formation of a crystalline phase is a negative value for the change in Gibbs free energy (ΔG) upon crystallization (Figure **2.7**).

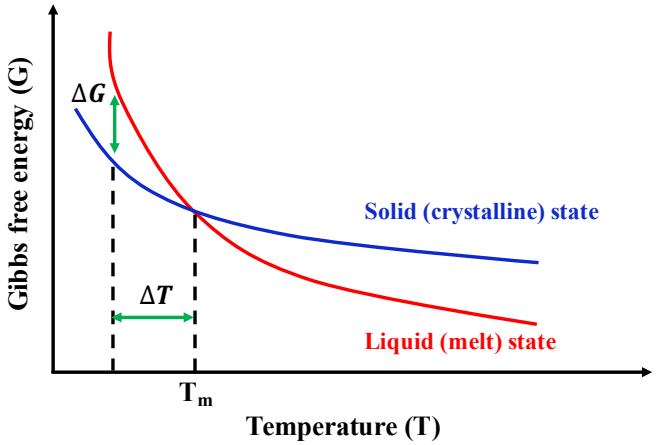

Figure 2.7: Graph showing the Gibbs free energy as temperature is varied for liquid and solid states demonstrating the stability of the solid at temperatures below and above T_m.

The Gibbs free energy (G) is given by equation (2.1):

$$G = H - TS \tag{2.1}$$

where H is the enthalpy, T is the temperature and S is the entropy.

Hence a change in the Gibbs free energy (ΔG) is given by equation (2.2).

$$\Delta G = \Delta H - T\Delta S \tag{2.2}$$

where ΔH and ΔS are the change of the enthalpy and entropy during the transition, respectively.

At temperatures higher than the equilibrium melting point (T_m) melting will occur spontaneously, while below this temperature (known as supercooling (ΔT)) crystallization will occur spontaneously.

ΔT, which is the difference between the melting point and crystallization temperature ($\Delta T = T_m - T_c$), is an essential factor that directly affects the crystal morphology and in turn the properties of the crystal. At low supercooling, the driving force for crystallization is low therefore the growth rate is slow. At higher supercooling, the growth rate increases since the driving force for crystallization increases.

2.3.2. Crystallization in Polymers

Crystallization in general, regardless of the class of material, proceeds through the stages of nucleation and growth. The crystallization process in polymers, however, can be further divided into three basic steps: (1) primary nucleation, (2) secondary nucleation or growth (primary crystallization), and (3) perfection or secondary crystallization (Figure **2.8**). Primary nucleation is the initial step of crystallization, and can be homogeneous or heterogeneous. If impurities or nucleating agents are not present, it is necessary for homogeneous nucleation to occur first so that a crystal can grow; otherwise, heterogeneous nucleation occurs. After the formation of crystal nuclei, the secondary nucleation takes place, where further polymer chains diffuse to the growth front and undergo further crystallization [17]. This will be discussed in more detail below.

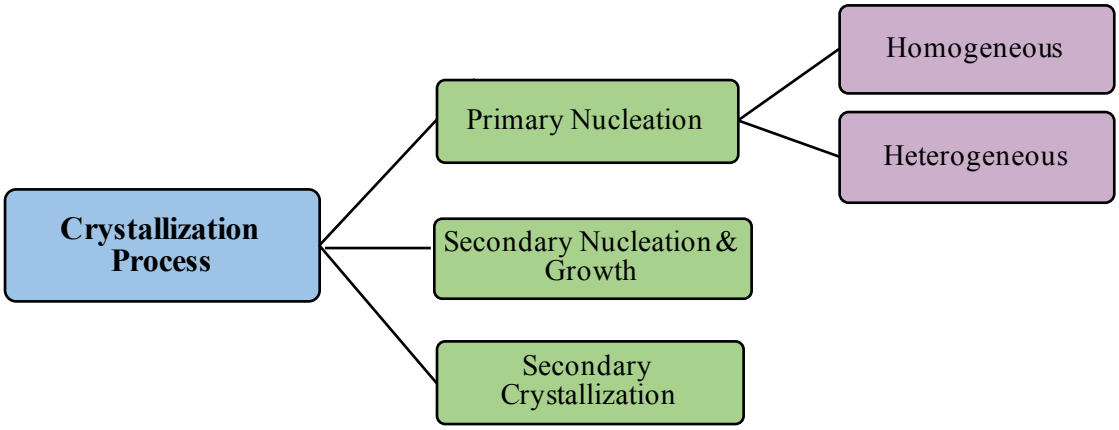

Figure 2.8: Outline of the crystallization process of polymers

In the following sections, the crystallization process is spilt into two sections: nucleation and crystal growth; the main theories related to each will be presented and discussed below.

2.3.2.1. Nucleation

Nucleation is the initial step of the crystallization process, whereby an 'embryo' (a nucleus) is formed.

Figure **2.9** shows the formation of nuclei in both (a) a small molecule system and (b) a polymer system [18]. The main difference between these two systems is that, in the case of a polymer, a single molecule can participate in several nuclei at once. This has the effect of producing less perfect crystals with the more disordered amorphous regions observed in polymer crystals.

The nucleation process can be spilt into two key classes: primary nucleation (which in turn can be divided into homogeneous and heterogonous nucleation) [19] and secondary nucleation (as previously mentioned). Heterogeneous nucleation occurs more often than homogeneous nucleation in polymer systems and has a lower free energy barrier. It

starts at nucleation sites on surfaces such as foreign bodies. In homogeneous nucleation, the polymer molecules aggregate spontaneously and randomly, due to local fluctuations, to form a nucleus [20].

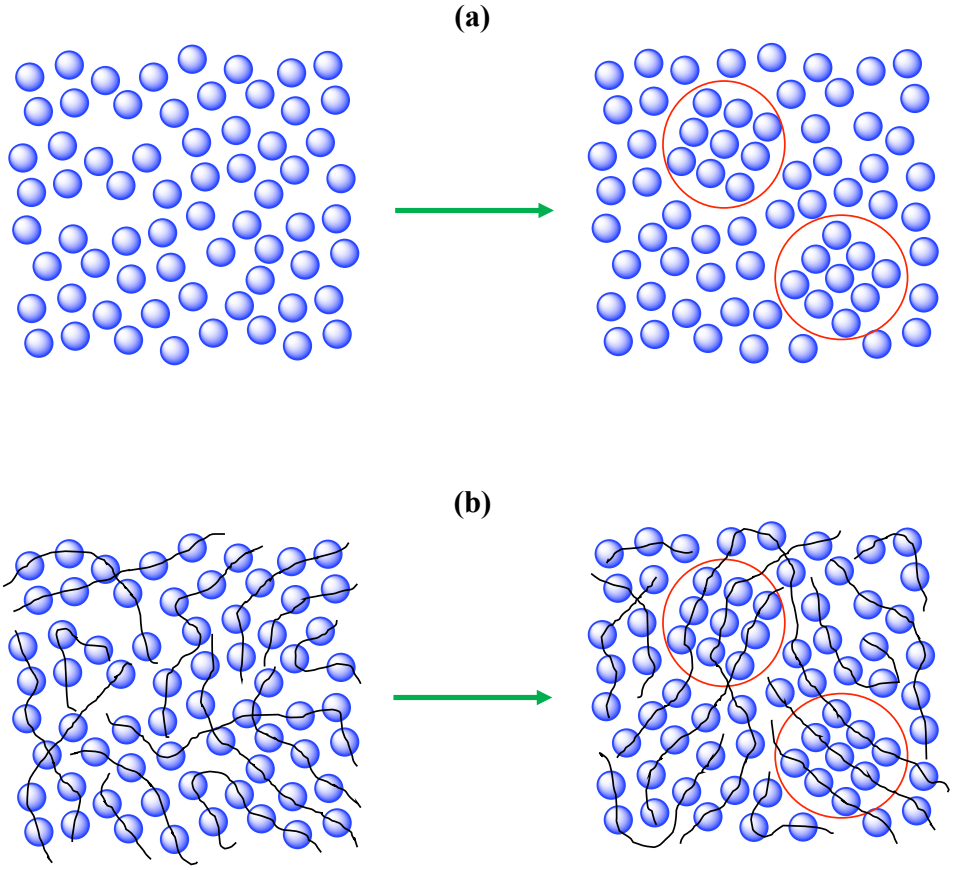

Figure 2.9: Schematic illustration of homogeneous primary crystal nucleation in (a) a small molecule system and (b) a polymer system. Each blue ball represents a single monomer.

The size of the critical nucleus can be estimated using the classical theories of nucleation in small molecule systems. This is done by balancing the increase in free energy due to the creation of a crystal-liquid interface against the reduction in energy due to the solid crystal being more stable than the supercooled melt. This is given by equation (2.3) below, where the nucleus is expected to be spherical.

$$\Delta G = \frac{4}{3}\pi r^3 \Delta G_v + 4\pi r^2 \sigma \tag{2.3}$$

where ΔG is the change in free energy, r is the radius of the nucleus, ΔG_v is the difference in free energy between the solid crystal and melt phases per unit volume, σ is the surface free energy of the interface between the nucleus and the melt. In the case of the formation of crystal, the first term is always negative while the second term is always positive.

For ΔG vs r, this function goes through a maximum at the critical nucleus size, showing that there is a free energy barrier to nucleation, as shown in Figure **2.10**, where r^* and ΔG^* are the critical radius of the nucleus and the energy barrier for nucleation, respectively. This free energy barrier must be overcome in order to initiate crystal nucleation, and this can be achieved by creating a nucleus at or above the critical size. Below the critical radius no stable nuclei can be formed, only unstable ones that form and then melt or dissolve; above this point, however, stable nuclei can form. Thereafter, the free energy is always further reduced by increasing the size of the nucleus more, which enables the nucleus to grow spontaneously and become a crystal [21].

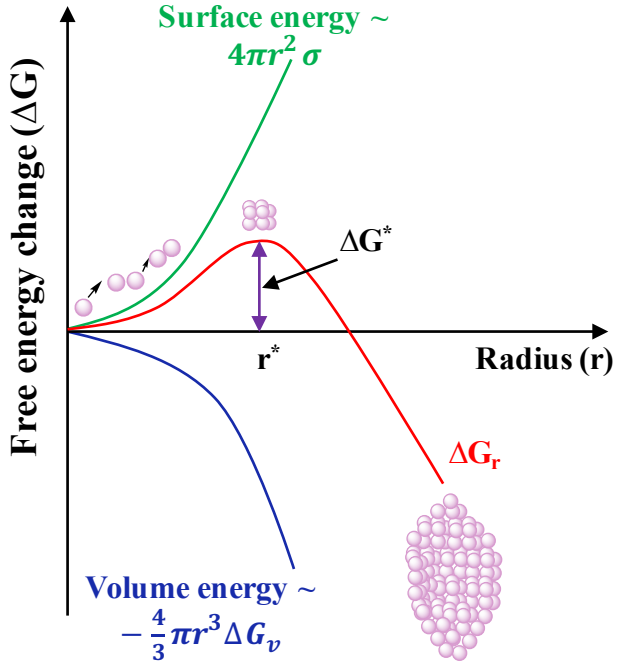

Figure 2.10: A schematic plot of total free energy (red curve) as a function of the radius of the nucleus (r), on which is shown the critical radius of nucleus r* and the energy barrier for nucleation ΔG^*. The contributions of surface free energy and volume free energy are represented by the green and blue curves, respectively. Image inspired from references [22–24].

The above equation (2.3) cannot be applied directly for polymer systems, however, since the nucleus of a polymer is not spherical as assumed in the classical theory for the small molecules. The equation has been modified, therefore, to take into account the special features of polymer crystals. These features include the shape of the polymer nucleus, which tends to be more like a cube than spherical [20, 25], the fact that a single polymer will form multiple unit cells of the crystal rather than a single unit cell, together with the fact that, in polymer crystals, the side surfaces and the fold surface have different free energies associated with them. For this reason, these terms have to be expressed separately as in equation (2.4) below:

$$\Delta G = -v\mu l a_o b_o \Delta G_v + 2v\mu a_o b_o \sigma_e + 2\sigma l(\mu b_o + v a_o) \qquad (2.4)$$

where v and μ are the number of polymer stems in the width and breadth, respectively; l is the thickness of the crystal; a_o and b_o are the cross-sectional dimensions of a stem; and σ_e and σ are the fold and side surface free energies of the crystal, respectively.

2.3.2.2. Growth

Growth or "secondary nucleation" is the second stage of the crystallization process. It occurs after the formation of the primary nucleus, where the nuclei grow from the microscopic scale into macroscopic crystals. The nucleus develops into a lamella and then the lamella branches and splays to create spherulite growth. The theoretical understanding of polymer crystal growth is incomplete, however, since no single theory can account for the wide range of different polymer crystal morphologies that are observed. At a microscopic level, however, a number of theories exist that provide insight into how individual molecules attach to the growth front, and these can, in a certain number of systems, account well for the observed crystallization habits. These systems are typically idealized and chemically simple PE systems [26], but in more chemically complex polymer systems the theories fail, indicating the need for more mesoscopic or macroscopic theories of spherulite formation to account for the wide range of observed polymer crystal morphologies.

Some selected studies that involve these two major events (nucleation and growth), will be presented and discussed later in Section 2.6, with an emphasis on AFM studies.

2.3.3. Secondary Nucleation Theory

In the 1960's, secondary nucleation theory, which is also known as Hoffman–Lauritzen theory (LH theory), was developed by Hoffman and Lauritzen [27, 28]. LH theory is the most successful and widely accepted theory, and is a molecular scale theory based on chain attachment during polymer crystallization, or secondary nucleation, to an existing crystal growth face or "substrate". Figure **2.11** shows a representation of polymer crystal growth based on LH theory where, after the initial attachment of a stem onto the substrate, further stem attachment occurs in the niches at either side of this initial stem [18].

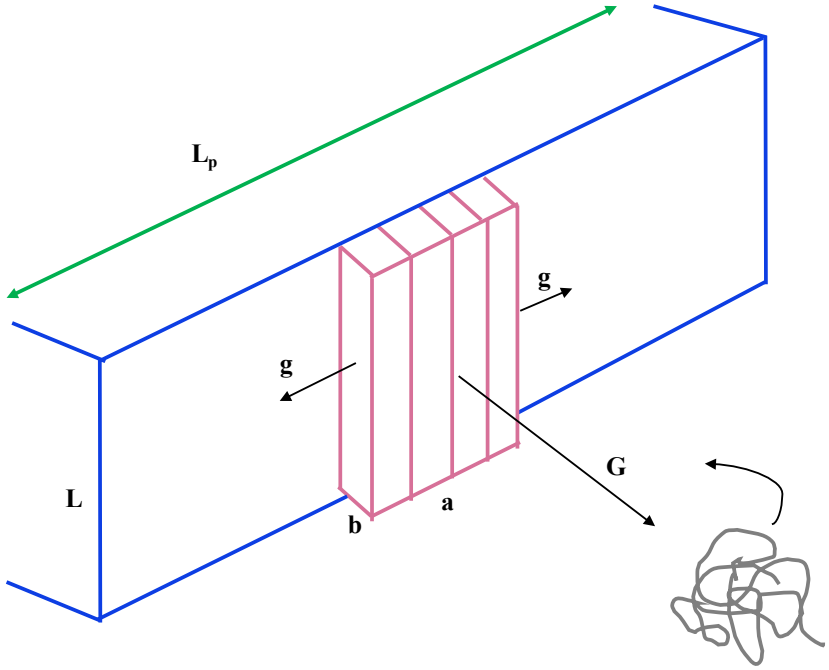

Figure 2.11: A schematic diagram showing the basic model of LH theory, where: L is the crystal thickness; L_p is the substrate length; a and b are the stem dimension; g is the substrate completion; G is the growth rate.

Generally speaking, the crystallization kinetics of polymers involve two essential stages: nucleation and the diffusion of crystallizable chains to the crystal front. The kinetic theories of crystallization from the melt generally lead to predictions of the temperature dependence of the transport of the crystallizing segments and the nucleation rate of the crystal [29].

The LH equation is given by equation (2.5), which describes the dependence of the linear growth rate on the temperature:

$$G = G_o \exp\left[-\frac{U^*}{R\,(T_c - T_\infty)}\right] \exp\left[-\frac{K_g}{T_c(\Delta T)f}\right] \tag{2.5}$$

where G is the growth rate, G_o is the growth rate constant, R is the gas constant, T_c is the crystallization temperature, $T_\infty = T_g$ - 30 (K), ΔT is the supercooling, equal to $T_m - T_c$, f is a factor given by $\frac{2T}{T_c+T_m}$, U^* is the activation energy for polymer diffusion (the transport of chain segments to the crystallization site), and K_g is the nucleation rate constant which is given by:

$$K_g = \frac{m\, b_o \sigma \sigma_e T_m}{\Delta h_f k_B} \tag{2.6}$$

where b_o is the layer thickness (width of chain), σ and σ_e are the layer and fold surfaces' free energy, Δh_f is the heat of fusion per unit volume, k_B is the Boltzman constant, and the value of *m* depends on the crystallization regime.

According to LH theory, the crystallization range of a polymer is divided into three different regimes (I, II and III), which depend on the rates of two key processes: secondary nucleation (i) and lateral spreading, or substrate completion (g). Figure **2.12** (a) schematically illustrates crystal growth onto a substrate for these three different regimes: (1) the initial step, which is formation of a nucleus, (2-4) the three regimes, along with a diagram for the crystal growth rate with temperature in Figure **2.12** (b).

These three regimes are summarized as below:

- **Regime I**: At high crystallization temperatures (low ΔT)
  - Low nucleation rate (sites or events)
  - Substrate completion rate >> secondary nucleation rate (g>>i)
  - Once a single nucleus forms, subsequent lateral growth will quickly overspread a layer, before the formation of another nucleus. Thus, the nucleation rate controls the crystal growth rate.
  - The secondary nucleation rate dominates the overall crystal growth rate.

$$G_I \propto i \tag{2.7}$$

- **Regime II**: At lower crystallization temperatures (medium ΔT)
  - There is competition between the nucleation rate and substrate completion rate (they are comparable) (g ≈ i).
  - Both the secondary nucleation rate and substrate completion rate are important to the overall crystal growth rate.

$$G_{II} \propto (2ig)^{1/2} \propto i^{1/2} \tag{2.8}$$

- **Regime III**: At even lower crystallization temperatures (very high ΔT)
  - The nucleation rate is much higher than the substrate completion (g<<i)
  - Nucleation is the dominant process.
  - The growth rate follows the same relationship as in regime I.

$$G_I \propto i \tag{2.9}$$

These three regimes have been experimentally observed for a large number of polymers. Depending on the crystallization conditions, such as molecular weight and atmospheric pressure, most polymers exhibit different regime behaviours. For instance the crystallization behaviour of PE shows Regime I and Regime II [30] while polypropylene shows Regime II and Regime III [31].

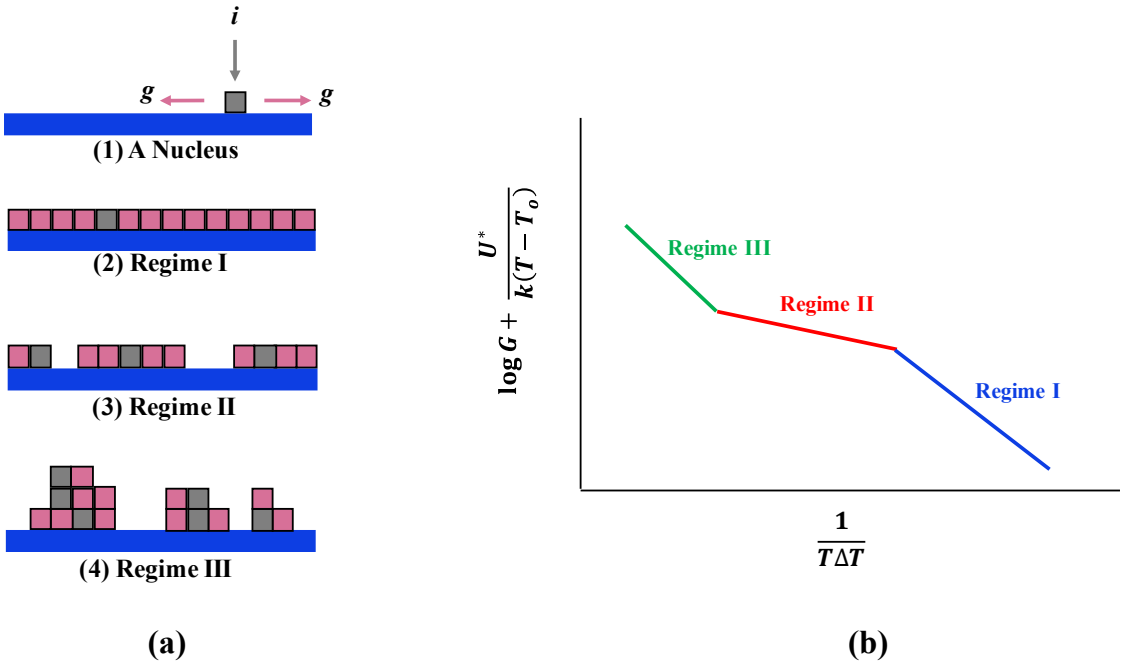

Figure 2.12: (a) Diagram showing the LH model. The grey blocks indicate the secondary crystal nucleation while the pink blocks indicate the substrate completion into the resultant niches in the different regimes of growth. *i* represents the stem nucleation rate while *g* represents the substrate completion rate. (b) Schematic representation of the temperature dependence of the crystal growth rate for the three regimes in LH theory [26].

2.4. Crystalline Morphology and Theories

The morphologies of polymer crystals and their evolution provide important information on the crystallization mechanisms as well as on the relationship between the crystalline states and their performances. Crystallization in polymers can be divided into three kinds: crystallization under quiescence, crystallization under flow and crystallization during polymerization. The final morphology of polymer crystals varies for each type, depending on the processing conditions. For example, crystallization from a quiescent diluted solution leads to the formation of a single crystal, while crystallization under flow leads to shish kebab crystals, as will be shown in more detail below. Moreover, dependent on the conformation of the polymer chain, two types of crystals can be formed; a random polymer chain will lead to lamellar chain folded crystals that finally form spherulite structures, and this occurs if polymers crystallize in a quiescent state (i.e. in the absence of flow or stress) [32], while a fully extended chain

will lead to extended chain crystals, finally resulting in shish-kebab structures, and this occurs if the polymer crystallizes under a strong enough flow or shear [32], otherwise (i.e. under a relatively weak flow) only oriented crystals will be formed (not a shish-kebab structure) (see Figure **2.13**).

The three main crystalline morphologies, which are single crystal, spherulite and shish kebab, are described and discussed below with their relevant proposed models.

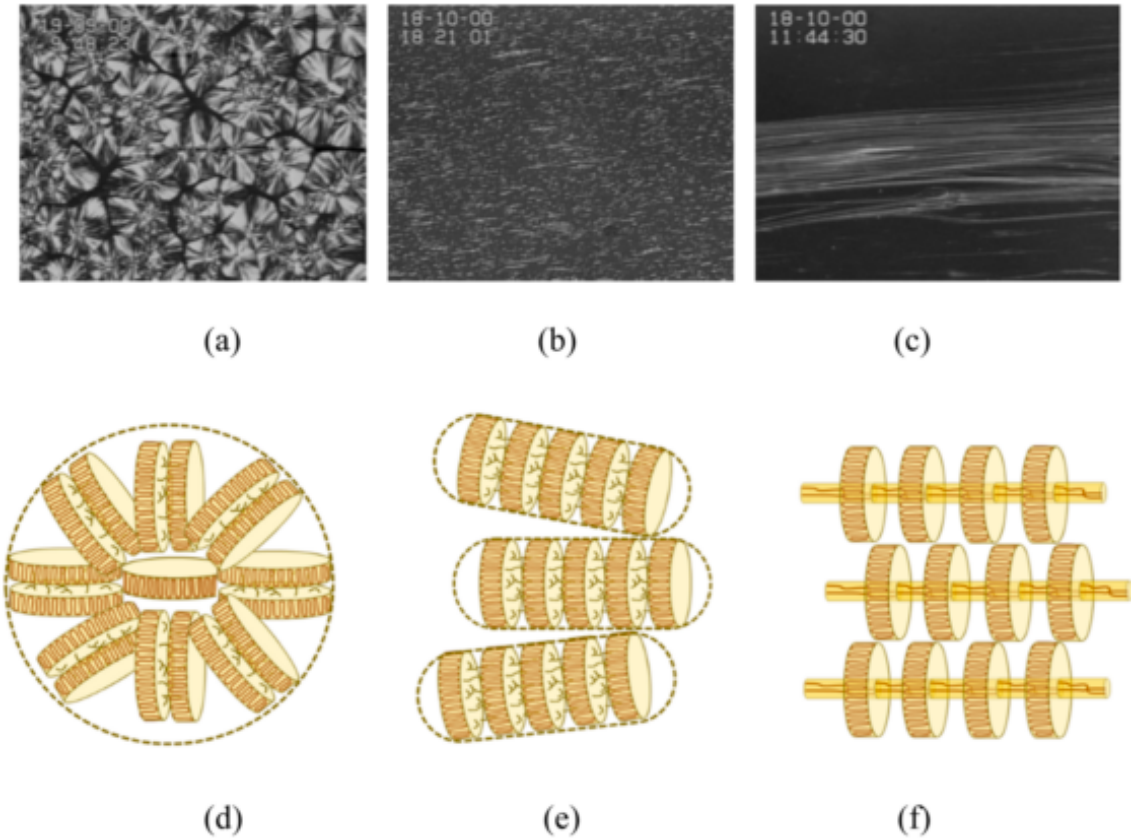

Figure 2.13: Typical morphologies of flow-induced crystallization with (a) no flow, (b) weak flow, and (c) strong flow. The difference in crystallite structures is illustrated by (d−f). Image adapted with permission of [24]. Copyright (2016) American Chemical Society.

2.4.1. Single Lamellar Crystals

A single crystal can form when a polymer crystallizes from a diluted solution or melt. Many studies have been performed to study single crystal polymers, leading to the discovery of a new feature of polymer crystallization and thus contributing to the

increased knowledge of this complex process. In 1957, in three different studies of PE by electron diffraction experiments, Keller [1], Till [33] and Fischer [34] found that, upon crystallization from dilute PE solutions, the polymer chains fold back and forth upon themselves to form platelet single crystals called lamellae (see Figure **2.14**), which is unique to polymers. This was in agreement with an earlier suggestion by Storks [35], who observed that the chain was much longer than the lamellar thickness, leading him to first propose a chain folded structure. The thickness of a typical lamella is around 10 nm while its lateral dimensions are in the order of a few μm.

After studying single crystals from dilute solutions [1, 33, 34], single crystals from melt were also studied by Keller and Toda [36]. Only a few studies have been conducted on single crystals from the melt, however, due to the difficulty of preparing single crystals from the melt.

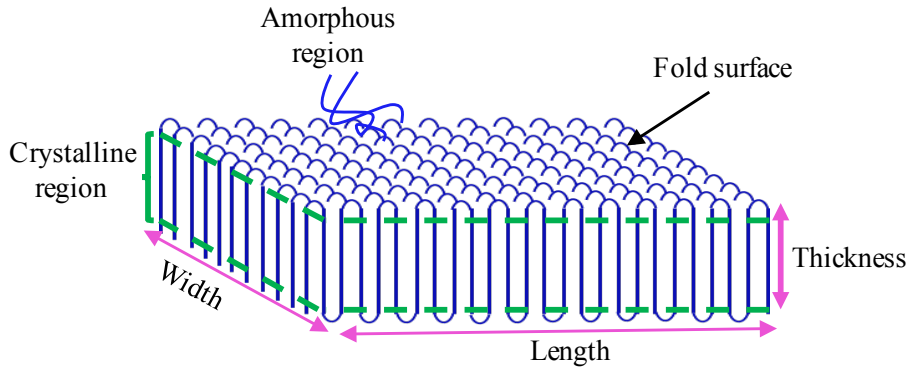

Figure 2.14: A typical lamellae structure

Three basic models of a folded chain lamellar structure have been proposed:

1. Smooth chain-folded surface, adjacent re-entry chain-folded model. There is a sharp phase boundary between the crystal and amorphous phase since the re-entry of the chains is regular (Figure **2.15** (a)) [1, 37].

2. Rough chain-folded surface, since the re-entry of the chains is irregular (Figure **2.15** (b)) [37].

3. Switchboard, random re-entry folded model where the chains randomly fold back into the same lamella or even participate in neighbouring lamellae (Figure **2.15** (c)) [38].

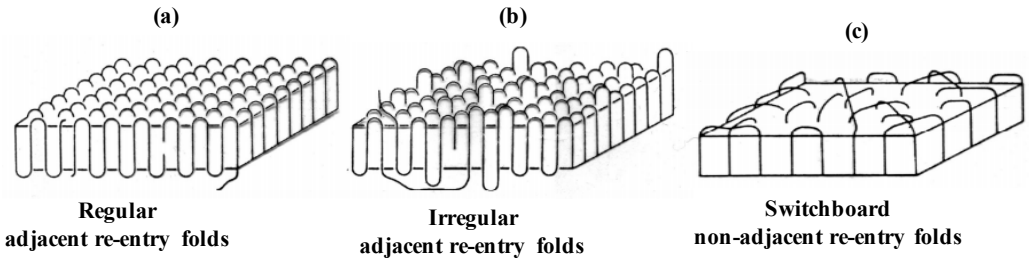

Figure 2.15: Folded-chain lamella models: (a) regular adjacent folds; (b) irregular adjacent folds; and (c) nonadjacent switchboard [37].

There are two basic lamellar orientations at the surface of a polymer film: edge-on and flat-on. Figure **2.16** shows a schematic illustration of these two possible orientations. The orientation of lamellae has been found to be dependent on factors such as crystallization temperature and film thickness. Flat-on lamellae tend to develop at low crystallization temperatures while edge-on lamellae develop at high crystallization temperatures. Additionally, flat-on lamellae are found more in ultrathin films while edge-on lamellae are more common in thicker films [39], even at very high crystallization temperatures. This is because flat-on lamellae take a long time to appear at the surface, since they originate at the interface between the substrate and polymer [40, 41].

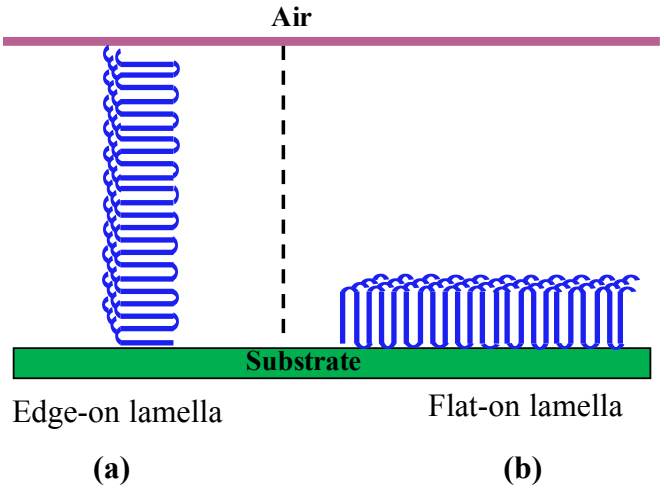

Figure 2.16: A schematic diagram showing the possible orientation of lamellae: (a) edge-on and (b) flat-on.

2.4.2. Spherulite: (Crystallization under Quiescent Conditions)

Spherulites are symmetrical spherical crystal colonies and are common structures for polymer crystallization from the melt, particularly when the polymer melt crystallizes in a quiescent state, when no external forces are applied, such as flow or shear, as mentioned above. An example of such a structure is shown in Figure **2.17**. They essentially consist of multiple lamellae, or single crystals, that grow from the nucleus and then branch and splay, resulting in the formation of spherulites. The size (or radius) of these structures increases linearly with time in most cases, until it stops growing as it impinges upon neighbouring spherulites, and can be in the order of 0.5-100 μm [29].

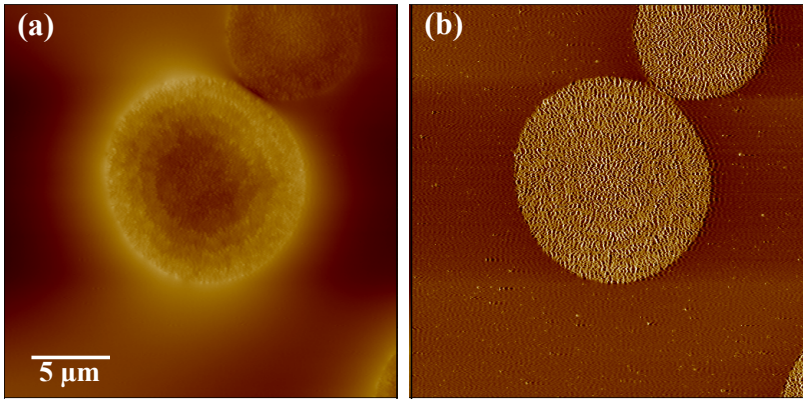

Figure 2.17: AFM (a) height and (b) phase images of spherulite PHB/V.

Based on the experimental results, there are two main categories of spherulite: category one and category two [42–44]. Category one spherulites consist of lamellae growing radially from some nucleation site, which occasionally branch in order to continue to fill space as required for radial growth. Category two spherulites are a single lamella which then grows and branches. As the category two spherulite grows, this branching of the original lamella leads to the formation of a crystal sheaf with two "eyes" at either of the lateral sides of the original lamellae. Eventually, after the formation of these "eyes", and further spherulite growth, category one and category two spherulites grow in a very similar manner, with radial growth and branching to fill space effectively (see Figure **2.18** (a)). Figure **2.18** (b) shows the development of a spherulite and its molecular sub-structure. It gives a rough indication of how a single lamella branches and how the separate branches then splay in three dimensions to form a spherulite.

The branching performed by the lamellae, which gives rise to the spherulite structure, is thought to occur due to dislocations of crystals [45] or impurities, which allow a deviation from the regular crystal structure [46]. No definitive answer as to how branching, and hence space filling, occurs during spherulite growth has yet been provided, however.

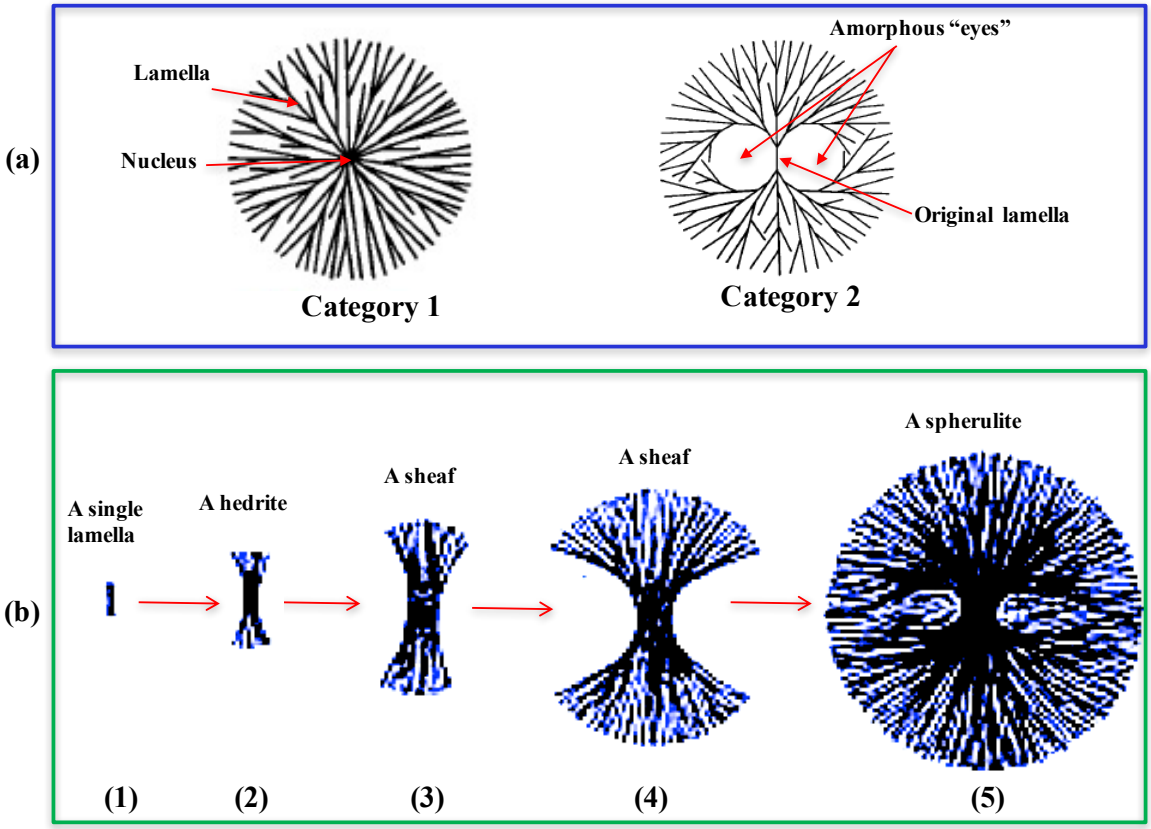

Figure 2.18: Schematic diagram showing (a) the two different categories of spherulites and (b) spherulite development stages that start from (1) a single lamella, (2) a hedrite, (3-4) a sheaf, and (5) a fully developed spherulite. Image copied from references [42, 43, 47].

Furthermore, the morphology of spherulites depends on many parameters such as lamellar twisting. Twisting is a relatively common feature amongst systems that form fibril-like structures upon crystallization, and has been known about for a long time. This feature was identified in 1929 by Bernauer [48], who recognized 135 organic compounds which gave rise to twisted structures upon crystallization. Twisting is displayed in many polymer systems, such as PE, Nylon and PET. Many mechanisms for lamellar twist in polymer spherulites have been proposed. Some of the suggested causes for lamellar twisting are listed below:

1. Surface stresses from crowded fold surfaces [28, 49].
2. Stresses on the lamellar edges from rejected impurities [50].
3. Unbalanced surface stresses deriving from chain tilting in lamellae (surface stresses experienced by the lamellae) [51].

4. Bending caused by the elastic bending of radially oriented lamellae (i.e. elastic bending of lamellar crystals caused by the chain folding in opposite directions on opposite faces of the lamellae) [52].

2.4.3. Fibre and Shish Kebab: (Crystallization under Flow)

The shish kebab structure was first observed by Pennings [53, 54] who worked on PE fractionation solutions. The term "shish kebab" was coined by Keller [55]. Shish kebab and fibre crystals form when polymer crystallizes under flow-induced conditions (when flow is applied to the melt) in contrast to spherulites, which form in the absence of flow (i.e. in a quiescent state). When flow or stress is applied to polymer melts or solutions, the chains are aligned and stretched in the direction of the flow. These stretched chain fibrils will be the central core, which is known as the "shish"; then folded chain lamellae, which are called "kebabs" in this case, grow perpendicularly on the shish, resulting in the final structure shown in Figure **2.19**.

Stretching or orienting the polymer chains affects the manner of crystallization and the resultant morphology. The crystallization behaviour therefore differs from that in crystallization from a quiescent state. For example, the crystallization process under flow conditions occurs at lower supercooling and the crystallization rate will be higher than that in quiescent conditions due to the decrease in the entropy of fusion. Moreover, since the formed morphologies are different, the properties of shish kebab crystals will be different from those in spherulites.

According to Keller and Kolnaar [32], chain extension promotes crystallization for two reasons. First, it increases the melting, and thus crystallization temperature, of the material due to the lower entropy, and thus higher free energy, of an extended chain compared to a random coil. Crystallization is enhanced, since the supercooling for any temperature below the melting temperature is increased. Second, the extended chain is closer to its final conformational state in a crystal and has, therefore, a lower kinetic barrier to overcome than a chain in a random state.

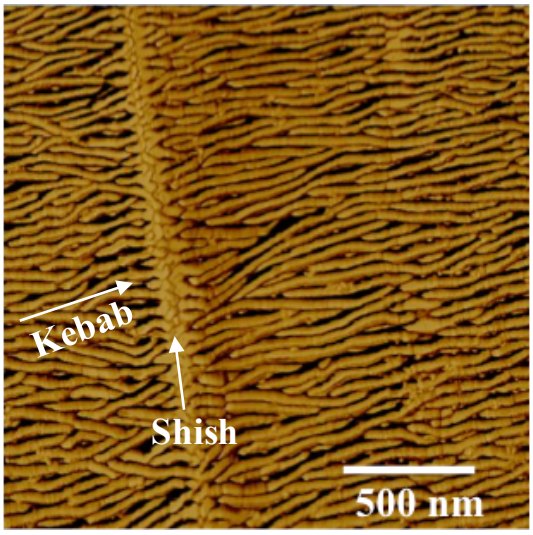

Figure 2.19: An AFM phase image showing the shish kebab structure that formed by shearing PE film using a similar approach as in [4, 56].

2.5. Block Copolymer

2.5.1. Introduction to Block Copolymers

A copolymer is a type of polymer that is synthesized from two or more different species of monomers that are covalently linked together, in contrast to a homopolymer where it is made of only one type, as mentioned above. According to the arrangement of these monomers along the chain, copolymers can be classified into different kinds including random, alternating, graft and block copolymers (see Figure **2.20**). Block copolymers can in turn be split into different classes such as diblock (consisting of two blocks) and triblock (consisting of three blocks). Since a diblock copolymer was used in this study (more details about the sample used are provided in Chapter 4), the focus in the sections below will be on the phase behaviour and crystallization of diblock copolymers.

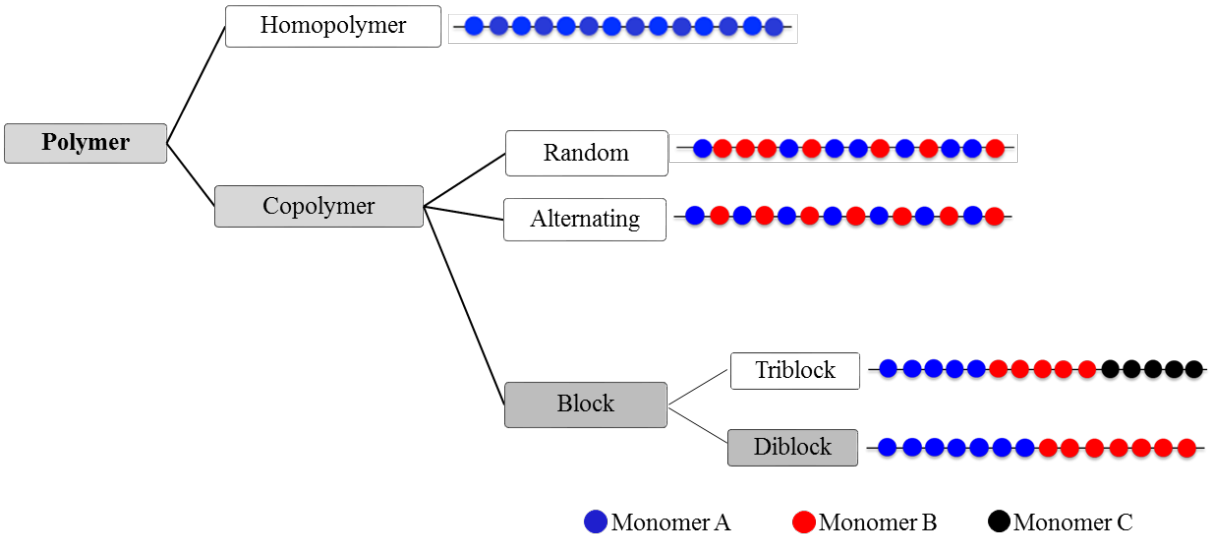

Figure 2.20: A diagram showing the difference between a homopolymer and copolymers, and the different types of copolymers based on the arrangement of the distinct monomers.

2.5.2. Diblock Copolymer Microphase Separation

As mentioned above, diblock copolymers (known also as an AB block copolymer) are a type of copolymer that consist of two chemically distinct blocks (i.e. A and B blocks) [11] that are thermodynamically immiscible with each other. The immiscibility or repulsion between blocks A and B causes them to separate (segregate) (Figure **2.21**), with features sized typically on the scale of tens of nanometres [57, 58]. This phenomenon, or process, is called "microphase separation" and the resulting morphologies are called "microphase-separated structures", or "microphase separation structures" or "microdomains" (i.e. A-rich and B-rich regions). The phase separation is a similar situation to that of oil and water; i.e. since oil is not miscible in water it separates into droplets. Since the unlike blocks in diblock copolymers are covalently bonded to each other, however, the kind of macroscopic phase separation one sees with oil and water (i.e. separation at large scale lengths) cannot occur. Thus, diblock copolymers microphase separate rather than separate macroscopically.

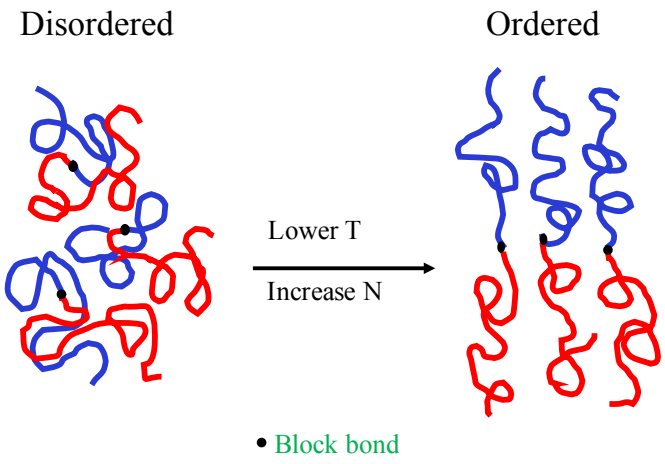

Figure 2.21: Microphase separation in diblock copolymer melt.

Figure **2.22** (a) demonstrates the various periodic structures that result from microphase separation of the copolymer blocks. These microphase separation structures (microdomains) include: lamellae, spheres, cylinders and gyroids. The exact morphology that is formed depends on three main factors: (1) the volume fraction of the block (*f*), (2) the degree of polymerization (N) and (3) the Flory–Huggins interaction parameter (χ) between the different blocks, which represents the strength of the repulsive interaction between two blocks (Figure **2.22** (b)) [11, 58–60]. The Flory–Huggins interaction parameter is inversely proportional to the temperature [61] (see equation (2.10) [62, 63]

$$\chi = A/T + B \tag{2.10}$$

where χ is the interaction parameter between the blocks, A and B are constant, and T is temperature.

At $\chi N \leq 10$, the system will be in a homogenous melt (i.e. a disordered phase). As the temperature decreases, χ increases, according to Equation 4, meaning that the degree of segregation increases. The degree of microphase separation (the interblock segregation strength) is controlled by the value of χN. At $\chi N \approx 10.5$, which is a critical value for a

symmetric diblock (i.e. where $f = 0.5$, and thus the volume fraction of blocks A and B are equal), phase separation occurs [64] (see Figure **2.22** (b)). This value has been shown to extend to around $\chi N \approx 20$ for a symmetric diblock [59].

The point at which phase separation occurs is known as the order-disorder transition (ODT), and the temperature at which this occurs is called the order-disorder transition temperature (T_{ODT}). As the value of χN increases further ($\chi N \geq 50$), a well-ordered phase separation is produced, with a sharply defined interface between the two blocks. Thus, as the χN increases the segregation strength increases. Three main regimes have been defined depending on the degree of segregation of the blocks (value of χN) [62]:

1. Weak segregation regime ($\chi N \approx 10$)
2. Intermediate (soft) segregation regime ($100 \geq \chi N \geq 10$)
3. Strong segregation regime ($\chi N \geq 100$)

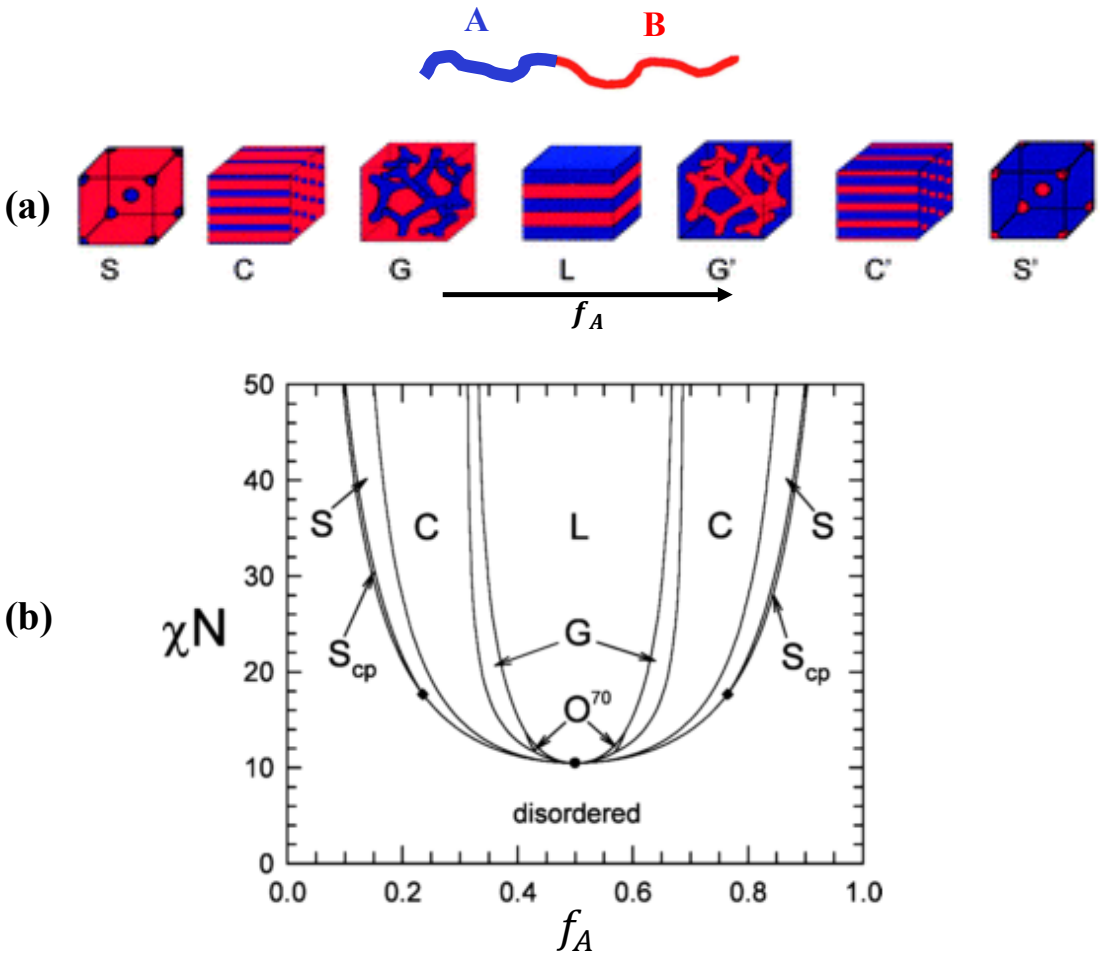

Figure 2.22: (a) The most common microdomain morphologies formed in diblock copolymers, including spheres (S), cylinders (C), gyroids (G), and lamellae (L), as well as the disordered (homogeneous) state at small interblock segregation strengths (χN). The two blocks A and B are indicated by the blue and red colour, respectively. As the volume fraction of A (f_A) increases (from left to right) it changes from being the minority block to being the majority one with the changing microdomain morphology: starting from a sphere when the f_A is lower (in the diagram (b) to cylinders, gyriods and lamellae. G', C' and S' represent the morphology when f_A increases to beyond 50%, meaning that the A and B microdomains are inverted. **(b)** Schematic of a diblock copolymer phase diagram. f = volume fraction of A block, χ = Flory interaction parameter, N = diblock degree of polymerization [65].

Along with the importance of χN in the phase behaviour of block copolymer, the volume fraction (f_A) of the block also plays an essential role in determining the structures that are formed. One of the components (A or B) will be the minority block and the other will be the majority block (i.e. the matrix).

How the f_A influences the structures that are formed is summarized below [66]:

1. f_A = 0-21% leads to the formation of spheres of A in a matrix of B.
2. f_A = 21-33% leads to the formation of cylinders of A in a matrix of B
3. f_A = 33-37% leads to the formation of gyroids of A in a matrix of B
4. f_A = 37-50% leads to the formation of lamellae (i.e. $f_A = f_B = 50\%$), this can be seen in the centre of the diblock copolymer phase diagram, Figure **2.22**.

As f_A increases further (i.e. more than 50%) the A block will be the majority block and B will be the minority one, which means A and B microdomains will be inverted. Thus, similar behaviour occurs but this time B microdomains will be in a matrix of A (see the right-hand side of Figure **2.22** (a).

2.5.3. Crystallization of Diblock Copolymers

The final morphology of a diblock copolymer that has a crystallizable block does not only depend on the microphase separation process driven by the incompatibility of the two blocks but also on the crystallization of one of the blocks [67]. The final structure is therefore a result of the interplay of several factors during crystallization. In this respect, the literature has reported a number of different situations. Loo *et al.* [68] classified crystallization in a diblock copolymer with one crystallisable block (as with the system studied in this project) into three crystallization modes: confined, templated and breakout crystallization (see Figure **2.23**). "Breakout" crystallization describes the situation where the growing crystals break out from the pre-existing microphase-separated structures (microdomains) to form a lamellar structure (the crystallization does not depend on the existing melt structure). "Confined" crystallization, however, describes the situation where individual crystallites are completely confined within pre-existing microdomains. "Templated" or "soft confined" crystallization represents the situation where the growing crystals generally follow the pre-existing microdomains, but would occasionally connect cylinders, such that many microdomains could ultimately be crystallized from one nucleus.

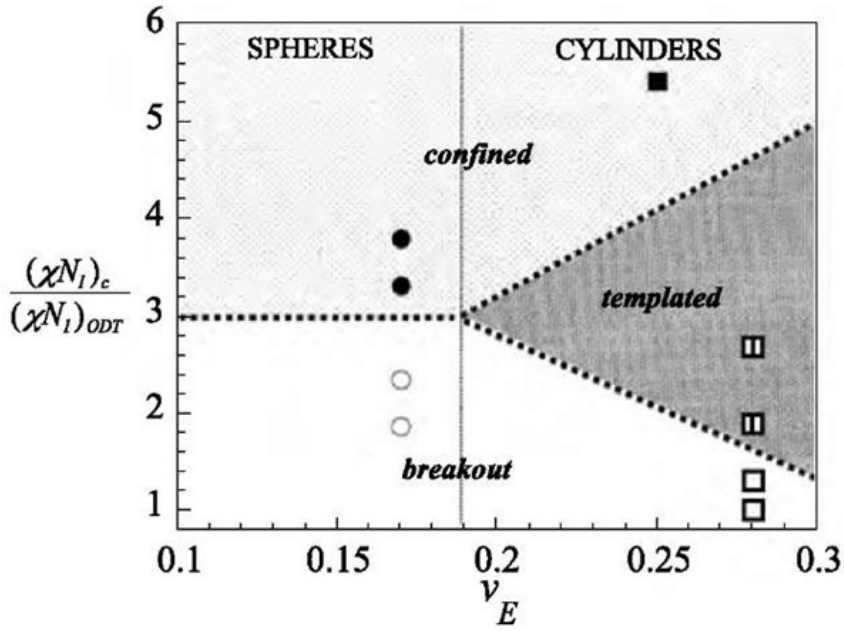

Figure 2.23: Classification map for semi-crystalline block copolymers with rubbery materials. Three modes of crystallization were observed: 'breakout' wherein the melt structure is completely destroyed upon crystallization; 'templated' wherein the melt structure is generally, but not fully, preserved in the solid state; and 'confined' wherein crystallization occurs within the microdomains prescribed by microphase separation so the nanoscale domains are effectively preserved upon cooling [68].

The final morphology of the crystalline-amorphous block copolymer also depends on the relationship between the T_{ODT}, T_c of the crystallizable block, and the T_g of the amorphous block. A summary of the different possible morphologies is illustrated in Table **2.1**.

In the case where $T_{ODT} > T_c > T_g$, there is a competition between the phase separation and the crystallization process. If the crystallization process is dominant, the resultant structure will be similar to the lamellae structure. This is in the case in weak segregation, where the crystallization destroys the domain structure allowing the lamellar structure to be formed. In strong segregation, however, the crystallization cannot break out from the microdomain structure. If the rate of diffusion of the

crystallizable block between domains is low enough, the growing crystals cannot grow between melt domains, so each nucleated crystal will crystallize the material in that domain, but will be unable to move to other domains to crystallize the rest of the material. This is known as confined crystallization. In soft confined systems, mixed behaviour can be exhibited (confined and breakout), this is called templated crystallization.

Table 2.1: A summary of the different possible morphologies of diblock copolymers with one crystallizable block, with the morphologies depending on the relationship of segregation strength and the three important temperatures (T_{ODT} ,T_c , and T_g).

Segregation	T_{ODT} /T_g /T_c	Crystalline Morphology
Strong segregation (High χN)	$T_{ODT} > T_c < T_g$	Hard confinement A strictly confined crystallization in a glassy matrix
	$T_{ODT} > T_c > T_g$	Soft confinement The crystallization is confined in a rubbery matrix
Intermediate segregation (Intermediate χN)	$T_{ODT} > T_c > T_g$	Slow cooling: breakout and lamellae are formed
		Fast cooling: confined crystallization
Weak segregation (Low χN)	$T_{ODT} > T_c > T_g$	Breakout and lamellae are formed
Homogeneous melt	$T_{ODT} < T_c > T_g$	Lamellae are formed and surrounded by amorphous material

2.6. Application of AFM in the Study of Polymers

2.6.1. Imaging the Crystallization Process

AFM has become one of the most significant and frequently used tools for the study of polymer crystallization and melting processes, due to its ability to image these processes at lamellar and sub-lamellar scales in real time with minimal sample preparation and high resolution. Some of the key studies that have been performed on different polymer systems by AFM and how this has contributed to the understanding

of polymer crystallization will be presented and discussed below, with an emphasis on the nucleation and growth of crystals.

2.6.1.1. Nucleation

The formation of a crystal nucleus is a complicated process to study due to the very small scale on which it takes place. AFM is a surface technique, which means there is a high probability of the crystallization process being affected by the AFM. Due to these issues, only a few studies have examined the nucleation process (e.g. [44, 68–71]).

A primary nucleus in a polymer was claimed to be visualized *in situ* for the first time by Lei *et al*. [68, 69]. They synthesized a series of poly(bisphenol-A-co-octane ether) (BA-Cn); this polymer crystallizes slowly at room temperature, making it ideal for studying the crystallization process *in situ* using AFM without a hot stage. The authors indicated that the nucleus appears if its size becomes larger than the critical value (stable nucleus), wherein it subsequently develops into an individual lamella; otherwise, if its size is lower than this value, the nucleus disappears. This means that the nucleus is unstable below the critical size. They concluded that the nucleus could be completely disintegrated into amorphous components, but a new nucleus might appear again in the same place if the disintegration is incomplete. When the nucleus reaches the critical size, it grows continuously and develops into a single crystal (a lamella). This lamella started branching when its size reached 1 μm [70]. The authors' use of AFM allowed them to observe the initial nuclei in melts and the development into lamellae at room temperature in real time. Nevertheless, as a result of the extremely small number of nucleation events happening on the surface, detailed kinetic information was not available.

The traditional droplet approach [73] has been used to study polymer systems in order to observe homogeneous nucleation. This approach is based on dividing the sample into small domains (droplets). This leads to the production of a large number of domains of highly supercooled melt; this number exceeds the number of defects or impurities. Hence, it is expected that homogeneous nucleation will occur in some of the defect-free domains.

This method was used by Massa *et al*. [73, 74] to study the nucleation of polyethylene oxide (PEO) using *ex situ* AFM. The nucleation rate was found to depend on the volume of the droplets. Kailas *et al.* [72] also used this approach to study the homogeneous nucleation in isotactic polypropylene (iPP) at high supercooling using AFM with a hot stage *in situ*. The nucleation process can be separated from the growth process only in the case of very small droplets, however. Moreover, the nucleation temperature was found to be dependent on the volume of the droplets and their thickness [72].

Depending on the droplet thickness, different modes of nucleation and growth were observed in iPP nanodroplets. One such mode was the formation of one nucleus, or multiple independent homogeneous nuclei, within a single droplet. Similar results in iPP droplets using AFM have also been obtained recently [76] when the volume of the droplet was less than 13×10^3 nm^3. Above this value, heterogeneous nucleation and fast crystallization occur in iPP droplets. It was indicated that for droplets that are smaller than the critical nucleus size in at least one dimension, the nucleation temperature strongly depends on the droplet height but does not noticeably depend on the volume.

2.6.1.2. Growth

Compared with nucleation, crystal growth has been investigated much more intensively. Following crystallization *in situ* in real time is crucial in order to investigate the internal structure and the formation mechanisms during crystallization. *In situ* AFM investigations of polymer crystallization started to be performed in the middle of the 1990s [3, 9, 76, 77]. Such studies were limited to ambient temperatures until the development of heating devices, however (e.g. [9, 44, 68, 69, 78]). Using AFM with suitable hot-stage devices has enabled the real-time examination of both the crystallization and the melting of a wide range of polymers with nanometre resolution [3, 9, 76, 79]. This has allowed the observation of spherulite growth at the lamellar scale, which has led to many important findings.

The first *in situ* observations of polymer crystallization were reported by Pearce and Vancso [76, 79] and by Hobbs *et al*. [9] . Pearce and Vancso used hot-stage AFM in contact mode to follow the crystallization of PEO, while Hobbs *et al*. used AFM in

tapping mode to follow the growth in poly(hydroxybutyrate-co-valerate) (PHB/V) in real time at the lamellar scale. This allowed the authors to observe the differences between the growth rates of the individual lamellae and that of the bulk spherulite.

Pearce and Vancso [76, 79] reported that their *in situ* AFM findings in respect to the growth rates of individual lamellae were consistent with existing findings obtained by optical microscopy at lower magnifications. Hobbs *et al.* [9] observed similar growth rates at the growth front, whereas their observations at the lamellar scale revealed for the first time that lamellae do not grow at a constant rate. It was found that the growth rate of individual lamellae is not constant at a particular temperature and also differs from one lamella to another. The overall growth rate of the spherulite was found to be constant, however. Similar observations were found in other studies (e.g. [7, 14–17]). Variations in growth rates at the lamellar scale have been confirmed by *in situ* observations of polyethylene shish kebab crystals [4], challenging existing models of polymer crystallization.

Moreover, from the AFM observations of the spherulite growth front [9], it was presented, for the first time, that the spherulite growth front is rough. This is in contrast to the results obtained at the larger scale of optical microscopy, where the spherulite growth front appears to be smooth. Thus, the experimental observations of spherulite growth obtained by AFM contradict classical theories based on optical microscopy, which assume that the growth rate is constant at a particular temperature. The authors therefore suggested that growth theories should be developed to include the implications arising from AFM observations.

Furthermore, shish kebab crystallization was studied for the first time *in situ* at high temperatures using AFM in sheared melts of PE by Hobbs *et al.* [4]. The resolution of the AFM images of PE crystallization was considered to be the highest resolution obtained *in situ* at that time. According to the observations, there are three likely behaviours for the lamellae in two neighbouring shish kebabs:

1. The two lamellae join each other and appear as a single lamella.
2. The two lamellae pass each other and keep growing in their initial growth directions.
3. The two lamellae change their growth directions in order to avoid contact.

This result is in full agreement with the results of the study of BA-C8 conducted by Li *et al.* [79].

Moreover, the isothermal crystallization of PE at a high temperature (133 °C) was followed in real time by AFM [81]. The initial crystallization occurred rapidly at 133 °C, where only a few primary lamellae grew. This was followed by slower branching and in-filling growth. These observations are in full agreement with the findings of previous work that used electron microscopy.

The growth front of the spherulite was observed over a wide temperature range (from just below the melting temperature to close to the glass transition temperature). The spherulite boundary at a low crystallization temperature (10 °C) appeared sharp; at a high temperature, however, this changed [82].

More recently, Mullin *et al.* [56, 82] succeeded in directly imaging the individual polymer chains of high-density polyethylene (HDPE) in ambient conditions with high resolution images (a resolution of 3.7 Å) using a new technology called torsional tapping AFM (TTAFM) with a T-shaped cantilever.

2.6.2. AFM Manipulation of Polymer Chains

AFM has been shown to have the ability not only to image and measure the polymer surface but also to manipulate polymer chains at the nanometre level. Some examples of this will be highlighted below.

2.6.2.1. AFM-Tip-Induced Crystallization

In the application of AFM to study polymer crystallization, a lateral force is required to minimize the influence from the AFM tip on the crystal morphology and the crystallization process (as is discussed in Chapter 3). Some studies, however, have been conducted on polymer crystallization induced by the AFM tip [68, 69, 76, 79, 83–86]. In AFM contact mode, it is expected that the possibility of AFM tip-induced nucleation could be increased by applying a large lateral force. According to a study conducted by Pearce and Vancso [76, 79] of PEO near its melting point, the AFM tip could not

induce crystallization. On the other hand, Beekmans *et al.* [84] reported that the AFM tip can induce poly(e-caprolactone) (PCL) nucleation. The nuclei then grow continuously and develop into lamellar crystals in the direction of the AFM tip scan. The difference in the strength of the lateral forces applied is considered to be the cause of the difference in the above two outcomes. A high lateral force will cause chain orientation at the surface of the melt.

In AFM tapping mode, however, the lateral force is lower than that in contact mode. This is because the tip touches the surface only for a short time (this is discussed in detail in Chapter 3). Using AFM tapping mode, Li *et al*. [68, 69] established that at high supercooling (ΔT = ~60 °C), there was no proof of crystallization induced by the AFM tip in the amorphous region around the crystal. Godovsky and Magonov [86] indicated similar results in polyethylene crystallization. Nevertheless, according to Magonov *et al*. [85], increasing the applied force from light to hard tapping may cause the AFM tip to penetrate the surface of the sample, touching the crystalline core. Thus, the polymer crystallization kinetics could be significantly affected by the AFM tip in tapping mode, and this could even induce polymer chains to pack together to form nuclei in the melt.

Recently, Zhu *et al*. [87] found that the average molecular weight (M_n) of the PEO governs the crystallization induced by the AFM tip. Crystallization of the PEO fractions with M_n below 1.0 x 10^4 g/mol cannot be induced, but crystallization will be inducted at higher M_n values.

2.6.2.2. Control Orientation by AFM

Orientating nano-scale structures within specific localized spaces of polymer films can be helpful in the preparation of nano-scale structures and devices; if carefully controlled, molecular orientation introduces the anisotropy of physical properties. Molecular orientation within polymer films is usually random in nature but a stretching method is usually used to orientate polymer thick films, whereby ordering will occur in bulk. This method is not suitable for ordering specific localized areas, therefore. The changes need to be applied at the molecular level, so some instrumental intervention at the nano level is required to create these localized structures.

In recent years, AFM has been investigated by scientists and has been found to be a suitable method for controlling the orientation of localized areas of polymer thin films. AFM cantilever tips have been successfully used in the modification of a number of polymer thin films at the required nanometre level resolution. In these studies, the tip was used to scan or indent the films, creating ripple structures perpendicular to the fast scanning direction [88]. The modification mechanism in this method is considered to be a mechanical deformation [88–92].

AFM has been used to control the orientation of molecules in various fields, such as in fields involving liquid crystals and polystyrene. In a study involving liquid crystals [93, 94], the ordering (which was driven by rubbing-induced grooves and structural changes) was used for nanolithography and other liquid crystal molecules ordering requirements. In another case, isotactic polystyrene (i-PS) was scratched or rubbed using AFM tips in contact mode at room temperature, and it was shown that both hard scratching and soft rubbing help to lower the nucleation barriers for polymer crystallization [96]. In a further study, under precisely controlled temperatures, AFM cantilever tips in contact mode were used to apply a load along the surface: this is called modification scan [96–98]. This enables the orientation to be controlled in localized areas and for high-density nucleation of edge-on crystals to occur within the disturbed areas. The resultant films are characterized using the same AFM *in situ* by removing a selected region of the well-aligned edge-on lamellae through a process of tip-sample force adjustments. This is called nanodosing.

It will be shown later how the AFM tip was used in this work to both control the orientation of block copolymer microdomains (Chapter 4) and to induce oriented crystals (Chapter 6).

AFM is considered to be the ideal technique for use for studying polymer crystallization compared to other techniques such as scanning electron microscopy (SEM), transmission electron microscopy (TEM), optical microscopy, and X-ray diffraction (WAXD and SAXS). For example, X-ray diffraction techniques are limited to crystalline or ordered structures at room temperature whereas AFM has the ability to achieve nanometre resolution of amorphous materials or disordered structures. Moreover, AFM has become a powerful technique used in *in situ* studies of polymer crystallization while TEM is only an *ex situ* technique, which is not appropriate for

investigating the growth of crystals in real time. Additionally, TEM requires expensive sample preparations and provides 2D images, unlike AFM, which does not require any special sample treatment, and in addition gives quasi-3D images. Besides, AFM provides *in situ* observations with high-resolution images unlike optical microscopes, which provide *in situ* images but at much lower resolutions.

Part II

Experimental

Chapter 3

Experimental Methods

3.1. Introduction

This chapter is split into two sections. The first section explains the main approaches used to prepare the samples, including melt casting, spin coating and drop casting. The second section gives a brief overview of the main experimental techniques that were used in this work, which were ellipsometry, differential scanning calorimetry (DSC), and atomic force microscopy (AFM). The primary focus of the discussion, however, is on the principles and operational modes of AFM, since this allows the *in situ* study of polymer crystallisation and was, therefore, the main technique used in this research. This chapter aims to explain how and why these methodologies were used in this work.

3.2. Sample Preparation

3.2.1 Melt Casting

Melt casting is a simple method that can be used to prepare polymer films. In this method, a small amount of polymer is placed on a clean substrate, such as silicon or glass, then heated above its melting temperature. The polymer is kept at that temperature for a couple of minutes to ensure melting of all the crystalline regions, then it is drawn across the surface of the substrate. In this work, the molten polymer was sheared by a razor blade to form relatively smooth polymer films with a thickness of a few micrometres (see Figure **3.1**). Although it is difficult accurately to regulate the final thickness of the films prepared by this approach, some degree of control can be

achieved by adjusting the amount of polymer deposited onto the substrate and the shearing or drawing force of the polymer across the surface of the substrate. The main advantage of using this method is that polymer films can be prepared without using solvents, which allows the films to be investigated without the effect of residual solvent.

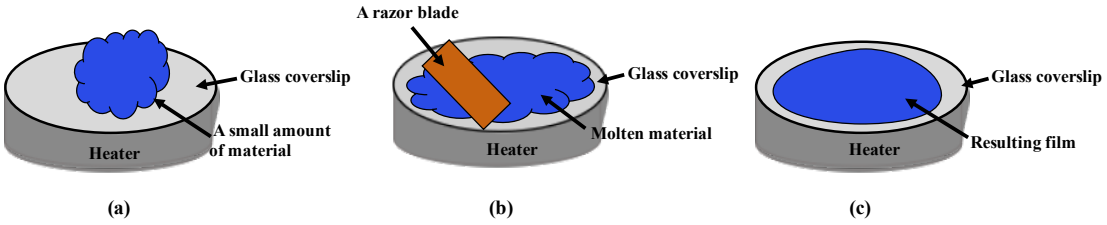

Figure 3.1: A schematic of the melt casting protocol used in this work: (a) applying a small amount of material, (b) heating it above its melting point and then shearing it with a razor blade and (c) the final film.

This method was used for preparing E/MB films as will be shown later in Chapter 4.

3.2.2. Spin Coating

Spin coating is an ideal method to prepare uniform thin films. In this method, an amount of polymer solution is applied onto a substrate, such as glass, silicon wafer or aluminium. Then, it is rotated at a defined speed (typically 1000-10,000 rpm), which serves to spread the fluid by centrifugal force. Finally, the solvent evaporates, leaving behind a relatively uniform and thin layer of the polymer coating the substrate [100]. Figure **3.2** shows the main stages of the spin coating process. The resulting film thickness depends on many controllable parameters, such as solution concentration, viscosity, spin speed and duration [101]. This method has the ability to produce a very thin film with a thickness of about 10 nm or even less.

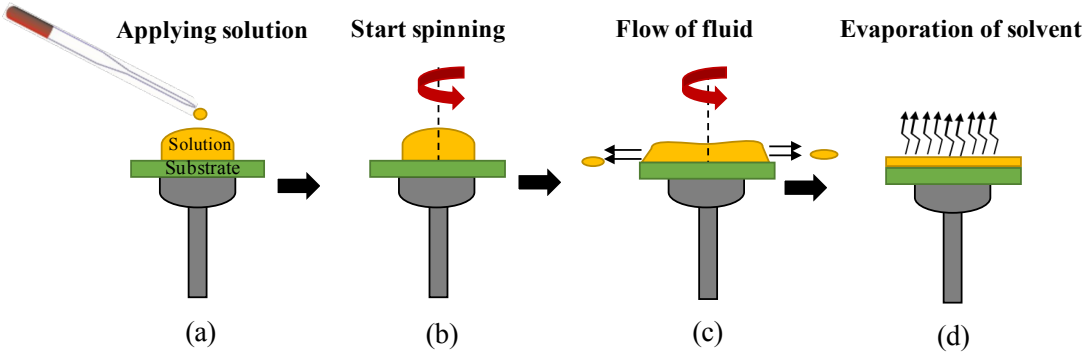

Figure 3.2: A schematic of the ideal process of the spin coating method: (a) drop solution onto the substrate, (b) start rotating it at the set speed and time, (c) the fluid is spread by centrifugal force and (d) the solvent evaporates, resulting in a thin, uniform film.

This was the second method used to prepare thin films of E/MB in order to study the effects of film thickness on the orientation and crystallisation behaviour, as will be shown later in Chapter 4. Film thicknesses were measured by both ellipsometry and AFM. These data are presented in Chapter 4.

3.2.3. Drop Casting

Compared to the spin coating method, drop casting results in thicker polymer films, but has the advantage of being a fast and available approach to generate relatively thin films with no waste of material. It involves placing a drop of polymer solution onto a substrate held at a high temperature (above the melting point of the polymer). Dropping the solution onto the heated substrate while it is kept on the heater speeds up the evaporation process of the solvent, besides melting the crystals of the material. The steps of this method are shown in Figure **3.3**.

One drawback of drop casting is that the ability to control the thickness of films prepared by this method is much more limited than with the other methods, because differences in concentration and variations in evaporation rates across the substrate can result in differences in film thickness. The thickness can be controlled to some extent, however, by careful selection of the solution concentration and the amount of solution that is used.

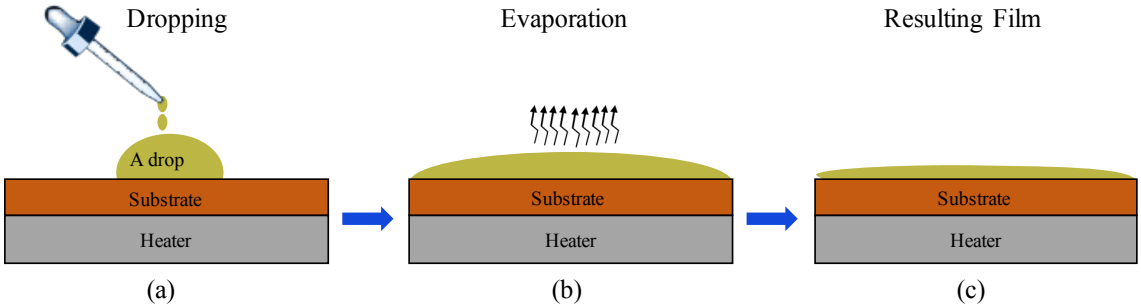

Figure 3.3: A schematic of the drop casting process: (a) depositing drops of solution onto a heated substrate, (b) the solvent evaporates and (c) the resulting film.

This method was employed for preparing PE samples, as will be shown later in Chapter 6.

3.3. Experimental Techniques

This section provides an overview of the main analytical techniques used in this work, which were spectroscopic ellipsometry, DSC and AFM. The discussion will focus on AFM, since this was the primary technique explored in this research.

3.3.1. Spectroscopic Ellipsometry

Spectroscopic ellipsometry is a non-destructive optical technique widely used in scientific research for analysing different surfaces, such as polymers, organics and metals. Ellipsometry is an accurate technique that provides several pieces of information about the sample, such as optical constants and the roughness and thickness of films, ranging from only a few angstroms to tens of microns. This information is obtained simply by analysing the reflected light beam.

Ellipsometry measures the changes in light polarisation, which is represented by two parameters: amplitude ratio (Ψ) and phase difference (Δ), as the light reflects from the surface of the material [102].

In this work, a M-2000V rotating compensator ellipsometer (J. A. Woollam Co. Inc., USA) was employed to measure the thickness of the samples. The samples were measured with a fixed incidence angle of 70° and Complete EASE software was used for the analysis. Measurements were conducted in dry conditions using a multilayer model of silicon and native and generic Cauchy (for the polymer thickness) layers. The averages of different measured thicknesses were taken. The results obtained are shown in Chapter 4.

3.3.2. Differential Scanning Calorimetry (DSC)

Differential scanning calorimetry (DSC) is one of the standard techniques used to measure the thermophysical properties of polymers, such as T_c, T_m, T_g and percent crystallinity. These are acquired by determining the heat flow into or out of a sample material relative to a reference sample [103]. The reference material is used to mark out the baseline for the DSC trace. An example of a DSC plot for a typical semi-crystalline polymer is shown in Figure **3.4**, representing changes in the heat flow that correspond to certain phase transitions (T_g, T_c, T_m), where the exact shape of the curve depends on the latent heat associated with the particular phase transition being investigated [104].

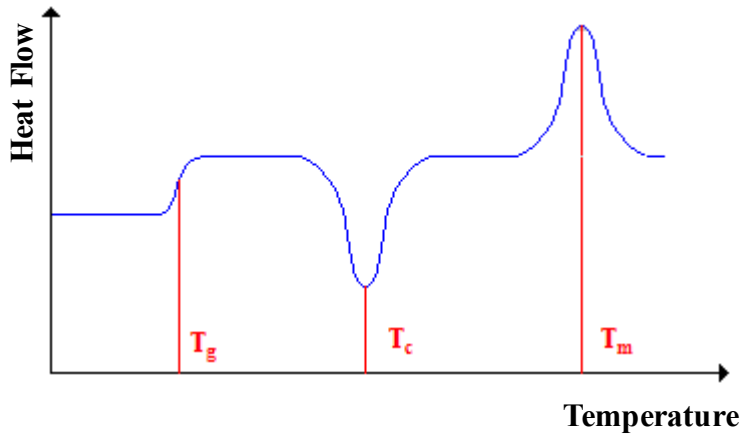

Figure 3.4: An example DSC plot for a typical semi-crystallisable polymer sample

In this work, DSC measurements were carried out using a PerkinElmer Pyris 1 DSC system under Nitrogen atmosphere, with a scan cycle in the temperature range 25–

200 °C, then cooled down from 200 °C to 25 °C at a heating/cooling rate of 10 °C/minute (see Table **3.1**). Measurements were taken on the second heating cycle so as to avoid any effect from the physical reorganisation of the sample within the pans during the first heating cycle. The obtained data are shown in Chapter 6.

Table 3.1: The temperature protocol of the DSC measurement.

	Initial temperature °C	Final temperature °C	Heating/cooling rate °C/ min	Evaluated parameter
1st step	25	200	10	T_m
2nd step	200	25	-10	T_c
3rd step	25	200	10	T_m

3.3.3. Atomic Force Microscopy (AFM)

The AFM is a high-resolution microscopic technique that is a branch of scanning probe microscopy (SPM). SPM instruments principally rely on the use of a sharp probe to study the surface topography and properties of materials at the atomic scale. In these techniques the interactions between the probe tip and the sample surface are measured as a function of the position between them, producing an image or a map of the material's topography. The first SPM technique that allowed the generation of real-space images of surface features with atomic resolution was the scanning tunnelling microscope (STM), which was invented in 1981. STM's ability was limited to the imaging of only conductive and semi-conductive samples, however. This meant that dynamic processes, such as crystallization, could not be studied in non-conducting samples using STM. To overcome this basic disadvantage with STM, AFM was invented in 1986 by Binnig *et al*. [2]. The main advantage of AFM over other techniques is that AFM has the robustness and ability to image almost any sample under any conditions. For example, imaging with AFM can be performed in air, liquid and a vacuum, through a range of temperatures. Moreover, AFM can be employed to study a range of different materials, such as soft biological samples and polymeric materials.

The resolution of AFM images depends on the sensitivity of the measurement of the probe position, and the sharpness of the probe or tip. High resolutions of around 5 nm, and even molecular resolutions, are possible using modern AFMs [104–106]. Furthermore, AFM is able to go beyond imaging actually to manipulate material surfaces (as discussed earlier in Chapter 2, Section 2.6), as well as being able to perform force spectroscopy, as will be shown below.

In the next sections, the principle work related to AFM, its main components and different operational modes, including what information can be extracted about a sample, will be presented and discussed in more detail.

3.3.3.1. Principles

The basic components of AFM are illustrated in Figure **3.5**. AFM uses a sharp tip (probe) attached at the end of a flexible cantilever, which is usually made of silicon or silicon nitride, moving over the surface of a sample in a raster scan. When the tip is brought into proximity with a sample surface, forces between the tip and the sample (attractive or repulsive) lead to a deflection (bending) of the cantilever (towards or away from the sample) according to Hooke's law (equation 3.1):

$$F = -k \cdot x \tag{3.1}$$

where F is the force between the tip and the surface of the sample, k is the spring constant (stiffness) of the cantilever, and x the tip-sample surface distance separation (the cantilever deflection). As the tip of the cantilever is scanned across the sample, the cantilever deflection is monitored by a laser beam, which is focused on the back of the cantilever. The laser beam is reflected onto a four-segment photodiode detector. If the cantilever bends, then the position of the laser beam changes on the photodetector. This change is fed back to the computer into a feedback loop which adjusts the base of the cantilever so as to keep the force between the tip and sample constant (see Figure **3.5**). AFM can scan in many different operational modes [107–109], the most common of which are discussed below.

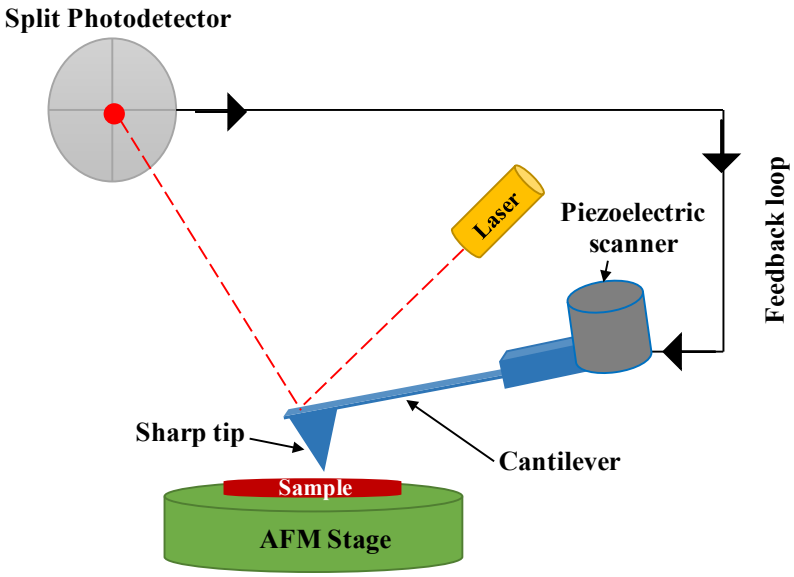

Figure 3.5: A schematic diagram of the fundamental components of the AFM.

3.3.3.2. Operational Modes

AFM can image in three basic modes, namely contact [2, 110], non-contact [112] and tapping (intermittent contact) modes [112, 113]. These three operating regimes are shown in Figure **3.6**, which is a theoretical curve (Lennard-Jones potential) of the main interaction forces between the tip and the surface of the sample, illustrating how the forces between the tip and the sample change according to their distance separation.

In the following sections, an overview of the contact and non-contact modes will be given, together with a more detailed description of the tapping mode, since this was the main mode used in this project.

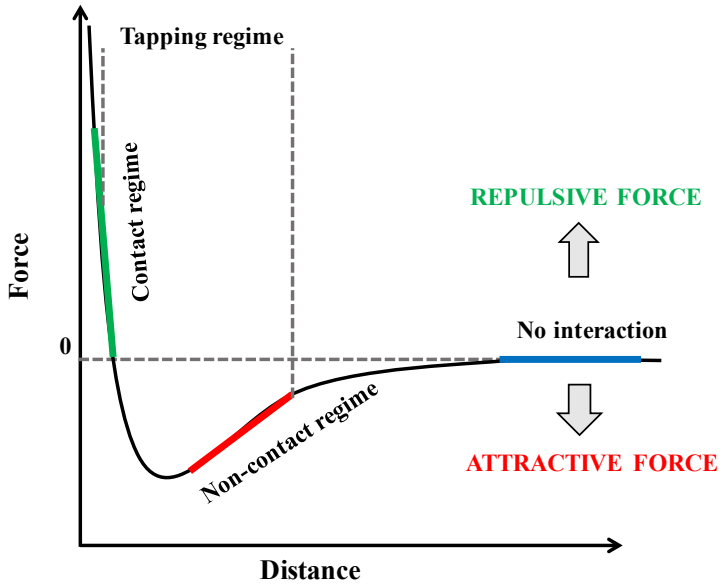

Figure 3.6: A curve of tip-sample interaction forces (Lennard-Jones potential) as a function of the separation distance between them for the contact, non-contact and tapping operating regimes in AFM.

3.3.3.2.1. Contact and Non-Contact Modes

In the contact mode, the tip is raster-scanned across the surface (dragging the surface), being in contact with the surface all the time. In this mode, the distance between the tip and the surface of the sample is just a few angstroms, and the interactive force between the tip and the surface of sample is repulsive (see Figure **3.6**). In the non-contact mode, meanwhile, the tip is oscillating and not touching the surface of sample (this can also be called the dynamic mode). In this mode, the distance between the tip and the surface of sample is in the order of tens to hundreds of angstroms and the interactive force between the tip and the surface of the sample are attractive (see Figure **3.6**).

The force versus distance curve (force spectroscopy) can be experimentally acquired in contact AFM (see Figure **3.7**), and this curve is like the previously mentioned curve in Figure **3.6**. The anatomy of this curve is as below:

(1-2) The separation distance between the cantilever and surface is large, meaning that there is no force interaction between them at this point.

(2-3) As the cantilever becomes close enough to the surface, attractive forces are generated (van der Waals) between the tip and the surface causing the tip to jump into contact.

(3-4) The tip remains in contact with the surface while the base of the cantilever continues to approach the surface until the separation between it and the surface becomes so small as to reach the setpoint; then the cantilever deflects, causing an increase in the repulsive contact force.

(5-6) When the cantilever is retracted from the surface, the cantilever is bent downwards but the tip remains in contact with the surface.

(6-8) The interaction force between the tip and the surface (adhesion) reduces as the separation between them increases until the tip breaks free from the surface.

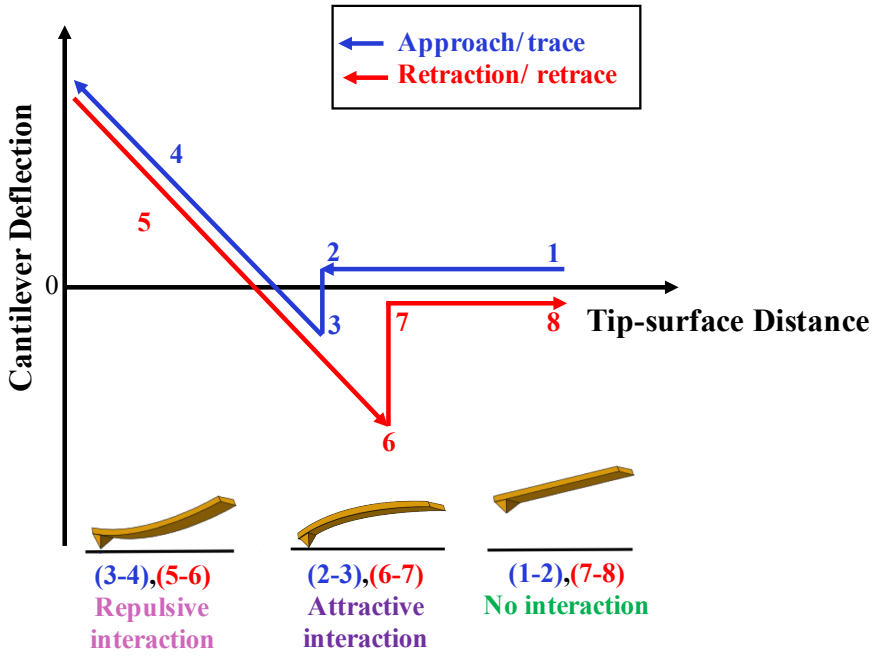

Figure 3.7: A typical force-displacement curve for an AFM tip

3.3.3.2.2. Tapping Mode

The tapping mode is referred to by various names, such as dynamic mode (the same as the non-contact mode), amplitude modulation AFM, and intermittent contact. It entails fluctuating between the contact and non-contact modes as the cantilever is oscillated at or near its resonant frequency, thus "tapping" the surface [114]. The term "tapping mode" is used throughout this thesis.

Tapping mode is a key advance in AFM and was invented to overcome the disadvantages of the contact mode. One of the key drawbacks of the contact mode is

that it is always in contact with the surface of the sample when scanning, which means that it always applies lateral forces that could easily damage weakly bonded particles or soft materials. The tapping mode minimizes these lateral forces since the tip contacts the sample for only a short time. This means that the tapping mode is safer and less likely to damage the surface of samples compared to the contact mode, making it an ideal tool for studying soft materials such as polymers and biological samples. Even when using this mode, however, where the tip was not in continuous contact with the sample surface, it nonetheless was able to exert some degree of influence on the sample surface (this is discussed in detail in Chapter 4).

Another advantage of the tapping mode over the contact mode is that it has the ability easily to distinguish between two different materials since it allows the properties of materials to be contrasted by means of phase imaging (this will be discussed later). It is therefore a very powerful tool to identify different domains, particularly in analyzing composites, blends and block copolymers. This means that the tapping mode AFM is an ideal tool for use in this work since it allows the crystallization processes of polymers to be visualized in real time, *in situ* at different temperatures, without special treatment or preparation of the samples [115].

In tapping mode, relatively stiff cantilevers, normally with resonant frequencies and spring constants from a few kHz to several hundred kHz and between 20-50 Nm^{-1}, respectively, can be utilized. A typical cantilever used in tapping mode is made of silicon and has a resonant frequency and a spring constant of ~300 kHz and ~40 Nm^{-1}, respectively. The resonance peak of such a cantilever is shown in Figure **3.8**.

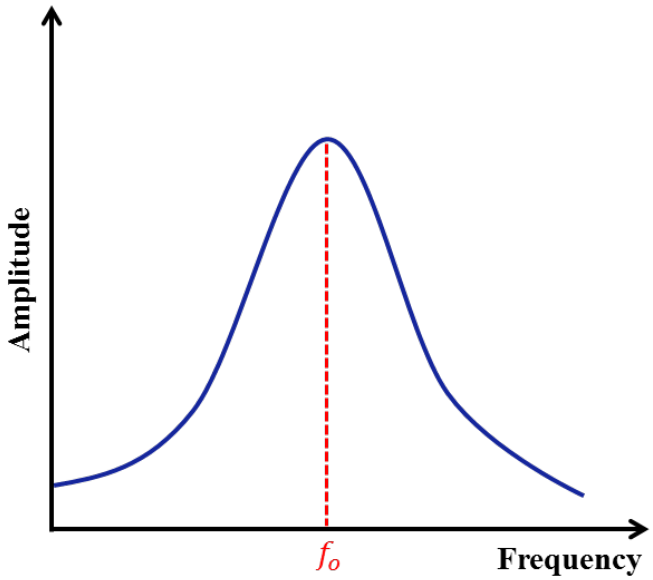

Figure 3.8: A typical curve of a cantilever resonant frequency.

In this operational mode, a resonance peak for the cantilever's oscillations is located (Figure **3.8**); then a lower frequency (slightly away from the peak) is selected. This is because when the frequency is selected to be exactly at the resonance peak any change in the frequency gives rise to a decrease in the amplitude of the oscillations while a frequency just away from the resonance peak allows for increases or decreases in amplitude corresponding to the increases or decreases in the vibrational frequency. Hence, to be able to detect the position of the AFM scan head relative to a surface effectively, a cantilever oscillation frequency just away from the resonance peak is needed.

A controlled piezoelectric actuator that the cantilever substrate is in contact with is then used to oscillate the cantilever near its resonance frequency (i.e. at the selected frequency) which will have some amplitude associated with it (up to 100 nm). As the cantilever taps on the sample, the amplitude of the cantilever that is oscillating in free air (A_o) reduces to match the setup amplitude, as shown in Figure **3.9**. These oscillations, and the changes in them, are detected by the photodetector.

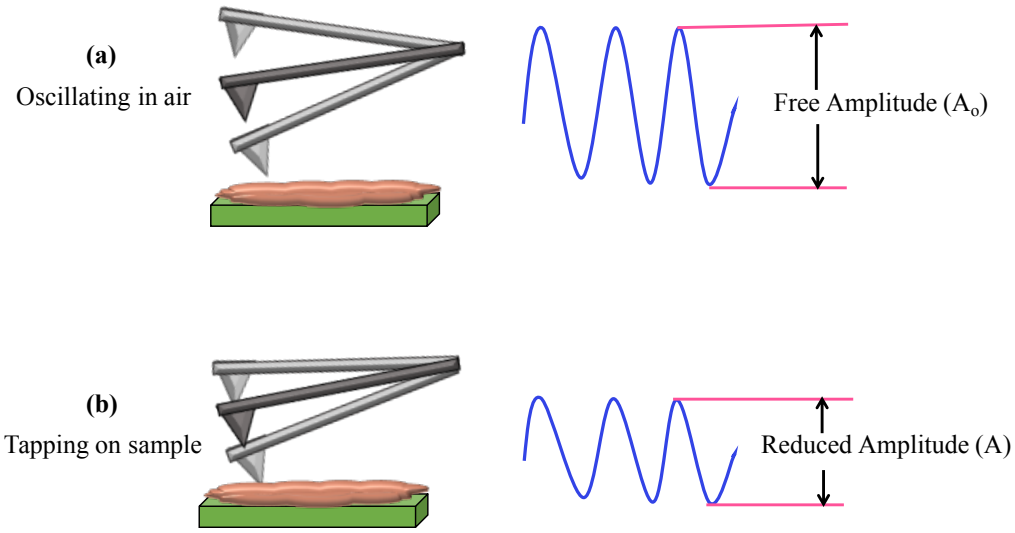

Figure 3.9: Schematic diagram showing the reduction in amplitude as the cantilever approaches the sample.

Height variations in the sample will change the root mean square (rms) of the cantilever's vibrations, which provides information about height, or a topographic map. The value of these cantilever oscillations is kept approximately constant by the feedback loop by adjusting the height of the probe (varying the position of the AFM scan head upwards and downwards) according to the surface feature's height, as shown in Figure **3.10**. This is then used to map the sample's topography and generate the height data.

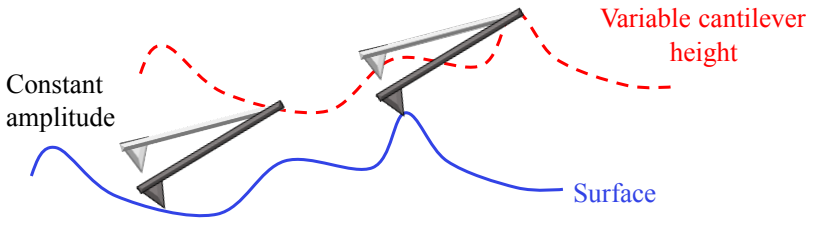

Figure 3.10: A cartoon showing the cantilever position under the action of a feedback loop for an AFM operated in tapping mode.

In addition to height, an image called the "phase image" is collected using tapping mode AFM. The phase image gives key information about the studied samples as will

be discussed below. Phase imaging monitors the phase lag (time delay or local holding time) between the input signal (the signal that drives the cantilever to vibrate) and the output signal of the cantilever oscillation (the oscillating response of the cantilever). A soft region has a big contact area between the tip and the surface and because of this contact area, there is more adhesion and the adhesion causes a delay. The phase lag will therefore be larger when the tip is scanning a softer area whereas it will be smaller when the tip is scanning a hard area (Figure **3.11**). In this manner, material properties such as elasticity, adhesion and friction can be mapped, in addition to the simultaneous capture of height. This makes the tapping mode a very powerful tool for mapping at very high resolution variations in sample properties, especially when looking at phase separated block copolymers, as in the work presented in this thesis.

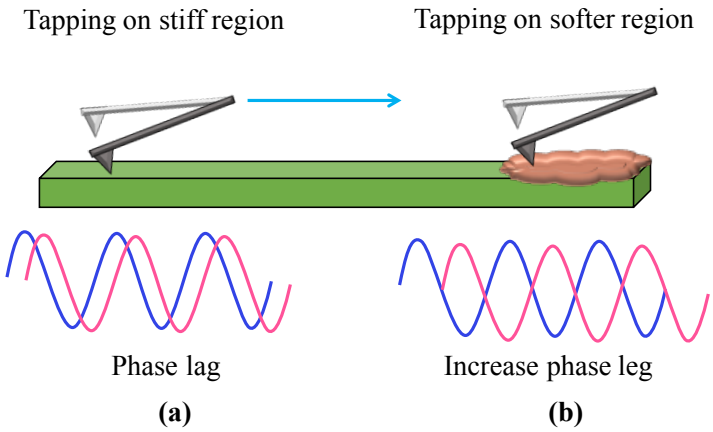

Figure 3.11: Schematic diagram showing the change of phase lag as a function of the sample surface properties, which is used to generate the "phase images" in tapping mode.

Unlike in the contact mode, the direct force (force spectroscopy) is not measured in tapping mode. Garcia and his co-workers, however, have provided an analysis that excludes the tip-sample power dissipation in order to calculate the average tip-sample force. Their expression is given by equation (3.2) [115, 116]:

$$< F_{ts} > = \frac{\mathrm{k}}{2Q} \left[A_o^2 - A_{sp}^2 \right]^{1/2} \tag{3.2}$$

Where F_{ts} is the force between tip and sample, k is the spring constant (stiffness) of the cantilever, Q is the quality factor of the cantilever, A_o is the free amplitude and A_{sp} is the amplitude setpoint. The Q can be written as in equation (3.3):

$$Q = \frac{f_o}{\Delta F} \tag{3.3}$$

where ΔF is the full width at half maximum and f_o is the resonant frequency

3.3.3.3 Applications of AFM in this Study

The specific types of AFM used in this work, the *in situ* AFM studies and the accessories that were used with the AFM are set out and discussed below.

3.3.3.3.1. AFM Used

In the present work, the data were collected using two different kinds of AFM: a Veeco Dimension 3100 AFM and a Multimode 8 AFM. The Veeco Dimension 3100 AFM with a Nanoscope IIIA controller (see Figure **3.12** (a)) was employed to investigate E/MB, while the Multimode 8 AFM with J heated scanner (Figure **3.12** (b)) was used in studying PE. This is because PE crystallization needs to be studied *in situ* at higher temperatures, and the Multimode 8 AFM is the most suitable for this since it has the ability to be used at up to 250 ºC whereas the Dimension 3100 AFM is limited for use at temperatures of around 120 °C.

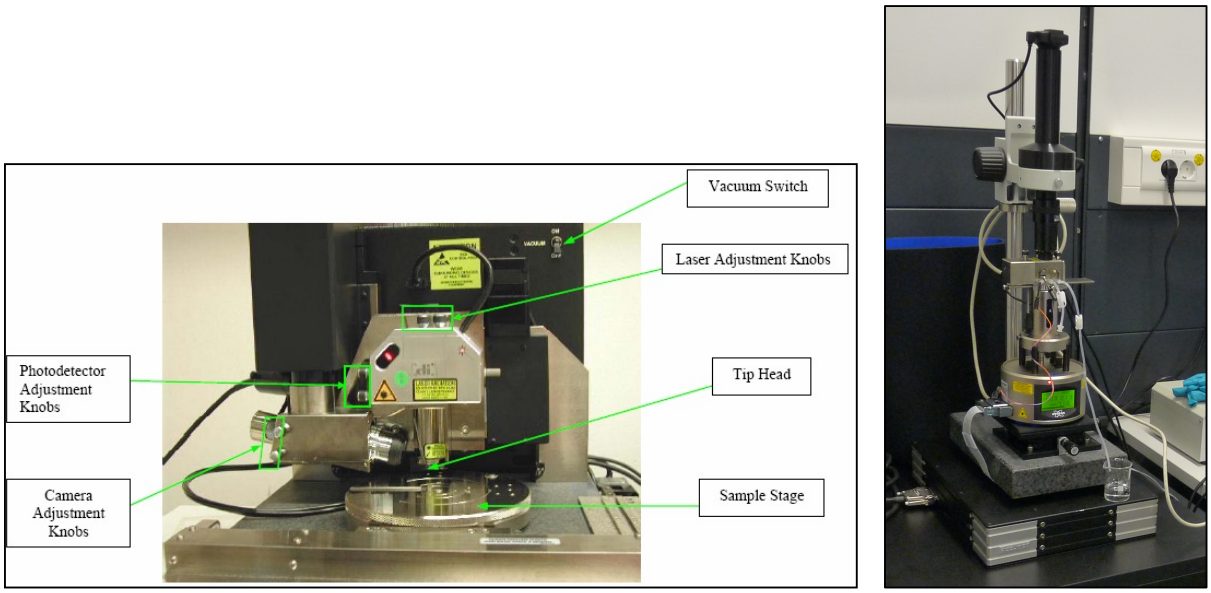

Figure 3.12: Photographs of (a) a Veeco Dimension 3100 AFM and (b) a Multimode 8 AFM used in this work.

In all the presented studies, either with the Dimension or Multimode 8 AFM, standard silicon tapping cantilevers (rectangular shaped) with a spring constant of about 40 N/m and a resonance frequency of about 300 kHz were used. TESPA-V2 type cantilevers were obtained from BRUKER and the properties of both the cantilever and the tip are given below in Table **3.2**.

Table 3.2: A table showing the geometrical parameter properties of the cantilevers used in this work.

Probe type	Material	R (nm)	T (µm)	L (µm)	W (µm)	f_o (kHz)	k (N/m)
TESPA-V2	Silicon	8	3.8	127	35	300	40

where R is the radius of the tip, T is the thickness, L is the length, W is the width, f_o is the resonance frequency, and k is the spring constant (stiffness) of the cantilever.

The majority of the presented images are phase images, which provided information crucial to understanding the crystallization process, since phase images provide a

contrast between crystalline and melt regions that allow detailed information about the behaviour of the crystals to be inferred. Additionally, all the images were captured at 256×256 or at 512×512 pixels in order to produce high-quality images. All the experiments were carried out in normal air. Image capture times varied and depended on the image size and the experiment temperature (or growth rate). For example, when following crystallization at low temperatures, in order to successful monitor the growth, images needed to be taken at a high rate since the crystals grow faster at low temperatures.

3.3.3.3.2. *In Situ* AFM Studies

In situ AFM studies have become significant for the study of polymer crystallization and melting in real time and at elevated temperatures with nanometre resolution and with the help of suitable hot stages [4, 5, 9, 76, 79, 117, 118]. Using AFM at temperatures higher than room temperature, however, could have some effects on the behaviour of the cantilever that in turn might affect the imaging process. Since the work presented here focuses mainly on *in situ* AFM observations of dynamic processes of polymer crystallization at a range of temperatures, an overview of the influence of this condition on the operation of the AFM, and potential mitigation techniques will be provided below.

When using an unheated cantilever, in order to allow the temperature of the sample to be altered as desired, the temperature of the cantilever will be lower than the sample temperature (see Figure **3.13**). This will affect the desired crystallization temperature, which in turn affects the crystallization behaviour. Thus, the whole AFM device was placed in a box in order to help the cantilever to reach thermal equilibrium with the sample and to reduce exposure to the convection currents (between the hot sample and the cool tip) formed by the heater heating the surrounding air. This helped in reducing the thermal gradient between the tip and the sample by allowing the cantilever to heat up to some extent, hence lowering the rate of heat transfer from the sample to the tip. It also reduced the air movement that could interfere with the cantilever and therefore cause poor-quality images.

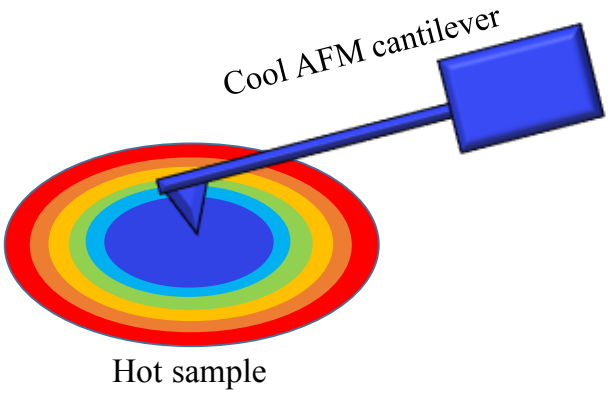

Figure 3.13: Schematic diagram showing the cooling effect of using a cool AFM cantilever on a hot sample.

Additionally, the probe was disengaged from the sample during the heating process; and at each temperature, the driving frequency was retuned. Periodically retuning the cantilever at each temperature was important because changing the temperature (whether decreasing or increasing it) during the experiment will result in a change in the temperature of the cantilever (cooling it down or heating it up), which in turn could cause shifts in the resonance frequency.

Importantly, to overcome the adhesive interactions between the AFM tip and the polymer, larger oscillating amplitudes were used for the probe (except when orienting the microdomain's block copolymer and inducing PE nucleation). Generally, this was considered preferable for the imaging of polymers close to their melting points. High oscillating amplitudes were also used in order to avoid contamination of the AFM tip by particles or molecules from the sample surface (i.e. the polymer attaching to the tip), which can lead to poor-quality images.

Due to their potential effects on the imaging process, some essential parameters (such as the scan rate, the scan size and the amplitude setpoint) were carefully controlled during each experiment. These parameters were critical in terms of obtaining high-quality AFM images, and in using these to allow the AFM tip to orientate the cylindrical microdomains before they crystallized. This was done in order to control the morphology of crystal growth and to reduce the influence of the tip on the sample surface. For instance, the amplitude setpoint plays a key role in terms of obtaining a high quality AFM image, as well as in allowing the AFM tip to align the phase-

separated microdomains of copolymer before they crystallized. An example showing the importance of this parameter is given in Figure 3.14. Here, the setpoint of image (a) was 1.5 V, and the setpoint of image (b) was 2.2 V and the free amplitude was ~ 3 V. From these two images it can be seen that the setpoint is an essential parameter in *in situ* AFM studies of crystallization. The crystals in image (b) are clearer in comparison to those in image (a). Careful attention should therefore be paid to this parameter in order to obtain an image of high enough quality to investigate crystal growth in real time.

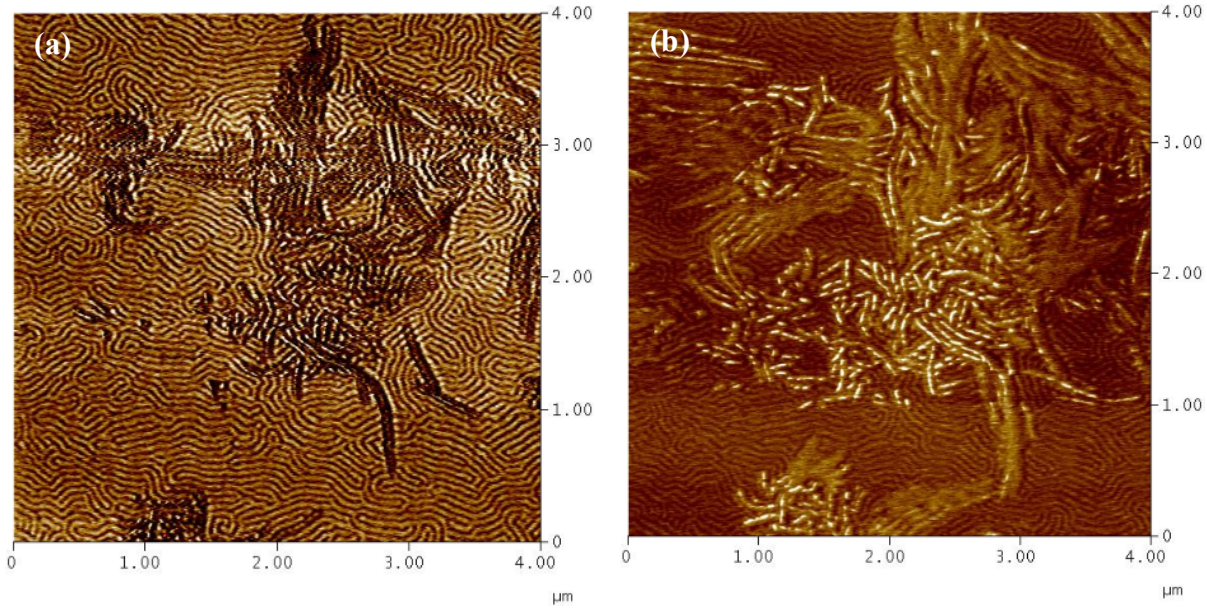

Figure 3.14: AFM phase images illustrating the effect of setpoint values on the clarity of crystallization at the same temperature (98 °C). In image (a) the crystals are not clear enough to be examined while in image (b) they are clearer. The setpoints of (a) and (b) were 1.5 V and 2.2V, respectively. Image (b) was taken about 3 minutes after (a).

3.3.3.3.3. Accessories and Temperature Calibration

Since in some cases it was essential to find the same examined region, a Transmission electron microscopy (TEM) grid was used (see Figure **3.15**). The TEM grid was either placed underneath or above the films in order to identify the area of interest and to relocate it at any time after the experiment, as will be shown later in Chapter 5. The TEM grid used in this work was made of copper, which is an appropriate material for high temperature applications. The TEM grid style is a 200 square mesh with a standard diameter of 3.05 mm.

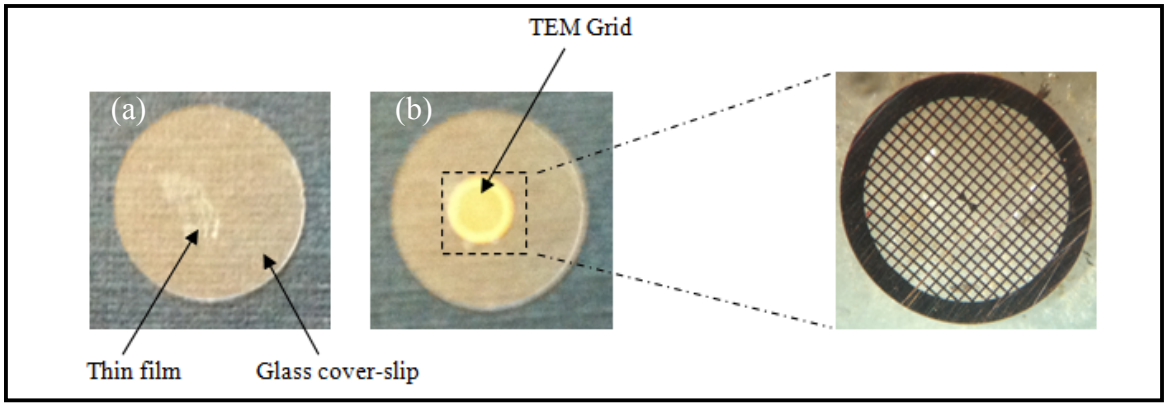

Figure 3.15: Photograph of (a) a thin film onto a glass cover-slip, (b) with a TEM Grid.

The temperature controllers used in the presented work were a Linkam TP94 hotstage (see Figure 3.16 (a)) which was used with the Veeco Dimension 3100 AFM, and a Nanoscope high temperature heater controller (see Figure 3.16 (b)), which was used with the Multimode 8 AFM.

(a) **(b)**

Figure 3.16: Photos of (a) the Linkam TP94 hotstage used with the Dimension AFM and (b) the Nanoscope high temperature heater controller used with the Multimode 8 AFM.

Since variation in the sample temperatures has a significant impact on the crystallization, it was essential to know the exact temperature at which crystallization occurs, especially since, in this study, the crystallization dynamic of polymers is studied as a function of temperature. As discussed above, using an unheated (cool) AFM tip will cause a temperature difference between the tip and the sample resulting in cooling of the area being scanning; since this will be colder than the rest of the material as the temperature will transit from the hot samples to the cold tips (Figure **3.13**). A calibration was therefore performed to account for the cooling effect of the scan head with sample

temperatures above room temperature. The calibration was performed using materials with well-defined melting point transitions (see Table **3.3**) and a Linkam TP94 hotstage.

This was done by first preparing films of these materials on a glass coverslip substrate by heating the substrate to a temperature above the melting point of the material and allowing it to spread as a liquid onto the substrate, before quenching these films to room temperature. The material films were placed under the AFM head while they were then heated slightly at a rate of 1 ºC/minute, using the Linkam, recording the temperature at which it melts. Finally, the difference between the recorded temperatures (Linkam displayed temperature) and the known or actual melting temperatures will be the extent of cooling that has been caused on the material by the AFM tips, a summary of the results of this measurement are presented in Table **3.3**.

Table 3.3: A table showing the substances used in the calibration, their actual melting points, Linkam displayed melting temperatures, and the difference between them.

Calibration Substance	Actual melting temperature (°C)	Experiment .No	Linkam temperature (°C)	Difference between actual and Linkam temperature (°C)
Stearic acid	69.7	1	70.3	0.6
		2	70.4	0.7
		3	70.3	0.6
		Average	**70.33**	**0.63**
Benzil	94.8	1	95.7	0.9
		2	95.5	0.7
		3	95.6	0.8
		Average	**95.6**	**0.8**
Acetanilide	113.9	1	114.8	0.9
		2	114.7	0.8
		3	114.9	1
		Average	**114.8**	**0.9**

Figure **3.17** is a calibration plot showing the correction that should be applied to the temperature displayed in the Linkam TP94 in order to acquire the actual sample temperature. Since the difference between the actual temperature and the heater temperature (the corrections) is less than 1 °C, however, the heater temperatures are given in this work. Error bars are the standard deviations from several measurements.

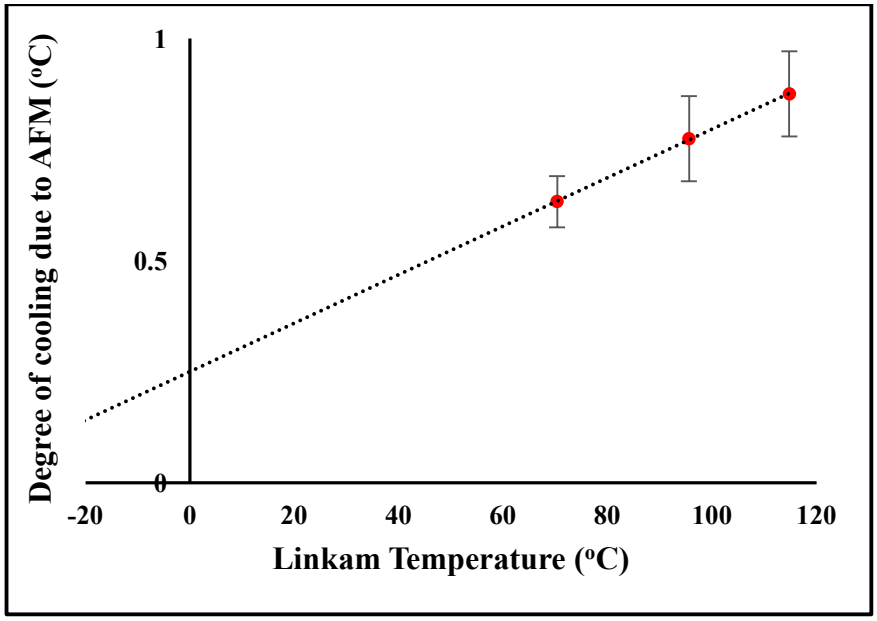

Figure 3.17: Calibration plot showing the correction applied to the Linkam TP94 display in order to acquire the actual sample temperature. The cooling effect of the AFM tip on sample temperatures was measured between approximately 70 °C and 115 °C. Error bars are the standard deviations from some measurements.

The results for controlling the orientation of the microdomain's block copolymer (E/MB) and the subsequent crystallization, and the results of the induced crystallization of PE will be presented and discussed later in Chapters 5, 6 and 7.

Chapter 4

Orientation Control of E/MB Microdomains

4.1. Introduction

Block copolymers have received great interest in science and technology due to their ability to self-assemble into nano-scale domains, which is a key requirement for a wide range of scientific and industrial applications, such as the fabrication of nanolithography masks and the miniaturization of electronic devices, and also due to their low-cost, fast, and easily scalable production, which makes them attractive for large-scale industrial applications. A variety of periodic structures such as lamellae, spheres, cylinders and gyroids can be produced by varying three main factors: the volume fraction of the block, the degree of polymerization (N) and the interaction parameters (χ) between the different blocks [11, 59]

The orientation of the microdomains within block copolymer films is usually random in nature, but being able to control the orientation of these microdomains within a specific localized region is essential for the development of novel nanometre structures and in various applications [12], such as data storage, lithography, computer memory and nanometre-scale templating [120]. The ability to control the orientation of block copolymer microdomains before they have crystallized allows the direction of the crystals to be defined so that they grow relative to the interface of the blocks; and, if carefully controlled, the molecular orientation introduces anisotropy into the physical properties, as well as making the analysis of the impact of microdomain orientation on growth easier to determine.

Several methods have been used to align block copolymer microdomains, including electric fields [120, 121], solvent fields [122–125], chemically patterned substrates [127], thermal gradients [128], shear [128–132] and, recently, AFM tips [134]. Using AFM tips to orient the microdomains has some advantages over the classical approaches: for example there is no need for doping or exotic material properties, no pre-patterning of the substrate is required, and it is possible to align microdomains over small (nano) length scales.

AFM cantilever tips have been successfully used in the modification of a number of polymer thin films at the required resolution at the nanometre level. For example, the tip can be used to scan or indent the films, creating ripple structures perpendicular to the fast scanning direction [135]. The modification mechanism in this method is considered to be mechanical deformation [88–92].

The aim of this chapter is to control the orientation of the cylindrical microdomains of E/MB at a local level by using the sharp tip of the AFM. This complements the next chapter (Chapter 5), which seeks to investigate the subsequent isothermal crystallization in real time, *in situ*, at different temperatures.

This chapter first presents the experimental method that was used, including sample preparation and the detailed conditions for controlling the orientations of the E/MB microdomains, such as tapping force and temperature. It presents the investigation into the conditions and temperatures under which the cylindrical melt structure can be orientated locally through the action of the AFM probe. The estimated tapping force of the cantilever on the sample was calculated theoretically and compared with the experimental results. The chapter also recounts the initial problems faced when attempting to align the microdomains using the AFM tip, including crystallization induced by the AFM tip and the breaking up of the cylindrical microdomains into smaller microdomains, and how these were later overcome. It then presents and discusses how the direction of orientation of the microdomains could be controlled by the AFM tip. Finally, elimination/minimization of defects was examined, since this plays an essential role in the optimization of the subsequent physical properties of the nanostructures.

Some of the data presented in this chapter has been published previously [136].

4.2. Method

A diblock copolymer named hydrogenated poly (1,4-butadiene)-b-(3,4-isoprene) was used. This diblock copolymer is denoted as E/MB where E is the hydrogenated high-1,4-poly butadiene (PE), which is the minority block, while MB is the majority block. The molar masses of the minority and majority blocks were 17 and 45 kg/mol, respectively. While E represents the crystallizable block, MB represents the rubbery amorphous block. The chemical structure of E/MB is shown in Figure 4.1. The T_g of the MB block is -17 °C, which is below room temperature. As was discussed in detail in Section 2.5.2 Chapter 2, this E/MB diblock forms a cylindrical mesophase of PE because the volume fraction for E, f_E, is 0.27.

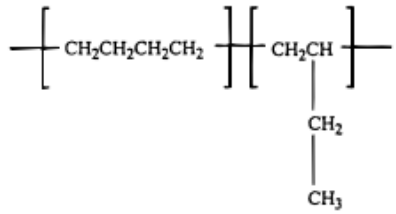

Ethylene Butene

Ethylene (E)

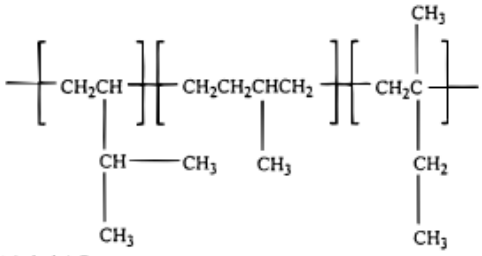

3-Methyl- 1-Butene Ethylene-Propylene 2-Methyl- 1-Butene

Methyl-Butene (MB)

Figure 4.1: The chemical structure of E/MB [137].

The synthesis and characterization of this E/MB diblock has been described in detail in [138]; some characterization data is shown in Table **4.1**.

Table 4.1: E/MB Molecular Characterization Data [138]

Sample	M_w E (kg/mol)	M_w MB (kg/mol)	f_E	T_{ODT} (°C)	T_m (°C)	T_g MB (°C)
E/MB	17	45	0.27	>260	105	-17

The E/MB samples were prepared using two different methods. Firstly, the samples were melt cast onto a glass coverslip at 130 °C (i.e. above the melting point) using a Linkam TP94 hotstage (see Chapter 3, Section 3.2.1). Then, they were thinned with a razor blade, producing films with a thickness of a few microns. The films were then quenched to the examined temperature at a cooling rate of 90 °C/min. The majority of the work was performed using this method.

The second method was spin coating, which was used to study the effects of the film's thickness on the orientation and crystallization behaviour. For this method, the samples were first dissolved in toluene at 80 °C to make solutions with concentrations ranging from 0.5-10 wt %. These solutions were then coated onto either a cleaned silicon wafer or a glass coverslip at 500-2000 rpm for 20-60 s, resulting in a range of thin film thicknesses from approximately 70-200 nm. Film thicknesses were measured by both ellipsometry and AFM and were in good agreement.

AFM was performed in tapping mode, using a Veeco Dimension 3100 AFM with a Nanoscope IIIA controller, as mentioned in Chapter 3, Section 3.3.3.3.1. The experimental setup is shown in Figure 4.2. Once the films had been prepared on the substrate, they were placed on a heater at a temperature range from 110–120 °C, since below 110 °C the tip induces crystallization, as will be shown below.

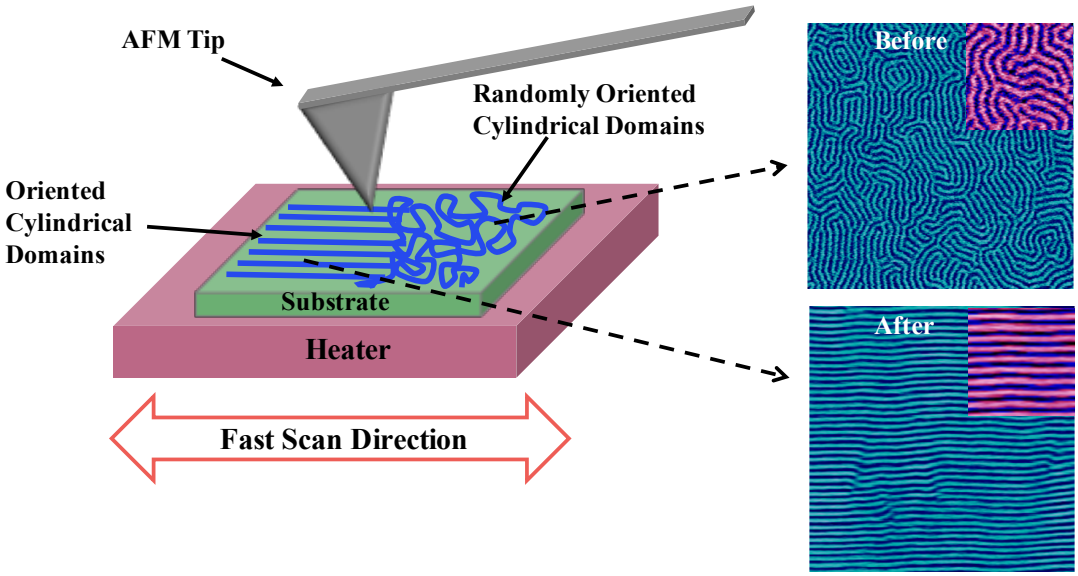

Figure 4.2: An illustrative diagram of the setup orientation experiment. The E/MB microdomains are randomly orientated in nature. When the film is heated above the melting point (i.e. 115 °C) by a Linkam heating stage, the E/MB microdomains can be oriented by a sharp AFM tip.

Following an initial imaging scan, the sample was imaged with high force over the area to be oriented, using a setpoint of 0.2-0.4 V compared to a free amplitude (i.e. amplitude when off the surface) of ~3 V (i.e. a relative setpoint, r_{sp}, of ~0.1), corresponding to an rms amplitude of ~1.8-3.5 nm and ~27 nm, respectively. Knowing these parameters with the spring constant and quality factor of the cantilever allows the tapping force that was used to orient the microdomains to be estimated, using equation 3.2 in Chapter 3. This equates to a force of approximately 3.7 nN, as calculated below:

$$< F_{ts} > = \frac{42}{300} \left[27^2 - (1.8^2 - 3.5^2) \right]^{1/2} \tag{4.1}$$

$$< F_{ts} > = 0.14 \left[729 - (3.24 - 12.25) \right]^{1/2} \approx 3.7\ nN \tag{4.2}$$

The average bending of the cantilever when carrying out this low amplitude imaging was 0.09 nm, corresponding to a force of approximately 3.8 nN, which was calculated using Hooke's law (assuming the nominal spring constant for the cantilevers used), in good agreement with the theoretical estimate. The area was then re-imaged at low force ($r_{sp} \sim 0.8$), to determine the impact of the orienting scan. Following this orientation procedure, the sample was cooled on the Linkam to the desired temperature with the tip retracted from the surface, and then imaged *in situ* during subsequent crystallization. This is shown in Chapter 5.

4.3. Results and Discussion

4.3.1. Sample Characterization

4.3.1.1. Film Thickness

Film thicknesses were measured by ellipsometry and AFM and the measurements were compared and found to be in good agreement. To measure film thicknesses using AFM, films were first scratched using a scalpel or razor blade in order to create a step in the film whose depth was that of the film. This scratch was then slowly scanned with AFM over a large scan size (e.g. 50 × 25 μm) at a low scan rate (e.g. 0.5 Hz). A typical example of such a scan is shown, with its corresponding height profile, in Figure 4.3, where the thickness measurement was taken as the height difference between the scratched area and the film surface. Scratching the surface could lead to more material being deposited around the scratch edges, however, which would make them higher than the surrounding polymer film. To avoid this, the measurements were taken between points away from such features.

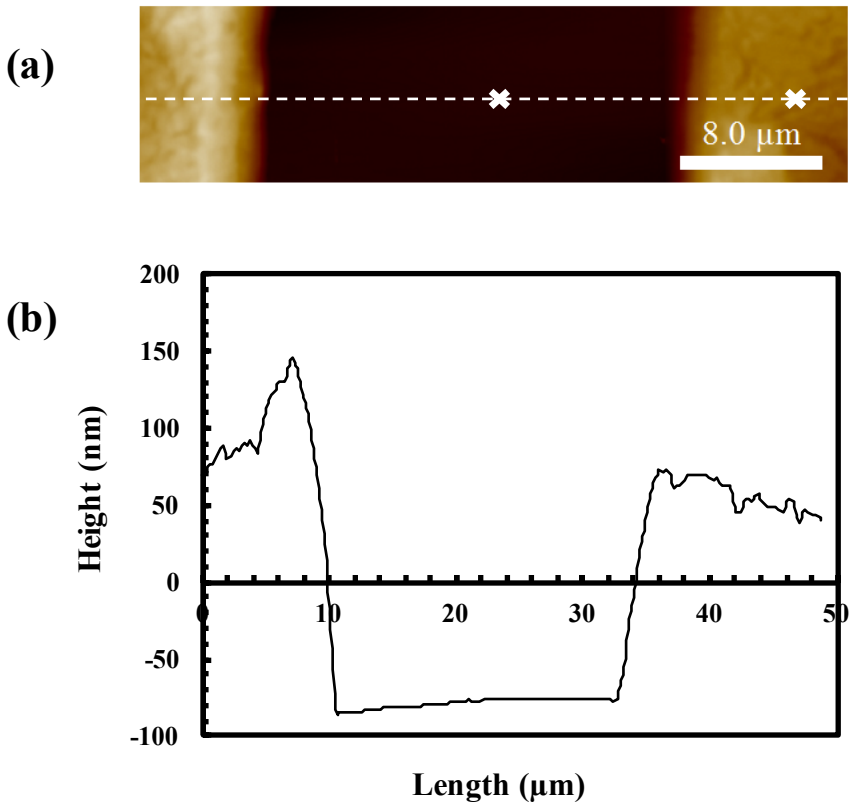

Figure 4.3: (a) an AFM height image showing the scratch that was made on the E/MB film. (b) A cross-sectional analysis corresponding to the dotted line in (a).

4.3.1.2. Melt Structure of E/MB

The initially prepared melt microdomain structure of the E/MB at 120 °C is presented in Figure 4.4. The E/MB formed cylinders of E in a matrix of MB, as would be expected from the fact that E has a higher surface energy than MB as a result of E's significantly higher solubility parameter [138, 139]. These cylinders can be seen to be lying mainly on the surface plane. Figure 4.4 (a) and (b) are AFM images showing the phase and the corresponding height, respectively. In the system studied, the temperature was well above the glass transition temperature of both components. Even under this condition, however, a clear phase contrast is visible between the two melt-rich components. The minor phase E block, which is the crystallizable unit and the major phase, MB matrix, which is the amorphous block, correspond to lighter and darker regions in the AFM images, respectively. The AFM technique uses the dissipative interactions between the tip and the surface to gather its data [141] and to generate the contrast between the different domains, as previously mentioned in Chapter 3.

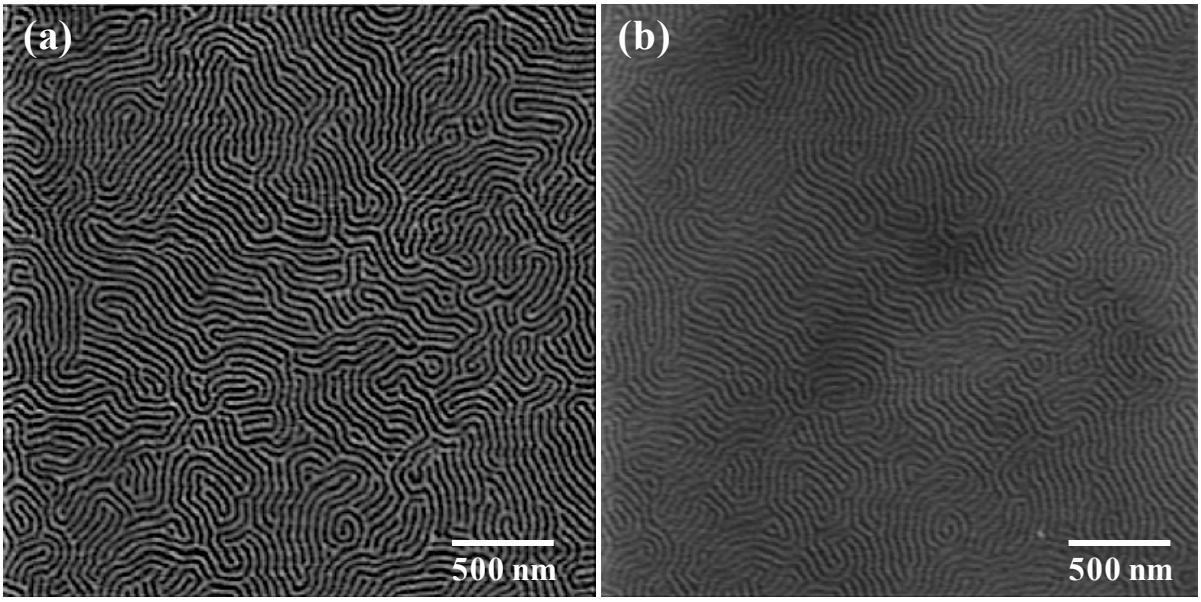

Figure 4.4: AFM (a) phase and (b) the corresponding height images showing the melt cylindrical microdomain structure in E/MB at 120 °C. Dark to bright represents a variation in phase and height of 8º and 20 nm, respectively.

4.3.2. Unexpected Outcomes

Before presenting the results of the orientation of the cylindrical microdomains in E/MB by the AFM tip, this section surveys the problematic outcomes that were observed during the initial experiments in order to understand their causes and to explain how they were overcome. Specifically, in the first attempts to orient E/MB microdomains using the AFM tip, there were two unpredicted observations: that the AFM tip induced crystallization, and that the cylinders were broken up into smaller grains (spheres). Both of these outcomes are discussed below.

4.3.2.1. Crystallization Induced by AFM Tip

In the first case, nucleation was induced in regions being scanned with a high tapping force (i.e. with a small amplitude setpoint) in order to align the E/MB microdomains. Four different examples of this situation are shown in Figure 4.5. The crystallization was clearly due to the influence that the AFM tip had on the sample surface, because the nucleation occurred only in the area that had been scanned by the AFM tip, while no nucleation was observed in the rest of the sample when the image was zoomed out (see Figure 4.5 (a'-d')). Figure 4.5 shows the E/MB film at 110 °C: (a) before, and (a′) after

scanning with high force (low A_{sp}), with the latter inducing nucleation in the scanning area. (a″) is a zoomed out version of image (a′). Figure 4.5 (b-d) shows the area that had been scanned with a high tapping force in order to orient the microdomains where the nucleation was induced. By increasing the scan size it was observed that the imaged region was the only area that had crystallized: no crystallization was observed outside that area, as can be seen from the examples in Figure 4.5 (b′- d′). Moreover, as the scan size was increased further, crystallization occurred each time in the new area being scanned, as shown in Figure 4.5 (b″- d″). The horizontal line at the top of Figure 4.5 (a′) is an image artefact due the door being closed during scanning.

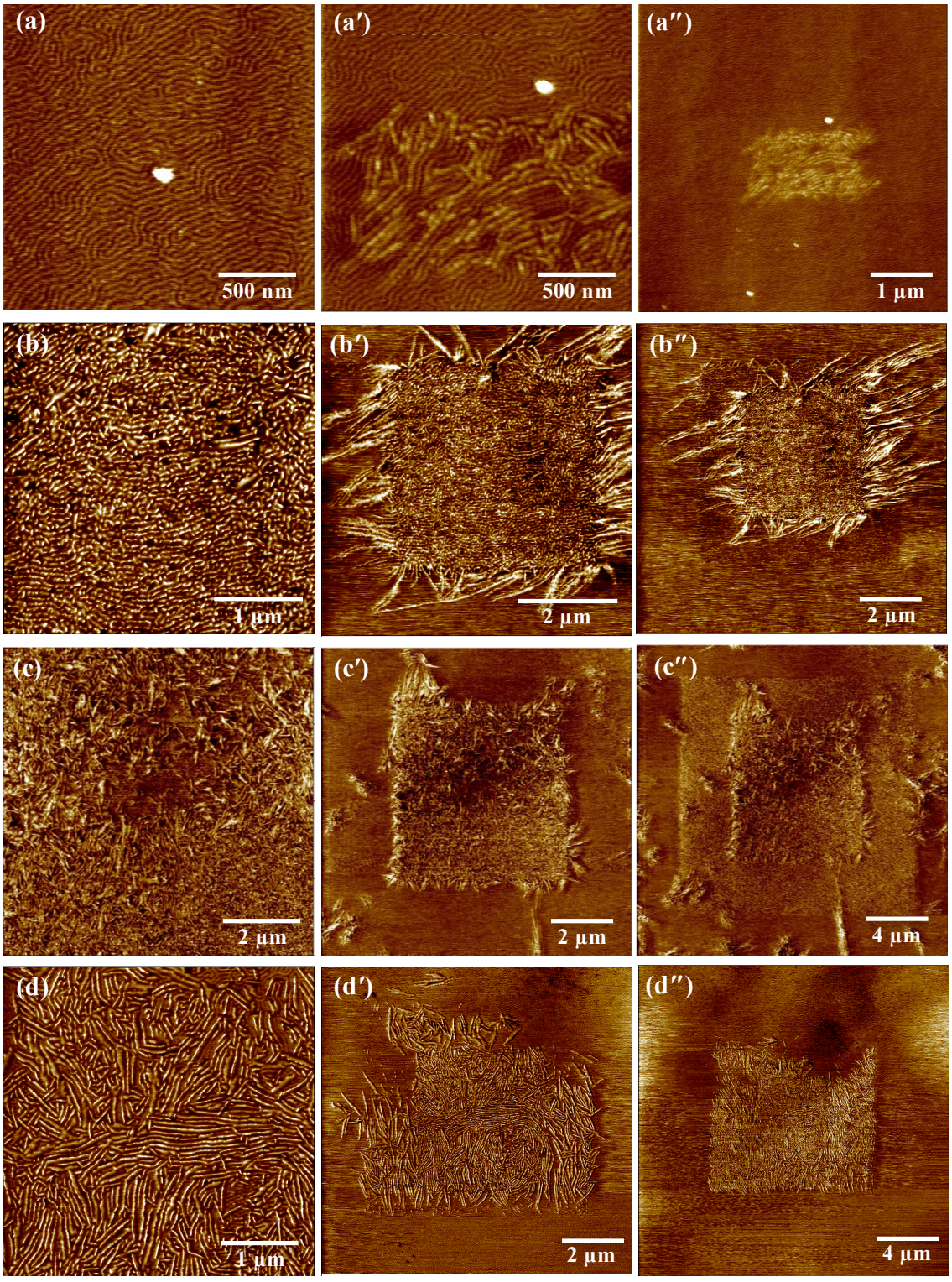

Figure 4.5: AFM phase images showing the nucleation induced by the AFM tip during the alignment of the cylindrical microdomains of the E/MB at 110 °C. (a-d) are four examples of different experiments. (a) Shows E/MB film before, (a′) after scanning with high force (low A_{sp}), inducing nucleation in the scanning area, and (a″) is the zoomed out image of (a′). (b-d) show the area in which nucleation was induced. (b′- d′) show the zoomed out images from (b-d), demonstrating that the area scanned with a high tapping force was the only area that had crystallized; (b″- d″) are zoomed out images of (b′- d′) showing the occurrence of crystallization each time in the new area being scanned.

A possible explanation for this result is that the scan was relatively fast and the surface was hit hard by the tip (at the low oscillating amplitude). Alternatively, it could have been that something in the tip (e.g. a bit of material attached at the end of the AFM tip), when crystallized, nucleated the surface being hit. This situation was only observed at temperatures lower than 110 °C, above this and the issue was not observed. This issue was therefore avoided by aligning the copolymer domains at relatively higher temperatures so that crystallization would not occur. The issue of AFM-tip-induced-crystallization during the aligning process, due to the tip's influence on the film, was therefore satisfactorily addressed.

4.3.2.2. Cylinders Breaking up into Spheres

Cylinder-to-Sphere Transition

In the second case, the cylindrical microdomains appeared as spheres in the area that had been scanned with a high tapping force at a temperature higher than 110 °C (to avoid the crystallization issue when attempting to align the microdomains at temperatures lower than 110 °C). Initially, it was not known whether the cylinders were aligned perpendicularly, instead of parallel to the surface, or whether they were being broken up into spheres. Figure 4.6 shows an example of such a situation: Figure 4.6 (a) presents an AFM phase image of the natural random orientation of E/MB microdomains in the melt state that was taken with normal scanning conditions. Figure 4.6 (b) illustrates the change of these cylindrical microdomains to a circular or spherical microdomain surface pattern resulting from scanning with the AFM tip with a high tapping force for a long period of time. Figure 4.6 (c) shows a zoomed out view of (b) where the area that had been scanned with a high tapping force and high scan rate for long time is in a matrix of random microdomains.

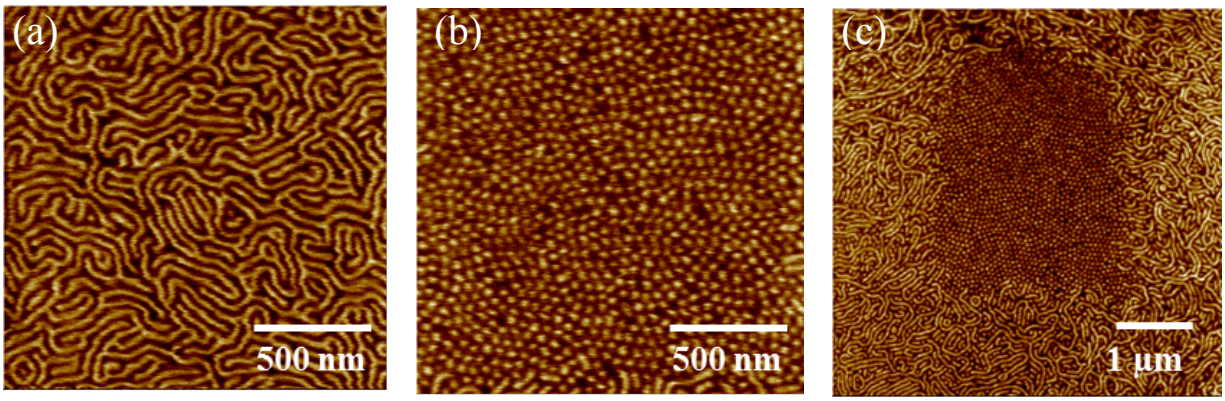

Figure 4.6: AFM phase images showing (a) randomly aligned E/MB microdomains that were imaged with normal scanning conditions, (b) cylinders appearing as spheres in the area that had been scanned with a high tapping force, and (c) zoomed-out view of (b). Images were collected at 112 °C and dark to bright represents a variation in phase of 1.5°.

Generally speaking, there are two main directions in which the cylinders can be oriented: parallel or perpendicular to the surface, as shown in the top of Figure 4.7. Perpendicular orientation has been shown in some cases to be associated with very thin films. It was therefore important to examine whether the AFM tip oriented the microdomains perpendicular to the surface (Figure 4.7 (b)) instead of the expected orientation, which is parallel to its scanning direction (Figure 4.7 (a)), due to the film's thickness. To explore this, film thicknesses were controlled by using the spin-coating method and several experiments were conducted with the resulting thin films.

No significant differences were found between thin and thick films, indicating that there was not a direct relationship between the film thickness and the orientation direction of the microdomains, or, more specifically, observations of the cylindrical microdomains breaking up into smaller microdomains like spheres. The only thing noticed was that the alignment was easier and faster in the thin films. This could be due to the fact that, in thin films, there are only one, or a few, layers of domains, which makes it easier to move the domains with the AFM tip since they are not tangled (connected) with other layers, in contrast to the case of thick films.

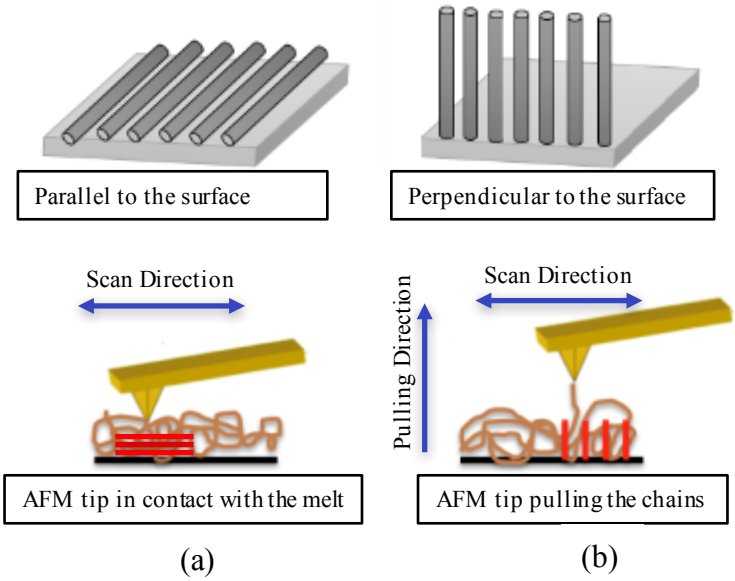

Figure 4.7: Schematic diagram showing the orientation of cylindrical microdomains by the AFM tip (a) parallel and (b) perpendicular to the surface.

A high force with a high scan rate was then applied for a shorter period of time in order to align the microdomains (i.e. the area was scanned once). The outcomes illustrated in Figure 4.8 (a) were obtained, in which the cylinders were relatively oriented in the direction of scanning. Re-imaging the same area with the same scanning conditions led to the results in Figure 4.8 (b). As can be seen, some cylinders had changed to smaller sphere-like microdomains (two examples are illustrated by the blue and yellow arrows in the highlighted area). With time, interestingly, these spheres, or the broken cylinders reconnected into cylindrical microdomains, became oriented parallel to the scanning direction, as shown in Figure 4.8 (c-d). This observation was previously reported in [142], where an electric field was used to align cylindrical microdomains of block copolymer. In that case, when an electric field was applied on the initial parallel cylinders to the surface, the cylinders fluctuated and then broke apart into spherical domains. These spheres, with time, deformed into ellipsoidal domains and reconnected into cylinders oriented at 45° with respect to the applied field direction.

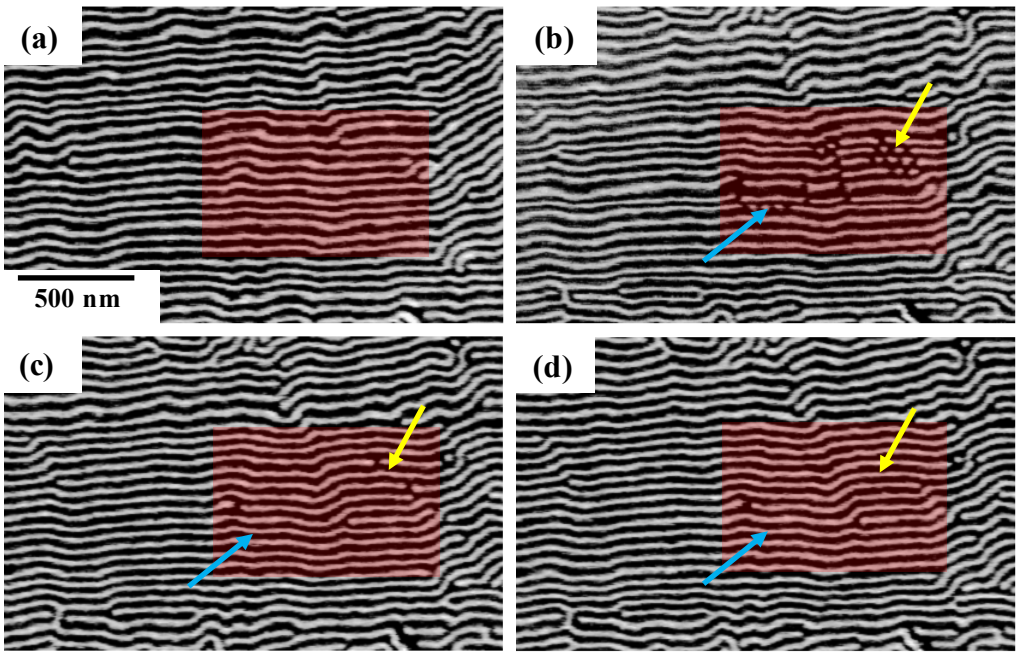

Figure 4.8: AFM phase images showing: (a) the relatively well-oriented cylindrical microdomains after application of a high tapping force with a high scan rate for a short time, (b) the transition of some cylindrical microdomains to spheres after orientation with a high scan rate for a longer time, and (c)-(d) the reconnecting of domains into cylinders with a normal scanning condition (low force and scan rate). The arrows and red rectangular highlighted area were added to aid the reader in following the transition or breaking up of cylinders into spheres and their reconnection.

Figure 4.9 shows another example of such a situation: consecutive AFM phase images show the process of microdomains interconnecting into cylindrical structures. Image (a) indicates the transition of the cylindrical microdomains to smaller grains (spheres) after application of a high tapping force with a high scan rate (~ 9 Hz), and images (b-d) indicate the interconnection of the microdomains into cylinders with time. The yellow dashed square indicates the area where the transition occurred and, inside this area, three regions are highlighted as examples to help the reader to follow the reconnection process.

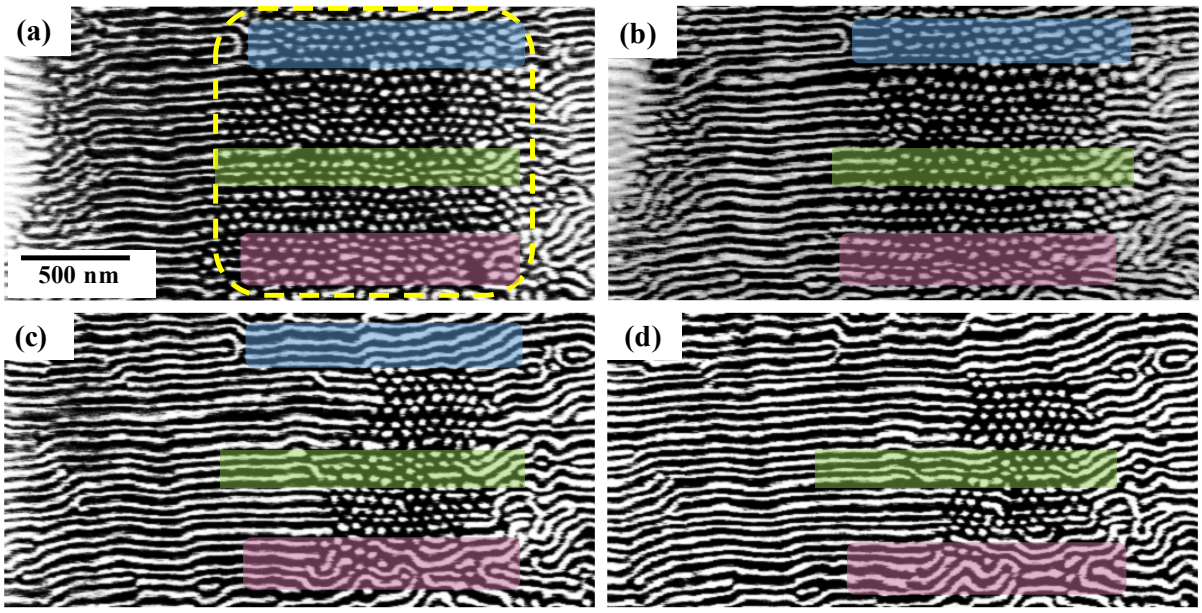

Figure 4.9: Consecutive AFM phase images showing: (a) the transition of the cylindrical microdomains to smaller grains (spheres) after application of a high tapping force with a high scan rate of 9 Hz, and (b-d) the interconnection of the microdomains into a cylindrical structure with time. The yellow dashed squared indicates the area where the transition occurred and inside this area three regions are highlighted as examples to help the reader to follow the reconnection process.

This observation indicates that the cylindrical microdomains were at first relatively aligned in the direction of the AFM tip scanning, but were then broken up into smaller microdomains (spheres). With time, the distorted cylinders became interconnected and appeared to be oriented parallel to the scanning direction (see the blue and green regions in Figure 4.9 (a-d)). Disordered microdomains can also be formed, however, as shown in the pink region highlighted in Figure 4.9 (c-d), in which the cylinders are not parallel to the scanning direction but instead appear to be randomly aligned. This suggests that it is not necessary for the microdomains to be oriented for them to be reconnected into cylinders. Although they do not have to be aligned (e.g. they may be dislocated, albeit sometimes clustered together), reconnection into oriented cylinders was observed more frequently than reconnection into a disordered orientation.

Another example of a situation where the cylindrical microdomains were broken into spheres and then reconnected into cylinders with time is shown in Figure 4.10 in the highlighted blue area.

It has been reported that shearing can induce both disordering and ordering of block copolymer-forming cylindrical microdomains. If the shear rate is high, the

microdomains tend to be disordered, but if the shear rate is low more ordered domains are induced [128, 142]. The authors suggested that if the inverse relaxation time (τ) of the cylinder fluctuations is much higher than the shearing rates the cylinders may not be able to react fast enough to the imposed shear, leading to disordering. So, this could be the case here.

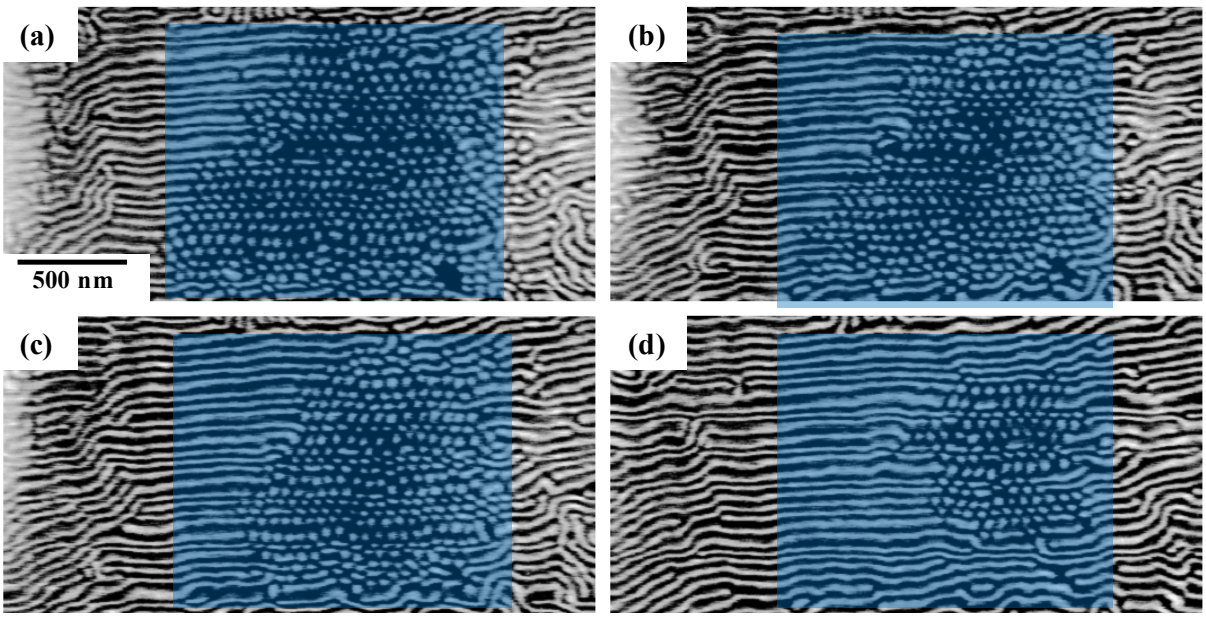

Figure 4.10: Consecutive AFM phase images showing the reconnection of distorted cylindrical microdomains into cylinders with time. The highlighted area was added in order to help the reader to follow the reconnecting process.

Over several experiments, it was found that this process of the breaking up (transferring) of the cylinders into spheres is associated with the scan rate and alignment duration. The amount of transition increased as the scan rate and alignment duration increased. This meant that these outcomes could be overcome by using a relatively low scan rate (~2 Hz) and a short scanning duration when scanning with high force to align the microdomains, as will be discussed in detail below.

4.3.3. Alignment of E/MB Microdomains by the AFM Tip

4.3.3.1. Orientation Control of Microdomains

The AFM tip was used as a tool to orient the crystalline cylindrical domains mechanically in the scanning direction before they crystallized. This crystallization behaviour will be examined *in situ* at different temperatures in the following chapter (Chapter 5).

Figure 4.11 (a) shows AFM phase images of the randomly oriented cylindrical microdomains in E/MB that resulted from the initial film preparation. Figure 4.11 (b) shows the cylindrical microdomains aligned to the scan direction after scanning with the AFM tip over the film surface, with a high tapping force. The Fast Fourier Transforms (FFTs) of the AFM images show the disorder, (a), and high degree of order, (b), of the cylindrical microdomains. Figure 4.11 (c) and (d) show further examples. A clear boundary between the oriented domains (in the top half) and the random domains (in the bottom half) can be seen in image (c). Image (d) illustrates the oriented cylindrical microdomains in a matrix of random cylinders where the aligned area was the only part that had been scanned with a low amplitude setpoint while the rest of the sample was scanned with a normal amplitude setpoint.

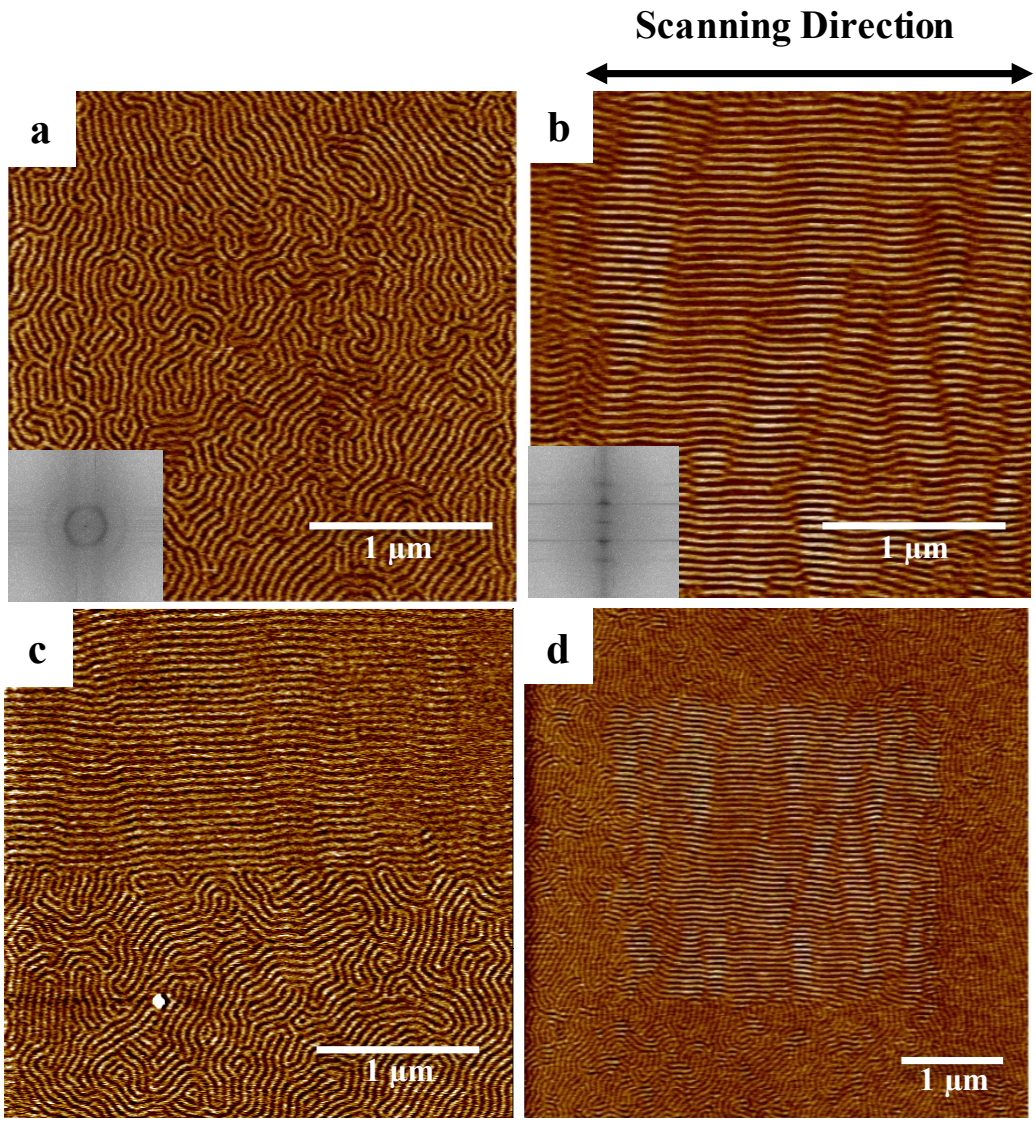

Figure 4.11: AFM phase images showing: (a) the natural random orientation of E/MB microdomains in the melt state, (b) the cylindrical microdomains oriented by the AFM tip, (c) the boundary between random and oriented cylinders, and (d) the oriented cylindrical microdomains in a matrix of random domains. The insets in (a) and (b) are the corresponding Fast Fourier Transform (FFT) patterns of the cylindrical microdomains showing the essentially random orientation in (a) and a high degree of orientation in (b). Colour scales represent a change in phase of (a,b) 5°, (c) 3°, and (d) 5°.

4.3.3.2. Aligning in Different Directions

The direction of orientation of the cylindrical microdomains can be controlled by varying the tip scanning direction. Figure 4.12 shows an example resulting after multiple tip scans were carried out on the sample. The tip first scanned parallel (at a 0° scan angle) over a 4×4 µm area (the yellow square in image (a)), aligning the random cylindrical microdomains along its scanning direction. Subsequently, the tip was scanned perpendicularly to the initial scan direction (at a 90° scan angle) over a

2.5×2.5 µm area (the white square in image (a)) in the approximate centre of the previously aligned microdomains, resulting in the reorientation of this area orthogonally to the previously aligned area in the matrix of a random region (image (a)). Figure 4.12 (b) is a magnified view of the region within the yellow square in image (a).

Three types of cylinder orientations are shown in Figure 4.12 (a): the parallel aligned cylinders (in the yellow squares), the perpendicular aligned cylinders (in the white square) and the matrix of random cylinders around the two squares. It should be noted that the orientation at the boundary between the two oriented regions is less clearly defined than that between oriented and disoriented areas, implying a greater barrier to the reorientation process.

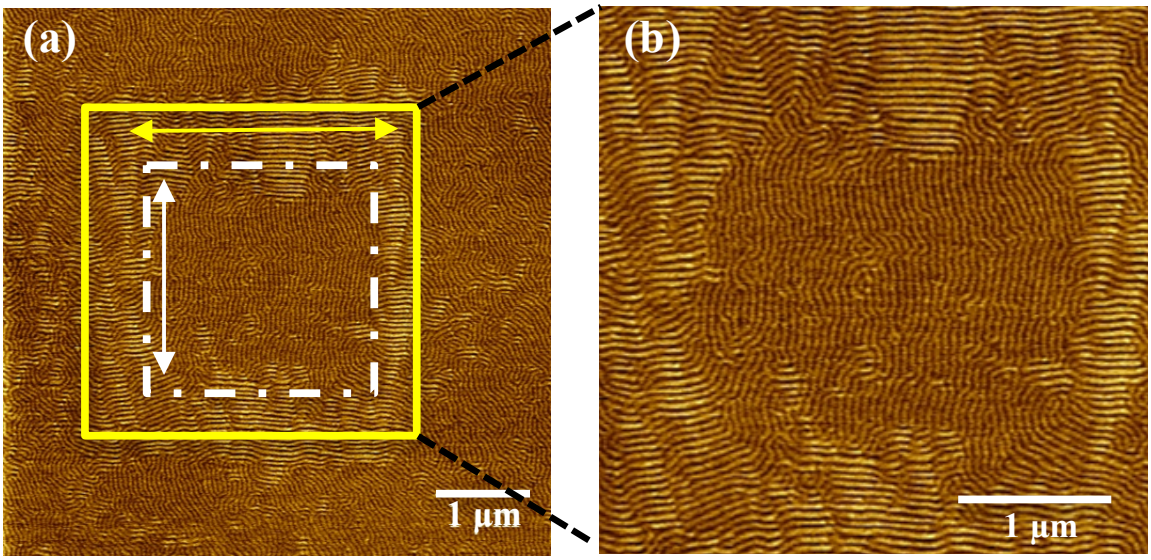

Figure 4.12: (a) AFM phase image showing aligned cylinders of E/MB in two different directions according to the AFM tip scanning direction. The arrows indicate the fast scanning direction in the two differently oriented regions (white and yellow squares). Image (b) is a magnified view of the region within the yellow square in image (a). The colour scale in (a) and (b) is 4°.

A further example showing the ability to control the orientation direction of the cylindrical microdomains is presented in Figure 4.13. Figure 4.13 (a) shows aligned cylinders (in the centre of the image) in a matrix of randomly orientated cylindrical microdomains. The yellow arrow indicates the first aligned area, while the blue and white arrows point to the second and third areas, which were aligned next, in different directions. In Figure 4.13 (b), the blue arrow indicates the direction of alignment of the second area, while the white arrow indicates the still randomly aligned cylinders that will be aligned next. Figure 4.13 (c) shows the three different directions of aligned

copolymer domains. The yellow, white and blue ovals indicate the first, second and third aligned areas with angles of 0°, 45° and 90°, respectively. These were achieved by changing the scan angle value and scanning once, then changing the scanning area and choosing a different scan angle. For example, after aligning the microdomains in an area in a specific direction (e.g. in the direction of the yellow arrow in Figure 4.13 (c)), another area was chosen to be aligned in another direction (e.g. in the direction of the blue arrow in Figure 4.13 (c)). This shows the ability of the AFM tip to align the cylinders in different directions (in the direction of its travel).

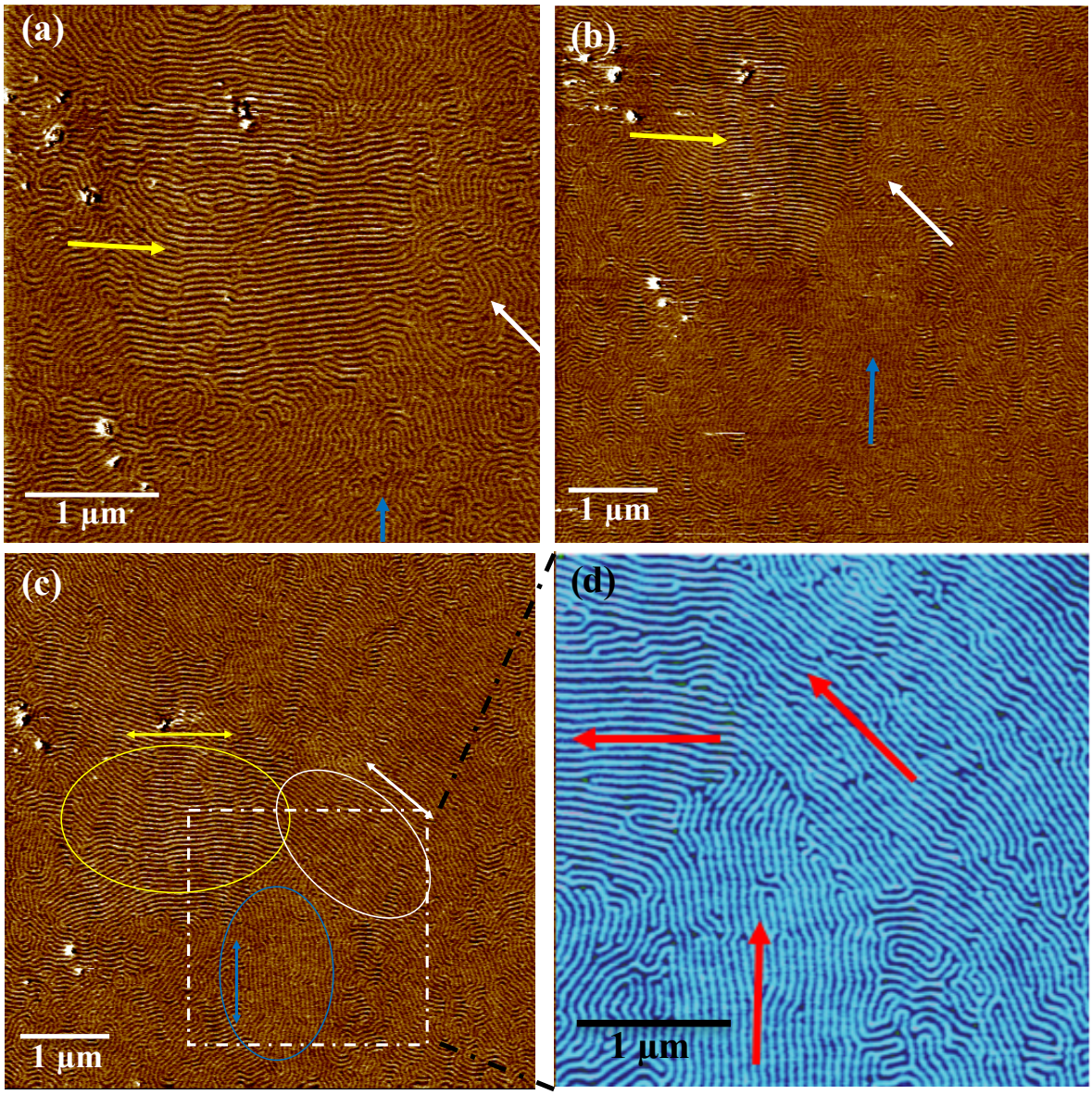

Figure 4.13: AFM phase images of the E/MB collected at 115 ºC showing cylinders aligned in three different directions according to the AFM tip scanning direction. Image (a) shows that the aligned cylinders (in the centre of the image indicated by the yellow arrow) are surrounded by randomly orientated cylinders. The white and blue arrows in image (a) refer to the random areas that were aligned later in different directions by the AFM tip. The yellow arrow in (b) indicates the corresponding area in (a), the blue arrow indicates the cylinders that were aligned after image (a), where the tip was scanned perpendicularly to the initial scan direction, and the white arrow indicates the random cylinders that were aligned next. Image (c) corresponds to (b): this image shows the three different directions of aligned cylinders: the yellow, white and blue ovals indicate the cylinders aligned with angles of 0°, 45° and 90°, respectively. Image (d) is a magnified view of the white square region in image (c). Colour scales are 4°.

The mechanism of alignment in this work is probably the shear force imparted by the AFM tip since it is well known that block copolymers (including thin films) align when a shear force is applied [128, 132]. Even though the imaging here was done in tapping mode, the tip is still in transient "contact" with the surface, and it is moving in the fast-scan direction. Thus, it would be expected that the film experiences lateral shear forces when the AFM tip scans with a low amplitude setpoint value, as in this study, and that the rate of these shear forces depends on the amplitude setpoint value. If the shear forces are sufficient, the cylindrical microdomains are aligned in the fast-scan direction, which was what was observed in this study.

Moreover, increasing the relaxation time favours the alignment of the domains. Here, the relaxation time is probably larger than the contact time between the AFM tip and the sample. Thus, the cylindrical microdomains were aligned, as the shearing was faster than their relaxation.

4.3.3.3. Enhanced Microdomain Ordering

The AFM tip is able to align cylindrical microdomains in its scanning direction, although in some cases defects—such as dislocations, or domains sometimes clustered together— were observed (Figure 4.14). The extent to which multiple scans affected the number of defects was explored.

Scanning the same area more than once (with the same hard tapping force conditions initially used for alignment, a low amplitude and a low relative set-point $r_{sp} \approx 0.1$) reduced the number of defects. This situation is shown in Figure 4.14. The cylindrical microdomains are highlighted, from which it can be seen that the number of defects was reduced simply by increasing the number of scans with the same hard tapping conditions.

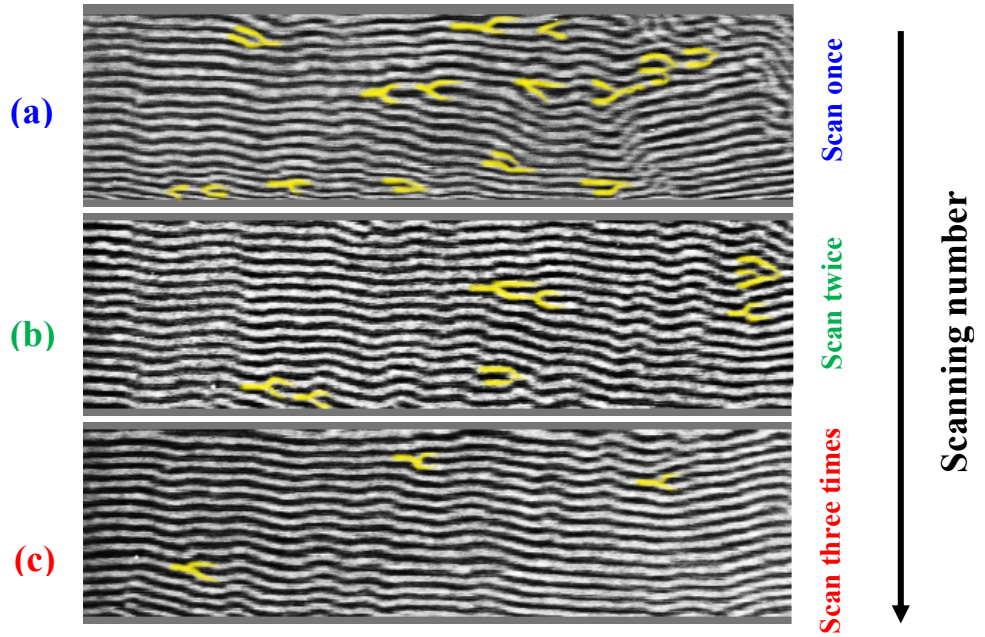

Figure 4.14: AFM phase images showing the effect of the number of scans on the defects per unit area, (a)-(c) 1st, 2nd and 3rd scans, respectively, with a relatively high tapping force (low amplitude and low $r_{sp} \approx 0.1$) at 115 °C. The defects are highlighted in yellow to help the reader follow the reduction in defects as a function of the number of scans. The image size is 3×0.75 μm and the black-to-white scale is 7°.

On the other hand, there were a few cases where some defects were formed when the number of scans increased (see Figure 4.15). For example, the highlighted red microdomains in Figure 4.15 (a) became more clustered together when scanning over them one more time, as can be seen in Figure 4.15 (b). In those cases, however, the number of defects per unit area was still reduced by increasing the number of scans over the film, resulting in better ordering in general. Figure 4.16 is a plot showing this result from nine experiments. The change in the number of defects was found to vary with the number of scans but was approximately linear, with an overall average decrease in the number of defects per square micrometre of 0.9 per scan.

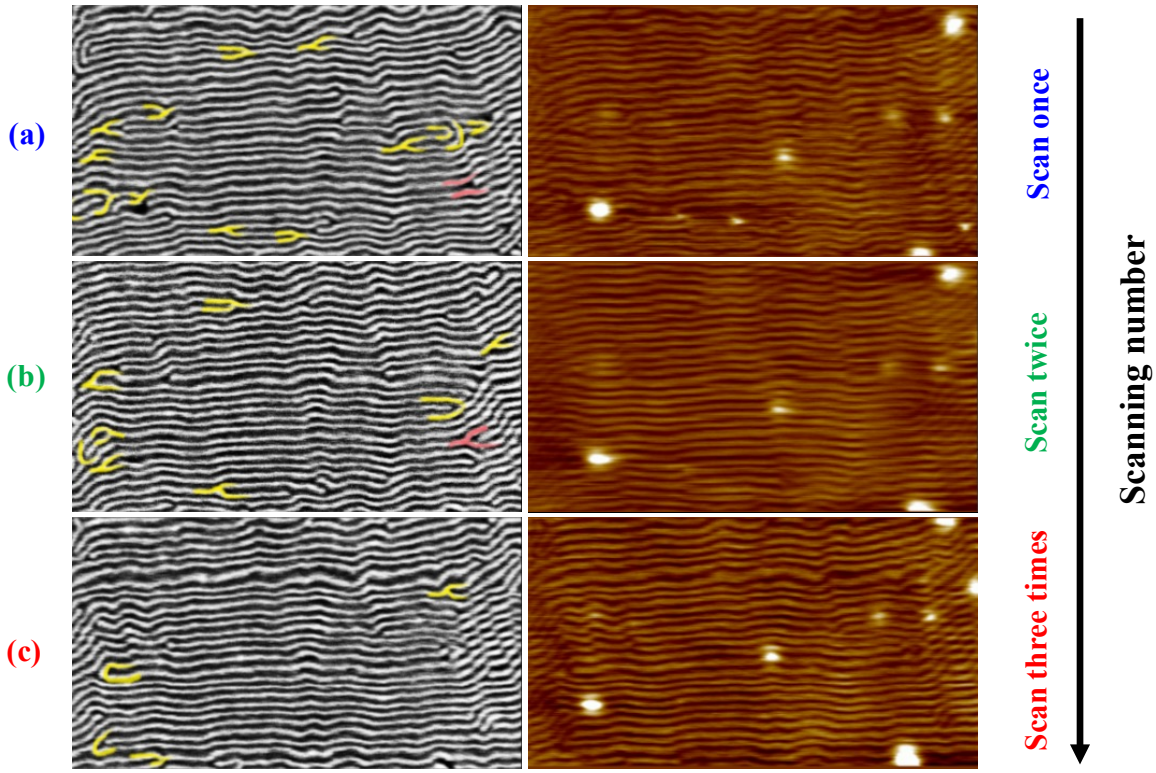

Figure 4.15: AFM phase (the left column) and height (the right column) images showing the effect of the number of orienting scans on the defects per unit area, (a)-(c) 1st, 2nd, and 3rd scan, respectively, with a relatively high tapping force (and a lower amplitude and lower $r_{sp} \approx 0.1$) at 115 °C. The defects are highlighted to help the reader follow the reduction as a function of the number of scans. The region highlighted in red shows an example of a new defect being produced with the same scanning conditions, even though the overall number of defects is still reduced. The image size is 3×1.5 μm and the black to white scale is 12°.

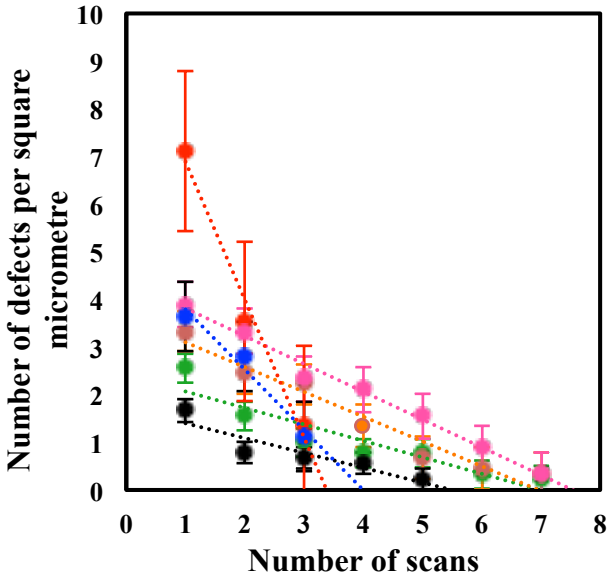

Figure 4.16: A plot showing the number of defects as a function of the number of scans (each colour indicates an independent experiment). Error bars are the standard errors.

Having formed oriented domains of cylinders in this chapter, the impact of orientation on subsequent crystallization is studied in the next chapter (Chapter 5).

4.4. Conclusion

The AFM tip was successfully used to control the orientation of the cylindrical E microdomains in different directions according to its scan direction. Scanning the AFM tip over the E/MB film oriented the microdomains parallel to the direction of tip scanning. Furthermore, if the tip scanning direction was varied, this was found to alter the direction of already aligned microdomains in subsequent alignment scans. The effect of shearing conditions, such as scan rate or tip velocity, r_{sp}, and shear temperature, on the orientation of E/MB was examined. It was found that the number of defects was reduced with an increase in the number of orienting scans. Thus, well-ordered microdomains were obtained by just scanning over the area of interest more than once.

In the course of the experiments it was found that the AFM tip induced crystallization when attempting to align the cylinders at temperatures lower than 110 °C (the crystallization occurred in the area of imaging before aligning these cylinders). At temperatures of 110 °C and above, however, this situation was not observed. This indicates that the ideal temperature to align the cylindrical microdomains of the sample investigated in this work was in the range of 110 °C and above. Moreover, scanning with a high scan rate for a long time resulted in the cylinders breaking up into smaller microdomains. Interestingly, in some cases, these distorted microdomains (the broken cylinders) were observed to reconnect into cylinders with time. This suggests that AFP tips could induce cylinder-to-sphere transition in diblock copolymer films.

Overall, three conditions were necessary for the orientation of microdomains by the AFM tip: (i) the temperature should be high enough, (ii), there must be a sufficiently high tapping force, and (iii) the scanning rate and duration should be carefully controlled. In the absence of these conditions, the tip would induce nucleation; the tip-surface interaction may not be strong enough to cause an orientation; the cylindrical microdomains may be broken up into smaller microdomains rather than being aligned.

Chapter 5

Crystallization in Pre-Oriented E/MB Microdomains

5.1. Introduction

Crystallization in a confined system has been a source of great interest in recent years [138], [144]–[154]. One reason for exploring confinement effects is that confined systems are becoming increasingly widespread as devices and materials are constrained due to miniaturization. Secondly, the fundamental understanding obtained from studies of confinement lengths approaching the intrinsic length scale of the system can be extended to gain an understanding of crystallization in general. Among the most convenient common methods to achieve confinement under nanoscales are crystalline–amorphous diblock copolymers [10] (with one crystallizable block), due to their self-assembled microdomains.

Block copolymers containing one crystallizable block from a phase-separated melt can be used as a model to understand a range of crystallization behaviours, from "break-out" (i.e. where the crystallization does not depend on the existing melt structure) to "complete confinement", where individual crystallites are completely confined within pre-existing domains. Careful control of the length of the polymer molecule, and of the temperature, allows varying strengths of phase segregation to be achieved, which can lead to a range of different behaviours [67, 154, 155]. Studying crystallization behaviour using such copolymers promises the ability to control the domain size, thereby also offering potential insights into the crystallization behaviour of homopolymers [143, 151, 156]

Even though the general behaviour of this crystallization is understood, there are many important questions that remain unanswered, such as how exactly the melt impacts on

the course of crystal growth, or what the relationships between growing crystals are. In addition, difficulties remain in interpreting *ex situ* observations of TEM, due to the inability to observe the length scales of the structures by optical microscopy. Hence, defining the morphology during crystal growth is not possible. In recent years, however, AFM has been successfully employed to study block copolymers [158]. For example, it has allowed direct visualizations of crystallization in both cylindrical and spherical microdomains [157].

Previous work on naturally random E/MB [6] has observed that, in some cases, crystals stopped growing for several minutes before crossing into another microdomain, whereas, in other cases, the crystals rapidly crossed several domain boundaries without signs of any decrease in growth rate. Since it is hard to assess this behaviour in randomly oriented microdomains, it is essential to investigate such crystallization in a well-ordered melt structure if we are to be able fully to understand those results. By comparing crystal growth along and against the direction of orientation, the degree of constraint, and how this changes with temperature, can be determined.

The main aim of this work, therefore, is to monitor the interplay between crystallization and mesophase formation in soft-confined crystallization in E/MB diblock copolymer, and to use control over the domain orientation to understand better how confined crystallization in block copolymers occurs.

In the previous chapter (Chapter 4), the orientation of the cylindrical microdomains of E/MB was controlled by the AFM tip before they crystallized. This allows the direction of the crystals to be defined so that they grow relative to the interface of the blocks; and, if carefully controlled, the molecular orientation introduces anisotropy into the physical properties, as well as making the impact of microdomain orientation on growth easier to determine. This chapter complements Chapter 4 by using AFM to investigate the subsequent crystallization behaviour and morphologies, from a soft rubbery confinement, in pre-oriented diblock copolymer microdomains (E/MB) in real time, *in situ* and *ex situ*, at different temperatures.

In this chapter, the formation of a crystal morphology from both unoriented and oriented cylindrical microdomains of E/MB was examined as a function of temperature, before then making a comparison between them in order to see the effect of orientation

on the crystallization. The behaviour of the crystallization in the pre-oriented microdomains at different temperatures is then presented and discussed. In addition, the growth rates of crystals growing parallel to the established melt structure were calculated and compared with those of crystals growing against the established melt structure, again as a function of temperature. Finally, the chapter discusses the transition from 'breakout' to 'templated' growth and the impact of this transition on the growth rate.

Some of the data presented in this chapter has been published previously [136].

5.2. Results and Discussion

In this chapter, after aligning the cylindrical microdomains of the E/MB by the AFM tip, as shown previously in Chapter 4, the subsequent crystallization behaviour was examined *in situ* and *ex situ* at different temperatures. In order to follow the subsequent crystallization, the samples were cooled to the desired crystallization temperatures (e.g. 100 °C) at a low rate of about 0.1 °C/min or 1 °C/min from the melt while the AFM was imaging. This very low rate of cooling was employed to avoid any unwanted changes on the surface during the imaging stage (i.e. to reduce thermal drift, which can produce warped images). The E/MB thin film was kept on the Linkam hot stage, which in turn was kept under the AFM scanner throughout the *in situ* experiment. The *ex situ* experiment was conducted first in order to examine the effect of crystallization temperature on the crystal morphology formed in both un-oriented and oriented cylindrical microdomains, as will be shown below in detail.

5.2.1. Crystal Morphology as a Function of Temperature

5.2.1.1. Morphology Formation from Un-Oriented Cylindrical Microdomains

The morphology formed depends on the temperature of crystallization. In order to see the effects of temperature on the structure of the crystals formed, therefore, the sample was isothermally crystallized at different temperatures. The sample was transferred very quickly from the heating stage held at 130 °C to another heating stage placed under the

AFM and held at the crystallization temperature for several minutes, allowing the sample to crystallize. The duration for which the sample was held at the specific temperature depended on the crystallization rate: e.g. crystallization at 50 °C took place very fast, so the sample was held at this temperature for 5 minutes to ensure complete crystallization; at higher temperatures, however, crystallization occurred more slowly, needing more time to be completed (e.g. at 100 °C the sample was held for ~ 5 hours to ensure complete crystallization). An example is shown in Figure **5.1**. The same sample was used to investigate both the effects of temperature on the structure of the crystals formed and the temperature at which the crystals would be completely confined within the microdomain melt structure. The order that these experiments were performed in was first at room temperature, then 50 °C, 60 °C, 70 °C, 80 °C, 90 °C and, finally, 100 °C.

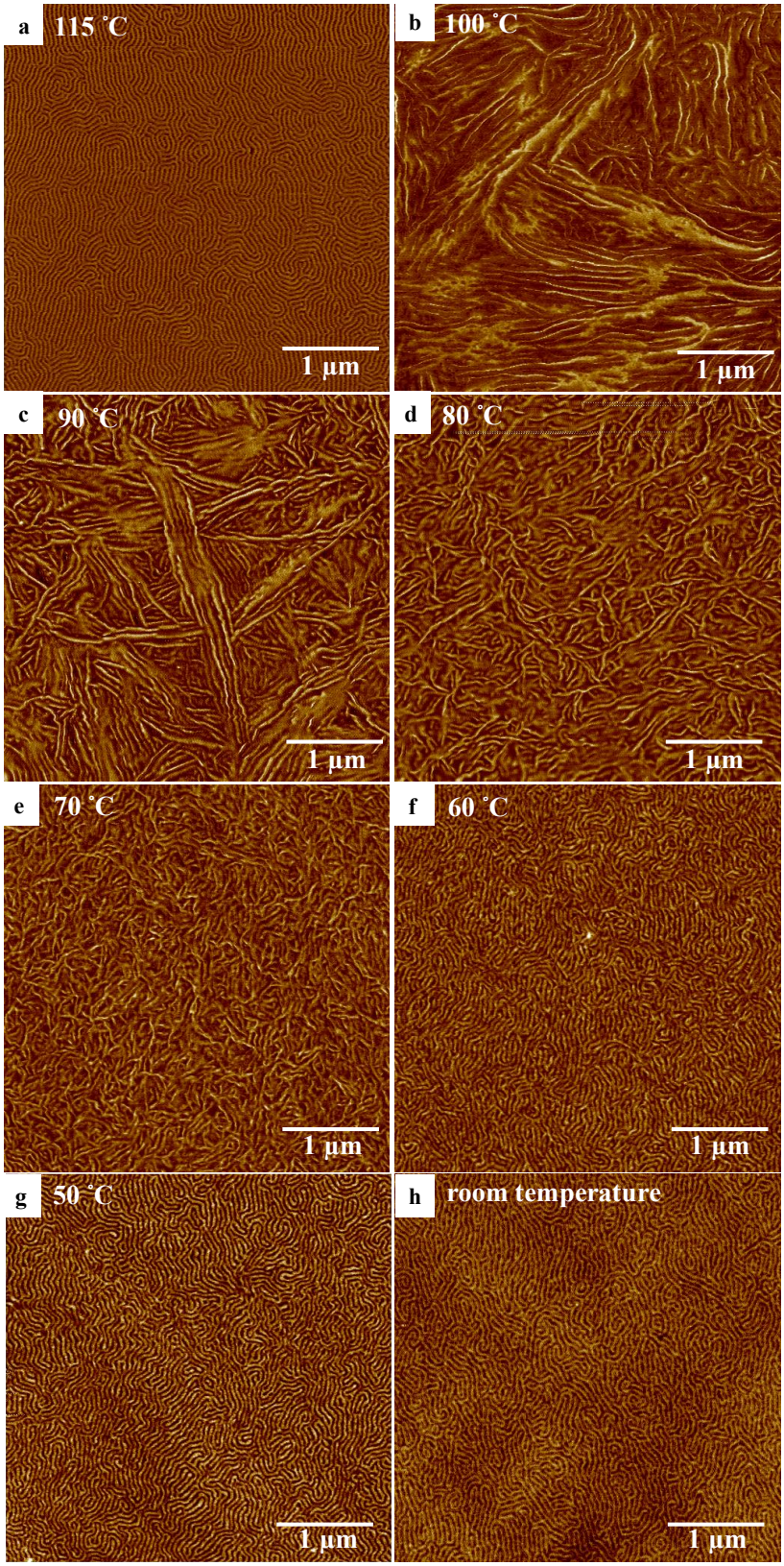

Figure 5.1: AFM phase images of (a) melt phase E/MB at 115 °C and (b-h) a fully crystallized E/MB sample after isothermal crystallization at (b) 100 °C, (c) 90 °C, (d) 80 °C, (e) 70 °C, (f) 60 °C, (g) 50 °C and (f) room temperature (un-oriented cylinders).

Figure **5.1** shows the melt structure of the un-oriented E/MB at 115 °C in image (a), and the different crystal morphologies formed isothermally at a range of temperatures: 100 °C, 90 °C, 80 °C, 70 °C, 60 °C, 50 °C and room temperature, in images (b-h), respectively. In general, confined crystallization can be observed in two cases: firstly when the T_c of the crystalline block (E, in this study) is lower than the T_g of the amorphous block (MB in this study) and secondly when both the crystalline and amorphous blocks are strongly segregated in the molten state and the degree of crystallinity is relatively low [145]. Although, here, in all cases, the T_c,E was greater than T_g,MB for the studied system, a range of crystallization modes was observed. At 100 °C, breakout crystallization was observed (i.e. where the spacing present in the melt was "rewritten" (to a larger value) by crystallization), with the initially cylinder-shaped crystals widening to form lamellae. The melt spacing of E/MB is shown in Figure **5.2**, which is 50 nm ±10 nm. On the other hand, at a temperature range from below 100 °C to above 50 °C, templated crystallization was observed (i.e. where the crystals generally (but not exclusively) grow parallel to the axes of the cylindrical microdomains – meaning that the melt spacing was preserved). At temperatures of 50 °C and below, however, the crystals were fully confined by the pre-existing cylinder microdomains.

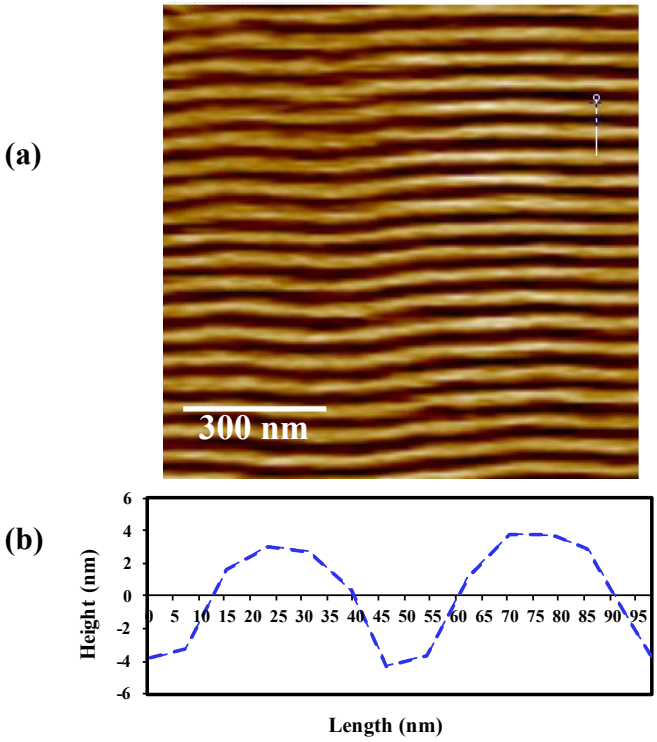

Figure 5.2: (a) AFM phase image and (b) the corresponding cross-section showing the melt spacing in E/MB. The width of the cylindrical microdomains melt is in the range of 40-60 nm.

Although in most cases, the difference between breakout and templated crystallization can be determined qualitatively, quantitative measurements were conducted in order to confirm these qualitative observations. This was done by measuring the width of the crystals and comparing these measurements with the pre-existing melt cylinders. If the size of the crystal was comparable to that of the melt cylinders, the crystal was said to be templated. If the size was larger than the melt structure, however, the crystals were classified as breakout. Section profiles of the crystal shown in Figure **5.18** (g) are used in Figure **5.3** as examples of these measurements. Specifically, Figure **5.3** presents two profile lines of crystals (b) growing perpendicular, and (c) parallel to the melt cylinders, corresponding to the yellow dashed line marked as "A" and "B" in image (a), respectively. The width of the crystal labelled "A" (which is growing perpendicular to the melt cylinders) was found to be ~ 115 nm, which is larger than the value of the cylindrical microdomain melt, while the width of the crystal labelled "B" (which is growing parallel to the melt cylinders) was found to be ~60, which is within the average value of the melt width. This means that crystal A is breakout while crystal B is templated.

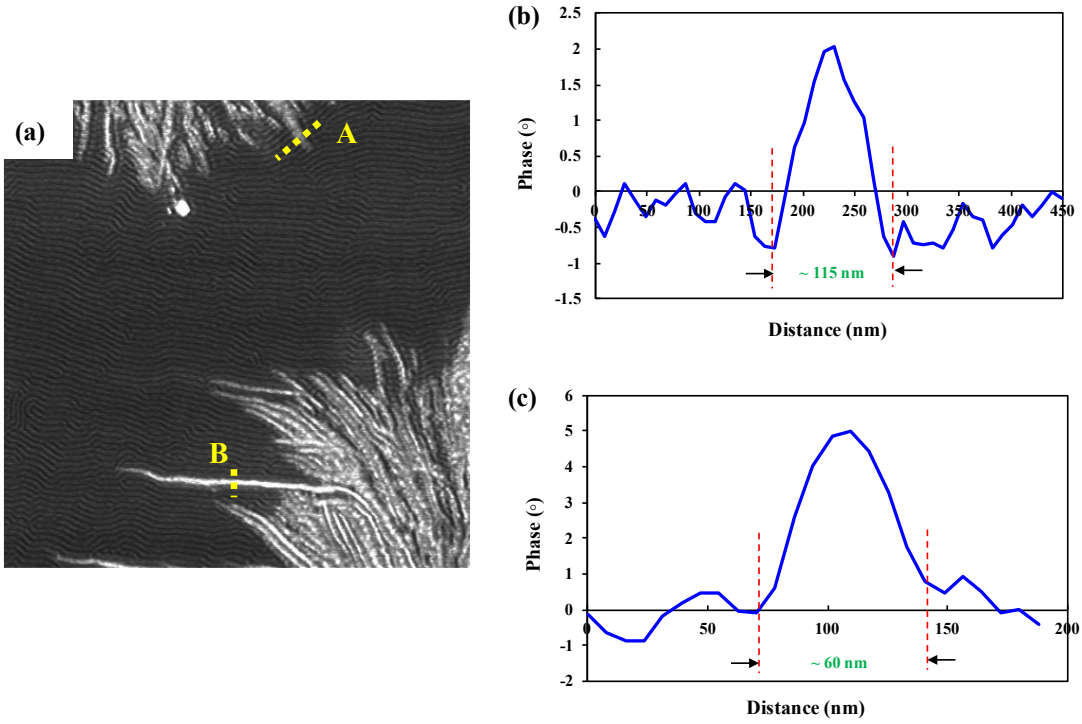

Figure 5.3: (a) an AFM phase image taken from Figure **5.18** (g), and (b-c) section profiles, which were taken from the yellow dashed lines marked as "A" and "B" on image (a). The line profile in (b) shows crystal "A" and illustrates the width of crystals growing perpendicular to the melt cylinders, while the line profile in (c) corresponds to crystal "B", which illustrates the width of crystals growing parallel to the melt cylinders.

Another example of the morphology formation as a function of temperature for samples that had not been pre-oriented is shown in Figure **5.4**, in this case examining the same area. In order to identify the same area of interest, and to relocate it at any time after the isothermal crystallization at different temperatures, a TEM grid was used, as indicated in Chapter 3, Section 3.3.3.3.3. Note that the vertical line in the centre of the images is a defect in the film that was used to help return to the same place each time. Figure **5.4** shows images of different crystal morphologies formed isothermally at a range of temperatures: 100 °C, 80 °C, 70 °C, 60 °C, 50 °C, and room temperature, although the order in which the experiments were carried out was from the lowest crystallization temperature to the highest. If these different crystal morphologies formed isothermally at various temperatures are compared with those in Figure **5.1**, it can be seen that similar results were obtained.

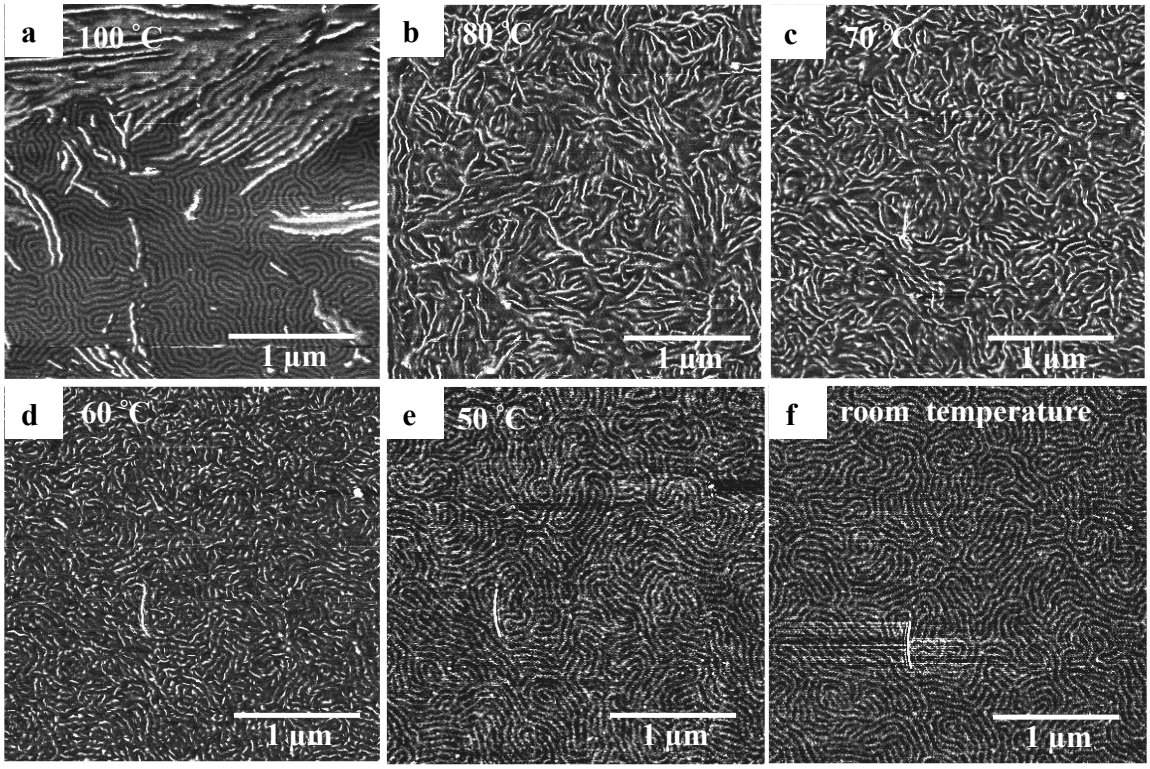

Figure 5.4: AFM phase images of crystallized E/MB after isothermal crystallization (focusing on the same area) at: (a) 100 °C, (b) 80 °C, (c) 70 °C, (d) 60 °C, (e) 50 °C and (f) room temperature (un-orientated cylinders). Colour scales are (a) 7°, (b-d) 11°, (e) 8°, and (f) 9°.

Moreover, by comparing the change in surface morphology caused by E crystallization at different temperatures, it is clear that the nucleation density quickly increased as the crystallization temperature was reduced. At low supercoolings (i.e. high temperatures), such as 100 °C, very few nucleation sites were found, as seen in Figure **5.4** (a). At higher supercooling (i.e. low temperatures), however, such as 80 °C and 70 °C, there was a significant increase in the density of nucleation sites.

The above work was performed on un-oriented microdomains but the same approach was now used to investigate how the morphology formed from oriented microdomains depended on the temperature of crystallization (Figure **5.5**). Similar results were obtained.

5.2.1.2. Morphology Formation from Oriented Cylindrical Microdomains

Figure **5.5** shows the melt structure of the oriented E/MB at 112 °C in image (a), and the fully crystallized film after quenching to room temperature in image (i). The crystals were strictly confined within the melt structure at room temperature.

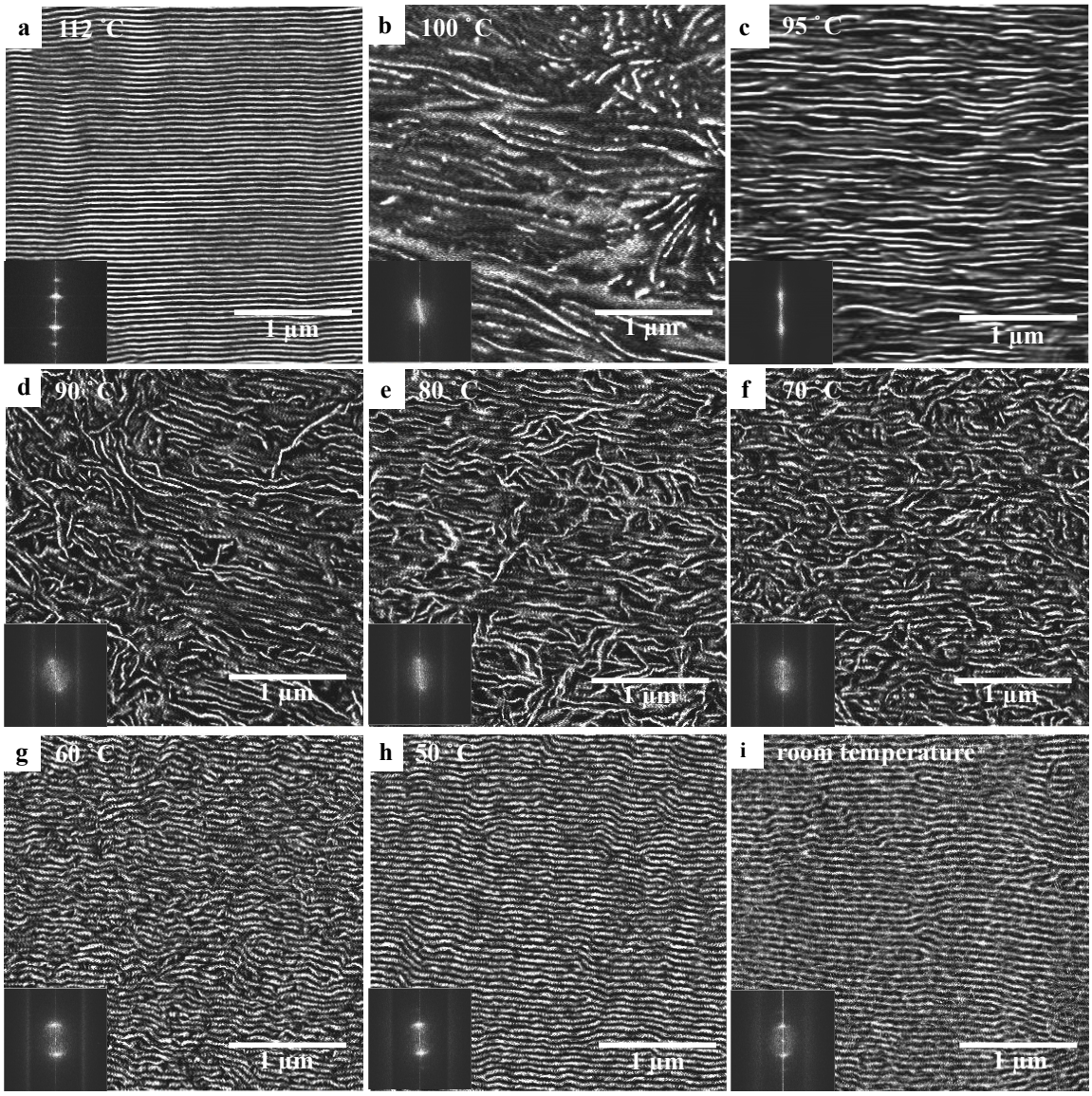

Figure 5.5: AFM phase images of E/MB showing (a) an orientated melt structure at 112 °C and images (b-i) showing crystallized E/MB after isothermal crystallization at: (b) 100 °C, (c) 95 °C, (d) 90 °C, (e) 80 °C, (f) 70 °C, (g) 60 °C, (h) 50 °C and (i) room temperature. The insets are 2D fast Fourier transforms of the images. Colour scales are (a) 8°, (b) 7°, (c) 8°, (d) 9°, (e-f) 10°, (g) 11°, and (h-i) 12°.

The change in crystal orientation with temperature is striking, with an initial increase in orientation on cooling, lower orientation at moderate supercooling (e.g. at 80 °C) and

then increased orientation at high supercooling. To explore this further we follow the crystallization process *in situ*.

5.2.2. Following Crystallization in Pre-Oriented Domains *in Situ*

After aligning the cylindrical microdomains in the melt phase with the AFM tip, the film was then cooled to the desired crystallization temperature to be isothermally crystallized in order to investigate the subsequent crystallization.

5.2.2.1. Crystallization Behaviours at Different Temperatures

The crystallization behaviour was investigated by observing the crystallization process in real time at various temperatures. Figure **5.6**–Figure **5.10** show some examples of crystallization at 99 °C, 98 °C, 97 °C, 96 °C and 95 °C, respectively. In order to study the influence of temperature on crystallization, the crystallization was followed in the temperature range of 95–101 °C, where the AFM was able to image the crystallization *in situ*. Below 95 °C, it was not possible to follow the crystal growth in real time, since, due to the large growth rate, the crystallization was found to be complete before the imaging could be carried out. Above 101 °C, no crystallization was observed, even after the experiment was run for several hours.

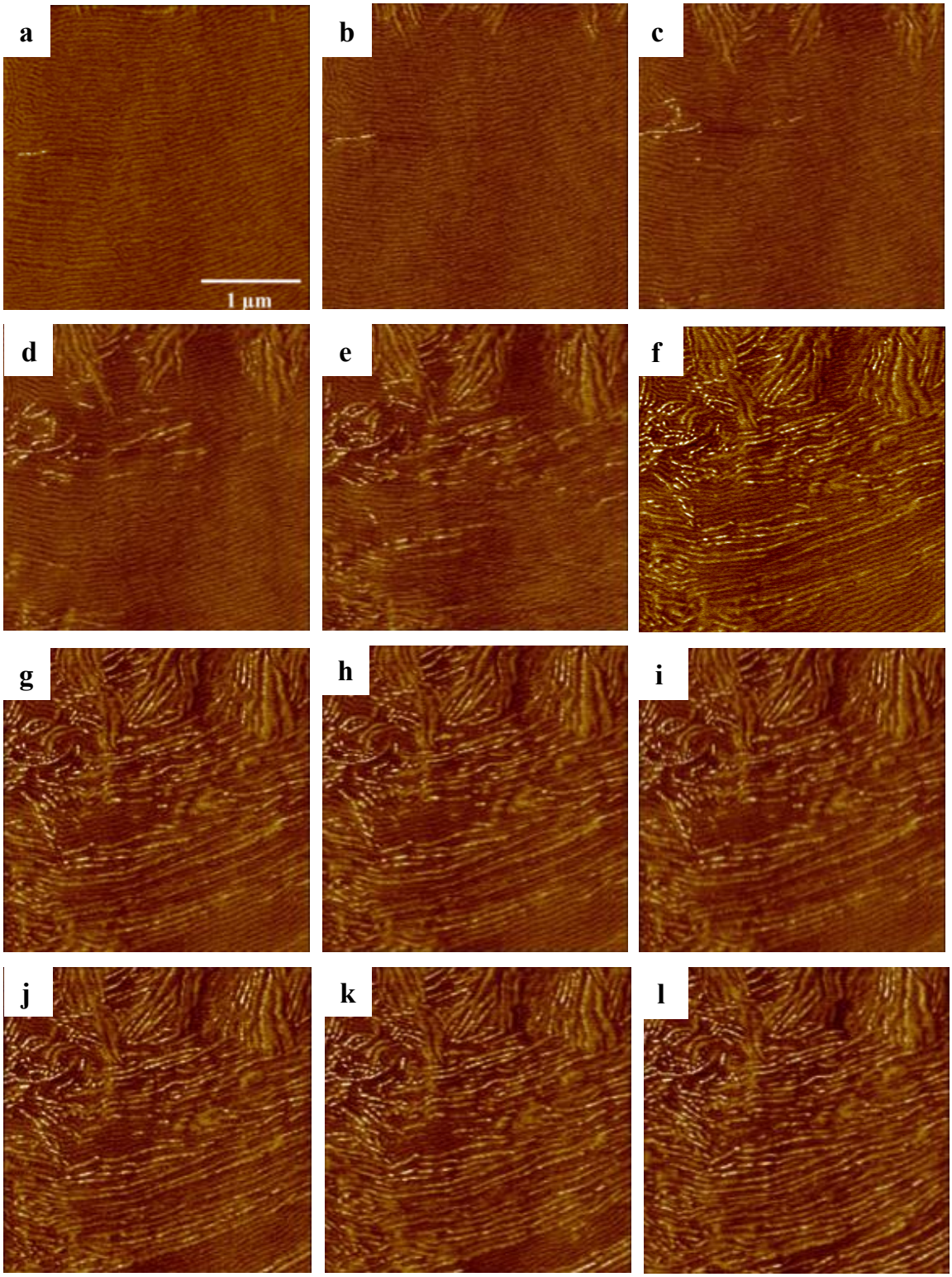

Figure 5.6: A sequence of AFM phase images collected at 99 °C showing the crystallization in E/MB from the aligned melt structure. Dark to bright represents a variation in phase of 7°.

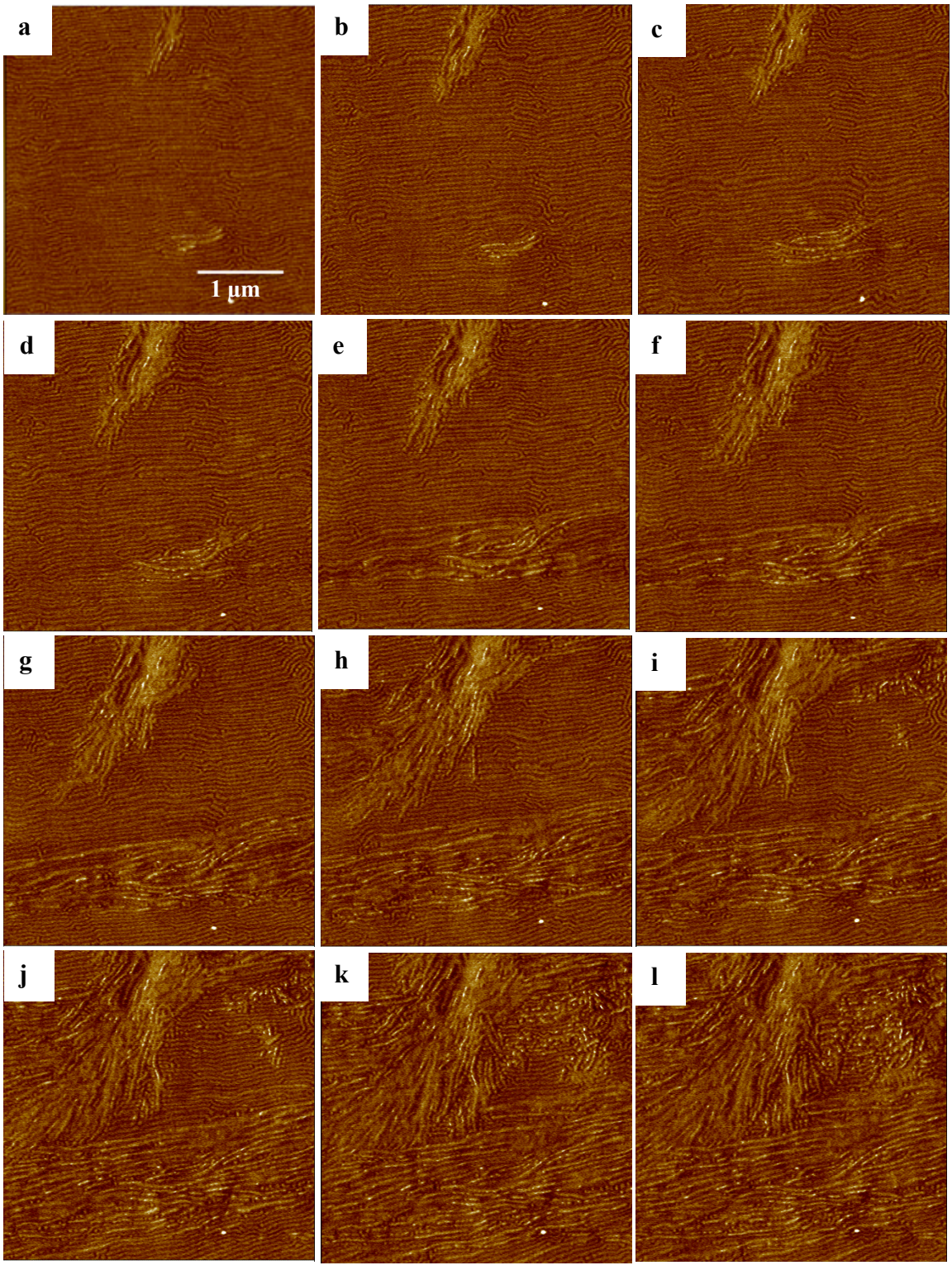

Figure 5.7: A sequence of AFM phase images collected at 98 °C showing the crystallization in E/MB from the aligned melt structure. Dark to bright represents a variation in phase of 8°.

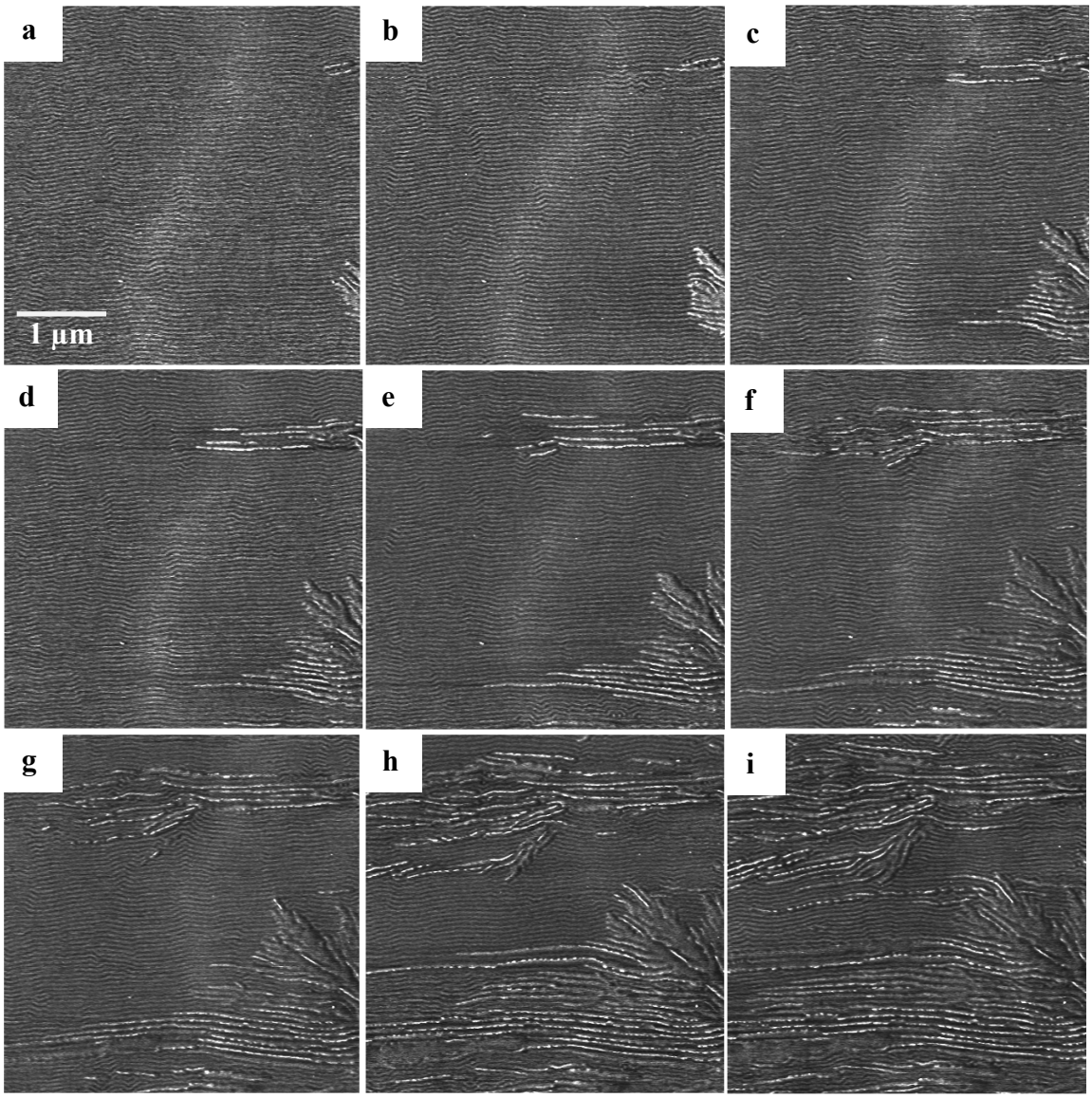

Figure 5.8: A sequence of AFM phase images collected at 97 °C showing the crystallization in E/MB from the aligned melt structure. Dark to bright represents a variation in phase of 4°.

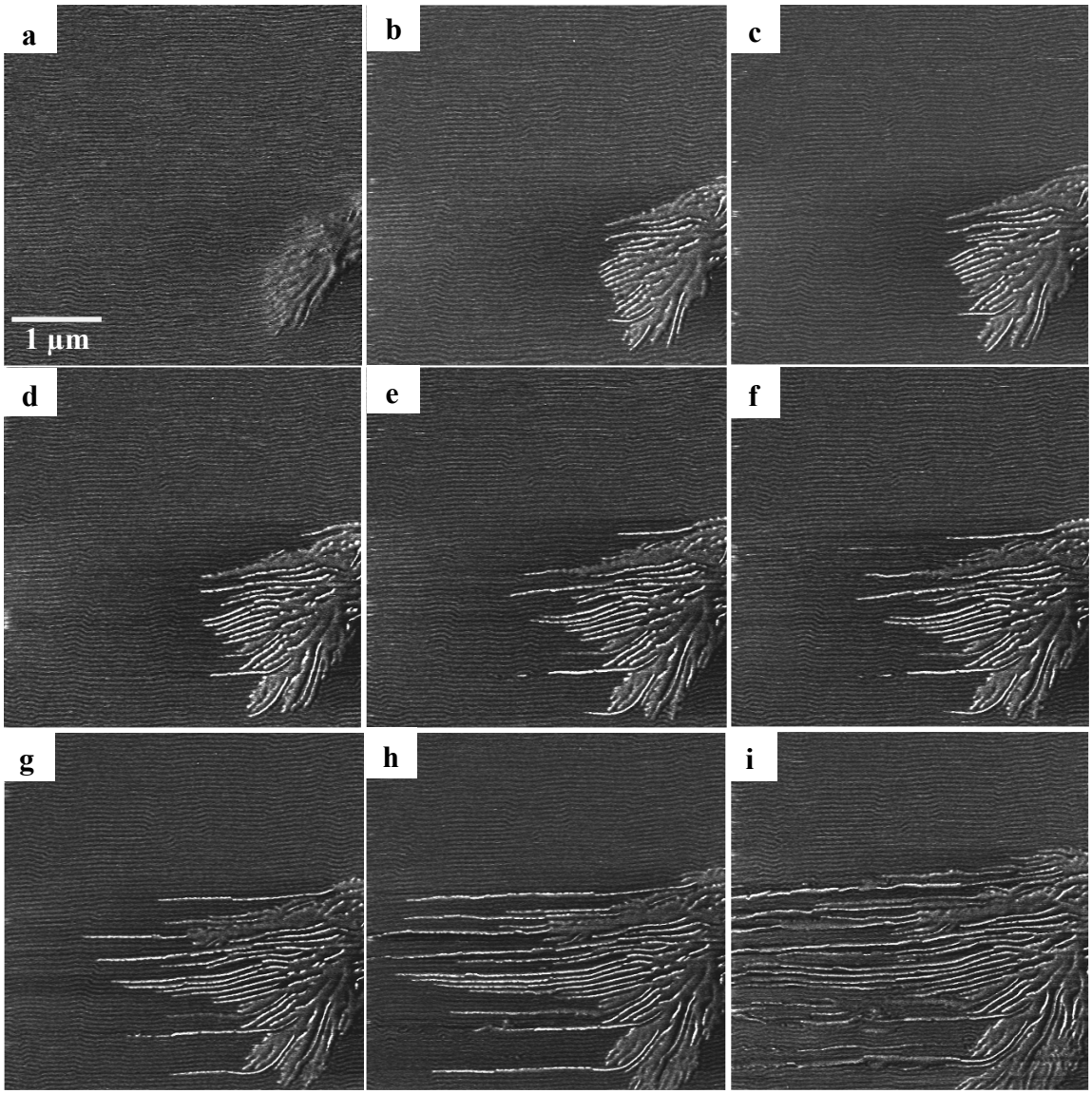

Figure 5.9: A sequence of AFM phase images collected at 96 °C showing the crystallization in E/MB from the aligned melt structure. Dark to bright represents a variation in phase of 10°.

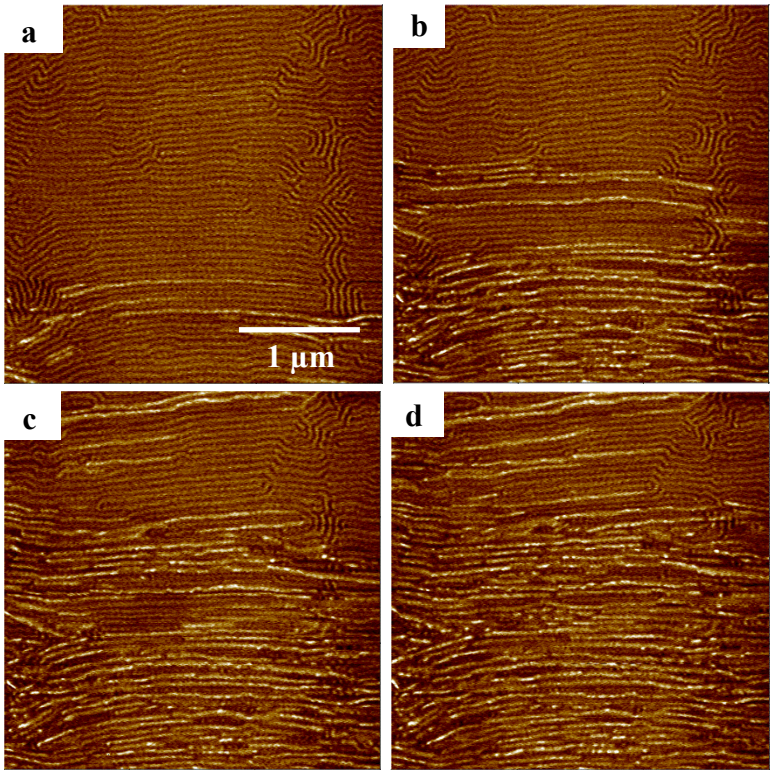

Figure 5.10: A sequence of AFM phase images collected at 95 °C showing the crystallization in E/MB from the aligned melt structure. The colour scale represents a change in phase of 5°.

Figure **5.6**-Figure **5.10** show a series of AFM phase images taken during isothermal crystallizations in pre-oriented microdomains at a temperature range from 99 °C to 95 °C, respectively. For all the images, a clear phase contrast can be seen between the two melt polymers (E and MB), as well as between the crystalline polyethylene and the melt. The brightest area indicates the crystalline polyethylene, while the darkest area indicates the MB-rich domain, followed by the E-rich area. This clear phase contrast allows the assessment of the effect of the melt structure on the crystallization process.

A mixture of templated and breakout crystallization was observed: templated where the crystals generally (but not exclusively) grow parallel to the axes of the cylindrical microdomains, and breakout crystallization where the crystals break out from the microdomains allowing lamellae to form. For example, in the top of Figure **5.6** some regions of breakout crystallization at 99 °C can be observed, as has previously been documented for this copolymer [6]. Figure **5.10** shows templated crystallization occurring at 95 °C, with the polyethylene crystals generally following the contours of the pre-existing E cylinders in the melt.

In these combined *in situ* and *ex situ* images we found interesting behaviour of crystals over a range of temperatures that can be divided into four categories. First, at a very high temperature (i.e. 100 °C), crystals crossed domain boundaries easily which led to breakout; in some regions, instead of the needle-like crystals present within cylindrical microdomains, flat lamellae lying in the plane of the sample surface could be observed. Second, as the temperature was reduced (i.e. to 95 °C) crystals grew much faster along the microdomains leading to templated crystallization, and the flat lamellae resulting from breakout were no longer generally observed. Third, as the temperature was reduced further (i.e. to 80 °C) crystals were observed to cross domain boundaries again, because the nucleation density had increased and the distance between nuclei, required for the growing crystals to reorient, was thus reduced. Finally, as the temperature was reduced even further (i.e. to 50 °C), crystallization became confined within the microdomains. It is unclear whether this was due to the confinement changing the growth direction, or because the nucleation density was so high that it dominated the growth, although the latter seems most likely. Formation of lamellae was only observed at high temperatures (i.e. 100 ºC) where the crystals widen and break out from the cylindrical microdomains, while at lower temperatures only needle-like crystals within cylindrical microdomains were observed. This is because at elevated crystallization temperatures (i.e. temperatures just below the melting point) only a very few nuclei are formed, and the crystal growth rate is low, in contrast to that at low crystallization temperatures. At this high temperature, the diffusion of the chains towards the growth front is high due to the high mobility of both blocks, which promotes large crystalline domains or lamellae.

In these studies of isothermal crystallization (i.e. not quenching to room temperature) the best orientation obtained was at 95 °C. If our hypothesis is correct, i.e. that it is nucleation that is dominating at the lowest temperatures, then although the crystal domains are oriented at these low temperatures, we would not expect the crystal lattice to be oriented; while at 95 °C, where it has grown along the orientation direction, we would expect both the domain and the lattice to have a common orientation. We were not able to test this in these experiments, however, due to the relatively small size of the oriented regions in our samples.

It was also worth looking into the crystallization behaviours in a mix of random and orientated melt structures. Figure **5.11** shows an example of this situation.

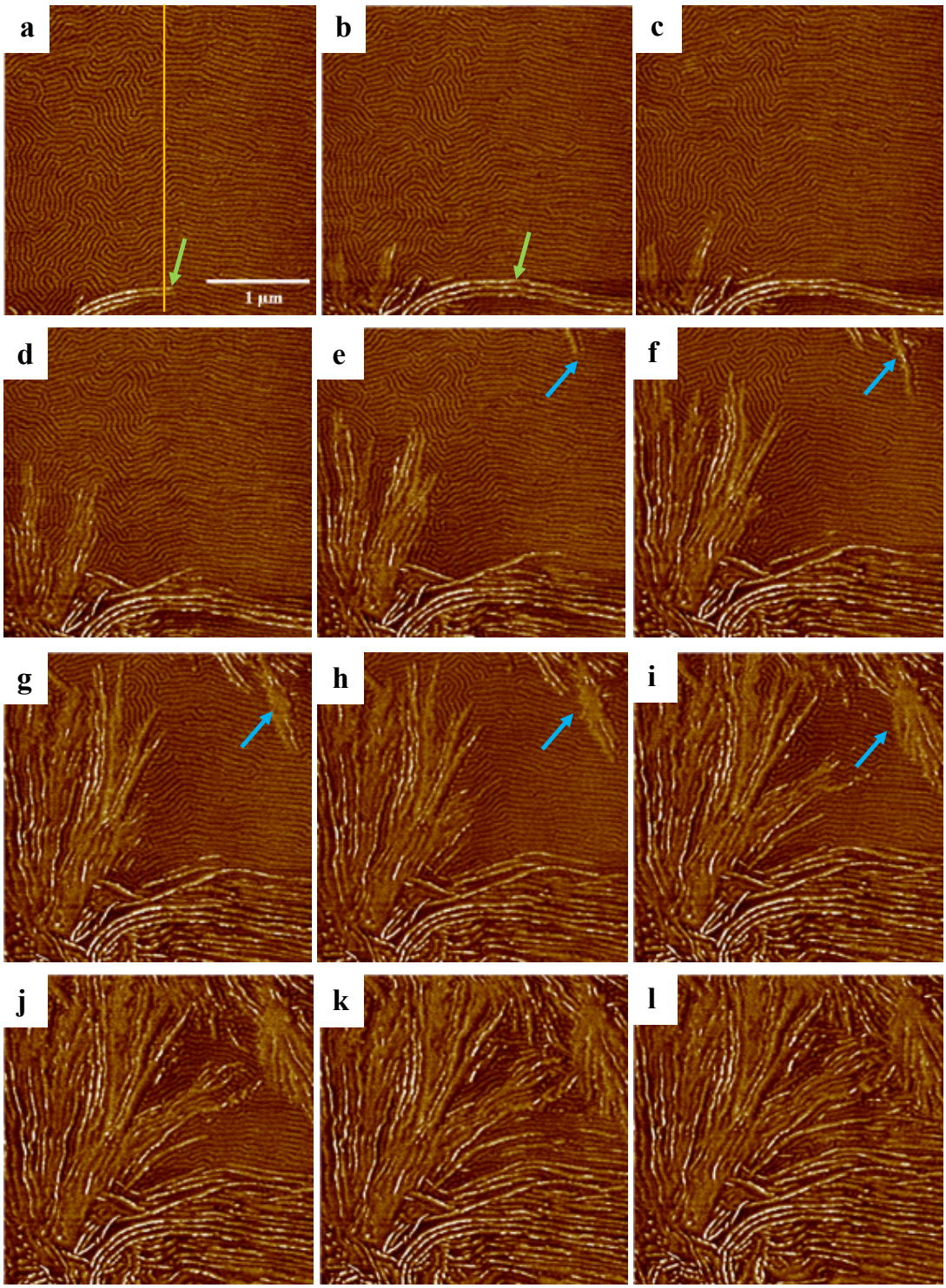

Figure 5.11: A sequence of AFM phase images showing E/MB crystallization at 97 ºC in a mixed orientation sample (half oriented and half random). The vertical yellow line in image (a) has been added to aid the reader to see the different orientations of the cylindrical microdomains: those on the left-hand side are random cylinders, while those on the right-hand side are orientated cylinders.

Figure **5.11** shows the crystallization in the case of the mixed orientation of cylinders: the orientated cylinders are on the left-hand side of the images, while the random cylinders are on the right-hand side (corresponding to the region that the AFM tip had scanned with a large drive amplitude). It was observed that the crystals tended to grow within and along the cylindrical microdomains in the aligned area, except when other crystals grew from the randomly orientated area towards the aligned area, as can be seen in the area indicated by the blue arrow in Figure **5.11** (e)–(l), or when the formed crystal is initially perpendicular to the cylinders.

5.2.2.2. Growth Rate

The growth rate of the crystals was studied as a function of temperature in order to obtain quantitative kinetic information about the crystallization behaviour. The distance of the crystal growth was measured in a succession of images by measuring how far the growth front of the crystal moved from one image to the next. The average growth rates of a number of crystallites growing parallel to the cylinder axes, as well as those growing perpendicular to the axes, were measured and compared at temperatures of 97–100 °C.

Figure **5.12**-Figure **5.15** show the lengths of several crystals growing parallel to the cylindrical microdomains and others growing perpendicular to them, in micrometres, versus time in seconds, at crystallization temperatures of 97–100 ºC, respectively.

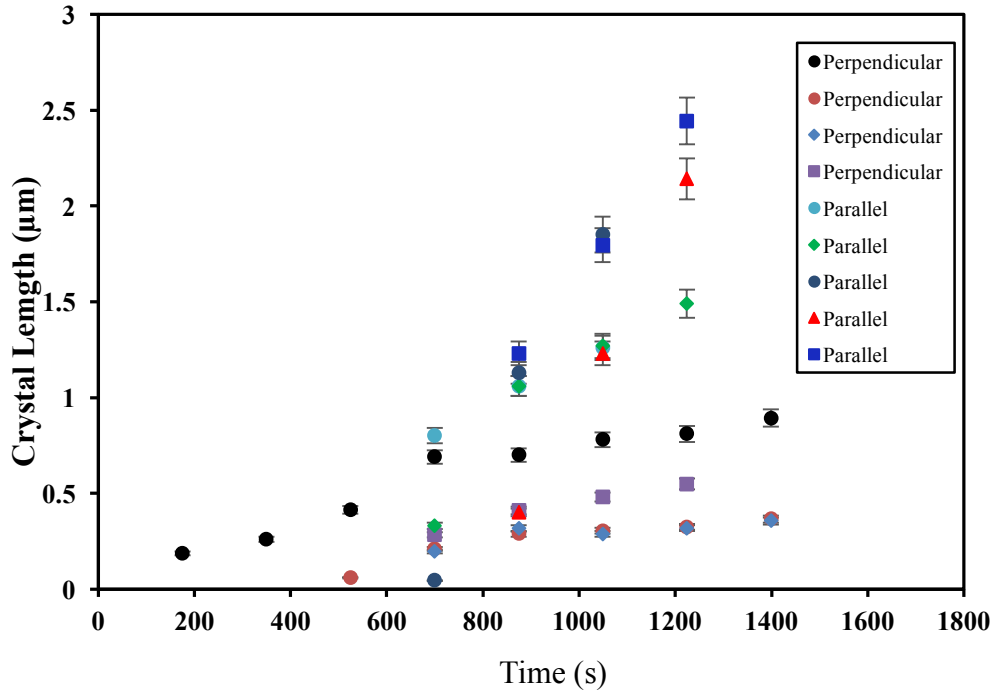

Figure 5.12: Graph showing the crystal growth lengths of some crystals (nine crystals) growing parallel to the melt structure, and those growing perpendicular to it, at 97 °C.

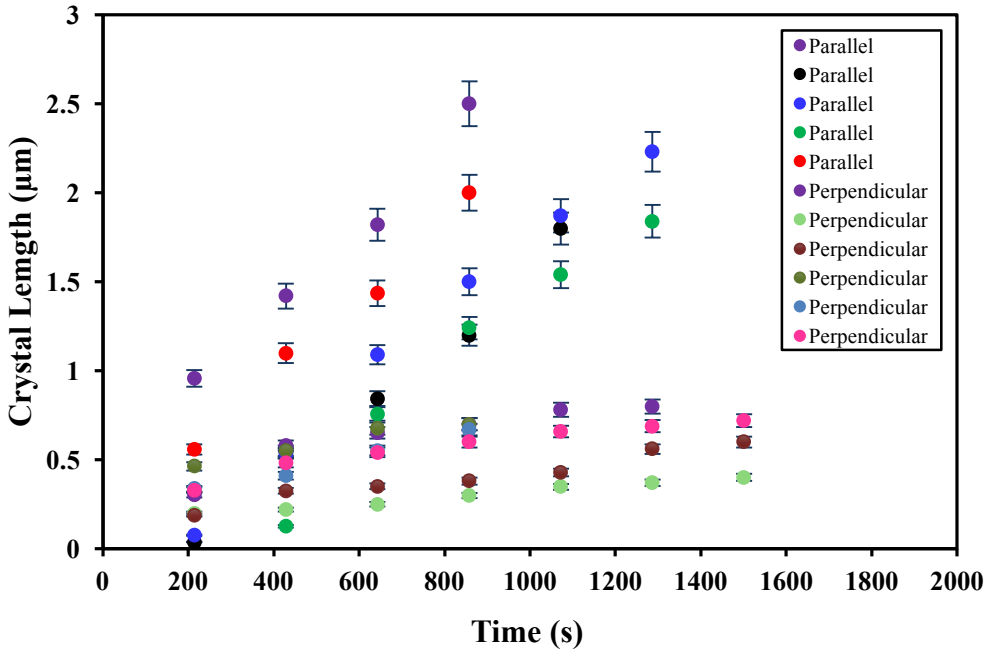

Figure 5.13: Graph showing the crystal growth lengths of some crystals (eleven crystals) growing parallel to the melt structure, and those growing perpendicular to it, at 98 °C.

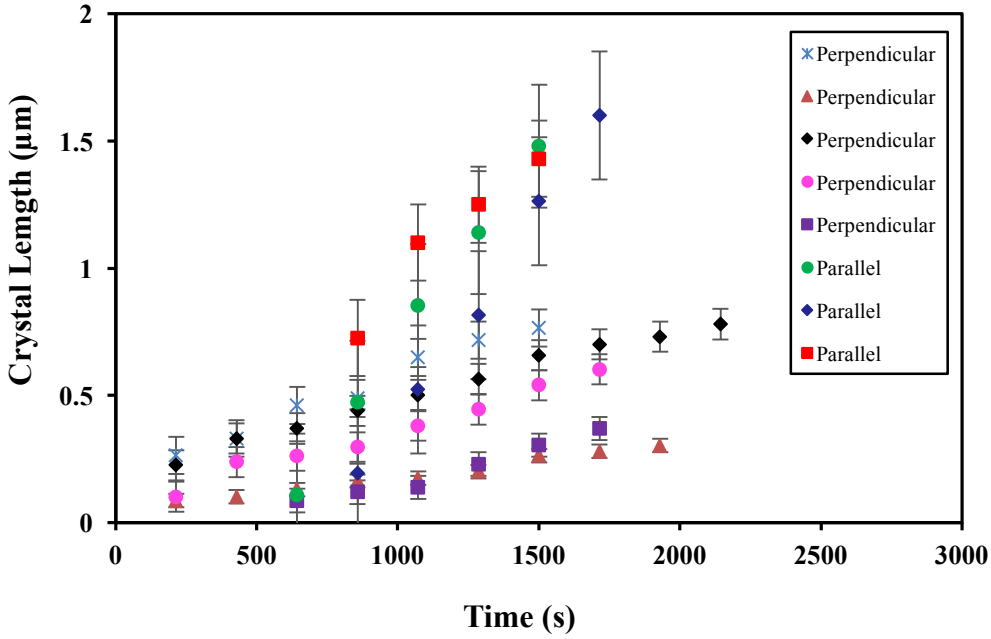

Figure 5.14: Graph showing the crystal growth lengths of some crystals (nine crystals) growing parallel to the melt structure, and those growing perpendicular to it, at 99 °C

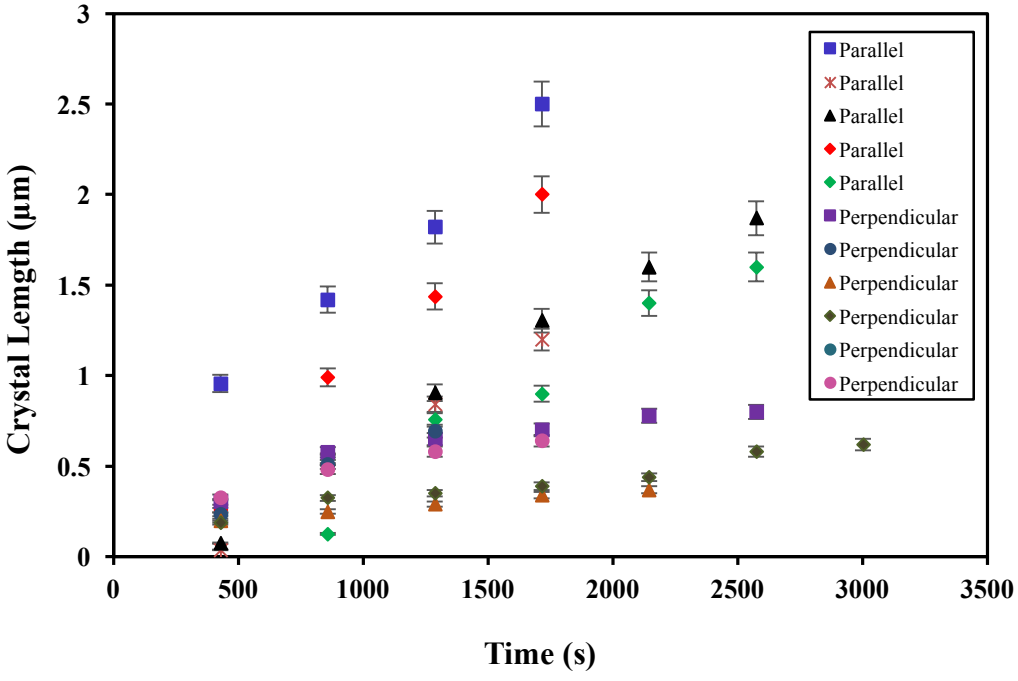

Figure 5.15: Graph showing the crystal growth lengths of some crystals (eleven crystals) growing along the melt structure (confined), and those growing against it (breakout), at 100 °C.

The growth rates were measured in nanometres per second by dividing the distance the crystal moved by the time taken from one image to the next (i.e. the time that had

elapsed between images). The growth rates of the crystals growing along and against the melt structure were measured and compared. The growth rates were examined as a function of temperature. Some growth rate values are given below in Table **5.1**.

Moreover, the growth rates of individual crystals were also measured as a function of time and were found to fluctuate with time for each crystal, as well as between crystals. Figure **5.16** shows two plots demonstrating such growth rate variations as a function of time at 99 °C and 98 °C, respectively. This result was found in previous studies on un-oriented E/MB domains [6], and in other systems such as polyethylene [4].

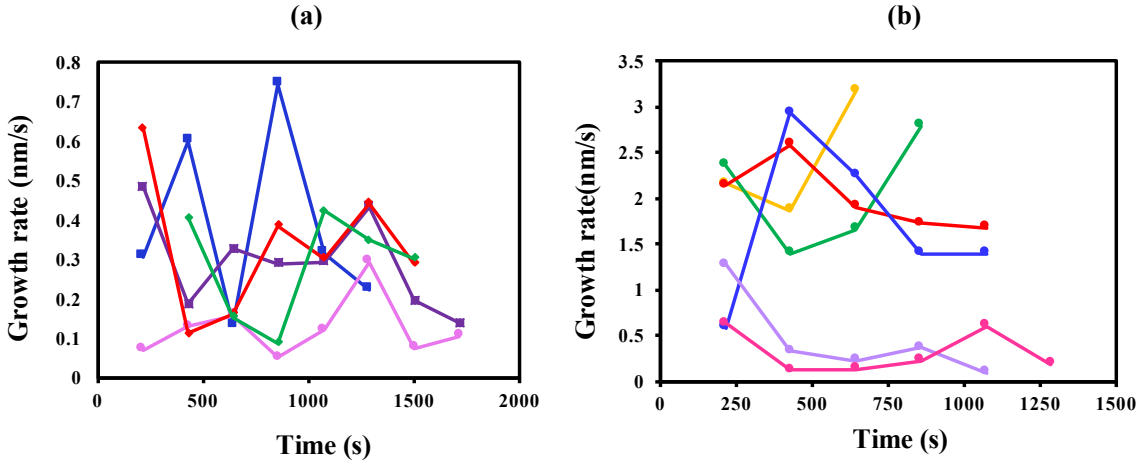

Figure 5.16: Plots showing the variations of the growth rate as a function of time for (a) five separate crystals at 99 °C and (b) six crystals at 98 °C.

Table 5.1: The growth rates of a number of crystals growing parallel to the cylindrical microdomains, and those growing perpendicular to them, at temperatures ranging from 97 °C – 100 °C.

Crystallization Temperature (°C)	**Crystal No.**	**Growth Rate (nms^{-1})**				
		Parallel to cylinders	Error (R^2)	Perpendicular to cylinders	Error (R^2)	Overall average rate
100	1	0.9	0.9876	0.2	0.8489	
	2	0.8	0.9601	0.19	0.9509	
	3	1.3	0.9905	0.2	0.9342	
	4	0.5	0.9862	0.17	0.9625	
	5	0.8	0.9915			
	6	1.2	0.9865			
		0.916		0.19		Average
99	1	1.6	0.9979	0.4	0.9805	
	2	1.7	0.9954	0.3	0.9888	
	3	1.1	0.9529	0.1	0.9801	
	4			0.3	0.9589	
	5			0.3	0.9788	
		1.46		0.28		Average
98	1	2	0.9934	0.5	0.9858	
	2	2.2	0.9915	0.4	0.9483	
	3	2	0.9706	0.4	0.8489	
	4	2	0.9862	0.3	0.9509	
	5	2.3	0.9867	0.3	0.9269	
	6			0.2	0.9864	
		2.1		0.35		Average
97	1	5	0.9993	0.6	0.9206	
	2	3.5	0.9984	0.5	0.9734	
	3	5	0.9866	0.3	0.8388	
	4	1.3	0.9948	0.3	0.7665	
	5	2.1	0.9851			
		3.4		0.425		Average

Table **5.1** shows the measured and average growth rates of a number of crystallites growing parallel to the cylindrical microdomains and those growing perpendicular to them at temperatures of 97–100 °C. This allows for the easy comparison of the growth rates of these crystallites at the different crystallization temperatures. It can be seen that the growth rate of the selected crystallites at 97 °C was almost twice that which occurred at 99 °C, which in turn was about double the growth rate at 100 °C. This

implies that even a small change in temperature can have a significant impact on the crystallization process. This also confirms the previous deduction and indicates that crystals tend to grow faster at lower crystallization temperatures. The measurement of the difference in the growth rates of the crystals growing parallel to, and perpendicular to, the cylinders is summarized in Table **5.2** (see the corresponding graphs of these values in Figure **5.17**).

Table 5.2: The ratios and overall average growth rates of 35 crystals growing parallel to the cylinder axis, and the growth rate perpendicular to the cylinder axis, at temperatures of 97 °C – 100 °C.

Crystallization Temperature (°C)	**Average Growth Rate (nms^{-1})**		**Ratio of growth rates**
	Parallel to cylinders	Perpendicular to cylinders	
100	0.916	0.19	4.8
99	1.46	0.28	5.2
98	2.1	0.35	6
97	3.4	0.425	8

Table **5.2** illustrates the ratios and overall average growth rates of a number of crystals growing along the melt structure and those growing against it at temperatures of 97 °C –100 ºC. Based on the values indicated in Table **5.2**, the two following graphs clearly show the relationship between the ratios and overall average growth rates along the cylinders and against them (see Figure **5.17**).

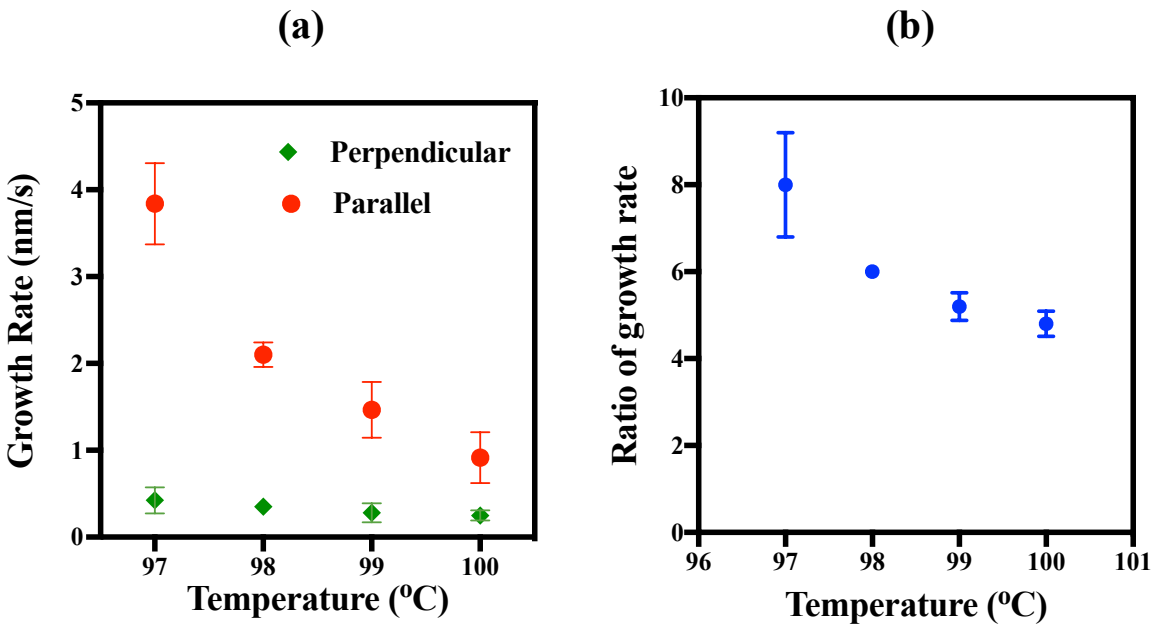

Figure 5.17: Graphs showing the relationship between temperature and (a) the average growth rates along the cylinder axis, and the growth rate perpendicular to the cylinder axis, and (b) the ratio of the two.

From Figure **5.17** (a) it can be clearly seen that the growth rates along cylinders are much higher than the growth rates perpendicular to them. Moreover, as the temperature increased, the growth rate ratio of the crystals growing along the cylinders compared to those growing against them decreased sharply from ~ 8 at 97 °C to ~ 4.8 at 100 °C as shown in Figure **5.17** (b). Hence, two outcomes were observed related to increasing the crystallization temperature: a decrease in the overall crystallization rate and a decrease in the relative difference between the growth rates along the cylinders and against them.

These data imply that, at high temperatures, an increase in the diffusion of E blocks between domains and a decrease in the rate of take-up of E chains onto the growth front combine to decrease the difference in growth rates along and against the cylinders, since the time for a chain to diffuse from one cylinder to another becomes comparable to the time required for a chain to add to the growing crystal, and thus breakout crystallization can occur.

5.2.2.3. The Transition from 'Breakout' to 'Templated' Growth

At low supercooling the nucleation density is low, so for crystals to grow relatively straight in un-oriented areas they must cross domain boundaries. Growth parallel to the oriented microdomains happens through re-orientation of the growth direction, either from bending or crystal branching. Such a process is shown in Figure **5.18** and, previously, in Figure **5.9**.

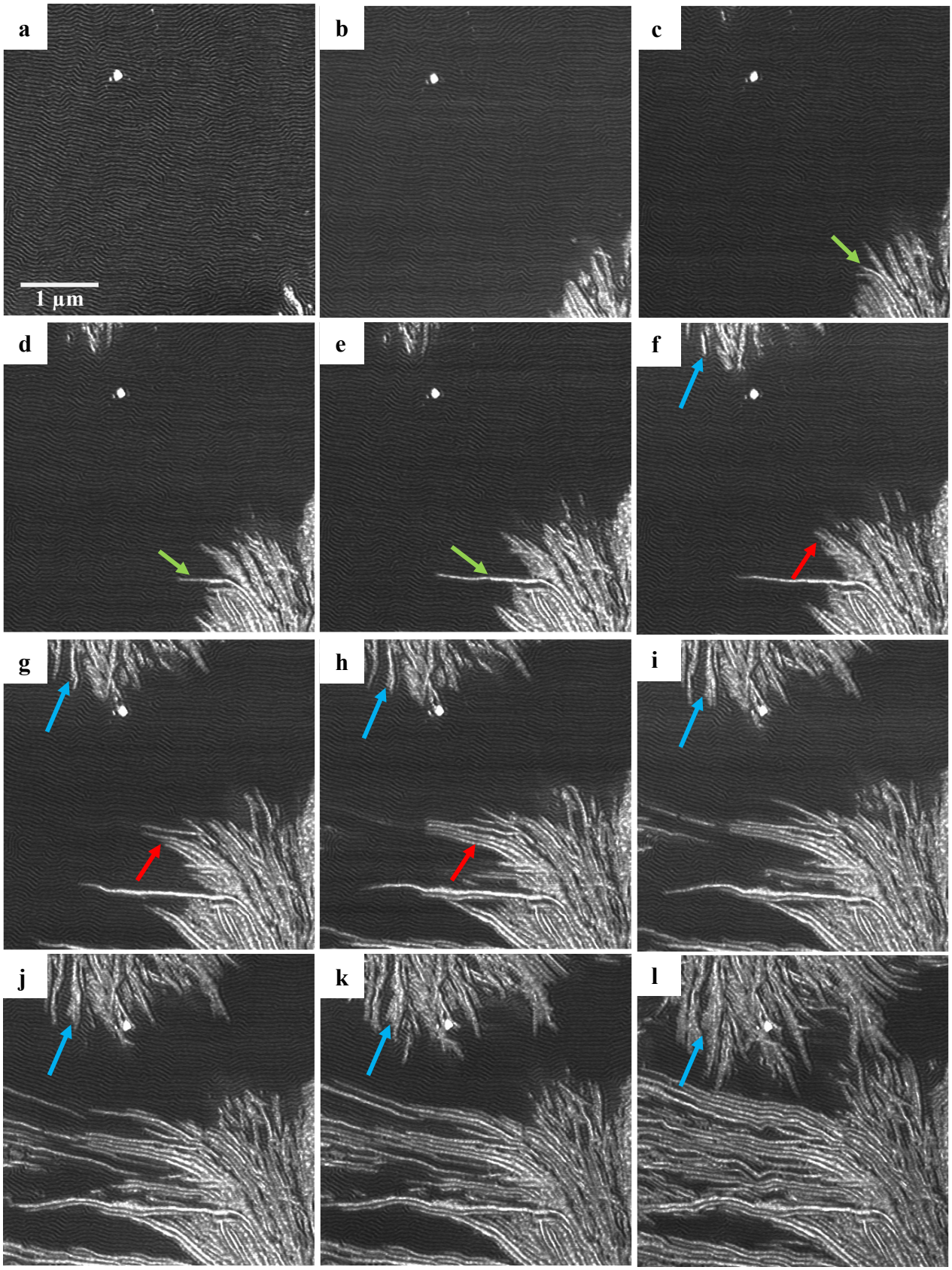

Figure 5.18: *In situ* AFM phase images showing E/MB crystallization at 101 °C. Each image was captured in 128 s and the black to white scale is 6°. Arrows have been added to aid the reader in following the branching and curving of crystals growing against the melt structure.

Figure **5.18** shows the partial branching of crystals that were growing against the melt microdomains. Two different behaviours for the branching crystals are illustrated:

a) Crystals thickening and branching (see blue arrows in Figure **5.18** (f-l)) until they meet another crystal, as shown in image (l).
b) Crystals adjusting their growth directions to be alongside the existing melt cylinders, with an increase in their growth rate, without any branching. Examples of such situations are indicated by the red arrows in Figure **5.18** (f-h) and the green arrows in Figure **5.18** (c-e).

Crystals growing parallel to the cylinder axes showed very low rates of branching compared with crystals growing perpendicular to the cylinders. In the case of crystals growing parallel to the cylinder axes, the crystallization front was always surrounded to the sides by uncrystallisable material. To branch into another domain would require a significant alteration of the local melt structure by diffusion of copolymer. Since this diffusive process is slow relative to the growth of the crystal along the cylinder, it becomes unlikely that the diffusive processes will have enough time to alter the domain structure at the growth front to form branches before the bulk of the material is consumed by the crystallization along the melt domain. In the case of crystals growing against the melt domain, on the other hand, the crystal front was constantly being forced to reorganize the local melt structure in order to grow. Under these conditions, crystal growth was slowed significantly, enabling effects such as the branching and thickening of the crystals to occur.

There was a gradual change in direction as the crystal moved from being perpendicular to the microdomains to being parallel to them. Although the growth rate throughout this transition remained roughly the same as the rest of the crystals that were growing perpendicular to the microdomains, once the transition had occurred (i.e. once the crystals had started to grow parallel to the microdomains) the growth rate increased to the rate of the other crystals that were growing along the microdomains. This is due to the high diffusion of the PE along the melt microdomains, and these crystals continued to grow parallel to the microdomains until they were blocked by another crystal.

This significant change in the growth rate was also demonstrated quantitatively by measuring the growth rate of the crystal indicated by the green arrow in Figure **5.18** (c) as it transited from being a breakout crystal to a templated one (see Figure **5.19**). In this case, the average growth rate increased significantly after the transition occurred, from just about 1.2 nm/s, when it was a breakout crystal, to approximately 4.7 nm/s when it became templated. The ratio of the growth rate of this crystal was found to be 3.9 (at 101 °C in this experiment), which is in a good agreement with the measurements conducted above.

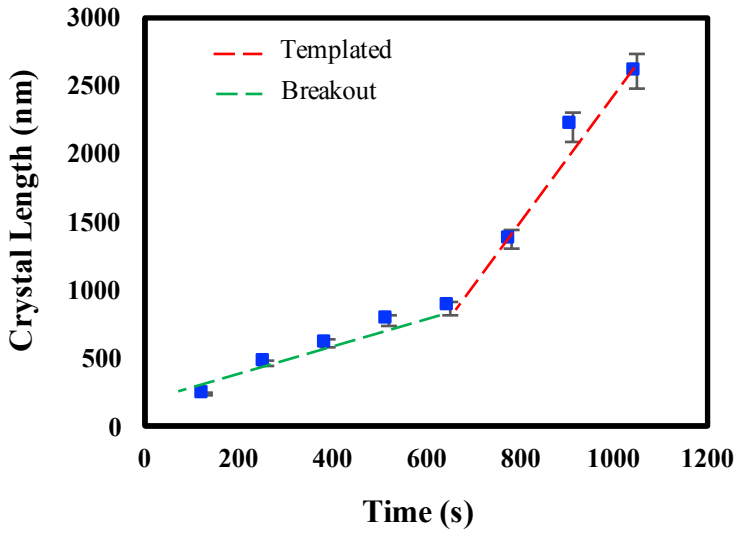

Figure 5.19: A graph showing the variation of crystal length as a function of time, as the crystal changes from being breakout (the green dashed line) to being templated (the red dashed line) at 101 °C. This measurement was taken from the crystal indicated by the green arrow in Figure **5.18** (c-e).

5.3. Conclusion

This chapter has investigated the crystallization behaviour of a cylinder-forming E/MB diblock copolymer in real time and using *in situ* combined with *ex situ* imaging by AFM. The crystallization in pre-oriented E/MB microdomains was followed in real time at various temperatures. Depending on the thermal conditions examined, a change from fully confined crystallization to templated and breakout crystallization was observed. Confined behaviour of crystals was observed at very high supercooling (room temperature and 50 °C), templated crystallization at intermediate temperatures, and a mixture of templated and breakout crystallization at the highest temperatures, e.g. at 100 °C. The difference in the morphology and the behaviour of crystals growing parallel to the axes of the pre-existing melt cylinders, and those growing perpendicular to the axes, was explored. The growth rates of crystals growing parallel to the established melt structure were higher than those of crystals growing perpendicular to them. As the crystallization temperature increased, the overall crystallization rate and the relative difference between the growth rates along the cylindrical microdomains and against them decreased. This indicates that small variations in crystallization temperature can have a significant effect on the morphology and properties, particularly where the melt has been pre-aligned, as may well happen during processing. Moreover, the growth rates fluctuated with time for each crystal, as well as between crystals at different temperatures.

It was also found that crystals could change their growth directions from being perpendicular to the microdomains to being parallel to them, and that this transition was associated with a clear and significant increase in the crystal growth rate.

Chapter 6

Shear Induced Crystallization of PE by AFM Tip

6.1. Introduction

Polyethylene (PE) is one of the most important commercial, industrial and scientific polymers due to its interesting mechanical properties, excellent characteristics and reasonable cost. It plays an essential role in modern life, especially in packaging, such as plastic bags, plastic films and containers, including bottles. Furthermore, PE has been extensively used as a model to study polymer crystallization due to its simple chemical structure (PE is the simplest commercial polymer) (see its chemical structure in Figure 2.1). A detailed understanding of the PE crystallization process could therefore be very useful for increasing overall knowledge about polymer crystallization, while also potentially expanding the field of application of PE. Many researchers have studied the crystal structure and crystallization process of PE in the past five decades.

The crystallization under flow of PE [4, 5, 158, 159], and of polymers in general [160–163], has been the subject of extensive study for many years due to its crucial role in determining the formation of crystal structures and the final properties of polymeric products. During processing, such as fibre spinning, injection moulding and film blowing, polymer materials are subjected to complex flow fields [159, 164], which affect their final structure and morphology (e.g. leading to extended-chain crystals) and the crystallization kinetics (such as nucleation density, nucleation rate), which in turn influence the final properties of polymeric products. It is, therefore, extremely important to understand how the processing influences microstructure formation in polymers. In contrast to crystallization under quiescent conditions, where spherulites form, the “shish-kebab” structure is often observed in flow-induced crystallization of

polymer melts and solutions. Thus, during polymer processing the crystallization kinetics and the final morphology are greatly influenced by the molecular orientation induced by flow (in the molten state) and deformation (in the solid state).

The crystallization of PE has been studied using a number of traditional techniques including: small-angle X-ray scattering (SAXS) [161, 165], wide-angle X-ray diffraction (WAXD) [167], small-angle neutron scattering (SANS) [168], optical microscopy (OM) [163, 168, 169], TEM [171], and AFM [4, 5, 171]. Among these techniques, AFM is the most ideal technique due to its ability to monitor polymer crystallization non-destructively *in situ*, in real time with atomic resolution, as mentioned in detail in Chapter 3, Section 3.3.3.

Although extensive studies have been conducted over the years on the crystallization process of polymers, and of PE in particular, and the complex structures that are formed by crystallization, these subjects are still far from being completely understood. Gaining new insights into crystallization is therefore essential to understand the mechanisms that determine crystallization fully. A better understanding of these processes is important to enable existing materials to be improved, and for the fabrication of novel materials with known properties.

This study differs from most previous studies on flow induced crystallization [172–175] in the sense that only small scale flow was induced locally by the AFM tip. Also, no external forces were needed here. The AFM tip deformed the molten surface only by scanning over the surface with a small amplitude setpoint (high tapping force). Then, the subsequent crystallization was followed *in situ*, in real time, using the same AFM tip. In other words, the AFM tip here was used as a tool to site-specifically initiate crystal nucleation and then to examine the subsequent crystal growth isothermally at different temperatures.

The initial aim of this chapter was to induce and control the nucleation of oriented PE crystals and the ultimate goal was to investigate the growth behaviour of these induced crystals with direct observation by AFM.

This chapter first presents the experimental method that was used, including sample preparation, the protocol used and the detailed conditions for inducing PE nucleation, such as temperature and the mechanical work of the cantilever. It presents the

investigation into the conditions and temperatures under which the nucleation can be induced locally through the action of the AFM probe. The estimated mechanical work of the cantilever on the sample was calculated. The chapter also recounts the initial problems faced when attempting to induce nucleation using the AFM tip, when using a cold tip and contact mode, and how these were later overcome. It next presents and discusses the effect of scan direction and scan rate on the induced crystals. The investigation of the subsequent crystallization behaviour at different temperatures is then presented and discussed. In addition, the height, and the rate of change in the height, of crystals were calculated in order to study the relationship between the height and the transition from edge-on to flat-on oriented crystals. Moreover, the effect of nucleation density on the behaviour of crystals was also presented. Finally, the chapter presents the induction process of a single crystal and its subsequent growth behaviour *in situ*, in real time, as a function of temperature and how this differs from that for multiple crystals.

6.2. Method

The standard PE ((Mw = 84 500 Da, M_w/M_n = 1.28) and Mw = 77 000 Da, Mw/Mn = 1.28,)) used in the present study was purchased from PSS. Samples were prepared by dissolving PE in p-xylen (puriss. p.a. ≥99.0%, purchased from Sigma-Aldrich) at 135 °C for ~30 minutes, resulting in a suspension with a concentration of 1% wt (Figure **6.1**). This suspension was then drop-cast onto a glass cover slip (see Chapter 3, Section 3.2.3) on a heating stage held at 160 °C for ~20 minutes so as to ensure that all the crystals were melted and to remove any thermal history. Then, the films were quenched to room temperature and the glass cover slip was stuck onto a magnetic disc using UV glue to reduce the amount of drift when under the AFM. The thermal protocol used in this work is presented below.

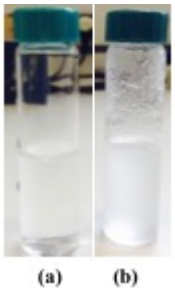

Figure 6.1: A photo of PE (a) hot solution immediately after removing it from the oil bath after dissolving the PE into the solvent at 135 ºC and (b) suspension a few minutes after removing the solution from the hot bath.

AFM was performed in tapping mode, using a Multimode 8 AFM with a high temperature heating system, which was used to control the tip and sample temperatures, as mentioned in Chapter 3, Section 3.3.3.3.3. The experimental setup is shown in Figure **6.2** (a) and the crystals that were formed are shown in Figure **6.2** (b). Once the films had been prepared on the substrate, they were placed on a hot AFM stage with heated tips, since using unheated tips caused the area near the tip to crystallize, as will be shown in more detail below. The AFM tip was used as a flow tool to orient the melt surface of the PE in order to induce oriented crystals. This was done by scanning over the surface of the molten PE with a low amplitude setpoint of the AFM tip (high tapping force) (a similar strategy to that in Chapter 4, section 4.2) with nucleation being observed when the temperature was within the range from 136 ºC to 129 ºC.

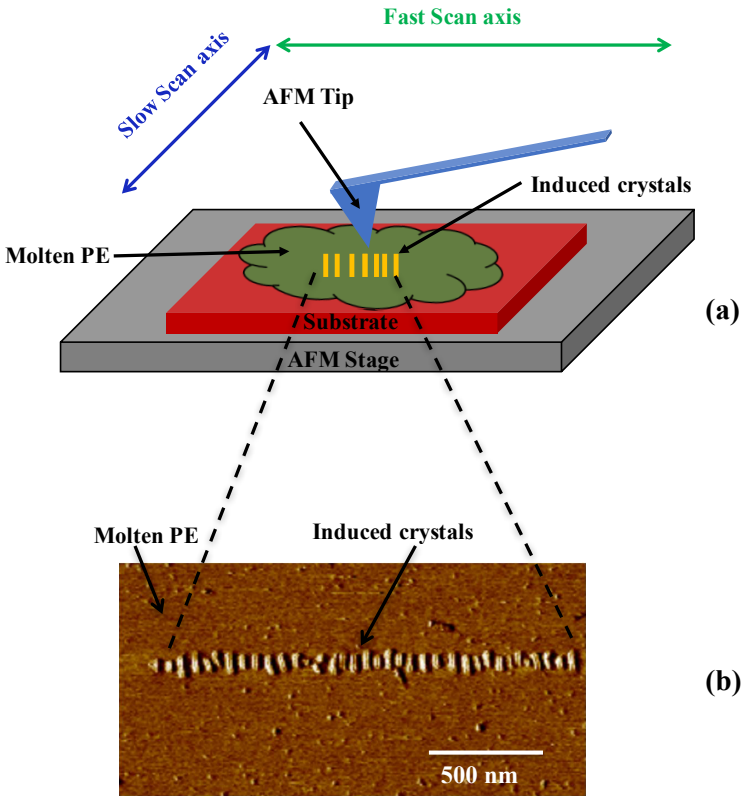

Figure 6.2: (a) Schematic diagram showing the experimental setup of the shear induced crystallization by AFM tip in this study and (b) AFM phase image of the induced crystals.

The thermal protocol used in this work in order to shear or nucleate the melt surface of PE by AFM tip is listed below (see also Figure **6.3**):

1) Heat the film from room temperature to 145 ºC (above melting temperature).
2) Maintain temperature at 145 °C for 5 min to erase any thermal history.
3) Lower temperature to the nucleation temperature (T_n).
4) Maintain temperature at T_n for ~5 min to stabilize the tip with the new temperature.
5) Use the AFM tip to induce nucleation by tapping hard on the surface with the AFM tip at T_n.
6) Lower temperature to the crystallization temperature (T_c).

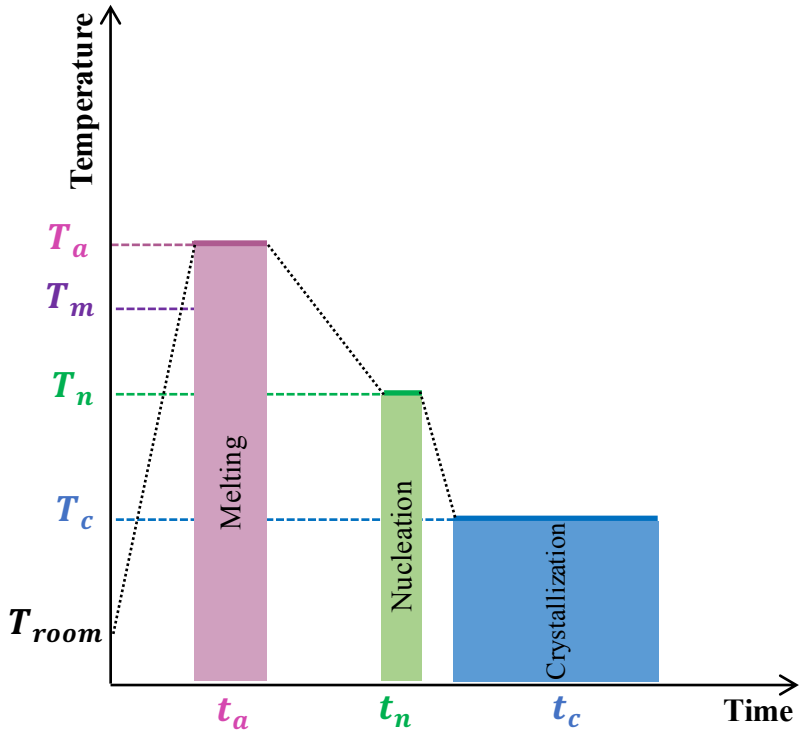

Figure 6.3: Schematic diagram showing the thermal protocol used in the experiments where T_{room}, T_c, T_n, Tm and T_a are room, crystallization, nucleation, melting and annealing temperatures, and t_a, t_n, and t_c are annealing, nucleation and crystallization time, respectively.

Following this induction procedure, the sample was cooled to the desired crystallization temperature and then the subsequent growth was followed isothermally *in situ* at a range of temperatures. This is shown later in this chapter.

6.3. Problematic Outcomes

6.3.1. Unheated AFM Tip

This section surveys the problems that arose during the initial experiments to induce crystallization in PE in order to understand their causes and to explain how they were overcome. Specifically, in the first attempts to induce crystals within the target area using the AFM tip, the AFM cantilever crystallized its surrounding area even before engaging (see Figure **6.4**). This was due to the large difference in temperature between the hot sample and the cold cantilever, which caused a reduction in the actual temperature of the sample. In order to overcome this problem it was decided to heat the cantilever. This was done by applying voltages to it using the same heating controller as

used in Chapter 3, Section 3.3.3.3.3. Guided by [177], a specific voltage was applied depending on the experiment temperature. For example, if the desired crystallization temperature was 125 °C, 10.8 V was applied to the tip, heating it to about 125 °C (according to [177]).

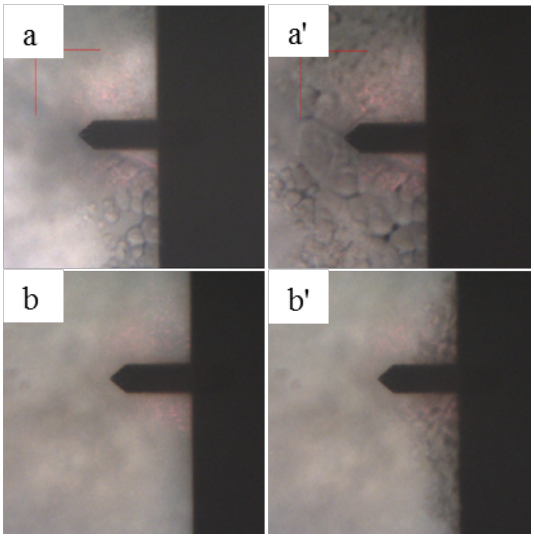

Figure 6.4: Optical micrographs showing the effect of variations in temperatures between the AFM cantilever and the sample. (a- a′) at 135 °C and (b-b′) at 139 °C. (a-b) The point at which the cantilever was brought above the sample (close to, but not in contact with the molten PE); and (a′-b′) after a few seconds.

6.3.2. Using Contact Mode AFM

When contact mode AFM was used to induce crystallization, the surface of the sample was damaged, even at the lowest possible forces (see Figure **6.5**). This result confirmed that the most appropriate mode for use in this kind of study is the tapping mode, as discussed in detail in Chapter 3.

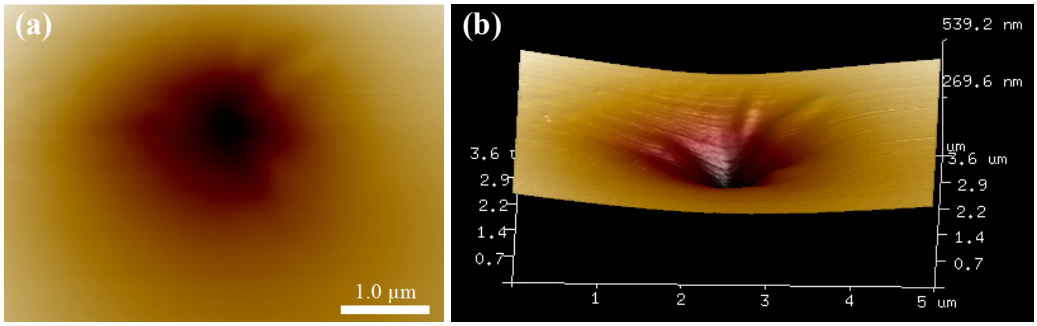

Figure 6.5: (a) AFM height image and (b) its corresponding 3D image that resulted from scanning over the PE melt surface with the AFM in contact mode.

6.4. Results and Discussion

6.4.1. Sample Characterization

DSC measurements were carried out using a PerkinElmer Pyris 1 DSC system, with a scan cycle over a temperature range of 25 °C to 200 °C, at a heating/cooling rate of 10 °C/minute under a Nitrogen atmosphere. The samples were first heated from 25 °C to 200 °C at a rate of 10 °C/min, then cooled at the same rate down to room temperature (Figure **6.6**). Both PE 77k and PE 85k showed similar results.

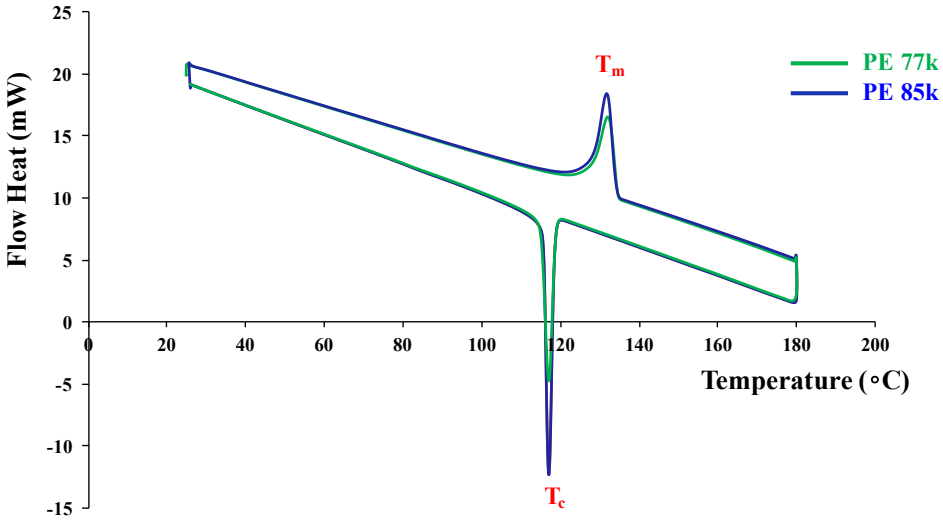

Figure 6.6: DSC curves taken in the range of room temperature to T_m of PE with Mw (a) 77k and (b) 85k, with a heating/cooling rate of 10 °C/min.

6.4.2. AFM Tip-Induced Nucleation of PE

To induce nucleation using the AFM tip the significant conditions that need to be considered include: the tapping force, the ideal (range of) temperature for inducing nucleation, and the mechanical work required of the tip to induce nucleation, as will be shown below.

a) Estimated force for inducing nucleation

The applied tapping force on the surface of the melt polymer plays an essential role in inducing nucleation. This is because, in order to induce PE nucleation, the PE molecular chains need to be aligned. In this study, this alignment was achieved by scanning with sufficient force over the desired position of the PE melt surface. This was done by scanning over the PE melt surface with a low amplitude setpoint of the AFM tip (a similar strategy to that used for orienting the block copolymer domains in Chapter 4, Section 4.2). Moving the AFM tip over the melt surface with such a high force caused the PE chains to align parallel to the moving (scanning) direction of the tip. When the AFM is operated in tapping mode, the PE chains may be aligned only in those areas which the tip touches (see Chapter 3, Section 3.3.3.2.2). On each occasion when the tip touches the melt surface it shears it, causing the chains to align at that position in its scanning direction. Then, these aligned chains could aggregate, resulting in the generation of nuclei which then develop into crystals that grow perpendicularly to the scanning direction (because the chains are aligned parallel to the scan direction). These stages of tip-induced nucleation and subsequent growth are shown in Figure **6.7**, while Figure **6.8** shows a real example resulting from this process.

This result implies that the energy barrier required to form nuclei is reduced when the polymer melt chains are oriented by shearing or flow.

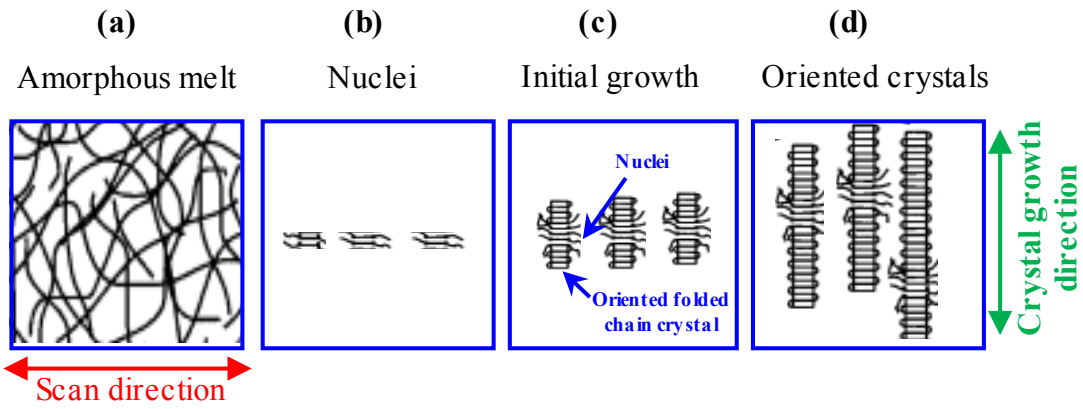

Figure 6.7: Schematic illustration showing the stages of tip-induced primary nuclei and the subsequent growth of oriented PE crystals: (a) before shear (amorphous melt), (b) a short time after shear (nuclei), (c) after nuclei growth (oriented crystals), and (d) the final growth of the oriented crystal.

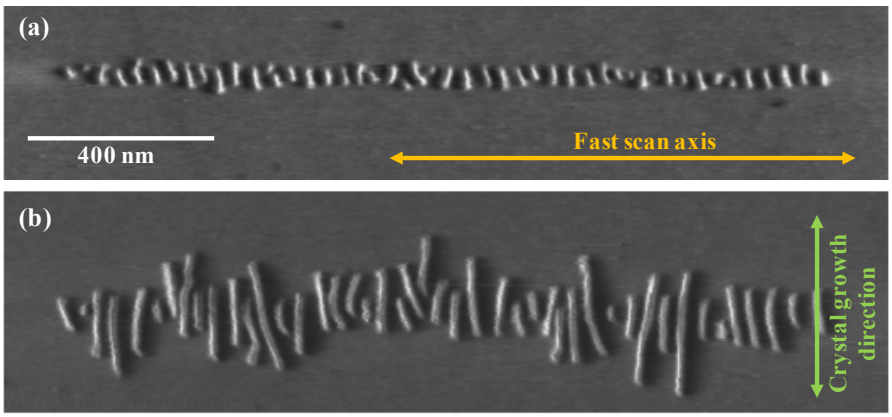

Figure 6.8: AFM phase images showing the tip-induced PE crystals (a) the initial growth stage and (b) after they had grown to some extent. It shows the growth direction of the induced crystals relative to the AFM tip scan direction.

Figure **6.9** shows how the direction of the formed crystals is dependent on the scanning direction of the AFM tip. The AFM tip aligns the PE chains at the surface of the melt in its scanning direction. Hence, the formed crystal will grow perpendicularly to the scanning direction.

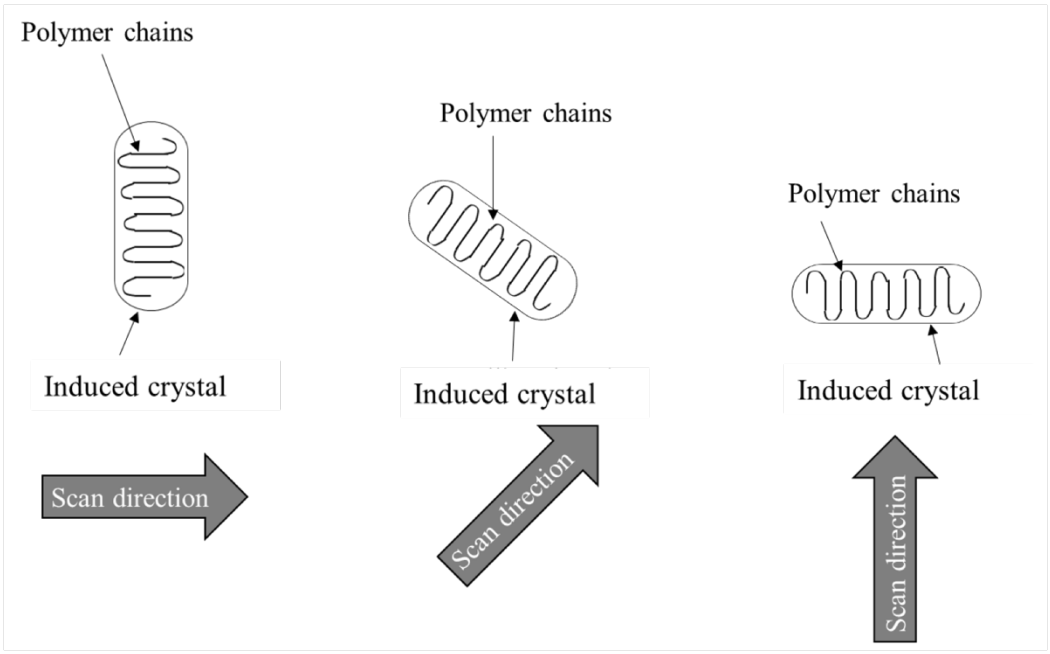

Figure 6.9: Schematic diagram showing the relationship between the AFM scanning direction and the orientation of the induced crystals. The AFM tip orients polymer chains parallel to its scanning direction resulting in crystals formed perpendicularly to the scanning direction.

b) Temperature range for inducing nucleation

The nucleation was induced between 129 °C and 136 °C. Above 136 °C, no nucleation was observed, or even if nuclei were induced at this high temperature, they melted immediately. Below 129 °C, nucleation was easily induced but the growth rate was very fast, making it hard to image the crystal growth with the AFM.

c) Estimated specific work (w) required to induce nucleation by the AFM tip

Previous studies have shown that there is a critical value for the amount of specific work (i.e. energy density or the work applied to the unit volume of the sample in Pa= J/m^3) that needs to be applied to a polymer melt in order to induce crystallization, with no nucleation being observed below this value [174, 175, 177]. The work was estimated using equation (6.1):

$$w = \int_0^{t_s} \eta\left(\frac{d\gamma}{dt}(t)\right)\left[\frac{d\gamma}{dt}(t)\right]^2 dt \tag{6.1}$$

$$w = \int_0^{t_s} \eta\left(\dot{\gamma}(t)\right)\dot{\gamma}^2(t)\, dt \tag{6.2}$$

where w is the specific work, η is the viscosity, $\frac{d\gamma}{dt}$ is the shear rate, t is the time and t_s is the entire time of shearing.

The shear rate in the case presented in this study could be calculated as follows:

$$\text{The shear rate } (\frac{\mathrm{d}\gamma}{\mathrm{dt}}) = \frac{\text{Tip velocity } (\mu\mathrm{m/s})}{\text{Penetration depth } (\mu\mathrm{m})} \tag{6.3}$$

While the tip velocity value was taken directly from the AFM software during scanning, and was around 10 µm/s, the penetration of the tip into PE melt needed to be measured. To calculate how far the tip penetrated into the melt, the amplitude needed to

be calibrated by taking an approach curve while in tapping mode onto a hard surface (e.g. mica or glass) and fitting the slope of the amplitude. This gave an amplitude sensitivity in nm/V. In order to calculate the amplitude sensitivity and calibrate it into nm instead of V or mV, a force curve was taken while in tapping mode, which produced an amplitude vs z curve. This showed a change from a constant amplitude to a relatively linear decrease once the probe started tapping on the sample. The amplitude sensitivity (nm/V) was also determined, which calibrates the voltage signal on the PSD into nm. Then, the amplitude in volts was multiplied by the slope of the amplitude approach curve to express the amplitude in nm (see equation (6.4) [179].

$$A_{sp}\,(in\ V) \times \text{Amplitude sensitivity}\,(in\ nmV^{-1}) = A_{sp}\,(in\ nm) \qquad (6.4)$$

To calculate the penetration depth, an image of the height where the nucleation was induced was first taken. Then, a section profile was taken in the vertical direction of the scan line, where the setpoint was lowered to orient the melt, as shown in Figure **6.10**. The flat regions indicate normal scanning while the dip illustrates where the setpoint has been reduced. From the section profile, it was possible to measure the depth of the dip. Then by subtracting (scanning setpoint - shearing setpoint) in nm from the measured depth (see equation 6.5), it was possible to calculate the depth of penetration into the melt when nucleation was being induced, relative to the tip position when scanning normally.

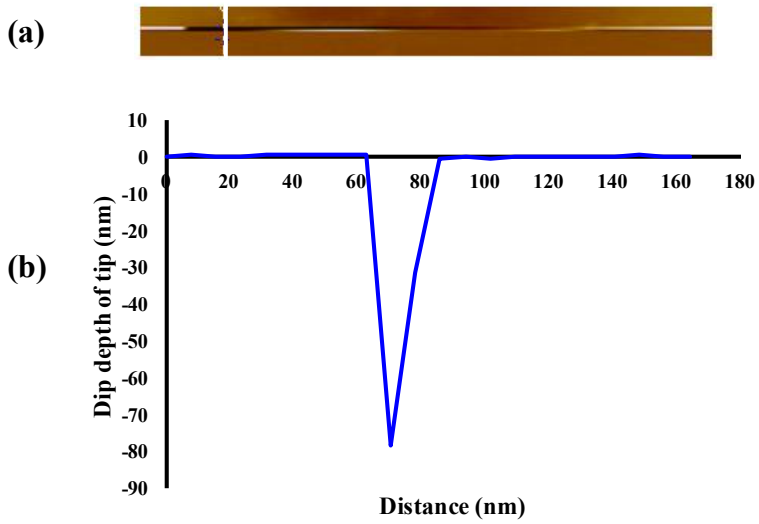

Figure 6.10: (a) AFM height image of the PE surface taken during hard tapping and (b) a representative cross-sectional image (height profile) of the PE melt surface during the hard tapping of the AFM tip, which was taken from the vertical white line in image (a).

$$Depth\ penetration = \left(Measured\ depth - \left(A_{sp} - A_n\right)\right) \times Amplitude\ sensitivity \quad (6.5)$$

$$Depth\ penetration = Measured\ depth - \left(A_{sp} - A_n\right) \quad (6.6)$$

where the measured depth is the depth of the dip of the tip that has occurred during scanning with a reduced setpoint amplitude, A_{sp} is the scanning setpoint amplitude, and A_n is the shearing setpoint amplitude at which the nucleation was induced.

Since the tip velocity, as indicated in the AFM software during scanning, was around 10 μm/s, and the penetration of the tip into the melt was in the order of 20-80 nm (as shown in Figure 6.10), then the shear rate applied by the tip on the sample could be calculated as follows:

$$\text{Shear rate } \left(\frac{d\gamma}{dt}\right) = \frac{10\ (\mu m/s)}{(20-80)\times 10^{-3}\ (\mu m)}$$

$$\text{Shear rate } (\frac{d\gamma}{dt}) = \ 500 - 125\ s^{-1}$$

The viscosity of the polymer melt was found in the literature to be in the order of 10^5 Pa.s [180]. Thus, the mechanical work done on the PE melt in this study was:

$$w = \int_0^{3\times10^{-3}\ s} 10^5\ Pa.s\ [10^2\ s^{-1}]^2\ dt \tag{6.7}$$

$$w = \int_0^{3\times10^{-3}s} (10^9\ Pa.s)\ \ dt \tag{6.8}$$

$$w = [10^9\ Pa.s]_0^{3\times10^{-3}} \tag{6.9}$$

$$w = \ 3\times10^6\ Pa \tag{6.10}$$

This value of w is similar to that observed macroscopically in [175].

Moreover, the scan rate (or tip velocity) plays an important role in the induction of nucleation. As the scan rate was increased (from 0.5 Hz to 6 Hz) while maintaining constant experimental conditions and parameters, such as the scan size, amplitude setpoint and temperature, the nucleation density also increased, as shown in Figure **6.11**.

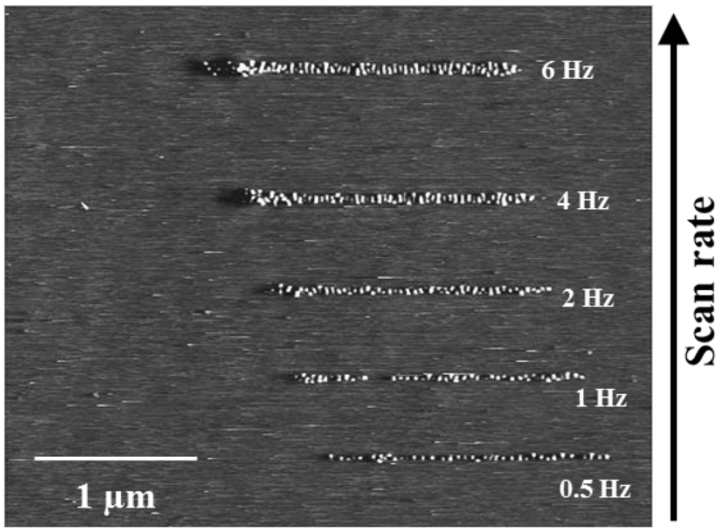

Figure 6.11: AFM phase image showing the effect of increasing the scan rate on the induced nucleation density at 131 °C.

Moreover, it was possible to control the separation distance, length, number, density, and direction of the crystals induced by the AFM tip, as shown in Figure **6.12**.

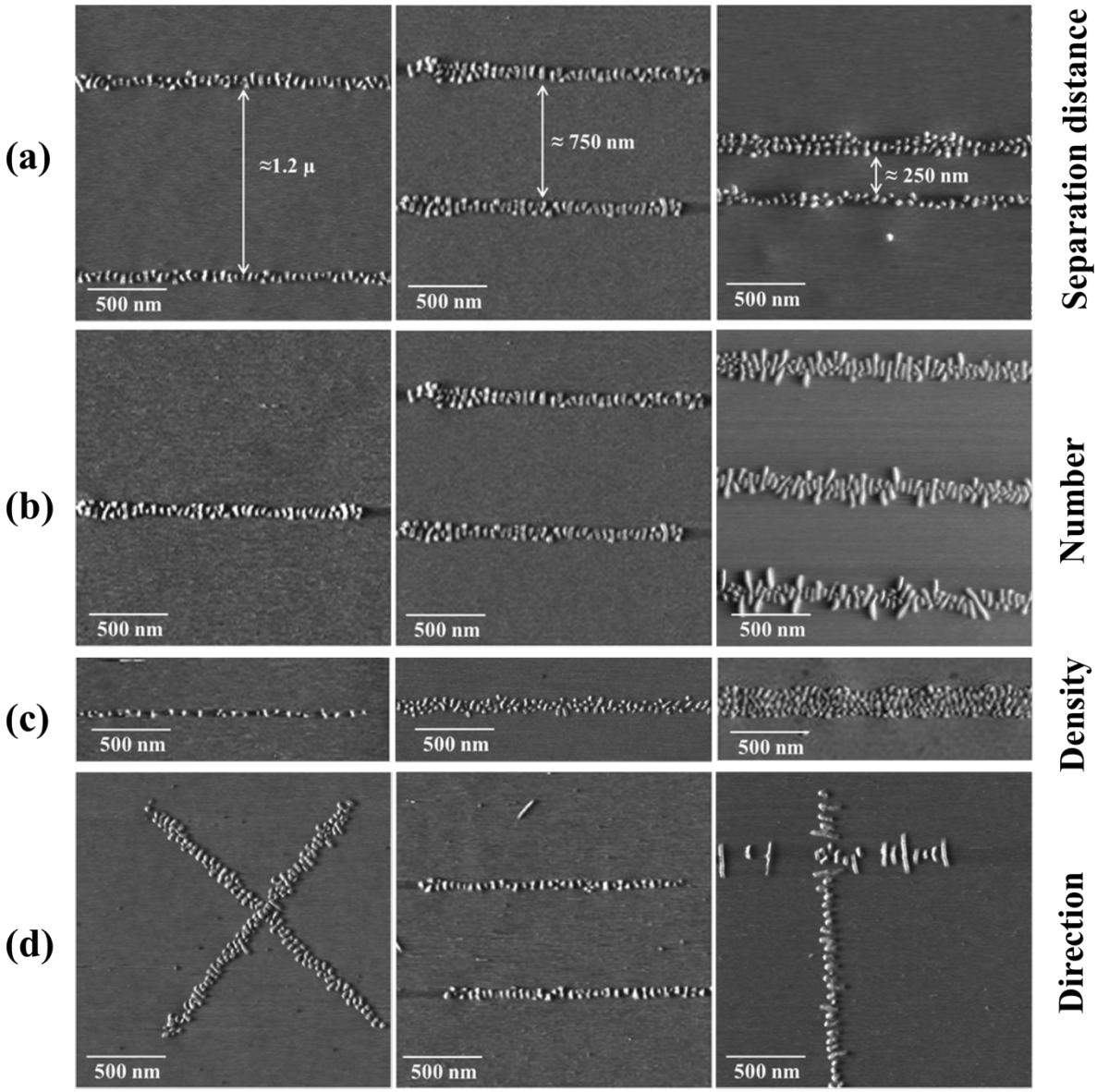

Figure 6.12: AFM phase images showing the ability of the AFM tip to control: (a) the separation distance between the induced nuclei rows, (b) their number, (c) density, and (d) the direction of orientation.

Having developed a new approach to control the nucleation of oriented crystals, the subsequent isothermal crystallization behaviour was then followed *in situ*, in real time, using AFM at a temperature range from 136 °C to 129 °C.

6.4.3. Behaviour of the Induced Crystals

After inducing the nuclei using the AFM tip, isothermal crystallization was performed in order to investigate the behaviour of the subsequent growth of the induced crystals *in situ*. The growth was followed in the temperature range of 136 °C to 129 °C, where the AFM was able to image the crystallization process, as discussed in 6.4.2 above.

In order to examine the growth over the course of the experiment, individual crystals were identified in sequences of AFM images. Crystals that could be clearly resolved in the first image were labelled, as in Figure 6.13 below. In each of the subsequent images, where these labelled crystals were present, the growth that had occurred during image acquisition could be monitored, allowing the behaviour of these individual crystals to be investigated as they grew.

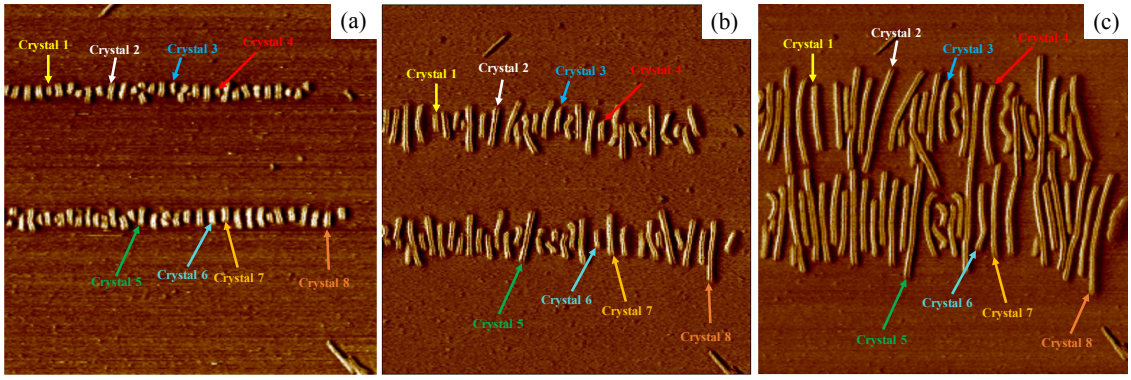

Figure 6.13: Diagram demonstrating the labelling scheme that was used to follow the growth of individual crystals. (a-c) are the 1st, 15th and 25th images captured for PE crystallization at 133 °C.

During the isothermal crystallization, interesting behaviours were observed, including pushing apart of neighbouring crystals, deformation, changes in the direction of growth, melting and aggregation into groups. These phenomena are presented and discussed below.

6.4.3.1. Interaction between Neighbouring Crystals

Figure **6.14** shows three independent examples (a-c) following crystallization at 130 °C, 131 °C and 133 °C, respectively. These three series of AFM images were taken from three independent experiments. Some interesting behaviour can be observed with the

PE crystals; some of them seem to force their neighbouring crystals apart when they are stuck between them, in order to grow between them, as shown in Figure **6.14** (a-c). The highlighted crystals represent both the crystals that crystallized initially under this constraint and the neighbouring crystals that were affected. For example, the two orange crystals in the series (a-a‴) that crystallized under the constraint of neighbouring crystals (yellow and pink crystals), can be seen to force those neighbouring crystals apart in order to provide more room to grow between them. The distance separation (red lines) between the two yellow crystals, and between the two pink crystals, becomes larger, as the middle (stuck) crystals continue to grow. Similarly, the orange crystals in the images series (b-b‴) and (c-c‴) continue growing between their two neighbouring crystals (yellow crystals in (b-b‴) and blue and green in (c-c‴)), increasing the separation with their neighbours. This behaviour was found relatively frequently.

Another interesting phenomenon observed here is that crystals can deform or reorganize themselves during the isothermal crystallization in order to be in a more stable state, as shown in Figure **6.14** (c-c‴) (pink crystal). Bent lamellae have previously reported during the growth of lamellae [69], but no explanation has yet been offered for this observation.

Furthermore, at later stages (e.g. Figure **6.14** (a‴-c‴)), crystals tend to become closer to each other (clumping into groups), as will be shown in more detail below.

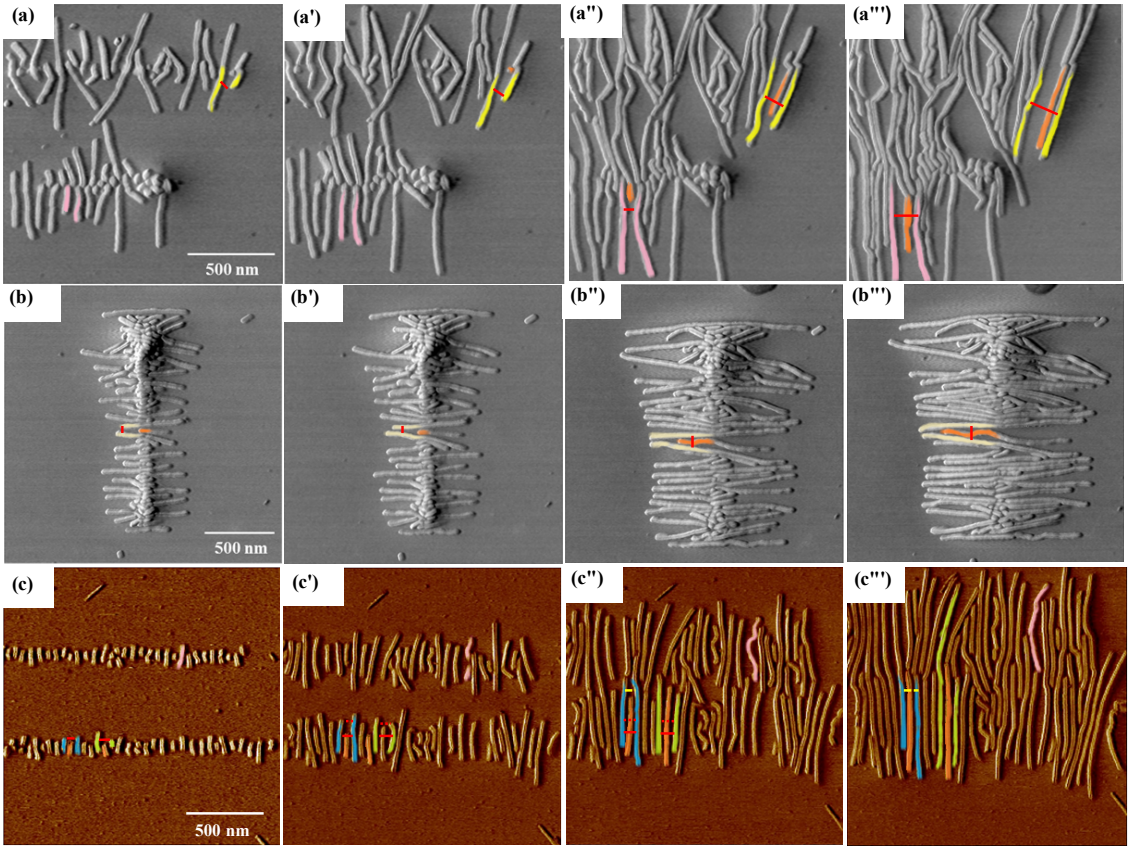

Figure 6.14: (a-c) Three independent series of AFM phase images showing the subsequent crystallization of PE at (a) 130 °C, (b) 131 °C, and (c) 133 °C. The orange highlighted crystals indicate crystals that are forcing apart their neighbouring crystals (coloured pink, yellow, blue, and green). The small red and yellow lines were added to aid the reader to see the increase in the separation distance between crystals as the middle crystal grows between them.

6.4.3.2. Aggregation of Crystals into Groups

In addition to the abovementioned behaviour of crystals pushing their neighbours apart to grow between them, another interesting phenomenon observed here was that as crystals grow, the gap between them may reduce and even disappear; in other words crystals appear to clump together (see Figure **6.15**). Although this behaviour can be determined qualitatively, quantitative measurements were also conducted in order to confirm these observations (see Figure **6.16**). This was done by measuring the spaces between crystals as a function of time. Although it was difficult to determine the absolute value of the space between crystals, as it was very small, the measurements give an idea of the changes in these spaces between crystals with time.

Interestingly, the orientation of the crystals labelled "A" was switchable between edge-on and flat-on with time, as can be seen from Figure **6.15** (g-p). The transition from

edge-on to flat-on started in image (h) and progressed until image (k). Then, it re-oriented gradually to be edge-on, as can be seen in images (i-m). Again, the transition occurred, and the crystal become flat-on in image (n). Finally, the crystal changed its orientation to be edge-on again between images (o) and (p). The reason for this behaviour is not clearly understood.

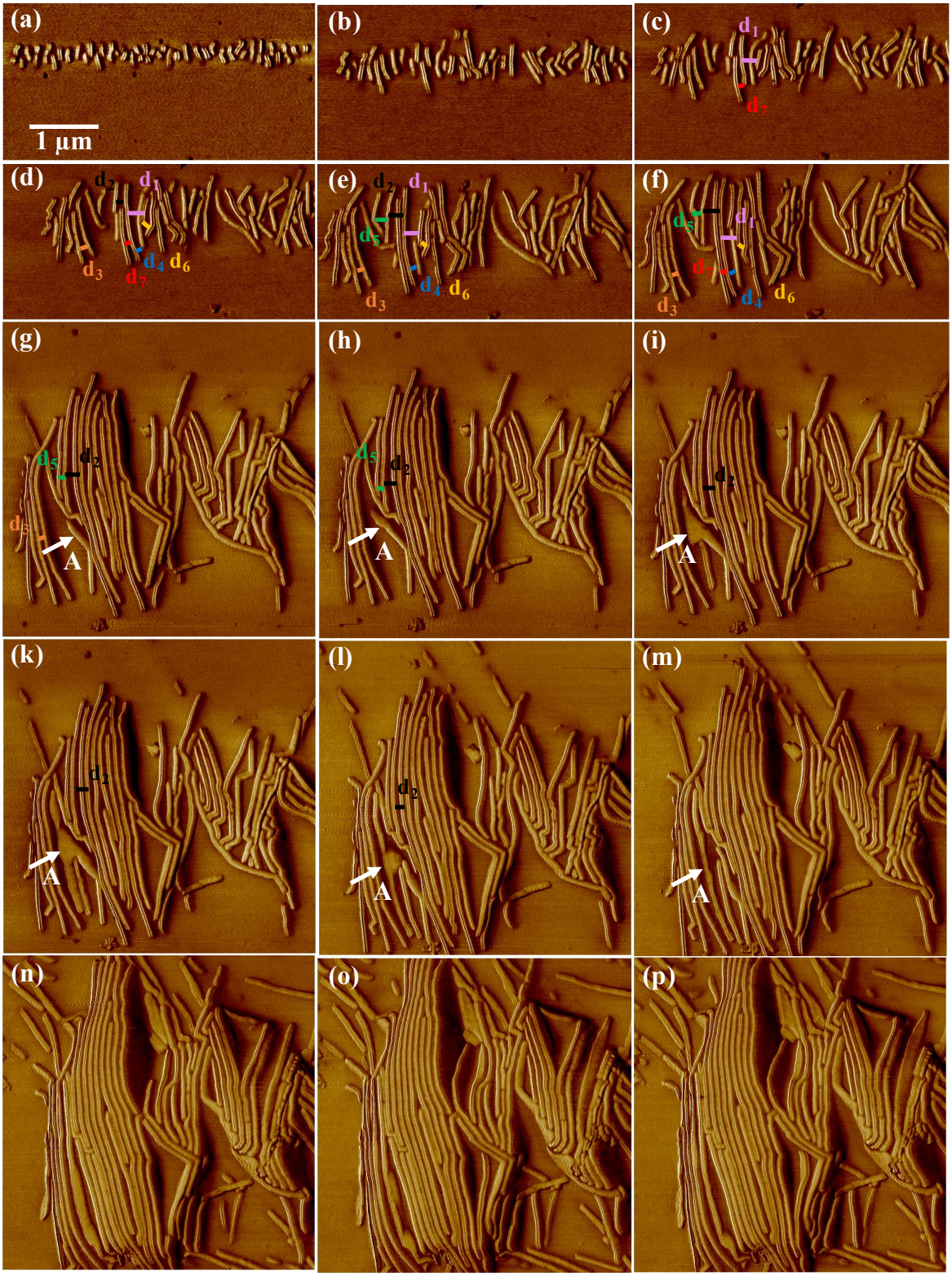

Figure 6.15: *In situ* AFM phase images showing the subsequent growth of PE induced crystals by the AFM tip at 129 °C.

Figure **6.16** shows the change in the separation distance between crystals as a function of time, using the data represented in Figure **6.15**. It is clear that the separation distances decrease with time in general, but there are two cases where the separation increased for a short time first before decreasing: see d_1 and d_2 in Figure **6.15**, the black and pink curves in Figure **6.16** , respectively. This initial increase in separation was due to the previously mentioned phenomenon of crystals forcing their neighbours apart in order to grow between them.

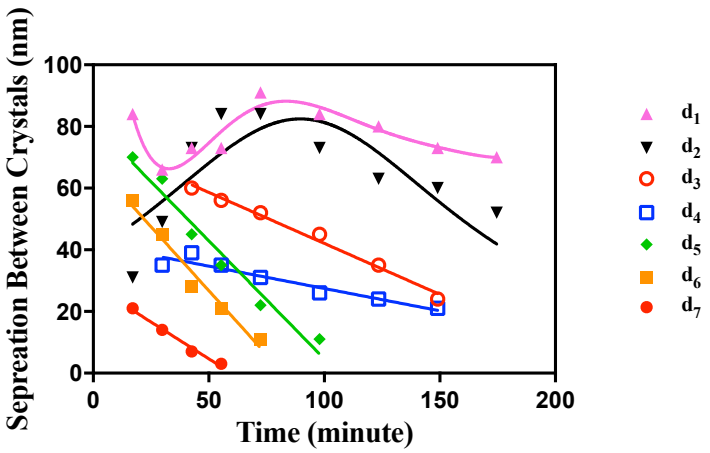

Figure 6.16: A plot showing seven separation distances between the crystals shown in Figure **6.15** as a function of time. ▲, ▼, ○, □, ◆, ■, ● are the separation distances labelled d_1, d_2, d_3, d_4, d_5, d_6, d_7, respectively, in Figure 6.15. The separation distances were measured at different times, and tracked for clarity.

This phenomenon raises important questions: are the crystals really clumping into a group? Or, do they only change their orientation from being edge-on to flat? If the latter is the case, is there any relationship between the increase in height and transition of the crystals' orientation that causes them to appear as if they are clumping into groups? Or, are the crystals changing their orientation as they reach a certain height?

The hypothesis is that as the height of the edge-on crystals increases, which means they grow away from the surface, they become unbalanced and, therefore, tend to change their orientation to be flatter on the surface. In order to test this, the height of individual crystals was first measured as a function of time, before determining the height at which they started clumping together or changing their orientation.

The height of the PE crystals was measured and was found to increase both with time and with supercooling, in that as the crystallization temperature decreased (increased supercooling) the height of the crystals increased sharply, as shown in Figure **6.17** (a). The height of the crystals also showed a nonlinear relation with time. This result is in a good agreement with that in [181]. The rate of change in height was not constant, however, but rather varied in time, as can be seen in Figure **6.17** (b).

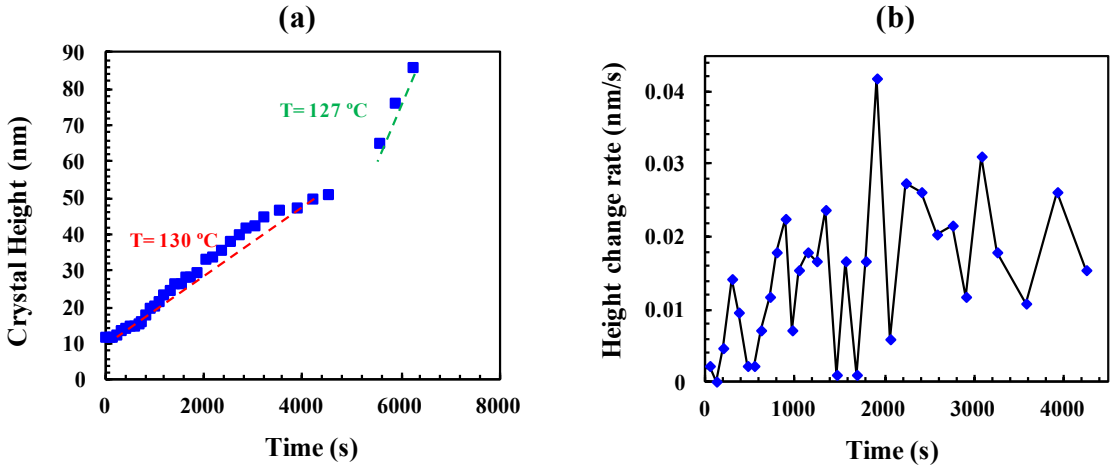

Figure 6.17: Plots showing (a) the height of the PE crystals shown in Figure **6.15** as a function of time at 130 ºC (red dashed line) and at 127 ºC (green dashed line) and (b) the rate of change in the height of those crystals at 130 ºC.

Another example of this behaviour, where the crystals appear to aggregate, is presented in Figure **6.18**. Here, four main observations are noteworthy. First, some crystals melted during the isothermal crystallization. An example of such a situation is indicated by the green arrow in Figure **6.18** (d-j). Second, a zigzag structure was observed, as indicated by the yellow arrow. Third, the transition from an initial edge-on orientation to a flat one was observed. Crystal "A" in Figure **6.18** (i) is an example of such a situation; the orientation of this crystal changed completely, in contrast to the other crystals which appear as if they had only partially changed their orientation. This could be due to the fact that crystal "A" had enough space around it, allowing sufficient room for growth in the direction of orientation, which was to the right side of the crystal. Finally, the crystals appeared to clump into groups as they grew. The initial spaces between the induced crystals were roughly equal, but as the crystals grew the spaces reduced,

meaning that the crystals become closer to each other. Here, the crystals have aggregated into three groups, indicated by the blue, red and green ovals in Figure **6.18** (h). The number of groups that crystals could aggregate into was not predictable, but usually they were three, two or even only one group, (see Figure **6.19** (a-b) which presents examples of crystals clumped into one and two groups, respectively). The width of the three groups shown in Figure 6.18 (h) was measured as a function of time, as will be shown below.

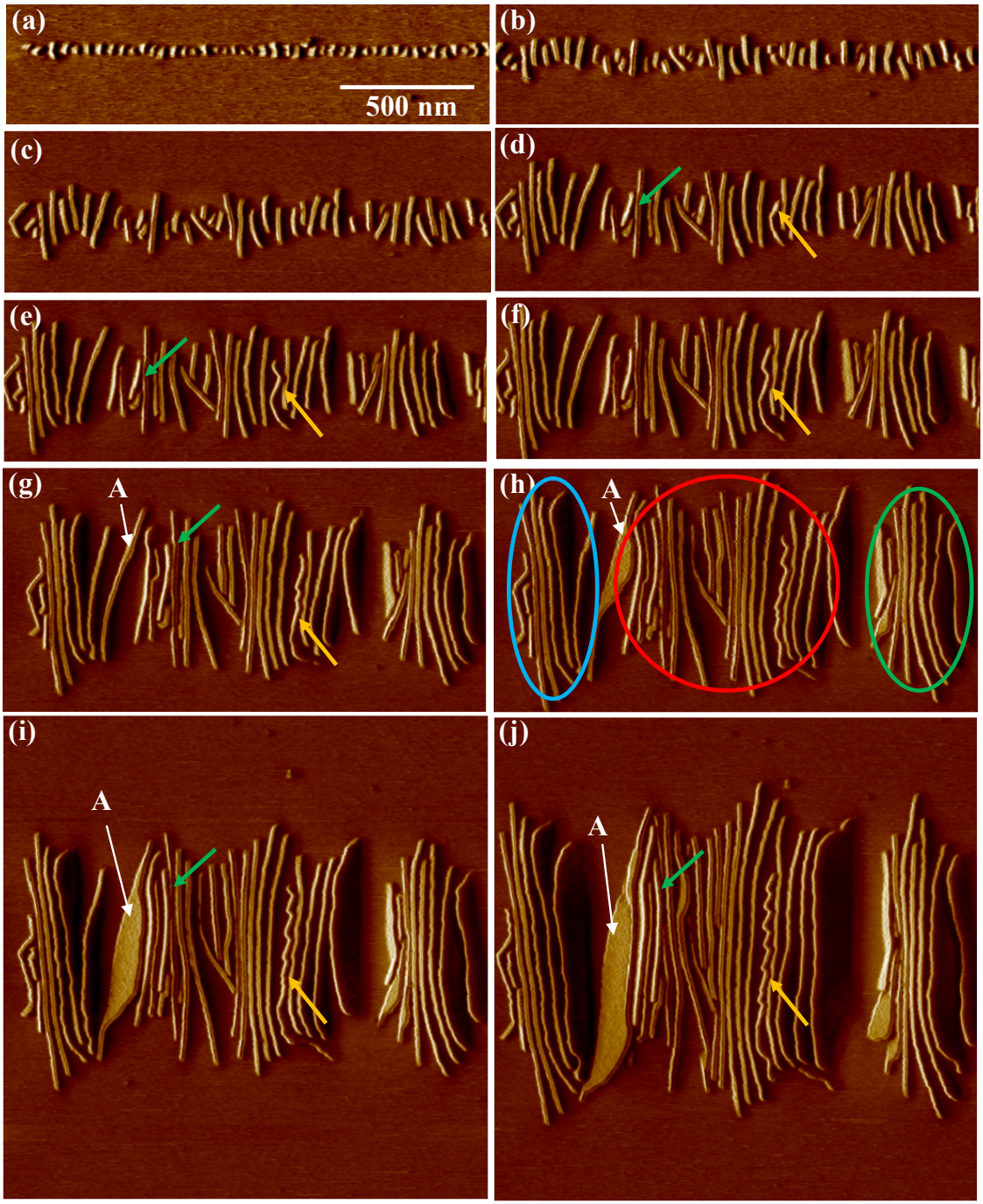

Figure 6.18: A sequence of AFM phase images showing the subsequent crystallization of the PE at 129 °C. The green arrow points to a crystal that was melting and the yellow arrow points to a crystal that was becoming zigzagged with time.

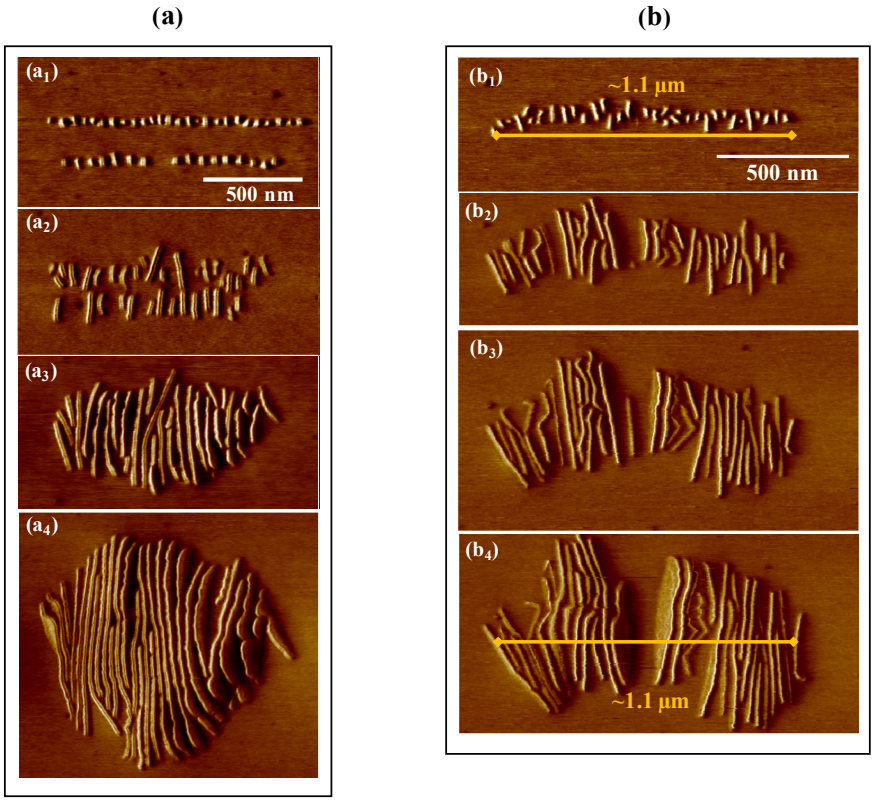

Figure 6.19: AFM phase images showing the aggregation of PE crystals into (a) one and (b) two groups as they grew.

The width of the three groups shown in Figure 6.18 (h) was measured as a function of time (see Figure **6.20**), and was found to decrease with time until the crystals become so close to each other that there was no more space between them.

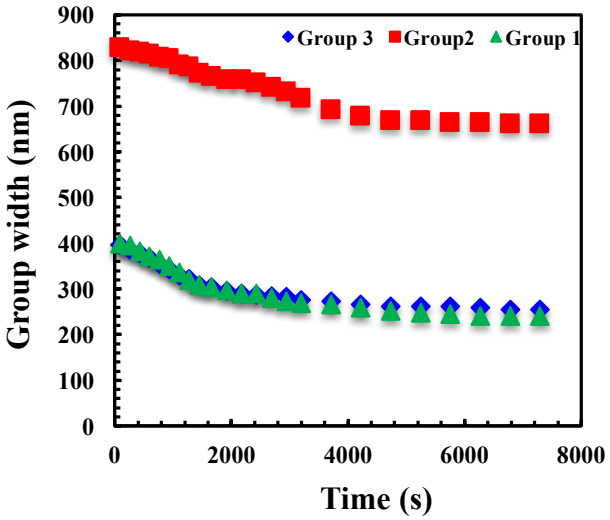

Figure 6.20: A plot showing the width of the three crystal groups indicated by the ovals in Figure **6.18** (h) as a function of time.

Figure **6.21** (a-b) are height images corresponding to the phase images shown in Figure **6.18**, and (a'-b') are the corresponding section profiles that were taken from the white lines in images (a) and (b), respectively. Three differences were found between the very early stages of the crystallization (a) and the later stage of crystallization (b): the space between individual crystals; the height of the crystals; and, the depth of the gap between groups of crystals.

First, the space between crystals reduced until it disappeared, as can be seen by comparing the section profiles (a') and (b') in Figure **6.21**. It is clear that there are many peaks in (a') but only three main peaks in (b'), indicating that the crystals have aggregated into groups with gaps existing just between these groups.

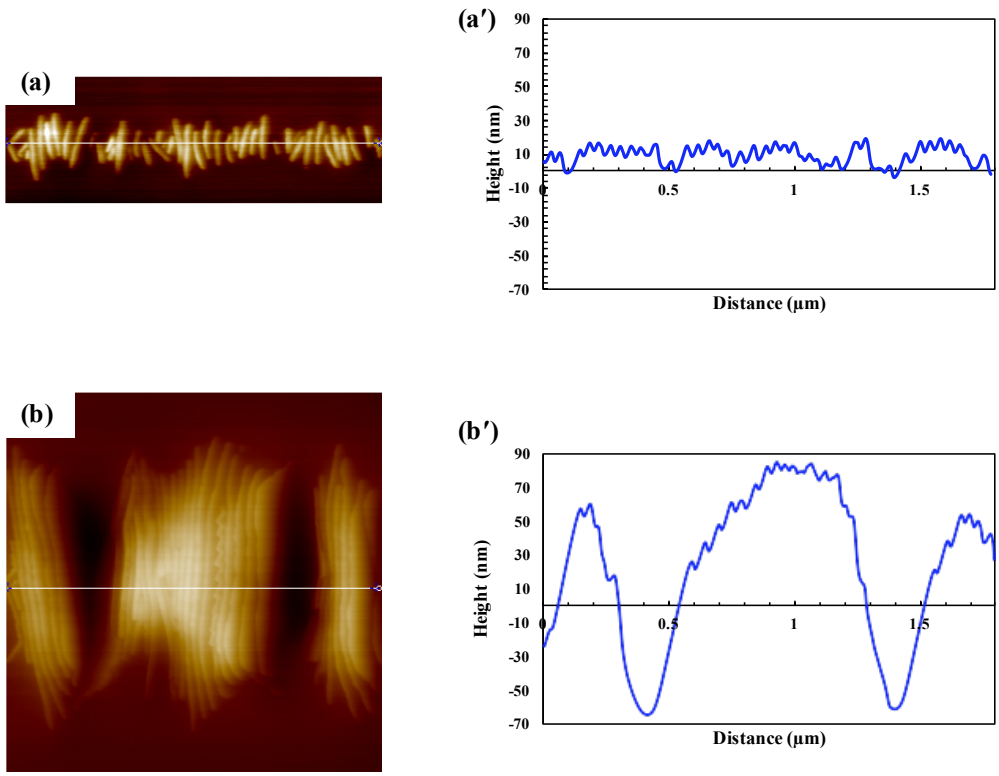

Figure 6.21: (a-b) AFM height images of PE crystallization at the initial and final stage, respectively, corresponding to the phase images in Figure **6.18** and (a' –b ') their cross-section profiles.

Second, Figure **6.22** (a) shows a series of 3D AFM height images taken from Figure **6.18**. It can clearly be seen that the height of the crystals increases with time. Quantitative measurement was done by plotting the height of the crystals against time,

and this was found to increase with time. Additionally, as the crystallization temperature decreased (increased supercooling), the height of the crystals increased sharply, as shown in Figure **6.22** (b), although the rate of change in the height was not constant, as can be seen in Figure **6.22** (c).

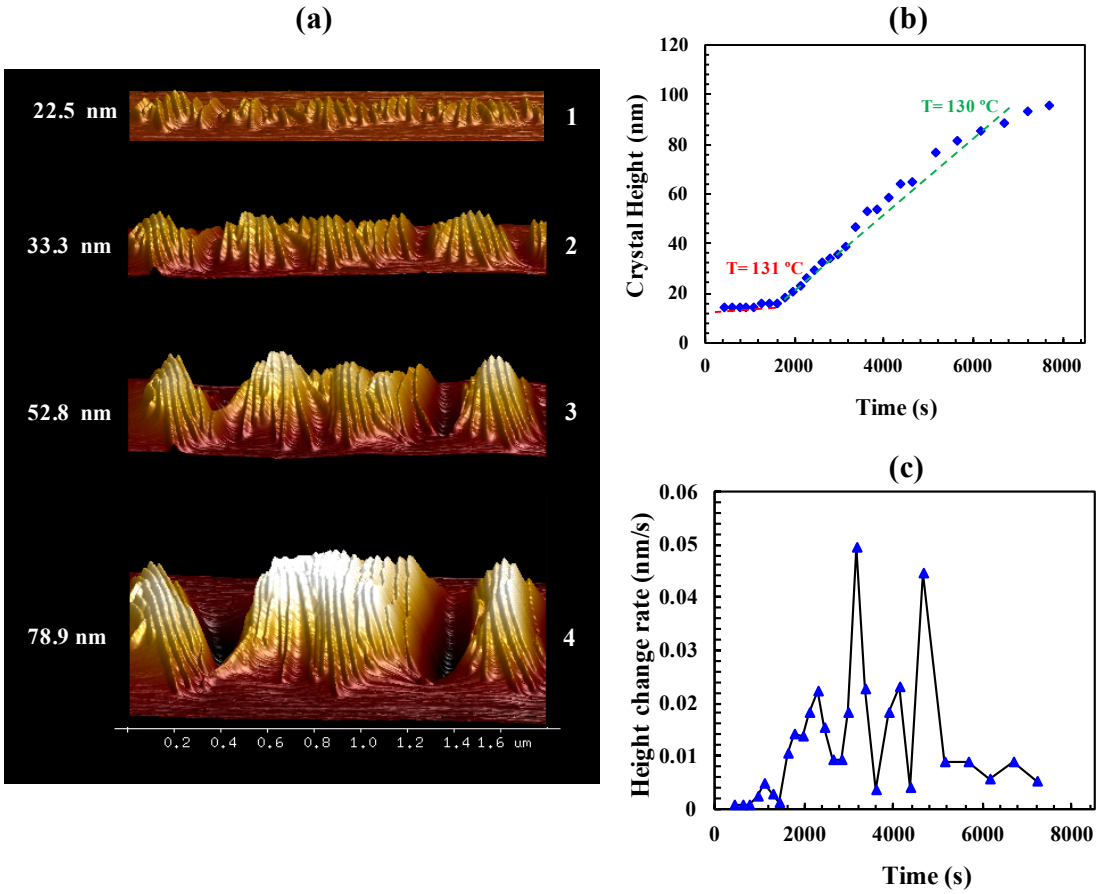

Figure 6.22: (a) AFM height images from 3D images showing the height of the whole crystals as a function of time. These images correspond to the images in Figure **6.18**. (b) Plot showing the height of the PE crystals shown in Figure 6.17 as a function of time at 131 ºC (red dashed line) and at 130 ºC (green dashed line), and (c) plot showing the rate of change in the height of those crystals.

From the 3D images (Figure **6.22** (a)) it is clear that the crystals clumped into groups as they grew, resulting in the creation of gaps between these groups, as shown above. Interestingly, these gaps increased in depth with time, or more precisely, as the crystals grew. The depth of the gap between the groups of crystals was measured in nanometres as a function of time. Figure **6.23** (a) illustrates the increase in the gap depth as a function of time. Moreover, the rate of change in the depth of the gap between crystals

was also measured as a function of time and found to fluctuate with time. Figure **6.23** (b) shows a plot demonstrating the variation of this rate of change in depth as a function of time at 131 – 130 °C. From the plot it is clear that the change over time was not constant, and indeed was rather random, although it does generally become smaller after a certain period of time.

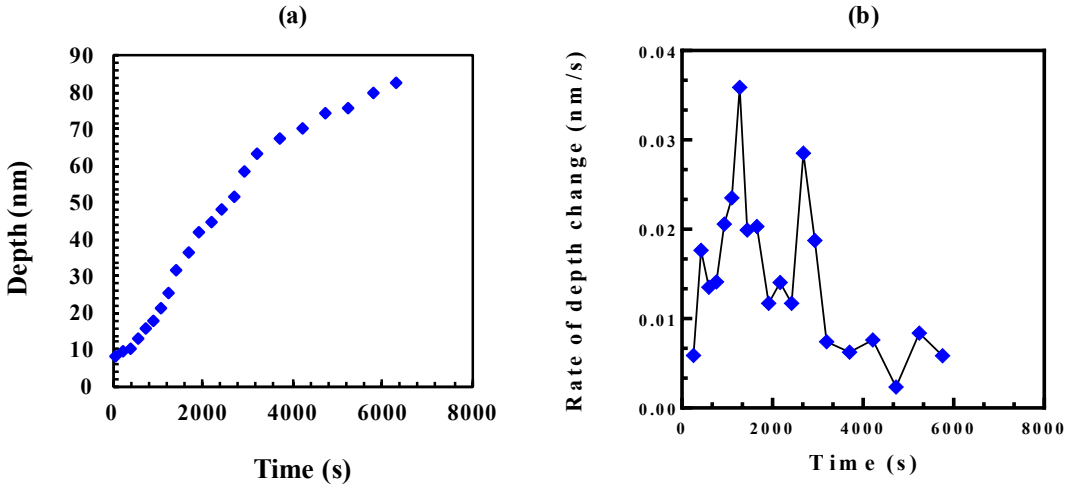

Figure 6.23: Plots showing: (a) the depth of the gap between the crystal groups indicated in Figure **6.22** (a) (the right hand side gab), and (b) the rate of change in the gap depth as a function of time.

6.4.3.3. Interdigitation of Crystals

Two nuclei-rows were induced by the AFM tip and the subsequent growth was followed in order to investigate the interdigitation of the crystallization.

Figure **6.24** and Figure **6.25** show two examples of interdigitation of PE crystals at 133 °C and 132 °C, respectively.

Figure **6.24** shows the interdigitation of two rows of oriented PE crystals during isothermal crystallization at 132 °C. It is clear that crystals can reorganize themselves, as can be seen in Figure **6.24** (a-d), where the shape changes from being bent (a-b) to being roughly straight in (d) and then continuing to grow in a straight line.

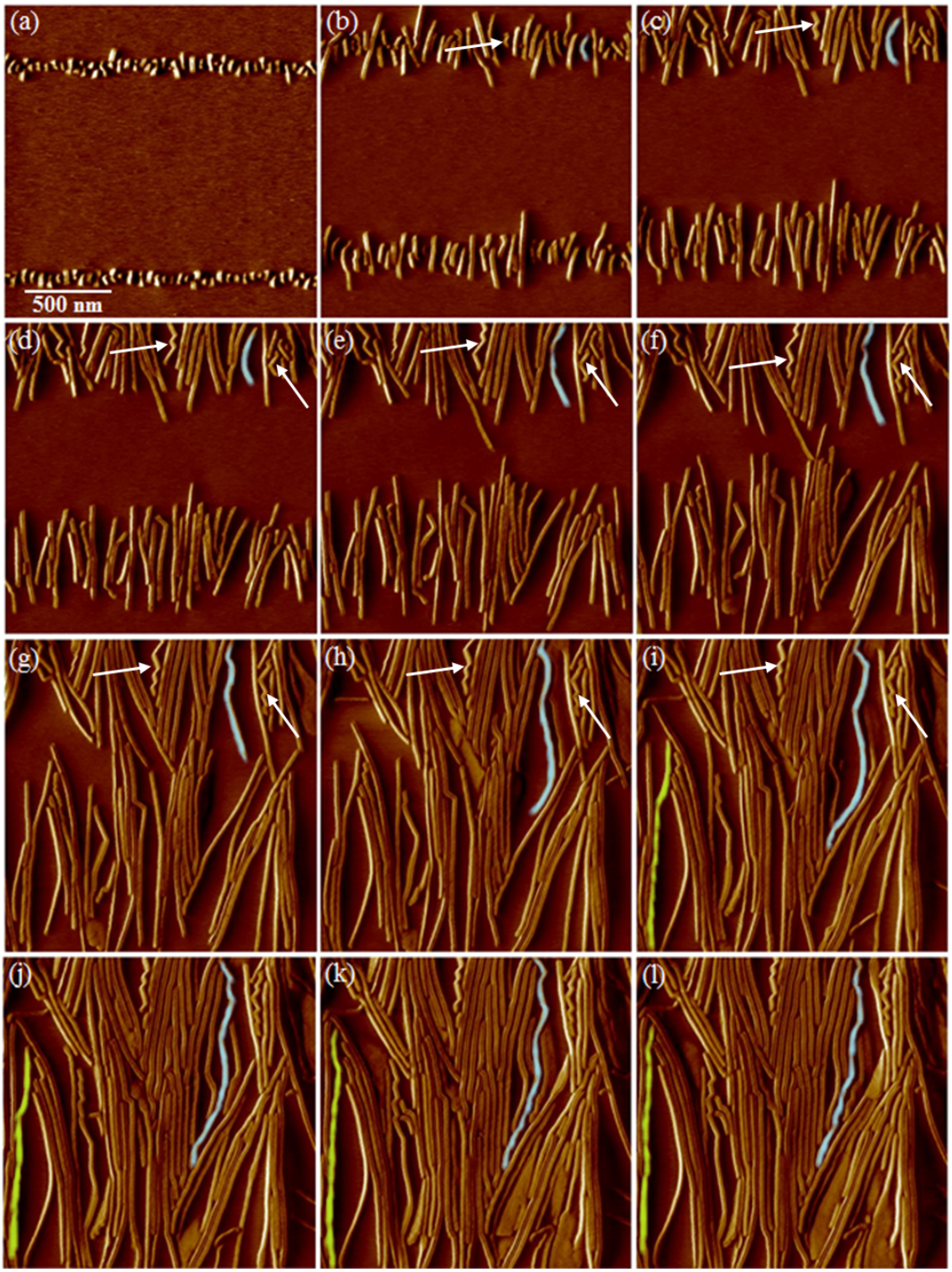

Figure 6.24: A sequence of *in situ* AFM phase images showing the growth of PE induced crystals at 132 °C. An example of crystals deforming is shown (highlighted crystals).

Figure **6.25** shows another example of the interdigitating of two rows of oriented PE crystals during isothermal crystallization, this time at 133 °C. Some crystals have been highlighted to make it easier for the reader to follow their behaviour. Interesting

behaviours were observed, for example, the grey crystal bent as the purple crystal grew towards it (c-g); the white crystals merged into one when they met (b-f); the blue crystal grew very slowly until sufficient room appeared, at which point it accelerated (e-l); the pink crystal deformed as it grew (e-l); the yellow crystal was inhibited by another crystal for a while before changing direction to an area with more room to grow into, and then increased its growth rate sharply (e-k); the green crystal collided with the red crystal for a short time before changing its direction of growth into an empty area and accelerating (e-h); the red crystal then collided with the pink crystal and stopped growing as there was not enough room to change direction (e-l).

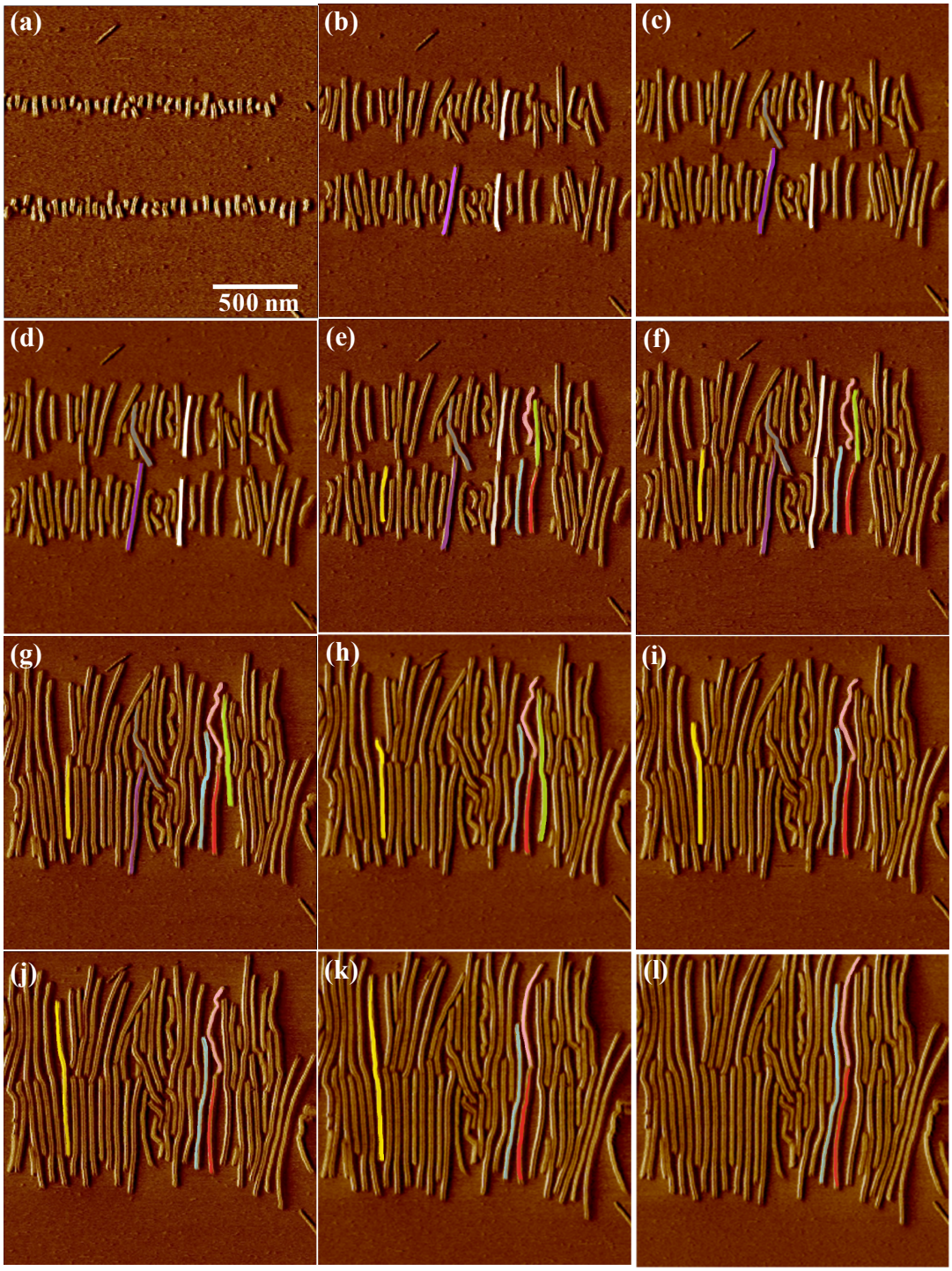

Figure 6.25: A series of AFM phase images showing the interdigitating of two rows of oriented PE crystals during isothermal crystallization at 133 °C. The images show the grey crystal bending as the purple crystal grows towards it; the white crystals merging into one when they meet; the blue crystal growing very slowly until it has enough room, at which point it accelerates; the pink crystal deforming as it grows; the yellow crystal inhibited by another crystal for a while before changing direction to an area with more room to grow into, and then increasing its growth rate sharply; the green crystal meeting the red crystal for a short time before changing its direction of growth into an empty area and accelerating; the red crystal then meeting the pink crystal and stopping growing as there was not enough room to change direction.

These habits for the crystals as they approached another neighbouring crystal are similar to those reported previously in an *in situ* study of the process of interdigitation of shish kebab crystals in PE, also using AFM [4]. Different behaviours exhibited by crystals as they approach another neighbouring crystal were suggested in this prior work: the two crystals can change their growth direction to avoid hitting each other; they can meet each other and therefore stop growing; they can join each other and become one crystal; or they may pass by each other without meeting and continue growing. The new habit observed here was that the two crystals could meet and stop growing for a while until one of them changes its direction of growth slightly so that its front becomes free and its growth is thus able to accelerate.

6.4.3.4. Melting During Crystallization

Figure **6.26** shows a series of AFM phase (a-f) and height images (d′-f′) presenting the isothermal crystallization of PE film at 131 °C, having been induced at 133 °C. Another interesting phenomenon was observed in this work, which was that some crystals melted during the isothermal crystallization while the remaining crystals continued growing, as can be seen in Figure **6.26** (d-f) and their corresponding height images (d′-f′). The arrows indicate the crystals that melted, each crystal indicated by different colour for ease of identification.

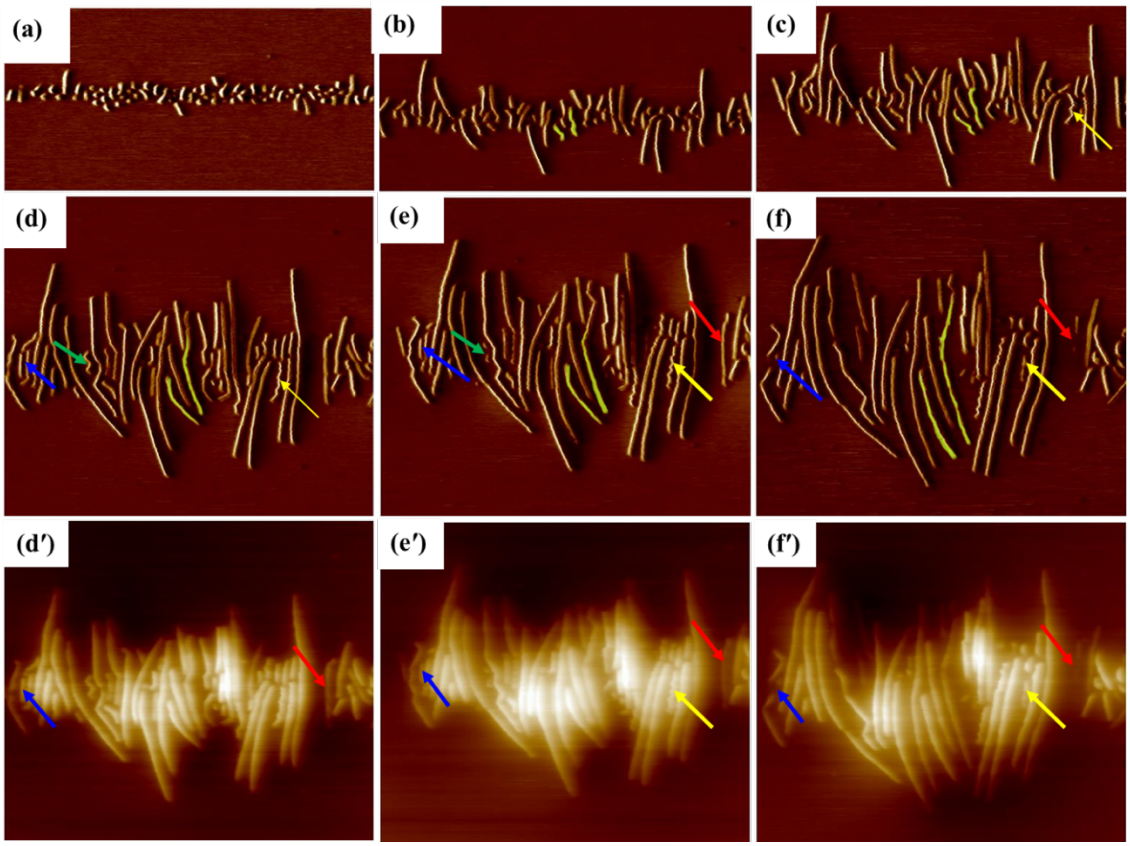

Figure 6.26: AFM phase images (a-f) and height images (d′-f′) corresponding to (d-f) showing; the melting of some crystals (indicated by arrows), and crystals being forced apart as others grow between them (green highlighted crystals) during the isothermal crystallization of PE film at 131 °C (scan size=1.8μ, rate=3.03 Hz (512/256). Each image was acquired in 84 s. Induced at 133 °C.

The possible reason for this melting was that the temperature of the top of the sample was not constant during the experiment (i.e. the temperature of the film surface potentially increased slightly due to the heater until it reached an equilibrium state where the temperature of both the film surface and the heater were equal such that there was no more variation in the temperature of the film). This slight increase in temperature would mean that there would be a variation in the average growth rate of crystals with time. In other words, the average growth rate of the crystals would not be constant but would reduce as a function of time, since an increase in the temperature of the sample leads to a decrease in the average growth rate of crystals. In order to check whether the change in the sample temperature is the reason behind the melting of the crystals during the crystallization, the average growth rate of the crystals was measured as a function of time in the cases where this phenomenon was observed. Figure **6.27** shows an example of such a measurement. The time at which the melting occurred was

somewhere between 1500-2000 s. It is clear that the average growth rate was almost constant all the time, which means that there was no change in the sample temperature during the growth, and in turn the melting of crystal was not caused by an increase in temperature.

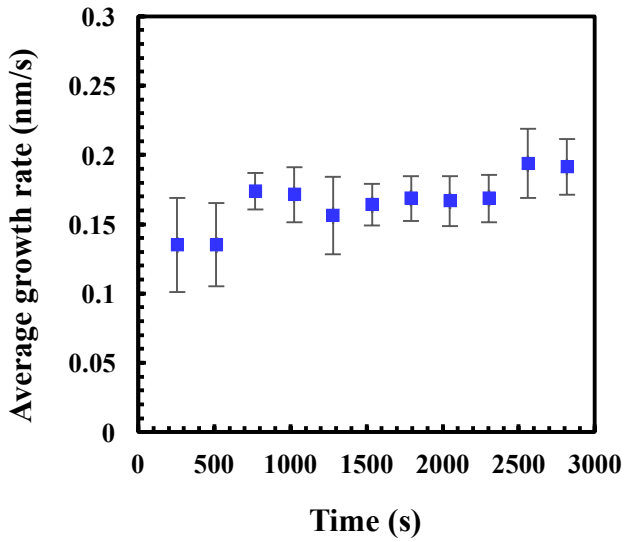

Figure 6.27: A plot showing the average growth rate of PE crystals as a function of time at 133 ºC.

Keeping the sample at a high temperature for many hours (131 °C in this case) could lead to some of the crystals melting, even those that had initially grown to some extent (see crystals indicated by the red arrow in Figure **6.26** (e-f)). A possible explanation for this melting, or disappearance, of crystals could be that these crystals were not stable enough, as suggested previously in [182]. Since the relaxation time of chains is proportional to the M_W, short chains would have a much shorter relaxation time than long chains, hence another possible explanation for the melting of the polymer during crystallization is that the crystals that melted may have been formed from shorter chains which then relax back quickly into the melt (i.e. relax back to a coiled state), in contrast to other crystals that formed from longer chains, meaning that there is insufficient time for them to relax and thus they remain in the oriented state.

6.4.3.5. Checking the Effect of Tip on the Crystal Behaviour

In all the results presented above, i.e. zigzag formations, clumping into groups, transition from edge-on to flat, it is possible that the effects were caused or influenced by the AFM tip. In order to verify that the AFM tip did not cause these observations, therefore, *ex situ* experiments were performed.

After inducing rows of nucleation using the AFM tip, the tip was withdrawn in order to allow the induced nucleation to be isothermally crystallized (at 131 °C for about an hour). Then, the same area was re-imaged to see if the zigzag crystal formations were similar to those observed during the *in situ* crystallization process. The resulting image is shown in Figure **6.28** (b), and since the same zigzag is clearly evident it can be demonstrated that the AFM tip did not significantly influence the results.

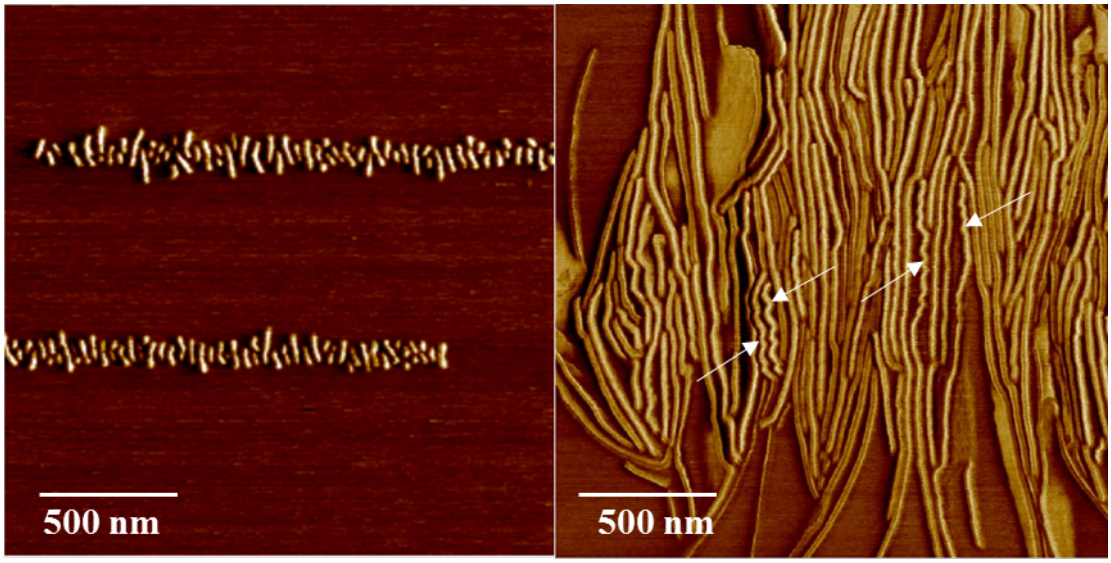

Figure 6.28:AFM phase images of (a) the crystals induced by the AFM tip and (b) *ex situ* image showing the formation of zigzag crystals (indicated by arrows) after isothermal crystallization of PE at 131 °C (without imaging by AFM).

Another *ex situ* AFM study was then done to examine whether the clumping of crystals into groups or the transition from an "edge-on" lamella to a "flat" lamella was caused by the force applied by the AFM tip. Again, after inducing the nucleation using the AFM tip, the tip was withdrawn in order to allow the crystallization to occur without scanning. After the experiment had run for a few hours, the AFM was used to re-image the same area. Similar results were obtained as with the earlier *in situ* AFM images.

Figure **6.29** shows an example of such a situation, where image (a) was taken immediately after inducing the crystals by the AFM tip and image (b) is the subsequent growth of those crystals without imaging by the AFM. This result proves that the clumping or transition from "edge-on" lamellae to "flat" lamellae is not induced by the AFM tip.

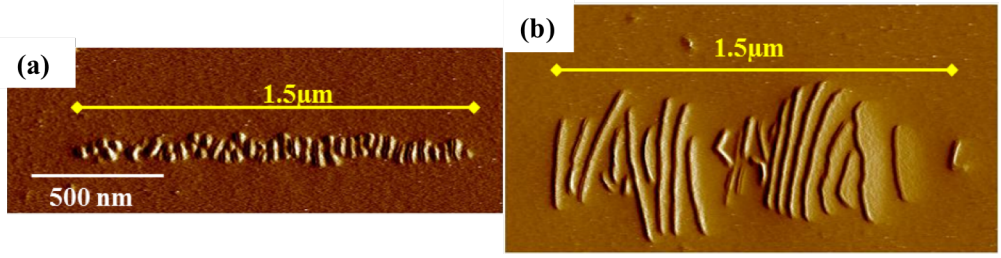

Figure 6.29: AFM images showing (a) the PE crystals induced by the AFM tip and (b) *ex situ* image showing the relative clumping of crystals into two groups after isothermal crystallization of PE (without imaging by AFM).

6.4.3.6. Effect of Nucleation Density on Crystal Behaviour

In the case of low nucleation densities (i.e. where there are a small number of nucleations), melting of crystals during the crystallization was observed, similar to cases of high nucleation density. An example is shown in Figure **6.30** (the pink highlighted crystal labelled as "6"). Crystals 8 and 9 caused crystal 6 to melt: its middle melted as crystal 9 grew towards it. Later, as crystal 8 grew towards it, it melted again.

Moreover, crystal 7 (blue) deformed during the crystallization, as shown in image (a)-(b). The crystal did not start straight but, as it grew, it deformed until it became completely straight, and then it continued growing in a straight line, as shown in image (d-e).

In comparison with the behaviour of crystals in the case of high density nucleation, in low nucleation densities the crystals moved more; i.e. there were more changes to their initial growth direction and they continued growing in this manner with time. This behaviour (movement of crystals) might be due to the fact that where there is less nucleation there are more spaces into which crystals can move or change their growth direction. Figure **6.30** shows an example of such a situation: crystals labelled "1-5" (Figure **6.30**) change their initial growth direction and rotate as they grow. Crystals 2-5 change the angle of their direction of growth over the period of crystallization by a

similar amount, in the range of 35-45º, while crystal 1 changed its angle by about twice that, ~ 75º. This difference may be because crystal 1 has more space (i.e. free space to its left) than the other crystals, allowing it to move more than them.

This was examined further by varying the density of nucleation and then investigating the associated changes in growth behaviour. This will be discussed in more detail later in this chapter.

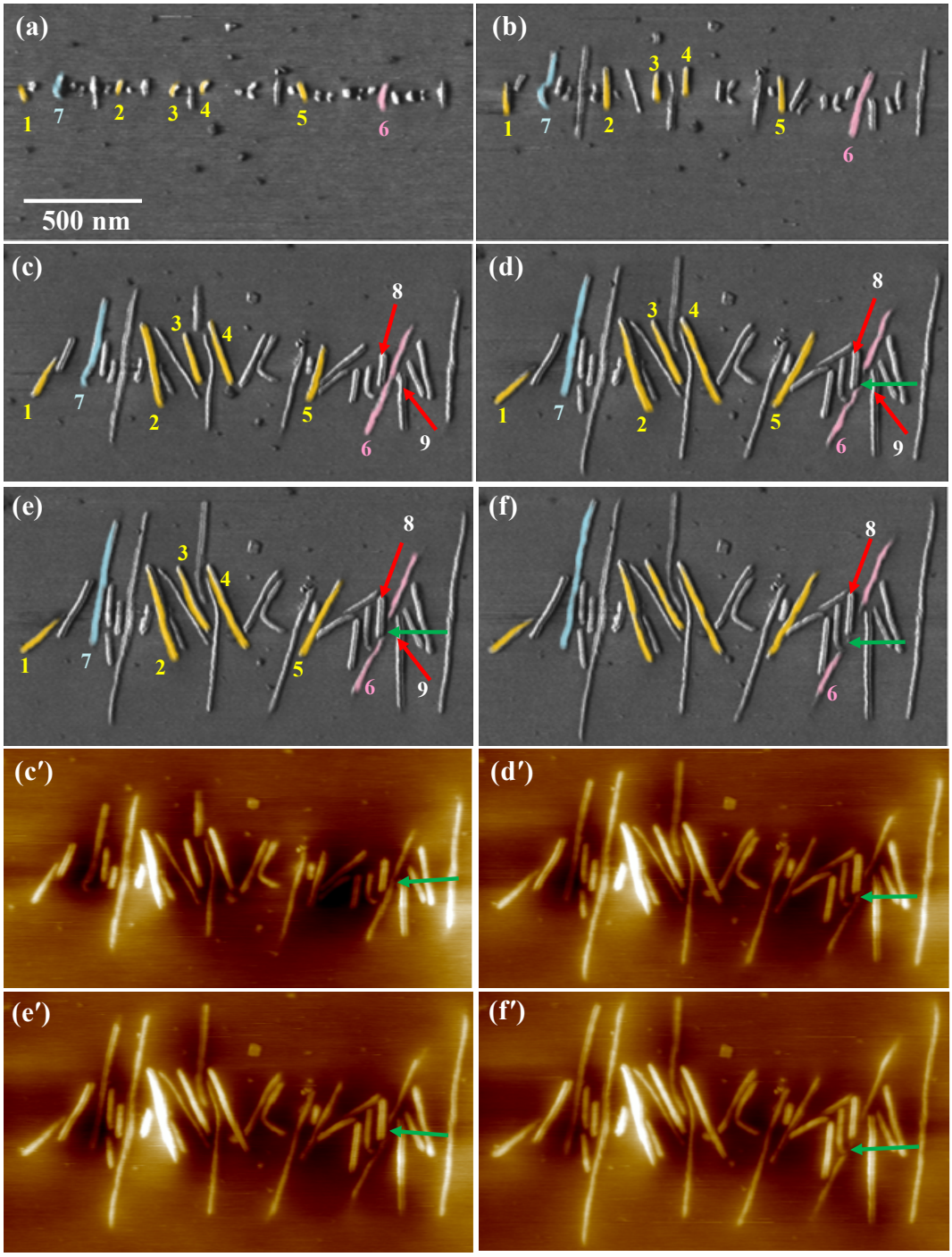

Figure 6.30: AFM (a-f) phase and (c′-f′) height images (corresponding to images (c-f), respectively) showing the crystallization of PE at 131-130 °C. Crystals labelled as "1"-"5" (yellow highlighted crystals) change their direction as they grow, nine crystals (1-9) have been highlighted to aid the reader to follow their growth behaviour.

Figure **6.31** provides further evidence that the AFM tip has no effect on the crystals' behaviour here. The images on the right in the Figure show the crystals that were induced first; then the AFM tip was moved to induce the crystals that are shown in the

left-hand images above. These (left-hand) crystals were scanned continuously (*in situ*) during their growth, as shown in Figure **6.30**, while the crystals on the right-hand side grew in the absence of scanning. Finally, the scan size was increased so as to be able to see both areas simultaneously in order to compare the crystals formed in the two areas. Obviously, the morphology in both areas is similar, indicating that the presence of the tip had no effect.

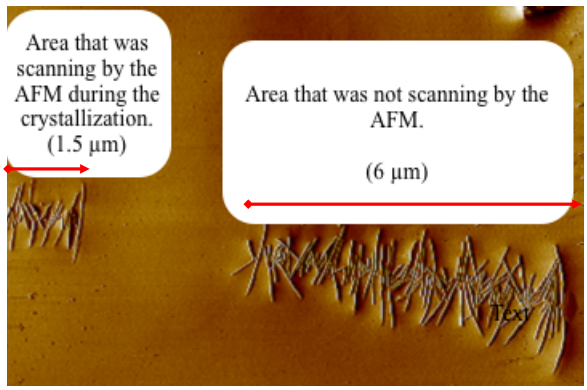

Figure 6.31: An AFM phase image showing the similarity in morphology of the two induced rows of crystals: one on the left (small row) that was scanned *in situ* during its growth and the other on the right (large row) that was just induced with the tip and then grew without scanning.

Figure **6.32** shows another example of crystallization with low density nucleation. It can clearly be seen how the crystals have changed their initial growth direction (angle) and how this change is maintained with time. For instance, the initial angle of the crystal labelled "1" in (a) was ~ 55º, and this changed to be ~ 92° in (d), a change of ~ 67% (i.e. of 37º).

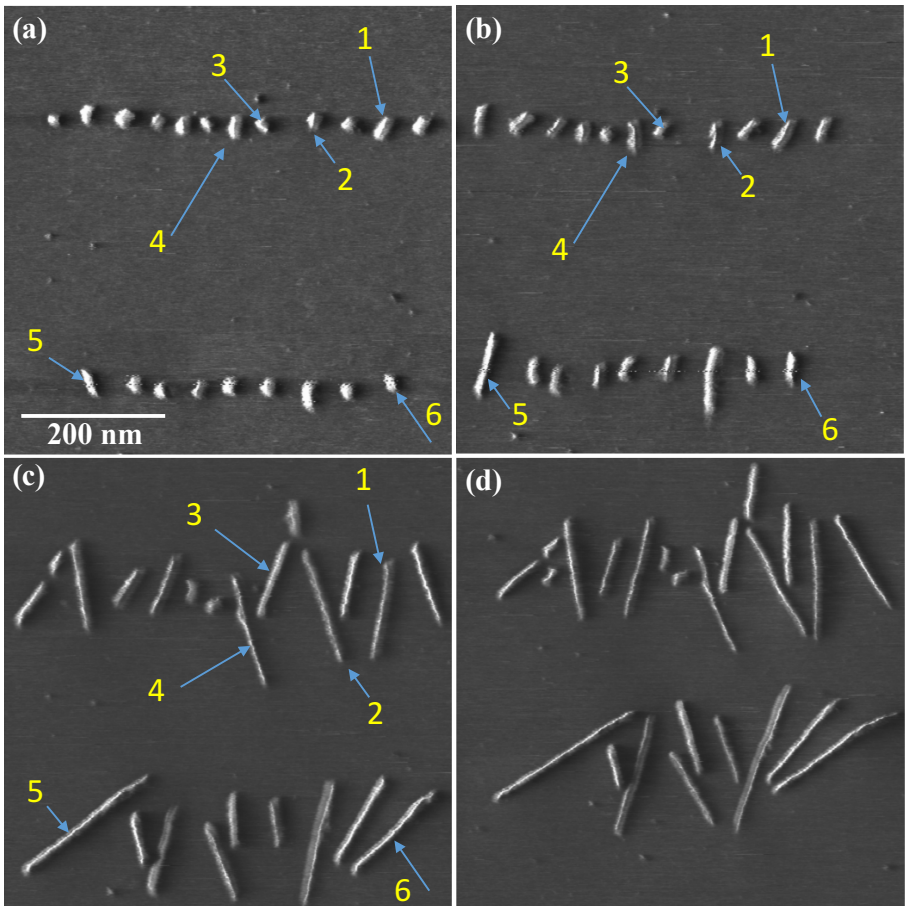

Figure 6.32: A series of AFM phase images showing the movement of some crystals as they grow in the case of low density nucleation at 133 °C.

To investigate this further, a single crystal was induced and its growth behaviour was examined *in situ*.

6.4.3.7. Single Crystal

To date, there have been few studies that have investigated single crystals from polymer melt, due to the difficulty in preparing such single crystals. Various special approaches have previously been used in an effort to prepare single crystals from the melt. These methods include applying chemical etching to remove surrounding single crystals [183], quenching and subsequent extraction in a solvent [36, 183–185]. In this work, for the first time, single crystals were produced directly from the melt without any special treatment of samples, and then the subsequent growth was studied *in situ*. A single crystal or a single nucleus of PE was formed by following the same approach used as that used earlier in the chapter to induce a row of nuclei, but instead choosing a small

scan area (i.e. 150 nm) and a low scan rate (i.e. 0.5 Hz). Figure **6.33** shows an example of one of the results of such an approach. After the formation of the single nucleus using the AFM tip, its subsequent growth was monitored in real time (see Figure **6.34**) to investigate its behaviour in the absence of the effects that could be caused by the presence of neighbouring crystals. This was intended to make it easier to identify the effect of multiple crystals on each other.

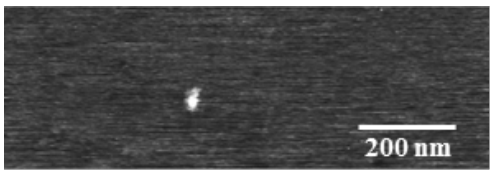

Figure 6.33: An AFM phase image showing a single crystal of PE induced at 133 ºC.

Figure **6.34** shows a series of AFM phase images collected at 133 °C during the isothermal crystallization of a single PE crystal from the melt.

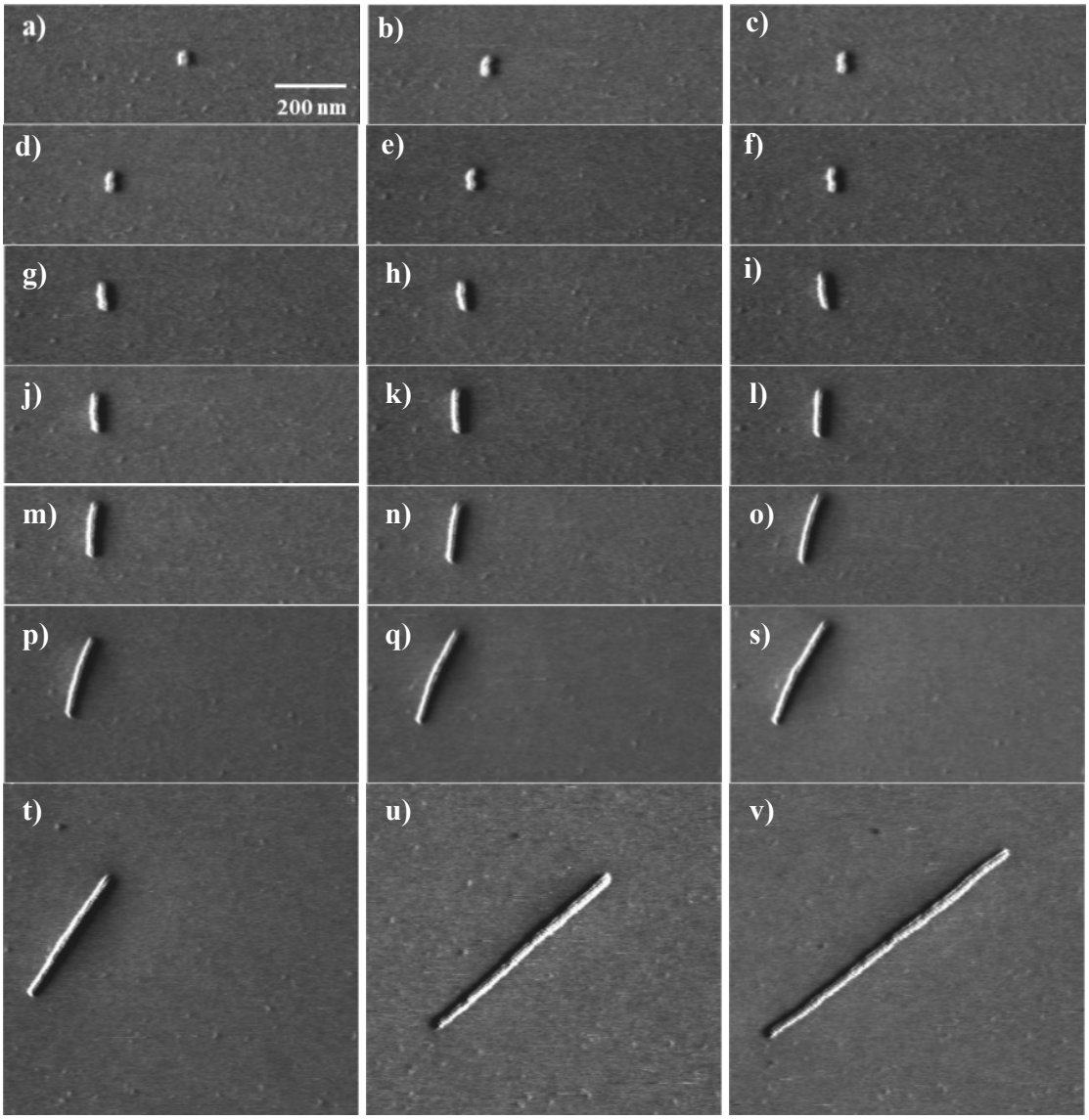

Figure 6.34: A series of AFM phase images showing the growth of a single crystal of PE.

Figure **6.35** shows another example where the single crystal rotated as it grew.

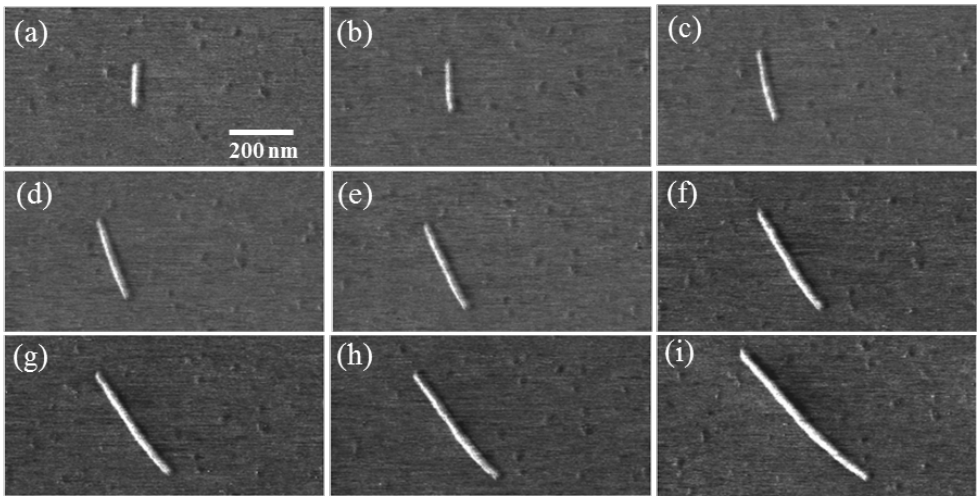

Figure 6.35: A series of AFM phase images showing the growth of a single crystal of PE at 130 ºC.

It was noted that when a single nuclei was formed the subsequent crystal appeared to rotate as it grew. The important thing here was to determine whether the AFM tip has caused this movement of the single crystal during the scanning. To verify this, after the nucleus was induced the sample was kept at the crystallization temperature for about 30 min without scanning with the AFM. Then, the AFM was used to image the crystal, as can be seen in Figure **6.36**. It is clear that crystal has still rotated despite not being imaged during growth.

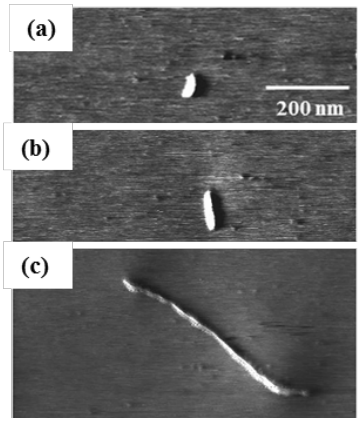

Figure 6.36: AFM phase images (a-b) the induced crystal and its initial growth and (c) after withdrawing the tip and then reimaging the same area by AFM.

Another approach that was used to examine whether the AFM tip influenced the direction of growth of the crystal or not was by scanning parallel to the initial growth

direction after inducing the crystal. This means scanning perpendicularly (i.e. scan angle= 90°) to the induction (initial) scanning direction (i.e. scan angle= 0°) of the single crystal. If the AFM tip were really causing the movement of the crystal, then in this case this movement would not appear. This was not what occurred, however: even in this case, where the tip was scanning in the same direction as the crystal growth, the crystal moved as it was growing and became perpendicular to the scanning direction (Figure 6.37). This is further evidence that the AFM tip was not causing the movement of the crystal.

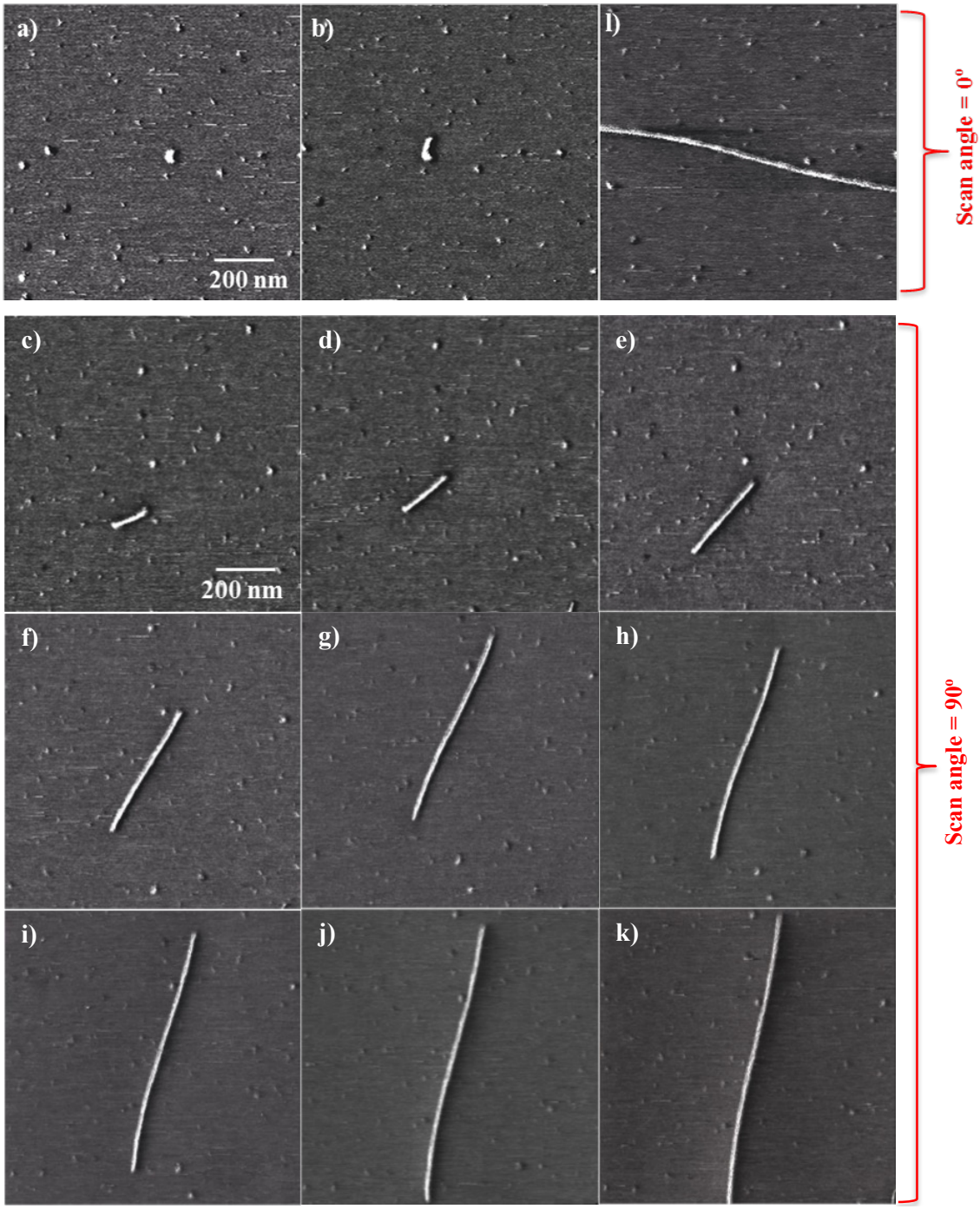

Figure 6.37: A series of AFM phase images showing the growth of a single crystal of PE at 132 ºC. (a-b) the initial images were taken with a normal scan direction (scan angle=0º) and (l) the final image was also taken at 0°, while (c-k) were taken with a vertical scan direction (scan angle=90º).

It is very clear that the AFM has no influence on the direction of growth and that the crystal growth direction is independent of the scanning direction. The growth behaviour of the single crystal was therefore investigated as a function of temperature in order to examine if there is a relationship between the amount of movement and the

crystallization temperature or, more precisely, the growth. This was done by crystallizing a single crystal at a lower temperature (e.g. at 130 °C) after inducing it, until it had grown to some extent. Then, the temperature was increased by two or three degrees (e.g. to 132 °C) and the growth was observed. Figure **6.38**-Figure **6.40** show three examples of such approaches.

In Figure **6.38** (a-d) the crystal was induced at 132 °C, then the temperature was lowered to 130 °C to allow the crystal to grow for some distance so as to make it easier to observe the change in its growth direction. Once the crystal had grown, the temperature was raised to 132 °C to determine if there was the same amount of movement. As can be seen in Figure **6.38** (e-m), the crystal was still moving with time but the amount of movement was reduced as the temperature was increased. To confirm this, the temperature was again reduced to the initial crystallization temperature (130 °C) and it was clear that the amount of movement then increased sharply, as can be seen in Figure **6.38** (n-q).

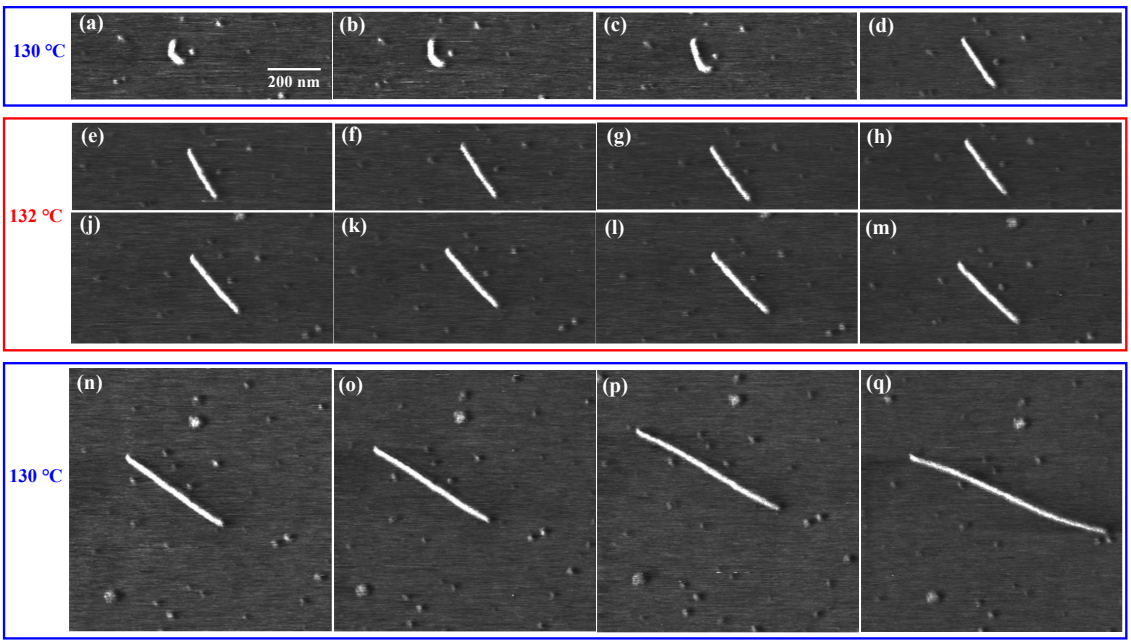

Figure 6.38: A series of AFM phase images showing the growth of a single crystal of PE at 130 °C and 132 °C.

Figure **6.39** indicates the second example studying the movement of the crystal as a function of temperature. In this case, the crystal was crystallized for a short time at 130 °C (a-f), then the crystallization temperature was increased to 133 °C (g-l) and finally the crystallization temperature was again reduced to 130 °C (m-r).

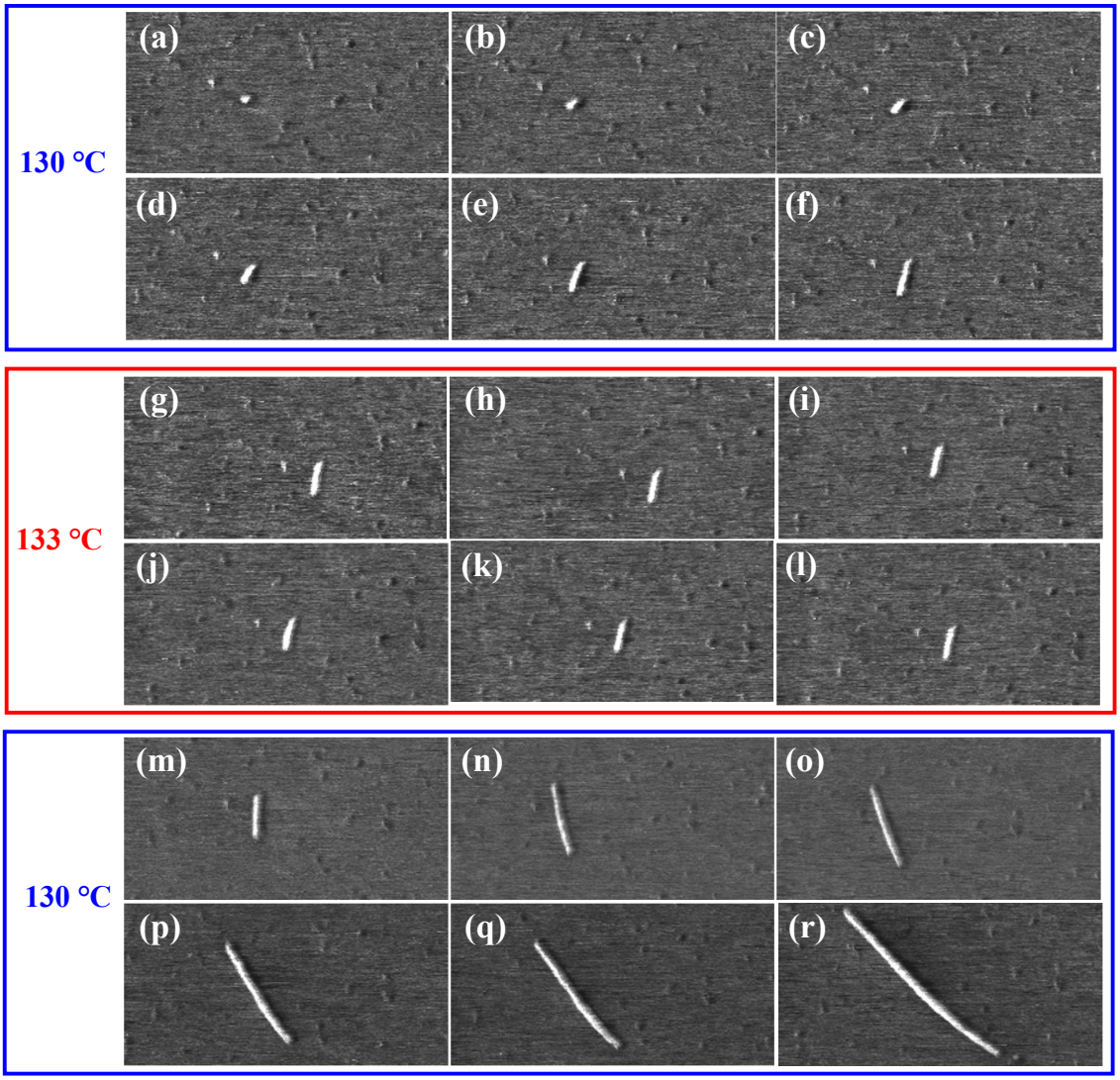

Figure 6.39: A series of AFM phase images showing the growth of a single crystal of PE at 130 °C and 133 °C.

Figure **6.40** shows the third example. In this case the crystal was crystallized at 130 °C for a short time, then the crystallization temperature was increased to 133 °C (a-c) and the sample was kept at this temperature for some time. After that, the temperature was reduced to 131 °C (d-f) and the crystal was allowed to crystallize at this temperature for a period of time. At this temperature, the amount of movement was slightly higher compared to what it was at 133 °C. Next, the temperature was lowered further to 130 °C for a short time (g-i), at which point the increase in movement became very obvious. Then, the temperature was raised again to 133 °C (j-l) for some time, with no movement apparent at this temperature. Finally, as the temperature was lowered again to 130 °C, the movement of the crystal was sharply increased, as can be seen in images

(m-o). These temperature changes caused an "S"-shaped crystal to be formed by the last stage of crystallization (o). This S-shaped morphology was reported previously by [12], although they report that the S shape forms when the lamellae length was 0.5-1 µm.

Across all the performed experiments, similar behaviour was observed: the movement of the crystal reduced when the crystallization temperature was increased. For example, at 132 °C the amount of movement was lower than that at 131 °C while at 131 °C it was lower than at 130 °C. Moreover, no lamellae branching or spiralling was observed.

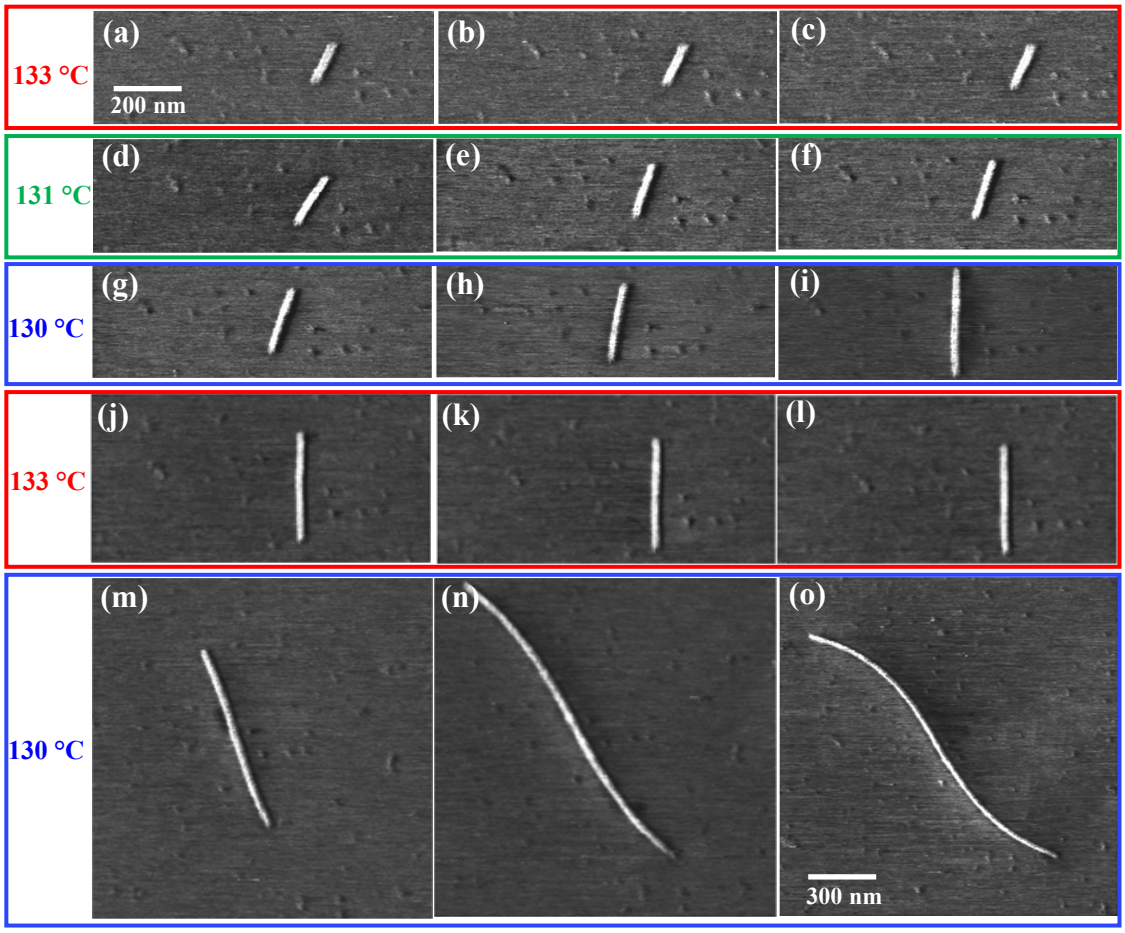

Figure 6.40: A series of AFM phase images showing the growth of a single crystal of PE at 133 °C, 131 °C and 130 °C.

The relationship between the crystallization temperature or, more precisely, the growth of the crystal, and the amount of movement was examined quantitatively. The lengths of these individual crystals were measured from the successive images as a function of time at different temperatures in order to investigate quantitatively the movement of crystals as a function of time, temperature and length of crystal.

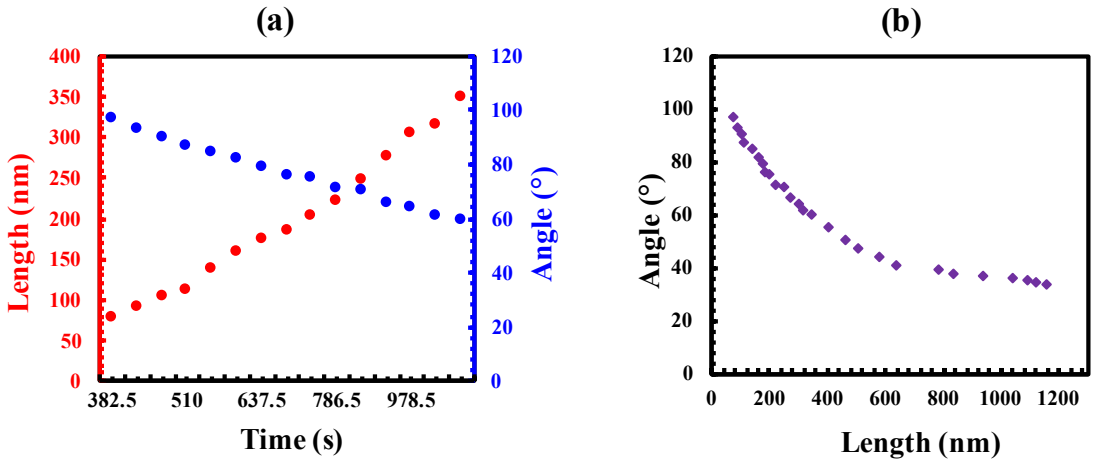

Figure 6.41: Plots showing (a) the angle of the single crystal of PE relative to the scan direction and its length as a function of time (b) the angle of the crystal as a function of its length. The measurements were taken from Figure **6.34**.

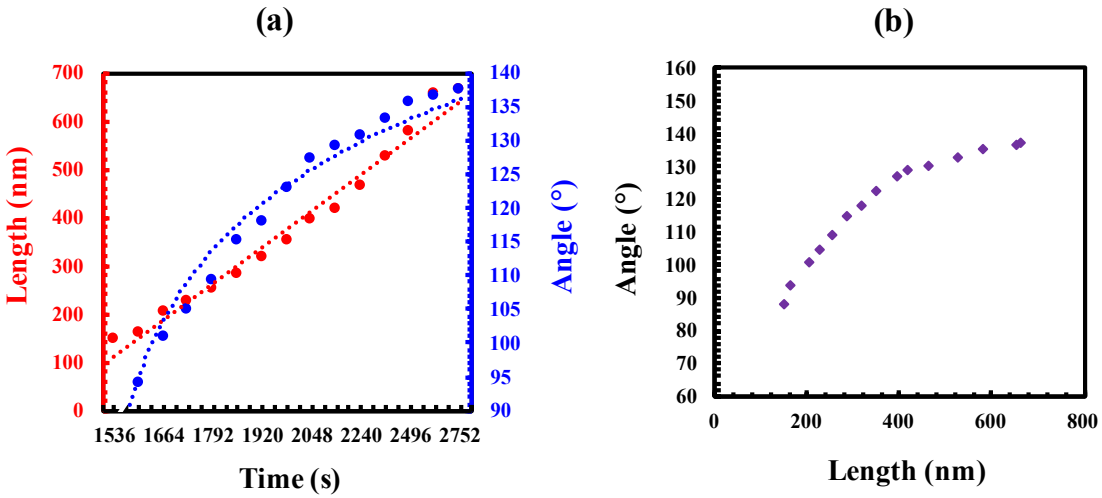

Figure 6.42: Plots showing (a) the angle of the single crystal of PE relative to the scan direction and its length as a function of time at 130 °C and (b) the angle of the crystal as a function of its length. The measurements were taken from Figure **6.35**.

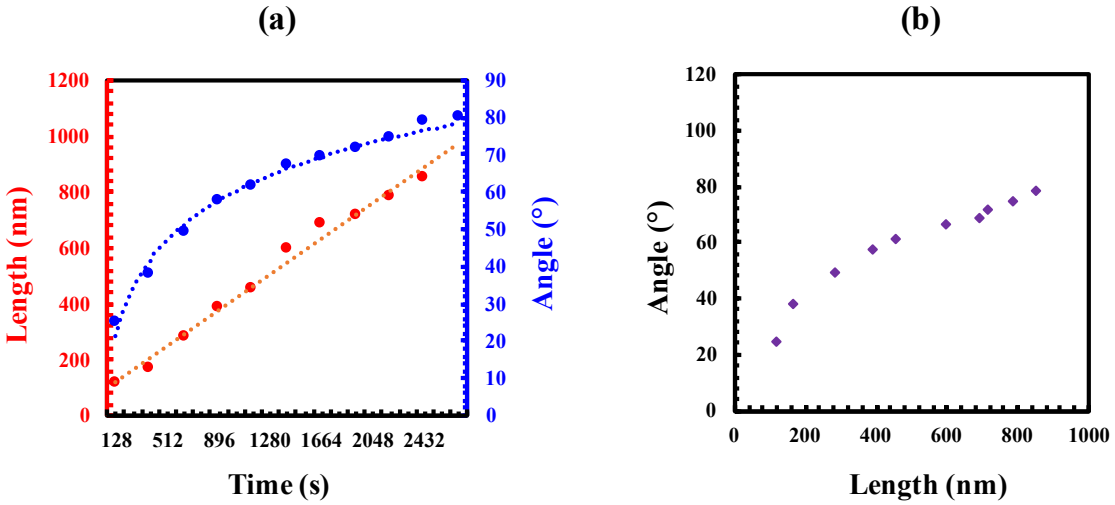

Figure 6.43: Plots showing (a) the angle of the single crystal of PE relative to the scan direction and its length as a function of time at 132 °C and (b) the angle of the crystal as a function of its length. The measurements were taken from Figure **6.37**.

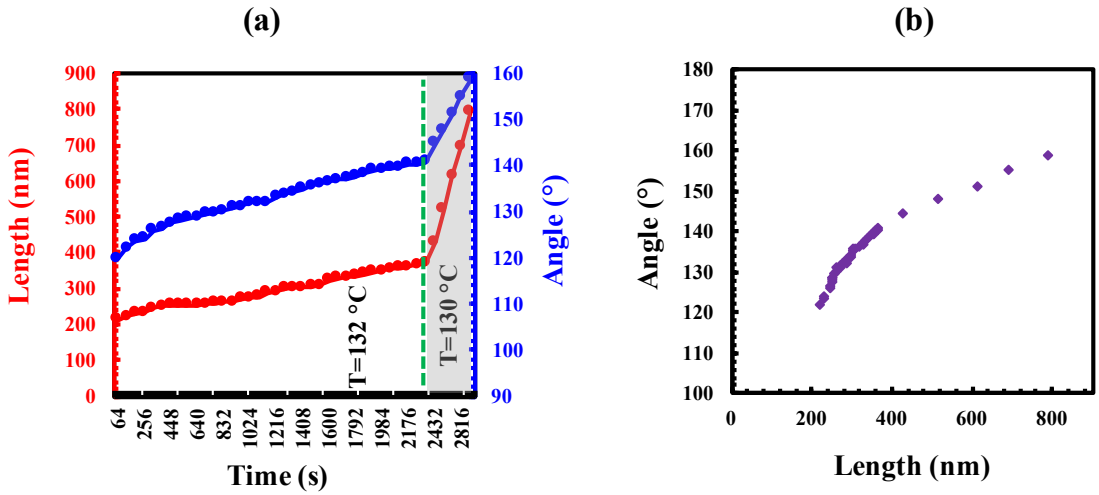

Figure 6.44: Plots showing (a) the angle of the single crystal of PE relative to the scan direction and its length as a function of time at 130 °C and 132 °C and (b) the angle of the crystal as a function of its length. The measurements were taken from Figure **6.38**.

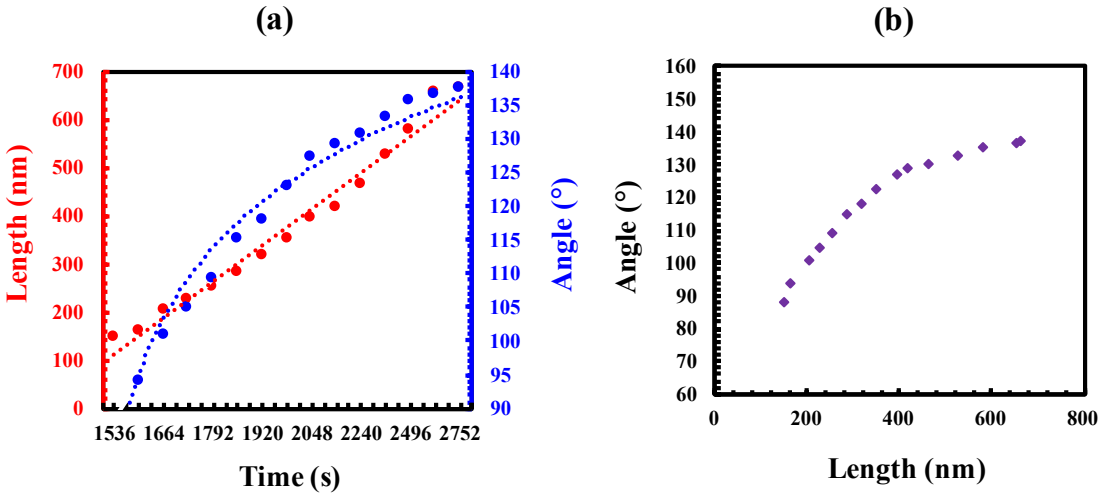

Figure 6.45: Plots showing (a) the angle of the single crystal of PE relative to the scan direction and its length as a function of time at 130 °C and (b) the angle of the crystal as a function of its length. The measurements were taken from Figure **6.39**.

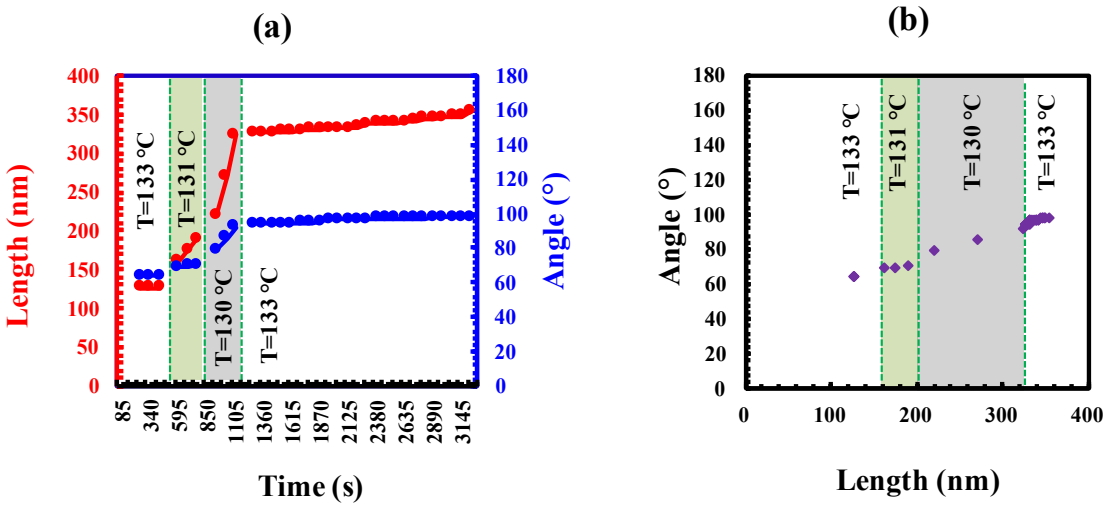

Figure 6.46: Plots showing (a) the angle of the single crystal of PE relative to the scan direction and its length as a function of time at 130 °C, 131 °C and 133 °C and (b) the angle of the crystal as a function of its length. The measurements were taken from Figure **6.40**.

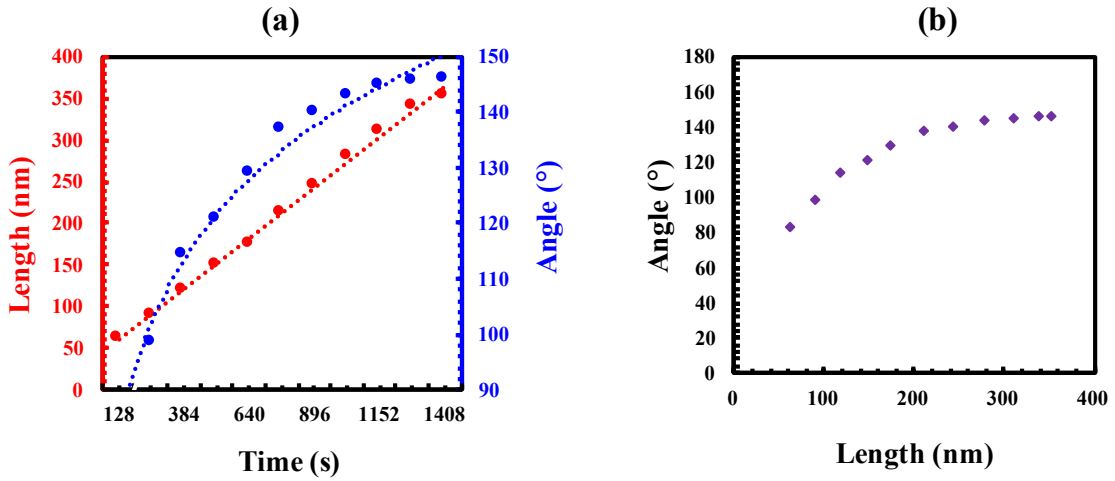

Figure 6.47: Plots showing (a) the angle of the single crystal of PE relative to the scan direction and its length as a function of time at 132 °C and (b) the angle of the crystal as a function of its length. The measurements were taken from data not presented here.

The growth rate of the single crystal and the rate of change of its angle were measured as previously explained in Chapter 5, once again being found to fluctuate with time, as can be seen in Figure **6.48**. This result has been discussed in Chapter 5.

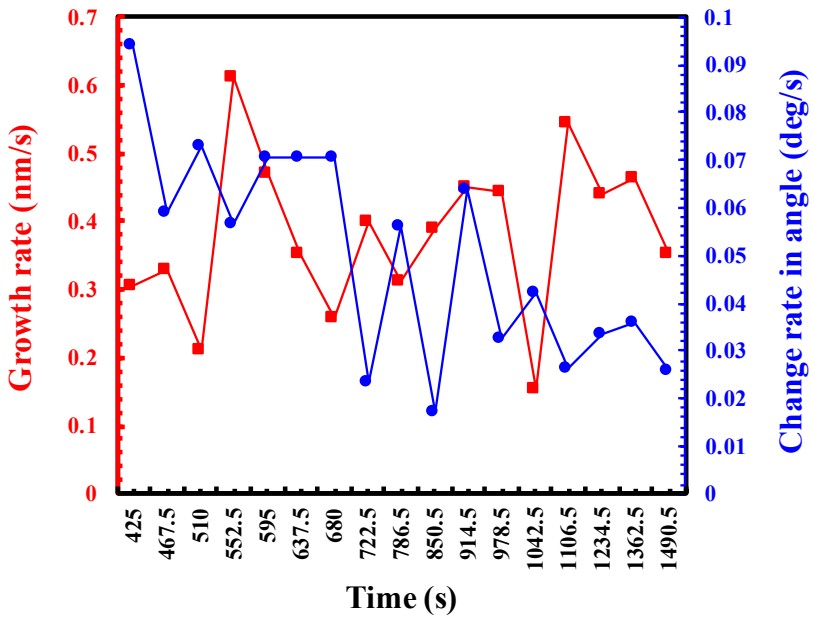

Figure 6.48: A plot showing the growth rate of the single crystal and the rate of change in its angle (amount of movement) as a function of time. The measurements were taken from Figure **6.34**.

Figure **6.49** shows the average growth rates of a number of single crystals at temperatures of 130–133 °C. It can be seen that the growth rate of the crystals at 130 °C was almost triple that which occurred at 131 °C, which in turn was about double the growth rate at 132 °C. This again implies that even a small change in temperature can have a significant impact on the crystallization process.

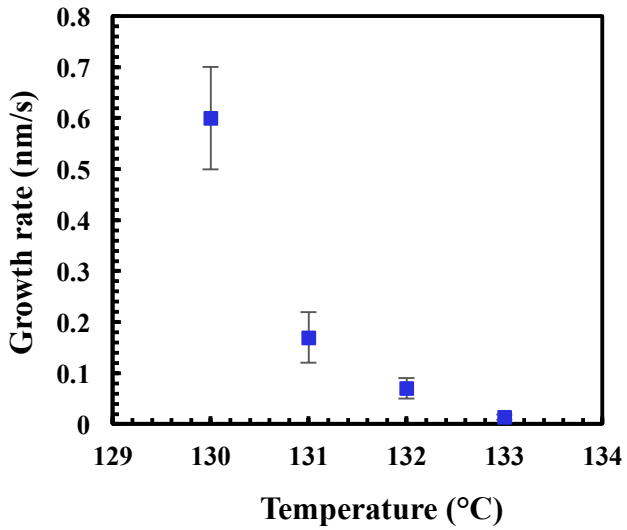

Figure 6.49: A graph showing the average growth rates of a number of single crystals as a function of temperature.

From all the data presented above, it is clear that the single PE crystal moves as it grows. It is difficult to explain this result, but there are some possible explanations.

The first was that this movement is due to relaxation of the melt. It was thought that during the induction of the nucleus, the AFM tip pushed hard on the melt, inducing a hole. Then, as the melt relaxed back the growing crystal appeared to move. This possible explanation was examined by changing the temperature of crystallization. If the explanation is correct, the movement of the crystal should be increased as the temperature increases and decreases, since the relaxation of the melt increases with temperature. The outcome, however, was the opposite of this, as the temperature decreased the movement of the crystal was increased. This implies that the movement of the crystals is connected with the growth rather than the relaxation of the melt.

This result may be explained by the fact that crystallization of polymers occurs by transporting the materials to the growth front (i.e. as the crystals grow they need to be transported to the growing tip). This suggests that stress is induced in the crystal due to

shear as those molecules are transported. Because the growth rate is so small at high temperatures those forces should be very small, but as the growth rate increases the force increases resulting in a more significant change in the angle of the crystal, perceived as movement of the crystal.

Another possible explanation for this is that this movement or rotation of the crystal may be related to surface stresses, which is one of the proposed driving forces behind the twisting of lamellae in spherulites. Crystal rotation may be caused by the unbalanced surface stresses on opposite fold surfaces resulting from the overcrowding and inefficient packing of the fast-growing lamellae [51]. As the crystal grows, the crystal surface becomes crowded, establishing a structural asymmetry that may result in surface forces that lead to crystal rotation, similar to lamellar twisting [187]. It has previously been reported that the scrolling of single crystals might be caused by the unbalanced surface stresses that result from overcrowding [188].

It may also be that as the nuclei were induced by the AFM tip they might be unstable, causing them to reorganize themselves to be in a more stable state, leading to the observed movement. This seems less likely as it is not just the nucleus that rotates but the whole crystal.

6.5. Conclusion

The purpose of this chapter was to first induce PE crystals, and then to investigate their subsequent growth behaviour *in situ* using the AFM. This is the first study that has attempted this. The AFM tip was successfully used to induce local nucleation in the PE film when significant conditions were controlled, such as the ideal (range of) temperature, the tapping force and the mechanical work of the tip that is required to induce nucleation. Nucleation was induced by increasing the tapping force and this was done by decreasing the amplitude setpoint of the AFM tip along a single line so as to initiate a contact and orient chains on the sample surface (i.e. the same approach to that used to orient the E/MB domains in Chapter 4). The induced crystals were initially observed to have only an edge-on orientation relative to the surface of the PE film (i.e.

no flat-on orientation was observed). At later stages of crystal development, however, a transition from an edge-on to a flat-on orientation was observed to occur.

In this chapter, novel observations in respect to the tip-induced oriented PE crystals were reported during isothermal crystallization between 134 °C and 129 °C. Firstly, some crystals were seen to have forced their neighbours apart so as to provide more room to grow between them. Moreover, a few crystals were found to be deformed or to have re-organized themselves as they grew, apparently attempting to be in a lower energy state. Secondly, at later growth stages, the gap between the growing crystals narrowed slightly, until they became adjoining to each other (i.e. the crystals clumped into groups). This could be due to the change in the crystal orientation from being edge-on to flat-on, as their height increased. Thirdly, on interdigitation, the crystals appeared to have similar habits as they approached other neighbouring crystals to those reported previously: i.e. two crystals could change their growth direction to avoid hitting each other; they could meet each other and therefore stop growing; they could merge with each other and become one crystal; or they could pass by each other without meeting and continue growing. Additionally, one new habit was observed: the two crystals could meet and stop growing for a while before one of them changed its growth direction slightly, opening up room for growth and allowing it to accelerate. Fourthly, some crystals melted or disappeared during the isothermal crystallization, suggesting that those crystals were unstable.

Furthermore, the effect of nucleation density on the behaviour of the crystals was examined. It was found that as the nucleation density reduced, the crystals moved (rotated) as they grew. To investigate this further, a single crystal was induced and its growth behaviour was studied as a function of temperature. It was found that, as the growth of the crystal increased, the change in its angle also increased. To the best of our knowledge, this is the first time that single crystals have been induced from the melt without special treatment. The movement of crystals has also not been observed previously.

Overall, no branching or splaying out of crystals was observed, which means that the process would not eventually lead to the formation of spherulites. Additionally, on isothermal crystallization, there was no sign of the formation of new nuclei or crystals,

but only the development of the previously induced crystals with time. This observation is consistent with the hypothesis of the dependence of nucleation on temperature.

These interesting observations could provide new insights into the crystallization kinetics of PE and of polymers in general.

Chapter 7

Kinetics of Flow-Induced PE Crystals by AFM Tip

7.1. Introduction

Since the development of AFM, it has been used for the study of polymer crystallization and melting in real time with nanometre scale resolution. In particular, AFM enables the crystalline lamellae to be resolved at the surface of the melt, thus allowing their growth to be followed *in situ* over the period of the image capture process. Some *in situ* AFM studies of lamellar scale growth have shown that the growth rate of individual lamellae fluctuates, both from lamella to lamella and in time. These observations have been found in a range of polymer systems, such as poly(hydroxybutyrate-co-valerate) (PHB/V) [9], PEO, PCL [8], BA-C8 polymer [79] and PE [4], PLLA and PHB [189]. This finding of fluctuating lamellar growth contrasts with older theories of polymer crystallization, which had predicted a constant lamellar growth rate at a particular temperature, based on macroscopic observations of polymer spherulite growth made by optical microscopy. For this reason alone, it is clear that our theoretical understanding of the process of polymer crystallization is incomplete. One reason for this discrepancy between theory and experiment may be the fact that polymer crystallization theories work on the assumption of idealized systems, whereas in real systems a range of molecular weights are typically present, along with impurities and other non-crystallizable components. Other effects typically not included in the initial assumptions of polymer crystallization theory are surface and interface effects and the effect of dislocations on crystal growth, although the influence of such variables is often discussed separately.

Notwithstanding the theory, based on the limited experimental evidence that exists at present, fluctuations in the growth rates of the lamellae could in fact be a general

feature of melt crystallization. For this reason, further observations of such phenomena are required so as to drive a better theoretical understanding of what gives rise to variations of individual lamellar growth rates. Since the original theories were mainly based on information from PE crystallization, it is particularly useful to examine the growth rates of this material in detail. The focus of this chapter, therefore, will be on the growth rate of individual lamellae in PE.

In this chapter, the method that was used to induce PE crystallization is first briefly presented. The behaviour of the subsequent crystallization in PE at different temperatures is then described and discussed. Ultimately, the chapter investigates both the variation in the growth rate of individual lamellae and the overall distribution of the lamellar growth rates as a function of temperature.

7.2. Method

The PE type, the sample preparation and the AFM mode used in the research presented in this chapter were the same as described in the previous chapter (Chapter 6). A different method was used to induce oriented crystals, however. In this case, the AFM tip was used as flow shear to induce oriented PE crystallization and then to investigate their subsequent growth behaviour, including crystal orientation and growth rate. This was done by bringing the tip into contact with the surface of the molten PE and then moving the stage in either the x-axis or y-axis. Since the tip was contaminated after this step, it needed to be replaced at this point. The experimental setup is shown in Figure **6.2** (a) and the crystals that were formed are shown in Figure **6.2** (b-d).

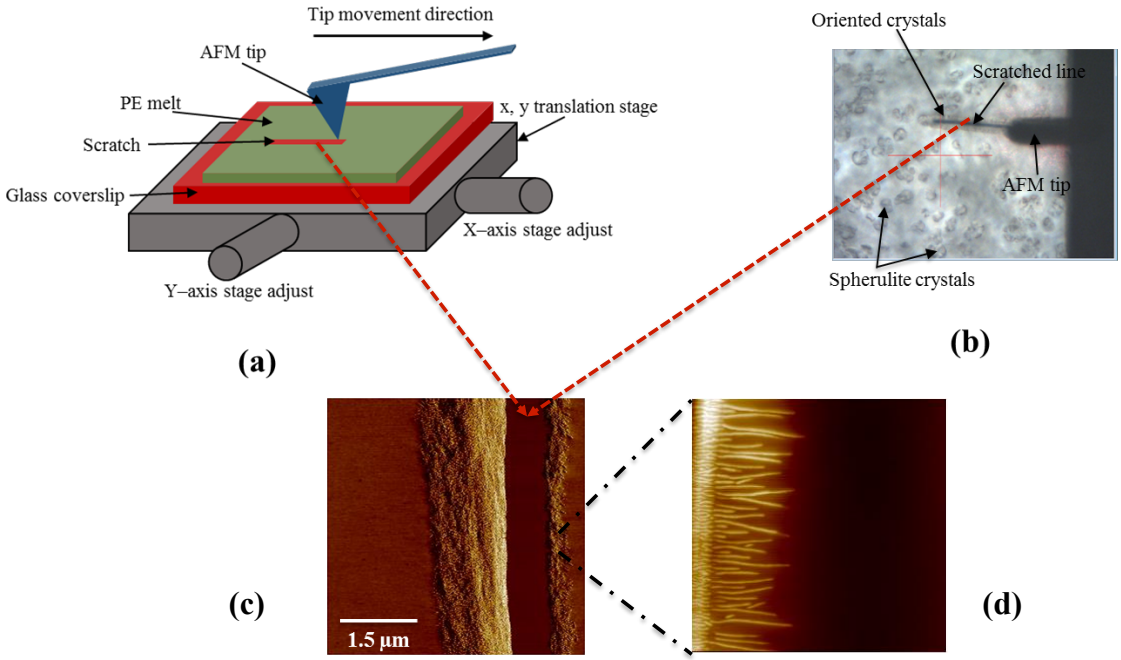

Figure 7.1: (a) Schematic diagram showing the experimental setup to enable the shear induced crystallization by means of the AFM tip, (b) optical image showing the oriented crystals at the edge of the scratched line and spherulites in the rest of the film where no shear was applied, (c) AFM phase image of the scratched film, and (d) magnified view of (c) showing the resulting oriented PE crystals.

7.3. Results and Discussions

7.3.1. Orientation- Induced Crystallization of PE by AFM Tip

Figure **7.2** shows the PE film after using the AFM tip at 130 ºC to induce crystallization by shearing. As can be seen in Figure **7.2**, a large number of nuclei form rapidly on the edge of the scratch line. This is due to the orientation of the PE chains in the direction of the scratch, which causes the crystals to form perpendicularly to the shearing direction. No nuclei were observed in the rest of the film, however.

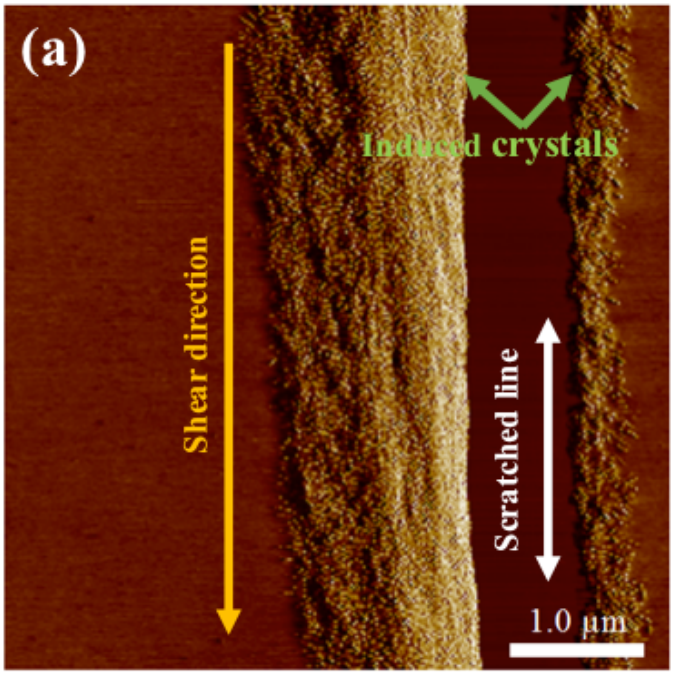

Figure 7.2: An AFM phase image showing the PE crystallization induced by the AFM tip at 130 ºC.

7.3.2. Crystallization Behaviour

After using the AFM tip to induce the PE crystals, the film was then cooled to the desired crystallization temperature in order to investigate the subsequent isothermal crystallization. The growth of oriented PE crystals was followed at the temperature range of 130–124 °C, at which the AFM was able to image the crystallization *in situ*. Below 124 °C, it was not possible to follow the crystal growth in real time, due to the large growth rate. Above 130 °C, no growth was observed over the several hours of the experiment, and the crystal tended to melt when kept at those high temperatures for a long time.

During the isothermal crystallization, similar behaviours to those described in Chapter 6 were observed, such as the pushing apart of neighbouring crystals, melting and changes in the orientation of crystals. These phenomena are presented and discussed below.

7.3.2.1. The Force of Crystallization

Due to the high density of nucleation at the edge of scratch line, a large number of edge-on crystals formed, and grew perpendicular to the scratch line (see Figure **7.3**).

Here, similar phenomena were observed to those described in the previous chapter, with crystals forcing their neighbouring crystals apart in order to grow between them. This similarity in behaviour was observed despite the different method used to induce crystallisation. Figure **7.3** and Figure **7.4** show two examples of such a situation. The highlighted crystals in Figure **7.3** represent the neighbouring crystals that were affected by the crystals that crystallized initially under this constraint. For example, the two blue and two green crystals that, in each case, constrained a middle crystal, can be seen to be forced apart by the middle crystal in order to provide more room for the latter to grow between them. The separation distance (red lines) between the two blue crystals, and between the two green crystals, became larger as the middle (constrained) crystals continued to grow. In the case of the two pink crystals, however, the constrained middle crystal was unable to move its neighbours apart, as in the two cases above. This could be because these two pink crystals were in turn constrained by other crystals, which prevented their movement.

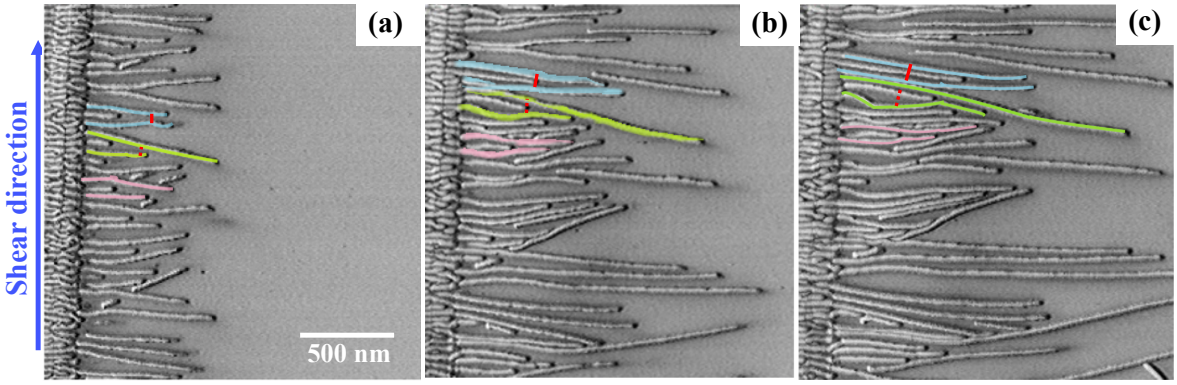

Figure 7.3: AFM phase images showing the growth of oriented crystals of PE at 130 °C. Some crystals are highlighted to aid the reader to follow the growth of those crystals. The blue arrow indicates the shearing area and its direction. The red lines and dashed lines indicate the distance separation between the two blue crystals and between the two green crystals, respectively. The black-to-white scale is 22º.

Figure **7.4** shows another example of a crystal pushing its neighbours apart to grow between them (the crystal between the two green crystals here). As the middle crystals continue to grow between these two crystals, the separation distance (red dashed arrows) between the two green crystals becomes larger.

Another interesting phenomenon observed here is that crystals can bend as other crystals join them, as indicated by the blue arrows in Figure **7.4**. This observation was

also presented in Chapter 6. A bend in lamellae during growth has previously been reported [69], but no explanation was given.

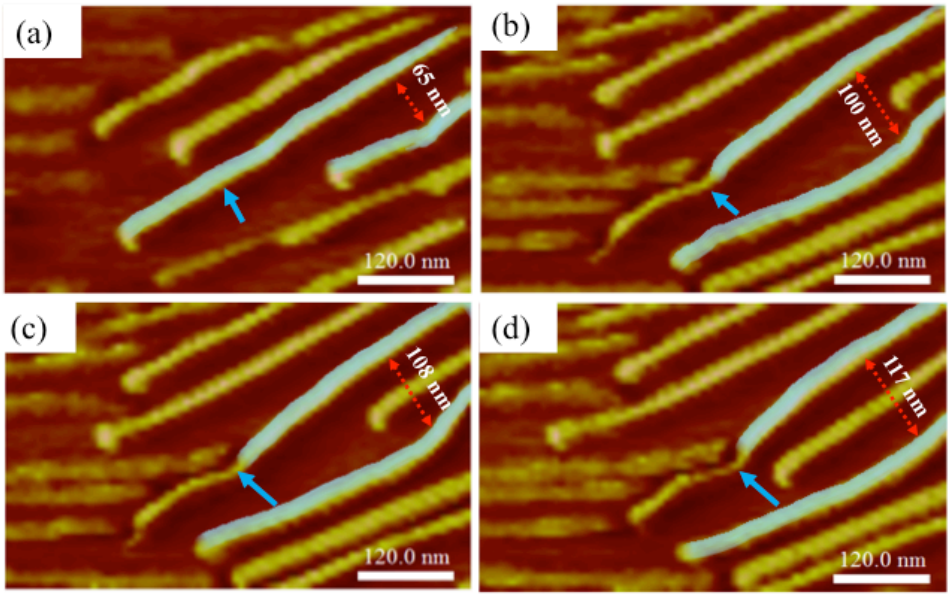

Figure 7.4: AFM phase images showing the movement and bending of some crystals due to the growth of others during isothermal crystallization at 129 °C. The red dashed arrows indicate the distance separation between the two green crystals and the blue arrows point out to the area where a crystal was bent by another crystal.

7.3.2.2. Melting During Crystallization

It was observed that some crystals melted during isothermal crystallization while the remainder continued growing (similar to what was observed in Chapter 6), as can be seen in Figure **7.5** (b-h) and their corresponding height images (d′, e′, f′ and h′). The arrows indicate the crystals that melted, each crystal indicated by different colour for ease of identification. The possible reasons behind this were discussed previously in Chapter 6, Section 4.3.4.

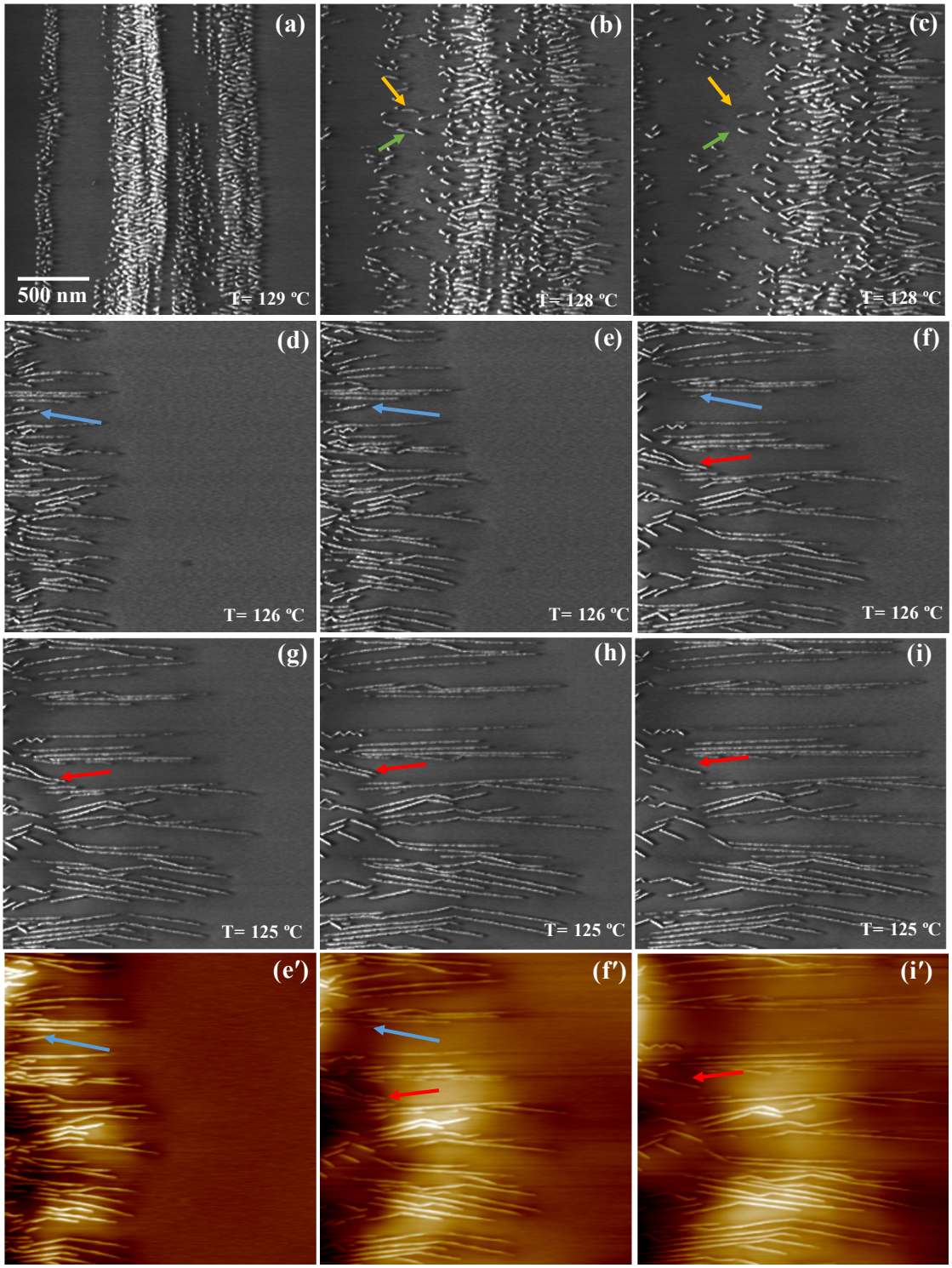

Figure 7.5: AFM (a-h) phase and (d′, e′, f′ and h′) height images showing the melting of some crystals during the crystallization of the oriented crystals, induced by AFM tip at 129-125 °C.

The crystallization behaviours presented above were similar to those observed in Chapter 6, where the crystallization was induced by tapping hard on the surface melt

using the AFM tip. For example, some crystals were moved or bent by other crystals and also some crystals melted during the isothermal crystallization.

7.3.2.3. Edge-on to Flat-on Transition

Figure **7.6** (a-c) shows the initial orientation of the induced crystals, which is edge-on, and they continued to grow edge-on for a while.

Figure **7.6** (d-l) shows the continued growth of crystals in the zone just at the left edge of the area shown in images (a-c). Interestingly, after this short distance from the scratch, the orientation of crystals changed to be flat-on and continued to grow in the same manner, which implies that the film was very thin.

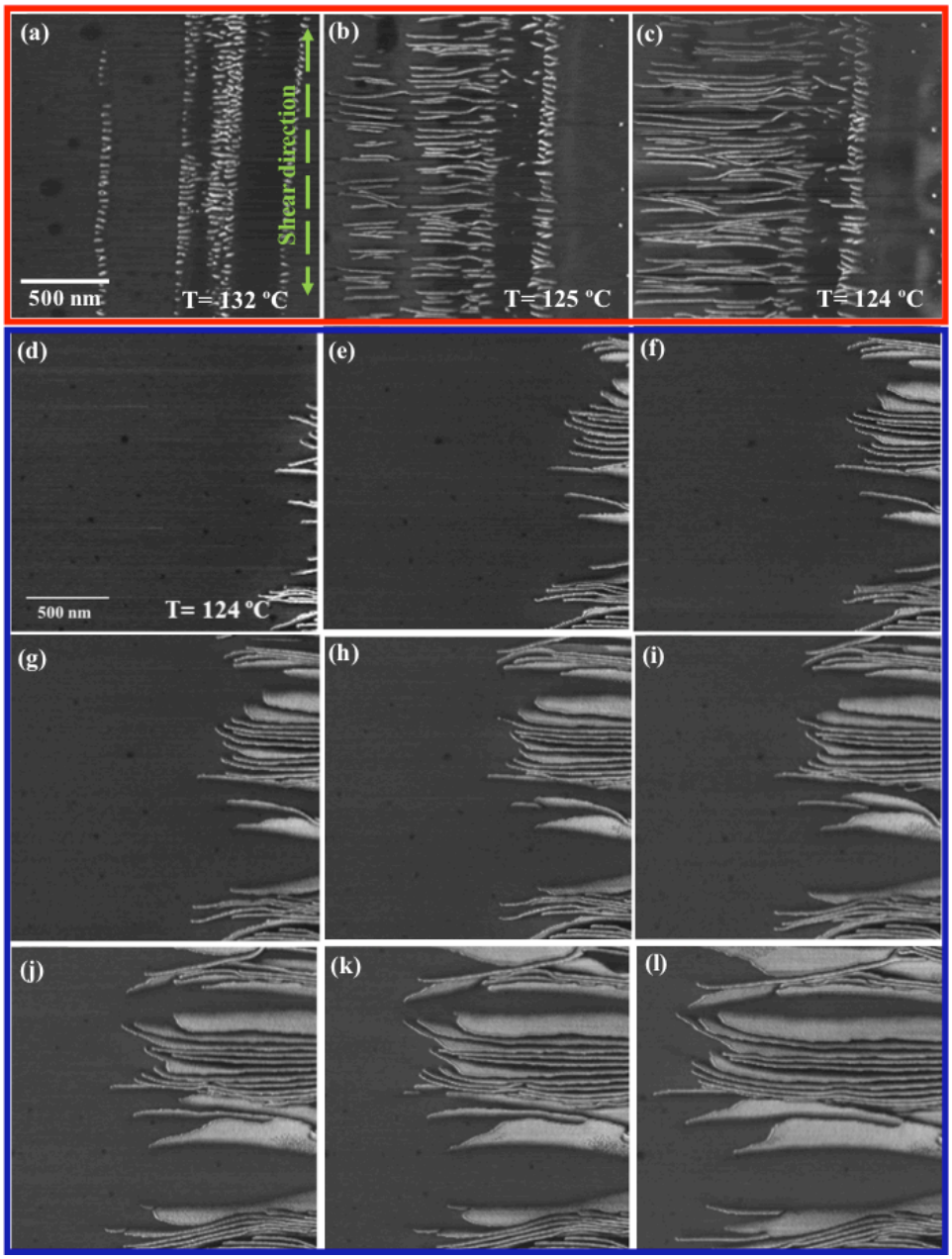

Figure 7.6: A series of AFM phase images showing the transition of orientation of PE crystals from being edge-on to flat-on as they grow further from the scratch line (at 124 ºC).

Although in almost all the conducted experiments it was observed that the initial crystals were oriented edge-on, at some later stages a transition from edge-on to flat-on was observed. Figure **7.7** shows two phase sequences and their corresponding height images, which represent a zoomed out view of the area that was scanned in

Figure **7.6**. This indicates the later stage of crystallization at 124 ºC where the transition from an edge-on to a flat-on orientation is clearly seen at a distance of ~ 1.5 µm from

the scratch line. This observation looks just like the twisting of lamellar crystals within a spherulite.

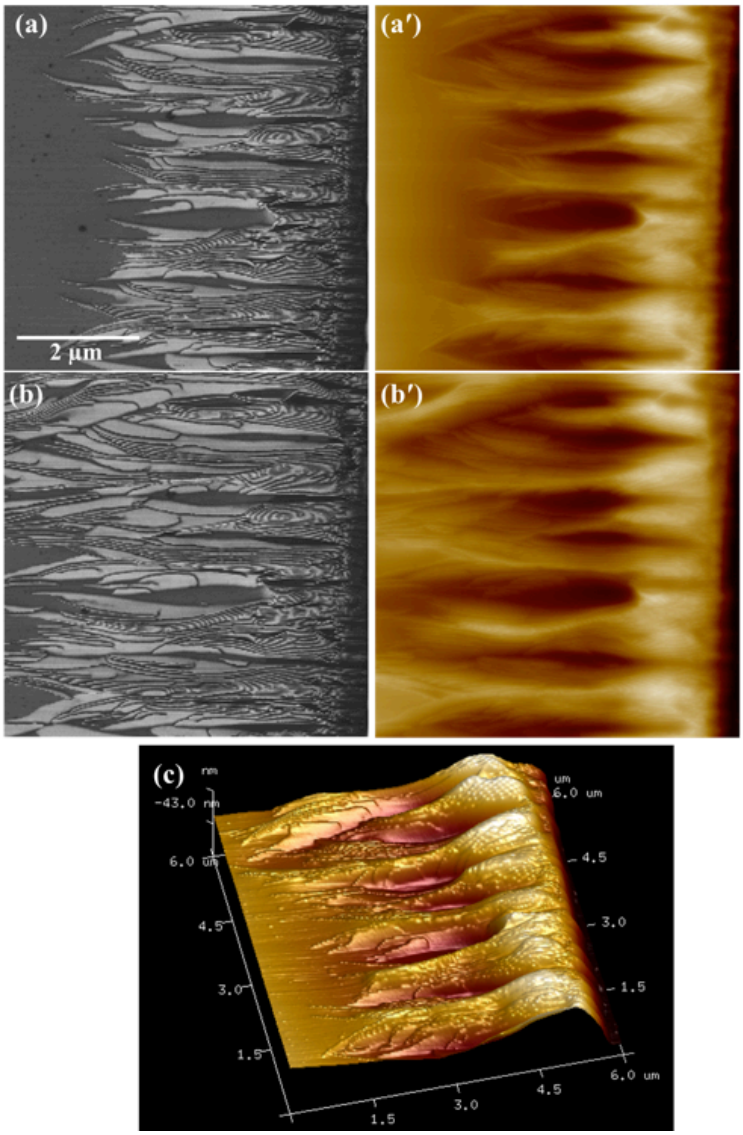

Figure 7.7: AFM phase sequences (a-b) and (a'-b') their corresponding height images showing the later stage of crystallization of PE crystals induced by shearing. (c) 3D image of (a′). These images are a zoomed view of the area that was being scanned in

Figure **7.6**.

This transition from edge-on to flat-on lamellae has also been reported in PCL [190] and isotactic polystyrene (i-PS) [96] systems.

The actual mechanism for this switching is not clear but a possible explanation for this transition here is that since the surface has been scratched by the AFM tip, most of the removed PE will be deposited at the edge of the scratched line which leads to the adjacent area becoming thicker than the rest of film. As the crystals grow some distance

from the scratched line (i.e. from thicker area to the thinner one) their orientation will be changed from being edge-on in the thicker area to being flat-on in the thinner area.

7.3.3. Growth Rates and Distribution

To obtain quantitative kinetic information about the crystallization behaviour, the growth rate of the crystals was examined as a function of temperature. To do this, individual lamellae were identified and labelled, as shown previously in Chapter 6, in order to follow their growth over the course of the experiment from one AFM image to the next. Measuring the growth rates of individual lamellae in this way allowed both the variation in the growth rate of individual lamellae, and the overall distribution of the lamellar growth rates to be investigated under isothermal crystallization conditions. Each lamella was followed until one of the following conditions was met: its growth had proceeded beyond the image area; its growth had terminated on another lamella; it had collided with impurities within the film and stopped growing.

In this section, the measurements of crystal length and their overall average growth rates as a function of time and temperature will be presented first, then the distribution of the PE crystal growth rates at different temperatures will be set out and discussed.

The measurements of crystal lengths and growth rates were done following the method previously explained in Chapter 5. Figure **7.8**-Figure **7.11** show the lengths of several PE crystals in micrometres versus time in seconds at crystallization temperatures ranging from 125–128 ºC.

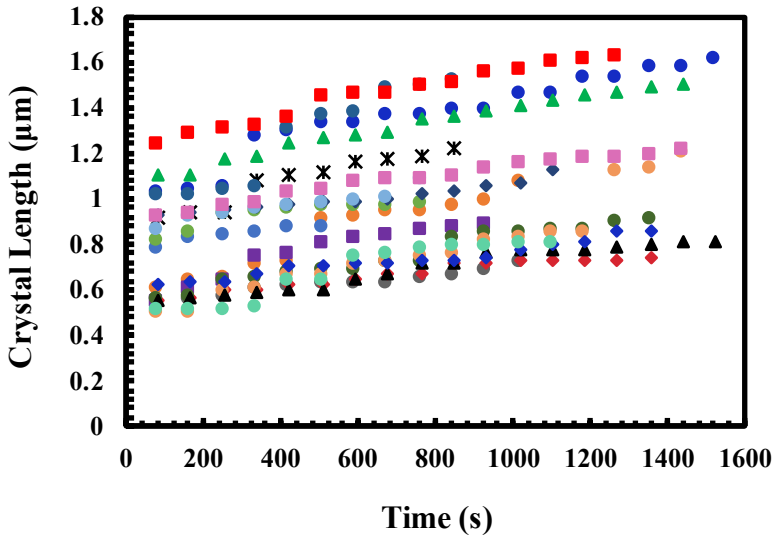

Figure 7.8: Graph showing the crystal growth lengths of a selection of nine crystals as a function of time at 125 °C.

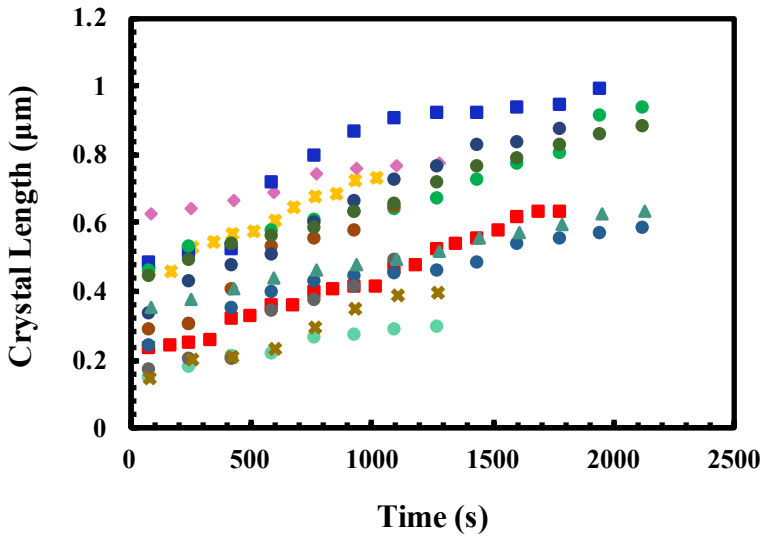

Figure 7.9: Graph showing the crystal growth lengths of a selection of nine crystals as a function of time at 126 °C

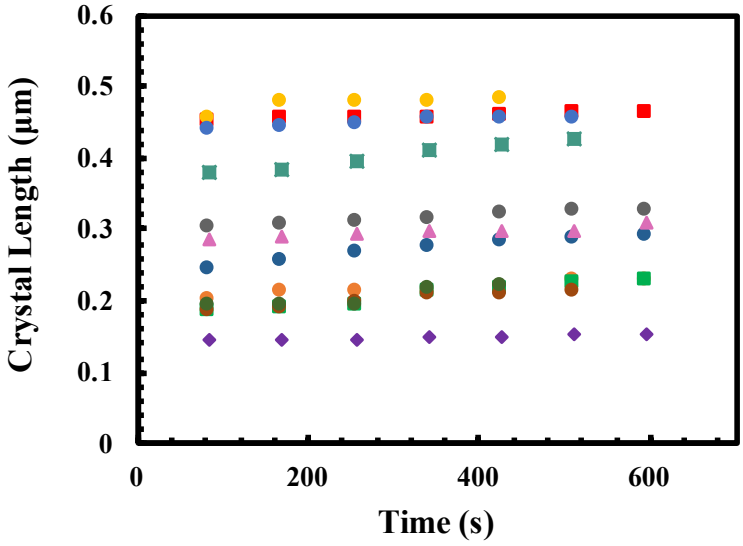

Figure 7.10: Graph showing the crystal growth lengths of a selection of nine crystals as a function of time at 127 °C.

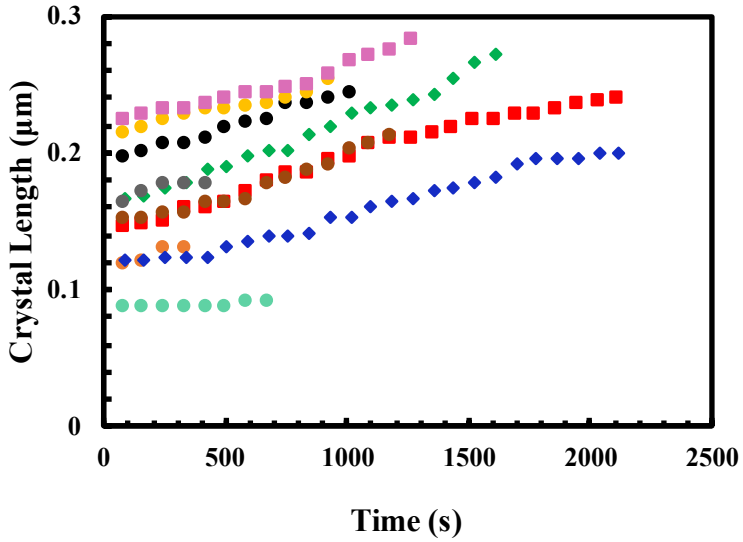

Figure 7.11: Graph showing the crystal growth lengths of a selection of nine crystals as a function of time at 128 °C.

From all the plots above it can be seen that the length of the crystals increased with time at each temperature, which is in agreement with the literature.

Figure **7.12** shows the average of the crystal lengths shown in Figure **7.8**- Figure **7.11** as a function of time. Obviously, the growth rate increases as the crystallization temperature decreases for PE.

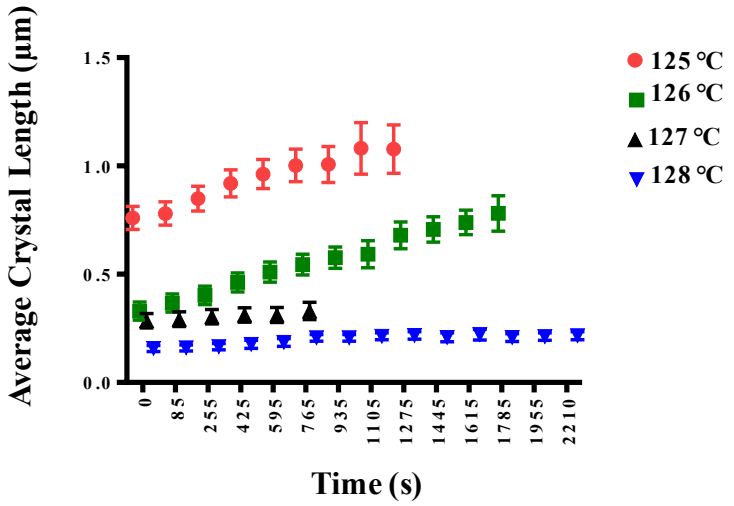

Figure 7.12: Graph showing the average length of PE crystals at 125-128 ºC as a function of time.

From the above data, the growth rate of crystals and the average growth rate were measured and compared as a function of temperature. It was found that the average growth rate decreases as the temperature increases, as can be seen in Table **7.1** and its corresponding graph in Figure **7.13**.

Table 7.1: The overall average growth rates of a number of PE oriented crystals growing at temperatures of 125–128 °C.

Crystallization temperature (°C)	Average growth rate (nms^{-1})
125	0.32
126	0.22
127	0.06
127.5	0.05

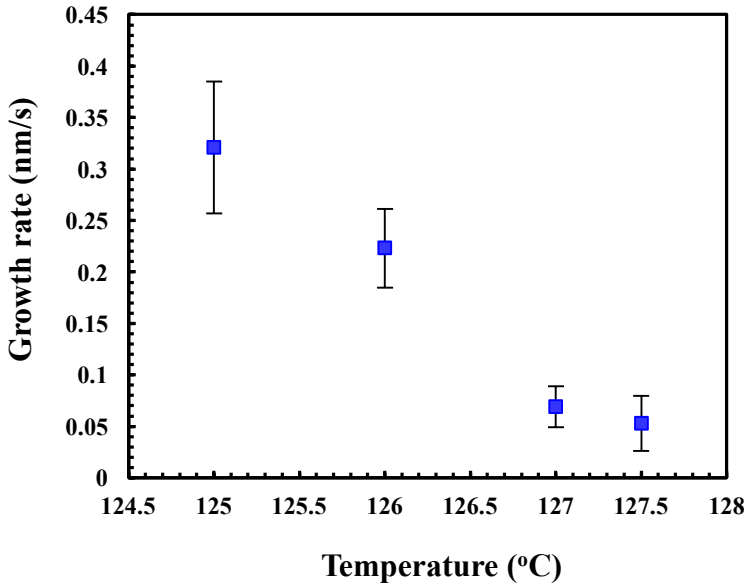

Figure 7.13: Graph showing the average growth rates of a number of individual crystals as a function of temperature.

The distribution of individual lamellar growth rates measured between consecutive frames was investigated by producing histograms of the growth rate data. Since different amounts of data were available for each of the experiments conducted, different bin sizes were used for the various histograms. The bin size for each histogram was selected in order to best represent the data; hence if more data was available for a particular plot this allowed smaller bin sizes to be used (relative to the overall width of the distribution). This information will be presented prior to each histogram. Four histograms reflecting the growth rate measured for PE crystals at 125 ºC, 126 ºC, 127 ºC, and 128 ºC, respectively, will be presented and discussed below.

Figure **7.14** (a) is a histogram of the measured growth rate data for PE crystallization at 125 °C, showing the distribution of individual lamellar growth rates where the bin size for the histogram is 0.1 nm/s. In this histogram, a total of 236 measured growth rates were used. Figure **7.14** (b) is a plot showing how the growth rates of these individual lamellae vary as a function of time. The measurements were taken from Figure **7.8**.

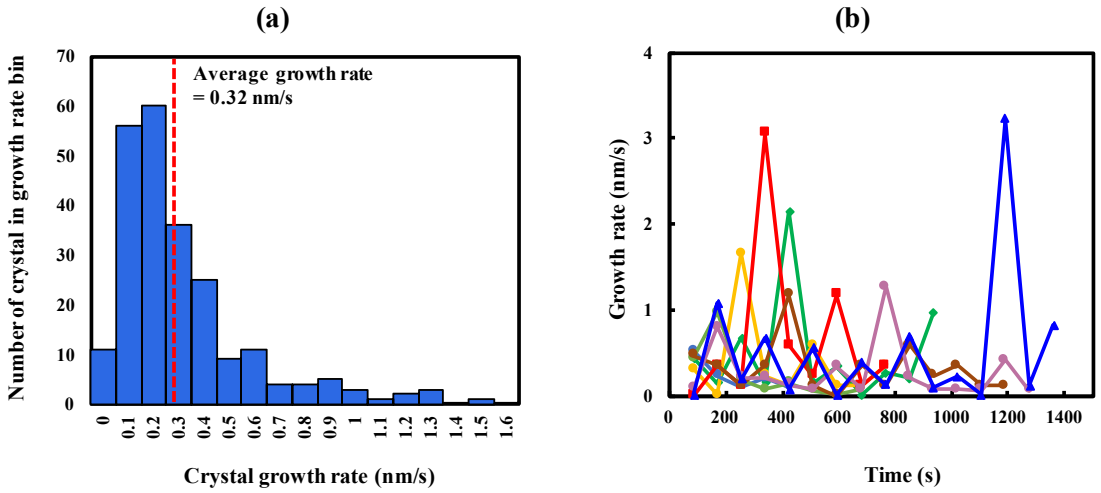

Figure 7.14: (a) Histogram of lamellar growth rates measured between consecutive AFM images for PE at an isothermal crystallization temperature of 125 °C. A total of 236 measurements are included in the histogram where the bin size of the displayed distribution is 0.1 nm/s. (b) A graph representing the growth rate variations of six individual crystals as a function of time at this temperature. The measurements were taken from Figure **7.8**.

Figure **7.15** (a) and (b) show the equivalent data as for Figure **7.14**, this time for PE crystallization at 126 °C, with a bin size of 0.1 nm/s based on a total of 102 measured growth rates.

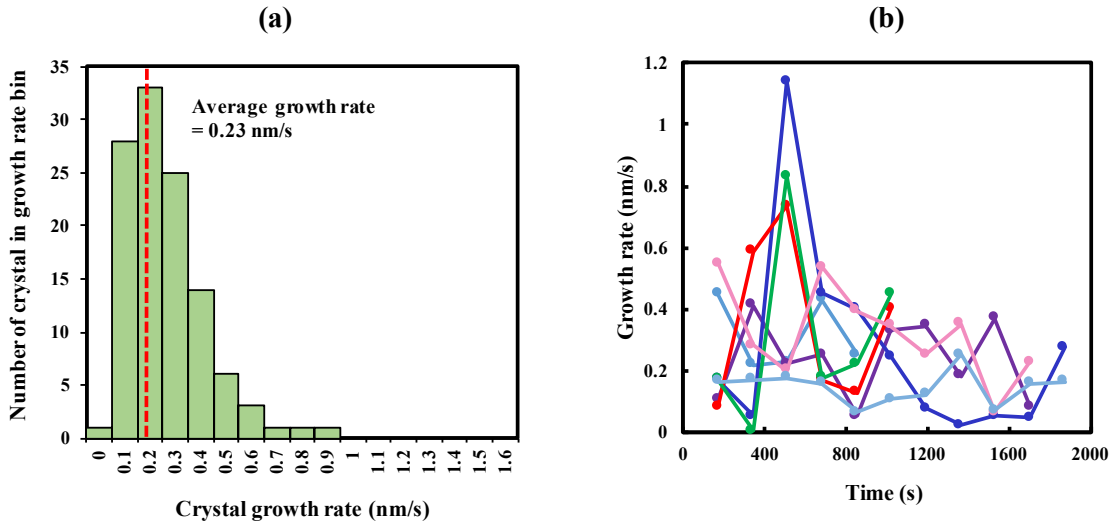

Figure 7.15: (a) Histogram of lamellar growth rates measured between consecutive AFM images for PE at an isothermal crystallization temperature of 126 °C. A total of 102 measurements are included in the histogram where the bin size of the displayed distribution is 0.1 nm/s (b) A graph representing the growth rate variations of six individual crystals as a function of time at this temperature. The measurements were taken from Figure **7.9**.

Figure **7.16** (a) and (b) show the equivalent data as for Figure **7.14**, this time for PE crystallization at 127 °C, with a bin size of 0.03 nm/s based on a total of 77 measured growth rates.

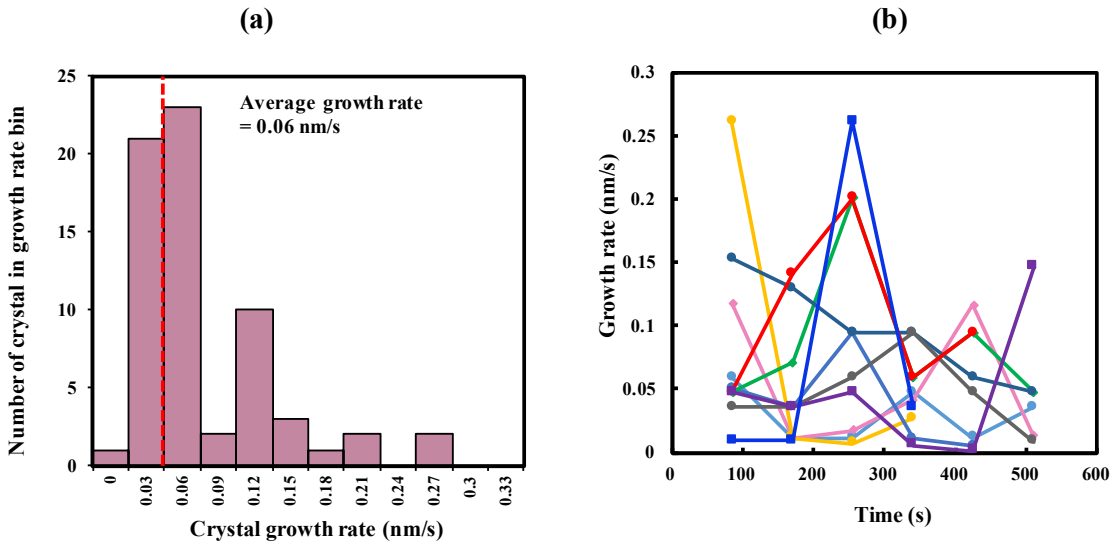

Figure 7.16: (a) Histogram of lamellar growth rates measured between consecutive AFM images for PE at an isothermal crystallization temperature of 127 °C. A total of 77 measurements are included in the histogram where the bin size of the displayed distribution is 0.03 nm/s. (b) A graph representing the growth rate variations of ten individual crystals as a function of time at this temperature. The measurements were taken from Figure **7.10**.

Figure **7.17** (a) and (b) show the equivalent data as for Figure **7.14**, this time for PE crystallization at 128 °C, with a bin size of 0.02 nm/s based on a total of 128 measured growth rates. The measurements were taken from Figure **7.11**.

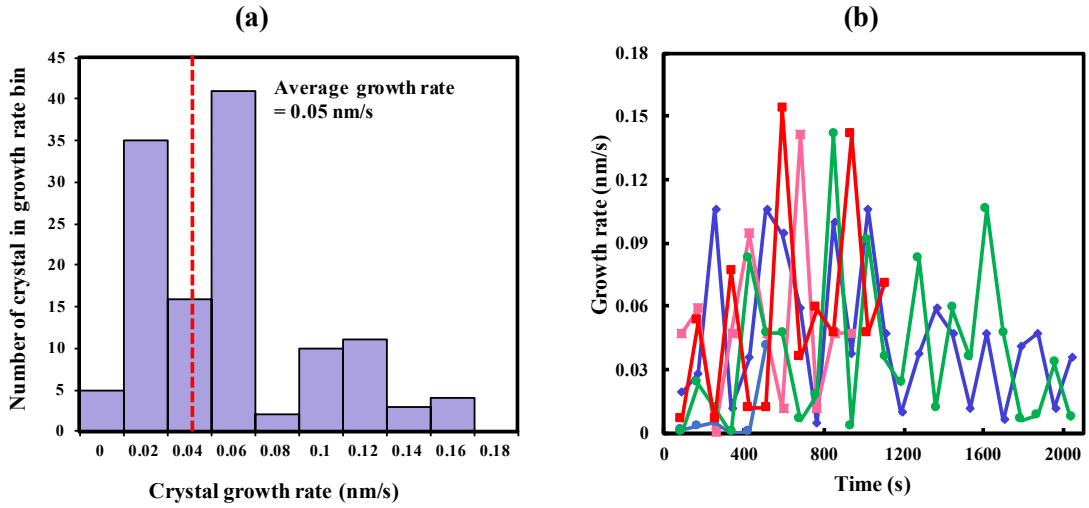

Figure 7.17: (a) Histogram of lamellar growth rates measured between consecutive AFM images for PE at an isothermal crystallization temperature of 128 °C. A total of 128 measurements are included in the histogram where the bin size of the displayed distribution is 0.02 nm/s. (b) A graph representing the growth rate variations of three individual crystals as a function of time at this temperature. The measurements were taken from Figure **7.11**.

Direct comparison between the four histograms reveals a large variation in the distribution of individual growth rates as a function of crystallization temperature. From these histograms it can be seen that even with only two degrees' difference in temperature, some of the crystals are still growing at a similar rate to the average. For instance, at 127 °C, some crystals grow at a rate of ~ 0.3 nm/s (Figure **7.16** (a)) which is not far from the average of the growth rates of crystals at 125 °C, which is 0.32 nm/s (Figure **7.14** (a)). Additionally, some crystals grow four times faster than the average at a particular temperature, as can be seen for example in Figure **7.14** (a), where some crystals grow at a rate of ~1.2 nm/s compared to the average of 0.32 nm/s. Likewise, at 126 °C, some crystals grow at a rate of 0.8 nm/s compared to the average at this temperature of 0.23 nm/s. The same pattern is evident in the histograms for the other temperatures. This indicates that some crystals grow very fast while others grow very slowly at the same temperature.

All of the plots showing growth rate variations for individual crystals display a variation of growth rates from crystal to crystal and as a function of time (see Figure **7.14** (b)- Figure **7.17** (b)). This is consistent with similar observations of non-constant growth rates for individual lamellae under isothermal conditions made by others [4, 9, 78, 190]. Such observations, however, are not compatible with current

polymer crystallization theories that, in general, predict a single constant crystallization rate at a constant temperature. It is not clear what gives rise to the variability observed experimentally in the growth rates of polymer crystals or how it can be accounted for theoretically.

7.4. Conclusion

The main purpose of the work presented in this chapter was to study the kinetics of flow-induced PE crystals at the level of a single lamella as a function of temperature with AFM. Shear flow was induced by scratching the PE melt with an AFM tip. Firstly, the induced crystallization behaviour was examined as a function of temperature. It was found that the crystallization behaviours in this work were similar to those in the previous chapter. These included some crystals that force their neighbours apart to provide more room to grow between them, and also some crystals that melted during the isothermal crystallization. This suggests that these behaviours could be general features for PE crystals or even for polymer crystallization in general. Furthermore, a high nucleation density of edge-on PE crystals oriented perpendicular to the flow direction was observed, although there was a transition from edge-on to flat-on lamellae beyond a certain distance from the edge of the scratched region.

Secondly, the kinetics of the individual crystals, which was the main focus of this chapter, was investigated as a function of time. The growth rates of individual crystals and the distribution of growth rates of these individual crystals were measured. It was found that the average growth rates increased as the crystallization temperatures decreased; but also that the rates fluctuated with time for each individual crystal. The distribution of the growth rates of individual crystals showed that there is a big variation in growth rates at any given crystallization temperature. These observations are in a good agreement with the observation of non-constant lamellar growth rates in some of the previous work on polymer systems. This implies that growth rate variations for individual lamellae may be a common feature in polymer melt crystallization. Further studies are therefore needed on other crystallizable polymer systems in order to confirm whether this observation is a general feature of polymer melt crystallization, as well as consideration of what causes these wide variations.

Chapter 8

Summary and Future Work

8.1. Summary

The direct observation of the crystallization process in polymers with high resolution and without damaging the sample, promises to make a significant contribution and improvement to knowledge in the field of polymer crystallization. This PhD thesis has presented a study into the crystallization of PE and PE containing block copolymer (E/MB) as a function of temperature. It has been shown that this can be achieved using AFM, and that this is a promising technique for the investigation of the crystallization process *in situ*, in real time, and with high resolution.

The direct observation of the isothermal crystallization process of PE presents some important scientific information. The aims of this study were to: 1) control the orientation of E/MB microdomains locally using the AFM tip; 2) examine the subsequent crystallization behaviour in these oriented domains, both *in situ* and with *ex situ* imaging, as a function of temperature; 3) investigate the behaviour of PE crystallization induced by shear using the AFM tip *in situ*, in real time, and; 4) examine the distribution of lamellar growth rates of PE under isothermal crystallization conditions.

The AFM tip was successfully used, for the first time, to orient the microdomains of a block copolymer locally and then to investigate the subsequent crystallization *in situ*. The AFM tip was also used to control the orientation of the cylindrical microdomains of E/MB effectively in different directions, according to its scan direction, before they crystallized. This enabled the direction of the crystals' growth to be defined relative to the block's interface. It was found that the number of defects reduced as the number of

oriented scans was increased. On subsequent isothermal crystallization in these pre-oriented microdomains, and depending on the thermal conditions examined, a change from fully confined crystallization to templated and breakout crystallization was observed. Confined behaviour of crystals was observed at very high supercooling, templated crystallization at lower supercooling, and a mixture of templated and breakout crystallization at the lowest supercooling. The difference in morphology, as well as behaviour, of crystals that grew parallel to the axes of the pre-existing cylinders, and of crystals that grew perpendicular to them was explored. It was found that the growth rates of the templated crystals were higher compared to the rates of crystals that grew against the melt structure. As the crystallization temperature increased, the overall crystallization rate, and the relative difference between the growth rates along the cylindrical microdomains and the growth rates against them decreased. This indicates that small variations in crystallization temperature can have pivotal effects on the crystallization process, including switching from being completely confined to largely breakout crystallization within just a small temperature range, with associated effects on the attributes and morphology of the product. It was also found that crystals can change their direction of growth from being perpendicular to the microdomains to being parallel to them, and that this transition was associated with a clear and significant increase in the crystal growth rate.

Oriented PE crystals were induced using two different methods. First, the AFM tip was successfully used to induce crystals locally by increasing the tapping force, and this was done by decreasing the amplitude setpoint of the AFM tip along a single line so as to initiate a contact with, and orient chains on, the sample surface (the same approach to that used to orient the E/MB domains in Chapter 4). Secondly, the surface of the molten PE was scratched by the AFM tip. In both cases, the initial induced crystals were observed to have only an edge-on orientation relative to the surface of the PE film (i.e. no flat-on orientation was observed). At later stages of crystal development, however, a transition from edge-on to flat-on orientation could occur. Furthermore, single crystals of PE were, for the first time, directly induced by the AFM tip without need for the kind of special treatments that have hitherto been described in the literature for inducing a single crystal from the melt.

Regardless of the approach used to induce PE crystals, similar behaviours were observed for the first time. These include some crystals that force their neighbours apart to provide more room to grow between them, and also some crystals that melted during the isothermal crystallization. This suggests that these behaviours could be general features for PE crystals, or even for polymer crystallization in general.

In addition to the abovementioned unusual behaviours of PE crystals, novel observations on the tip-induced oriented crystals of PE were observed during isothermal crystallization between 134 °C and 129 °C. Firstly, a few crystals were found to be deformed, or re-organized themselves as they grew, apparently in an effort to attain a lower energy state. Secondly, at later growth stages, some PE crystals appeared to clump together: i.e., as they grew, the gap between them reduced and even disappeared. This could be due to the transition in the orientation of the crystals from being edge-on to being flat-on, as their height increased. The height of these lamellae was measured and found to be non-linearly related with time. Thirdly, on interdigitation, the crystals exhibited similar habits when they approached another neighbouring crystal as those reported previously in the literature: i.e. two crystals could change their growth direction to avoid hitting each other; they could meet each other and therefore stop growing; they could join each other and become one crystal; or they could pass without meeting and continue growing. Additionally, one new habit was observed: the two crystals could meet and stop growing for a while before one of them changed its growth direction slightly, opening up room for growth and allowing it to accelerate. Fourthly, some crystals melted or disappeared during the isothermal crystallization suggesting that those crystals were unstable and relaxed back to the melt state.

Furthermore, the effect of nucleation density on the behaviour of the crystals was examined. It was found that as the nucleation density reduced, the crystals moved (rotated) as they grew. To investigate this further,, a single crystal was induced and its growth behaviour studied as a function of temperature. It was found that as the length of the crystal increased the amount of change in its angle increased.

Overall, no branching or spraying out was observed in the induced PE crystals, which means that the process would not eventually lead to the formation of spherulites. Additionally, on isothermal crystallization, there was no sign of the formation of new nuclei or crystals but only the development of the previously induced crystals with time.

This observation is consistent with the hypothesis of the dependence of nucleation on temperature.

The growth rates of individual PE crystals, and the distribution of the growth rates of individual crystals, were measured under isothermal conditions at different temperatures. It was found that the average growth rates increased as the crystallization temperatures decreased; but also that the rates fluctuated with time for each individual crystal in both the PE and E/MB systems, which is not accounted for by current polymer crystallization theories. The distribution of the growth rates of individual crystals showed that there is a big variation in growth rates as a function of supercooling. These observations are in line with some of the previous work on polymer systems that have also observed non-constant lamellar growth rates. These measurements demonstrate the need for a better theoretical understanding of the crystallization process in polymers so that such seemingly generic behaviour can be accounted for.

The current findings add to a growing body of literature on PE crystallization and on polymer crystallization generally.

8.1. Future Work

8.1.1. Further Study in Different Polymer Systems

This study of PE crystallization has demonstrated interesting behaviour such as crystals forcing their neighbours apart and re-organizing themselves as they grow. Exactly what causes these behaviours is still unknown, however. It would therefore be interesting to check whether similar phenomena can be observed in other crystallizable polymer systems. This could be done by inducing crystals using the same approach used in this project and then investigating the behaviour of the subsequent growth of these induced crystals. If similar observations are found this could mean that these phenomena are a general feature for polymer crystallization from melt.

Moreover, it would be interesting to repeat the experiment on PE but using thin films (with different range of thicknesses) in order to examine the relationship between film thickness and crystallization behaviour, especially in terms of whether the orientation of

the lamellae in thin films is initially edge-on, as in the relatively thick films used in the current study, or flat-on.

The observations made in this research of fluctuations in the growth rates of the individual lamellae, and their distributions at any given crystallization temperature, are limited to the PE system investigated in this study. Further studies are therefore needed on other crystallizable polymer systems in order to confirm whether this observation is a general feature of polymer melt crystallization, as well as to help understand what causes these wide variations.

Furthermore, well-ordered microdomains of block copolymers were obtained in this study by scanning over the area of interest with the AFM tip so as to provide a very quick and simple approach to define the direction of growing crystals relative to the interface of blocks, and thus making it easier to assess the behaviour of the subsequent crystallization. It would therefore be of interest to apply the same approach used in this study to control the microdomain orientation of other types of block copolymer and even to study the crystallization behaviour in those systems. This will make it easier to determine the impact of microdomain orientation on growth, which in turn could give insights into block copolymer crystallization in general.

8.1.2. Continued Development of the AFM Technique

Over the past 60 years there has been extensive debate and theoretical development on the physical processes that occur during polymer crystallization. Fundamental questions such as why are crystals thinner than expected from equilibrium thermodynamics, how chains fold back to re-enter the same crystal, and the roles played by ‘loose loops’ and ‘tie chains’ in the mechanical properties of bulk films, still await definitive answers. A lack of direct imaging data at the molecular scale has made it difficult to reach a consensus on these issues which are at the heart of our understanding of this important class of materials.

This study has shown that following crystallization *in situ* in real time is crucial in examining the internal structure and formation mechanisms during crystallization. Watching the crystal growth *in situ* at the lamellar scale with high-resolution AFM, and

combining this with molecular resolution *ex situ* images of crystalline regimes could allow a better understanding of how morphological development is linked to molecular scale conformational changes. Continuing advances in AFM, particularly in the area of high speed scanning and high resolution imaging, could allow further investigation of the crystallization process *in situ*, in real time, even in more complex polymers.

In addition, many potential uses of block co-polymers have been proposed for different nanotechnologies, based principally on their ability to form interesting patterns. The main challenge in the use of block co-polymers, however, lies in the control of microdomains. Achievement of precise microdomain location and orientation, and the elimination of various defects, requires the introduction of external fields during the processing step. In this study, the AFM tip technique has shown its ability to control some parameters, and to manipulate and guide the microstructure of block co-polymers. It is important now to continue to experiment with this technique in other more complex block co-polymer systems.

References

[1] A. Keller, "A note on single crystals in polymers: Evidence for a folded chain configuration," *Philos. Mag.*, vol. 2, no. 21, pp. 1171–1175, 1957.

[2] G. Binnig and C. F. Quate, "Atomic Force Microscope," *Phys. Rev. Lett.*, vol. 56, no. 9, pp. 930–933, 1986.

[3] J. M. Schultz and M. J. Miles, "AFM study of morphological development during the melt-crystallization of poly(ethylene oxide)," *J. Polym. Sci. Part B Polym. Phys.*, vol. 36, no. 13, pp. 2311–2325, 1998.

[4] J. K. Hobbs, A. D. L. Humphris, and M. J. Miles, "In-situ atomic force microscopy of polyethylene crystallization. 1. Crystallization from an oriented backbone," *Macromolecules*, vol. 34, no. 16, pp. 5508–5519, Jul. 2001.

[5] J. K. Hobbs and M. J. Miles, "Direct observation of polyethylene shish-kebab crystallization using in-situ atomic force microscopy," *Macromolecules*, vol. 34, no. 3, pp. 353–355, Jan. 2001.

[6] J. K. Hobbs and R. a. Register, "Imaging Block Copolymer Crystallization in Real Time with the Atomic Force Microscope," *Macromolecules*, vol. 39, no. 2, pp. 703–710, Jan. 2006.

[7] W. S. Chow, Z. A. Mohd Ishak, and J. Karger-Kocsis, "Atomic force microscopy study on blend morphology and clay dispersion in polyamide-6/polypropylene/organoclay systems," *J. Polym. Sci. Part B Polym. Phys.*, vol. 43, no. 10, pp. 1198–1204, 2005.

[8] G. J. Vancso, L. G. M. Beekmans, R. Pearce, D. Trifonova, and J. Varga, "From microns to nanometers: Morphology development in semicrystalline polymers by scanning force microscopy," *J. Macromol. Sci.*, vol. B38, no. 5–6, pp. 491–503, 1999.

[9] J. K. Hobbs, T. J. McMaster, M. J. Miles, and P. J. Barham, "Direct observations of the growth of spherulites of poly(hydroxybutyrate-co-valerate) using atomic

force microscopy," *Polymer (Guildf).*, vol. 39, no. 12, pp. 2437–2446, Jan. 1998.

[10] L. Zhu, S. Z. D. Cheng, B. H. Calhoun, Q. Ge, R. P. Quirk, E. L. Thomas, B. S. Hsiao, F. Yeh, and B. Lotz, "Phase structures and morphologies determined by self-organization, vitrification, and crystallization: confined crystallization in an ordered lamellar phase of PEO-b-PS diblock copolymer," *Polymer (Guildf).*, vol. 42, no. 13, pp. 5829–5839, 2001.

[11] F. S. Bates and G. H. Fredrickson, "Block copolymer thermodynamics: theory and experiment.," *Annu. Rev. Phys. Chem.*, vol. 41, no. 1, pp. 525–557, 1990.

[12] Y. Chen, H. Cui, L. Li, Z. Tian, and Z. Tang, "Controlling micro-phase separation in semi-crystalline/amorphous conjugated block copolymers," *Polym. Chem.*, vol. 5, no. 15, p. 4400, 2014.

[13] U. W. Gedde, *Polymer Physics*. Springer Netherlands, 2013.

[14] L. C. Sawyer and D. T. Grubb, *Polymer Microscopy*. Dordrecht: Springer Netherlands, 1987.

[15] J. J. Breen and J. E. Stephens, "'The Glass Transition Temperature and the mechanical properties of asphalt.' Report No. JHR-67-16." p. 6, 1967.

[16] R. O. Ebewele, *Polymer Science and Technology*. CRC press., 2000.

[17] J. Li, W. Li, H. Cheng, L. Zhang, Y. Li, and C. C. Han, "Early stages of nucleation and growth in melt crystallized polyethylene," *Polymer (Guildf).*, vol. 53, no. 12, pp. 2315–2319, 2012.

[18] M. Muthukumar, *Nucleation in polymer crystallization*, vol. 128. 2004.

[19] G. Reiter and G. R. Strobl, *Progress in Understanding of Polymer Crystallization*. Springer, Berlin, Heidelberg, 2007.

[20] G. Qipeng, *Polymer morphology: principles, characterization, and processing*. Hoboken, NJ, USA: John Wiley & Sons, Inc, 2016.

[21] B. Wunderlich, *Macromolecular Physics: Crystal Nucleation, Growth, Annealing*. New York: Academic Press, 1976.

[22] R. Boistelle and J. P. Astier, "Crystallization mechanisms in solution," *J. Cryst. Growth*, vol. 90, no. 1–3, pp. 14–30, 1988.

[23] P. G. Vekilov, “Nucleation of protein crystals,” *Prog. Cryst. Growth Charact. Mater.*, vol. 62, no. 2, pp. 136–154, 2016.

[24] E. Saridakis and N. E. Chayen, “Towards a ‘universal’ nucleant for protein crystallization,” *Trends Biotechnol.*, vol. 27, no. 2, pp. 99–106, 2009.

[25] G. R. Mitchell and A. Tojeira, *Controlling the Morphology of Polymers: Multiple Scales of Structure and Processing*. Springer International Publishing, 2016.

[26] J. D. Hoffman and R. L. Miller, “Kinetic of crystallization from the melt and chain folding in polyethylene fractions revisited: theory and experiment,” *Polymer (Guildf).*, vol. 38, no. 13, pp. 3151–3212, 1997.

[27] J. I. Lauritzen and J. D. Hoffman, “Theory of formation of polymer crystals with folded chains in dilute solution,” *J. Res. Natl. Bur. Stand. Sect. A Phys. Chem.*, vol. 64A, no. 1, p. 73, 1960.

[28] J. D. Hoffman and J. I. Lauritzen, “Crystallization of Bulk Polymers With Chain Folding : Theory of Growth of Lamellar Spherulites,” *J. Res. Natl. Bur. Stand. - A. Phys. Chem.*, vol. 65, no. 4, p. 297, 1961.

[29] D. C. Bassett, *Principles of polymer morphology*. New York, 1981.

[30] J. J. Point, “Crystal growth rate as a function of molecular weight in polyethylene crystallized from the melt: an evaluation of the kinetic theory of polymer crystallization,” vol. 30, no. 1, pp. 2292–2296, 1989.

[31] S. Z. D. Cheng, J. J. Janimak, and A. Zhang, “Regime Transitions in Fractions of Isotactic Polypropylenet,” *Macromolecules*, vol. 23, no. 1, pp. 298–303, 1990.

[32] A. Keller and H. W. H. Kolnaar, *Flow-Induced Orientation and Structure Formation*. Materials science and technology, 1997.

[33] P. H. Till, “The growth of single crystals of linear polyethylene,” *J. Polym. Sci.*, vol. 24, no. 106, pp. 301–306, 1957.

[34] E. . Fischer, “Stufen-und spira1formiges Kristallwachstum bei Hochpolymeren,” *Z. Naturforsch*, vol. 12, no. 9, pp. 753–754, 1957.

[35] K. H. Storks, “An Electron Diffraction Examination of Some Linear High

Polymers," *J. Am. Chem. Soc.*, vol. 60, no. 8, pp. 1753–1761, 1938.

[36] A. Toda and A. Keller, "Growth of polyethylene single crystals from the melt: Morphology," *Colloid Polym. Sci.*, vol. 271, no. 4, pp. 328–342, 1993.

[37] L. Hoffman, "Theoretical Aspects of Polymer Crystallization with Chain Folds: Bulk Polymers," *Polym. Eng. Sci.*, vol. 4, no. 4, pp. 315–362, 1964.

[38] P. . Flory, "On the Morphology of the Crystalline State in Polymers," vol. 84, pp. 2857–2867, 1962.

[39] Y. Wang, S. Ge, M. Rafailovich, J. Sokolov, Y. Zou, H. Ade, J. Lüning, A. Lustiger, and G. Maron, "Crystallization in the thin and ultrathin films of poly(ethylene-vinyl acetate) and linear low-density polyethylene," *Macromolecules*, vol. 37, no. 9, pp. 3319–3327, 2004.

[40] Y. Wang, C. M. Chan, K. M. Ng, and N. Li, "What controls the lamellar orientation at the surface of polymer films during crystallization?," *Macromolecules*, vol. 41, no. 7, pp. 2548–2553, 2008.

[41] C. Chan and L. Li, "Direct Observation of the Growth of Lamellae and Spherulites by AFM," vol. 188, no. 1, pp. 1–41, 2005.

[42] D. R. Norton and A. Keller, "The spherulitic and lamellar morphology of melt-crystallized isotactic polypropylene," *Polymer (Guildf).*, vol. 26, no. 5, pp. 704–716, 1985.

[43] L. Gránásy, T. Pusztai, T. Börzsönyi, G. I. Tóth, G. Tegze, J. A. Warren, T. Pusztai, T. Börzsönyi, G. I. Tóth, G. Tegze, and J. A. Warren, "Polycrystalline patterns in far-from-equilibrium freezing : a phase field study," *Philos. Mag.*, vol. 68, no. 24, pp. 3757–3778, 2006.

[44] Y.-G. Lei, C.-M. Chan, Y. Wang, K.-M. Ng, Y. Jiang, and L. Lin, "Growth process of homogeneously and heterogeneously nucleated spherulites as observed by atomic force microscopy," *Polymer (Guildf).*, vol. 44, no. 16, pp. 4673–4679, 2003.

[45] K. Izumi, G. Ping, A. Toda, H. Miyaj, M. Hashimoto, Y. Miyamoto, and Y. Nakagawa, "Atomic force microscopy of isotactic polystyrene crystals," *Jpn. J. Appl. Phys.*, vol. 33, no. 11B, pp. L1628–L1630, 1994.

[46] H. D. Keith and F. J. Padden, “Spherulitic crystallization from the melt. I. Fractionation and impurity segregation and their influence on crystalline morphology,” *J. Appl. Phys.*, vol. 35, no. 4, pp. 1270–1285, 1964.

[47] B. Crist and J. M. Schultz, “Polymer spherulites: A critical review,” *Prog. Polym. Sci.*, vol. 56, pp. 1–63, 2016.

[48] F. Bernauer, “Gedrillte Kristalle,” *Bontraeger*, 1929.

[49] K. Okano, “Note on the lamellar twist in polymer spherulites,” *Jpn. J. Appl. Phys.*, vol. 3, no. 6, pp. 351–353, 1964.

[50] M. Herner, “Note on the origin of twisting orientation in fibrillar crystals,” *Polym. Sci.*, vol. 31, no. 156, pp. 4–7, 1961.

[51] H. D. Keith and F. J. Padden, “Twisting orientation and the role of transient states in polymer crystallization,” *Polymer (Guildf).*, vol. 25, no. 1, pp. 28–42, 1984.

[52] A. J. Owen, “A note on twist-banding in spherulites of poly(3-hydroxbutyrate),” vol. 38, no. 14, pp. 3705–3708, 1997.

[53] A. J. Pennings, “Fractionation of polymers by crystallization from solutions,” vol. 16, no. 3, pp. 1799–1812, 1967.

[54] A. J. Pennings, J. M. A. . van der mark, and H. C. Booij, “Hydrodynamically Induced Crystallization of Polymers From Solution II. The effect of secondary flow,” *Polymer (Guildf).*, vol. 236, no. 2, pp. 99–111, 1970.

[55] A. Keller, “Unusual Orientation Phenomena in Polyethylene Interpreted in Terms of the Morphology,” *Polym. Sci.*, vol. 15, no. 79, pp. 31–49.

[56] R. C. Savage, N. Mullin, and J. K. Hobbs, “Molecular Conformation at the Crystal–Amorphous Interface in Polyethylene,” *Macromolecules*, vol. 48, no. 17, pp. 6160–6165, 2015.

[57] F. S. Bates and G. H. Fredrickson, “Block Copolymers—Designer Soft Materials,” *Phys. Today*, vol. 52, no. 2, pp. 32–38, 1999.

[58] I. W. Hamley, *The Physics of Block Copolymers (Oxford Science Publications)*, vol. 19. New York: Oxford University Press, 1999.

[59] M. W. Matsen and F. S. Bates, “Unifying weak- and strong-segregation block copolymer theories,” *Macromolecules*, vol. 29, no. 4, pp. 1091–1098, 1996.

[60] I. W. Hamley, *Developments in Block Copolymer Science and Technology*. Chichester, UK: John Wiley & Sons, Ltd, 2004.

[61] Frank S . Bates, “Polymer-Polymer Phase Behavior,” *Adv. Sci.*, vol. 251, no. 4996, pp. 898–905, 1991.

[62] I. W. Hamley, *The Physics of Block Copolymers*. Oxford University Press, 1998.

[63] W. Hu, *Polymer physics: a molecular approach*. Springer Science & Business Media, 2012.

[64] L. Leibler, “Theory of Microphase Separation in Block Copolymers,” *Macromolecules*, vol. 13, no. 6, pp. 1602–1617, 1980.

[65] F. S. Bates and G. H. Fredrickson, “Block Copolymers—Designer Soft Materials,” *Phys. Today*, vol. 52, no. 2, pp. 32–38, 1999.

[66] C. Park, J. Yoon, and E. L. Thomas, “Enabling nanotechnology with self assembled block copolymer patterns,” *Polymer (Guildf).*, vol. 44, no. 22, pp. 6725–6760, 2003.

[67] S. Naylor, A. J. Ryan, W. Bras, D. H. Adamson, L. J. Fetters, P. Rangardan, and R. Register, “Dynamics of Structure Formation in Crystallizable Block Copolymers,” *Macromolecules*, vol. 28, no. 5, pp. 1422–1428, 1995.

[68] Y. Loo, R. A. Register, and A. J. Ryan, “Modes of Crystallization in Block Copolymer Microdomains : Breakout , Templated , and Confined,” pp. 2365–2374, 2002.

[69] L. Li, C.-M. Chan, J.-X. Li, K.-M. Ng, K.-L. Yeung, and L.-T. Weng, “A Direct Observation of the Formation of Nuclei and the Development of Lamellae in Polymer Spherulites,” *Macromolecules*, vol. 32, no. 24, pp. 8240–8242, 1999.

[70] Y.-G. Lei, C.-M. Chan, J.-X. Li, K.-M. Ng, Y. Wang, Y. Jiang, and L. Li, “The Birth of an Embryo and Development of the Founding Lamella of Spherulites As Observed by Atomic Force Microscopy,” *Macromolecules*, vol. 35, no. 18, pp. 6751–6753, 2002.

[71] H. Schönherr, R. M. Waymouth, and C. W. Frank, "Nucleation and Crystallization of Low-Crystallinity Polypropylene Followed in Situ by Hot Stage Atomic Force Microscopy," *Macromolecules*, vol. 36, no. 7, pp. 2412–2418, 2003.

[72] L. Kailas, C. Vasilev, J. Audinot, H.-N. Migeon, and J. K. Hobbs, "A Real-Time Study of Homogeneous Nucleation , Growth , and Phase Transformations in Nanodroplets of Low Molecular Weight Isotactic Polypropylene Using AFM," *Macromolecules*, vol. 40, no. 20, pp. 7223–7230, 2007.

[73] B. Vonnegut, "Variation with temperature of the nucleation rate of supercooled liquid tin and water drops," vol. 3, no. 6, pp. 563–569, 1948.

[74] M. Massa and K. Dalnoki-Veress, "Homogeneous Crystallization of Poly(Ethylene Oxide) Confined to Droplets: The Dependence of the Crystal Nucleation Rate on Length Scale and Temperature," *Phys. Rev. Lett.*, vol. 92, no. 25, p. 255509, 2004.

[75] M. Massa, J. Carvalho, and K. Dalnoki-Veress, "Confinement Effects in Polymer Crystal Nucleation from the Bulk to Few-Chain Systems," *Phys. Rev. Lett.*, vol. 97, no. 24, p. 247802, 2006.

[76] J. Zhao, B. Xing, Z. Peng, and J. Zhang, "A real-time AFM study on crystal nucleation and growth in nanodroplets of isotactic polypropylene," *Chinese J. Polym. Sci.*, vol. 31, no. 9, pp. 1310–1320, 2013.

[77] R. Pearce and G. J. Vancso, "Observations of crystallization and melting in poly(ethylene oxide)/poly(methyl methacrylate) blends by hot-stage atomic-force microscopy," *J. Polym. Sci. Part B Polym. Phys.*, vol. 36, no. 14, pp. 2643–2651, 1998.

[78] R. Pearce and G. J. Vancso, "Real-time imaging of melting and crystallization in poly(ethylene oxide) by atomic force microscopy," *Polymer (Guildf).*, vol. 39, no. 5, pp. 1237–1242, 1998.

[79] L. Li, C.-M. Chan, K. L. Yeung, J.-X. Li, K.-M. Ng, and Y. Lei, "Direct Observation of Growth of Lamellae and Spherulites of a Semicrystalline Polymer by AFM," *Macromolecules*, vol. 34, no. 2, pp. 316–325, 2001.

[80] R. Pearce and G. J. Vancso, “Imaging of Melting and Crystallization of Poly (ethylene oxide) in Real-Time by Hot-Stage Atomic Force Microscopy,” vol. 9297, no. 97, pp. 5843–5848, 1997.

[81] J. Hobbs, “in Situ Afm of Polymer Crystallization,” *Chinese J. Polym. Sci.*, vol. 21, no. 2, pp. 135–140, 2003.

[82] J. K. Hobbs, N. Mullin, C. H. M. Weber, O. E. Farrance, and C. Vasilev, “‘Watching’ processes in soft matter with SPM,” *Mater. Today*, vol. 12, no. 7–8, pp. 26–33, 2009.

[83] N. Mullin and J. K. Hobbs, “Direct Imaging of Polyethylene Films at Single-Chain Resolution with Torsional Tapping Atomic Force Microscopy,” *Phys. Rev. Lett.*, vol. 107, no. 19, p. 197801, 2011.

[84] L. G. M. Beekmans and G. J. Vancso, “Real-time crystallization study of poly(epsilon-caprolactone) by hot-stage atomic force microscopy,” *Polymer (Guildf).*, vol. 41, no. 25, pp. 8975–8981, 2000.

[85] S. N. Magonov and D. H. Reneker, “Characterization of Polymer Surfaces With Atomic Force Microscopy,” *Annu. Rev. Mater. Sci.*, vol. 27, no. 1, pp. 175–222, 1997.

[86] E. Section, “Atomic Force Microscopy Visualization of Morphology and Nanostructure of an Ultrathin Layer of Polyethylene during Melting and Crystallization,” *Langmuir*, vol. 16, no. 10, pp. 3549–3552, 2000.

[87] D. Zhu, X. Shou, Y. Liu, E. Chen, and S. Z. Cheng, “AFM-tip-induced crystallization of poly(ethylene oxide) melt droplets,” *Front. Chem. China*, vol. 2, no. 2, pp. 174–177, 2007.

[88] “orintation by AFM 1992.pdf.” .

[89] E. Hamada and R. Kaneko, “Micro-tribological evaluations of a polymer surface by atomic force microscopes,” *Ultramicroscopy*, vol. 44, pp. 184–190, 1992.

[90] J. . Pickering and G. . Vancso, “On the formation of oriented nanometer scale patterns on amorphous polymer surfaces studied by atomic force microscopy,” *Appl. Surf. Sci.*, vol. 148, no. 3–4, pp. 147–154, 1999.

[91] R. N. Leach, F. Stevens, C. Seiler, S. C. Langford, and J. T. Dickinson, "Nanometer-Scale Solvent-Assisted Modification of Polymer Surfaces Using the Atomic Force Microscope," *Langmuir*, vol. 19, no. 24, pp. 10225–10232, 2003.

[92] R. H. Schmidt, G. Haugstad, and W. L. Gladfelter, "Scan-Induced Patterning and the Glass Transition in Polymer Films: Temperature and Rate Dependence of Plastic Deformation at the Nanometer Length Scale," *Langmuir*, vol. 19, no. 24, pp. 10390–10398, 2003.

[93] B. Gotsmann and U. Dürig, "Thermally activated nanowear modes of a polymer surface induced by a heated tip.," *Langmuir*, vol. 20, no. 4, pp. 1495–500, 2004.

[94] J.-H. Kim, M. Yoneya, J. Yamamoto, and H. Yokoyama, "Surface alignment bistability of nematic liquid crystals by orientationally frustrated surface patterns," *Appl. Phys. Lett.*, vol. 78, no. 20, p. 3055, 2001.

[95] M. Rüetschi, P. Grütter, J. Fünfschilling, and H. J. Güntherodt, "Creation of liquid crystal waveguides with scanning force microscopy.," *Science*, vol. 265, no. 5171, pp. 512–4, 1994.

[96] K. Jradi, S. Bistac, M. Schmitt, A. Schmatulla, and G. Reiter, "Enhancing nucleation and controlling crystal orientation by rubbing/scratching the surface of a thin polymer film.," *Eur. Phys. J. E. Soft Matter*, vol. 29, no. 4, pp. 383–389, 2009.

[97] K. Kimura, K. Kobayashi, H. Yamada, T. Horiuchi, K. Ishida, and K. Matsushige, "Orientation control of poly(vinylidenefluoride-trifluoroethylene) crystals and molecules using atomic force microscopy," *Appl. Phys. Lett.*, vol. 82, no. 23, p. 4050, 2003.

[98] K. Kimura, K. Kobayashi, H. Yamada, T. Horiuchi, K. Ishida, and K. Matsushige, "Orientation Control of Molecular Chains in Polymers Using Atomic Force Microscopy," *Jpn. J. Appl. Phys.*, vol. 43, no. 7B, pp. 4575–4579, 2004.

[99] H. Yamada, K. Matsushige, K. Kobayashi, T. Horiuchi, K. Kimura, and K. Ishida, "Orientation control of ferroelectric polymer molecules using contact-mode AFM," *European Polymer Journal*, vol. 40, no. 5. pp. 933–938, 2004.

[100] S. L. Hellstrom, “Basic Models of Spin Coating.” p. 2012, 2007.

[101] D. B. Hall, P. Underhill, and J. M. Torkelson, “Spin Coating of Thin and Ultrathin Polymer Films,” *Polym. Eng. Sci.*, vol. 38, no. 12, pp. 2039–2045, 1998.

[102] H. Fujiwara, *Spectroscopic ellipsometry Principles and applications*. John Wiley & Sons, Ltd, 2007.

[103] G. W. H. Höhne, W. Hemminger, and H.-J. Flammersheim, *Differential Scanning Calorimetry*. Springer Berlin Heidelberg, 2003.

[104] G. W. H. Höhne, W. Hemminger, and H.-J. Flammersheim, “The DSC Curve,” in *Differential Scanning Calorimetry: An Introduction for Practitioners*, Berlin, Heidelberg: Springer Berlin Heidelberg, 1996, pp. 81–104.

[105] J. D. Batteas, C. A. Michaels, and G. C. Walker, *Applications of Scanned Probe Microscopy to Polymers*. American Chemical Society, 2005.

[106] S. Minko, A. Kiriy, G. Gorodyska, and M. Stamm, “Single flexible hydrophobic polyelectrolyte molecules adsorbed on solid substrate: transition between a stretched chain, necklace-like conformation and a globule,” *J. Am. Chem. Soc.*, vol. 124, no. 13, pp. 3218–3219, 2002.

[107] J. Kumaki, T. Kawauchi, and E. Yashima, “Reptational” Movements of Single Synthetic Polymer Chains on Substrate Observed by in-Situ Atomic Force Microscopy,” *Macromolecules*, vol. 39, no. 3, pp. 1209–1215, 2006.

[108] F. L. Leite, L. H. C. Mattoso, O. N. Oliveira, and P. S. P. Herrmann, “The Atomic Force Spectroscopy as a Tool to Investigate Surface Forces : Basic Principles and Applications,” *Méndez-Vilas A Díaz J. Mod. Res. Educ. Top. Microsc.*, pp. 747–757, 2007.

[109] F. L. Leite and P. S. P. Herrmann, “Application of atomic force spectroscopy (AFS) to studies of adhesion phenomena: a review,” *J. Adhes. Sci. Technol.*, vol. 19, no. 3–5, pp. 365–405, 2005.

[110] S. N. Magonov, V. Elings, and M.-H. Whangbo, “Phase imaging and stiffness in tapping-mode atomic force microscopy,” *Surf. Sci.*, vol. 375, no. 2–3, pp. L385–L391, 1997.

[111] H. K. Wickramasinghe, “Progress in scanning probe microscopy,” *Acta. Mater.*, vol. 48, no. 1, pp. 347–358, 2000.

[112] Y. Martin, C. C. Williams, and H. K. Wickramasinghe, “Atomic force microscope-force mapping and profiling on a sub 100-Å scale,” *J. Appl. Phys.*, vol. 61, no. 10, pp. 4723–4729, 1987.

[113] C. A. J. Putman, K. O. Van Der Werf, B. G. De Grooth, N. F. Van Hulst, and J. Greve, “Tapping mode atomic force microscopy in liquid,” *Appl. Phys. Lett.*, vol. 64, no. 18, pp. 2454–2456, 1994.

[114] R. García and R. Pérez, “Dynamic atomic force microscopy methods,” *Surf. Sci. Rep.*, vol. 47, no. 6–8, pp. 197–301, 2002.

[115] R. Babu and E. Singh, “Atomic Force Microscopy : A Source of Investigation in Biomedicine,” vol. 7, no. 1, pp. 59–66, 2014.

[116] T. R. Rodríguez and R. García, “Theory of Q control in atomic force microscopy,” *Appl. Phys. Lett.*, vol. 82, no. 26, p. 4821, 2003.

[117] A. San Paulo and R. García, “Tip-surface forces, amplitude, and energy dissipation in amplitude-modulation (tapping mode) force microscopy,” *Phys. Rev. B*, vol. 64, no. 19, pp. 1–4, 2001.

[118] R. Pearce and G. J. Vancso, “atomic force microscopy,” vol. 39, no. 5, pp. 1237–1242, 1998.

[119] J. K. Hobbs, O. E. Farrance, and L. Kailas, “How atomic force microscopy has contributed to our understanding of polymer crystallization,” *Polymer (Guildf).*, vol. 50, no. 18, pp. 4281–4292, 2009.

[120] O. Gazit, R. Khalfin, Y. Cohen, and R. Tannenbaum, “Self-Assembled Diblock Copolymer ‘Nanoreactors’ as ‘Catalysts’ for Metal Nanoparticle Synthesis,” *J. Phys. Chem. C*, vol. 113, no. 2, pp. 576–583, 2009.

[121] T. L. Morkved, M. Lu, a. M. Urbas, E. E. Ehrichs, H. M. Jaeger, P. Mansky, and T. P. Russell, “Local Control of Microdomain Orientation in Diblock Copolymer Thin Films with Electric Fields,” *Science (80-.).*, vol. 273, no. 5277, pp. 931–933, 1996.

[122] T. Thurn-Albrecht, J. Derouchey, T. P. Russell, and H. M. Jaeger, “Overcoming interfacial interactions with electric fields,” *Macromolecules*, vol. 33, no. 9, pp. 3250–3253, 2000.

[123] G. Kim and M. Libera, “Morphological Development in Solvent-Cast Polystyrene - Polybutadiene - Polystyrene (SBS) Triblock Copolymer Thin Films,” vol. 9297, no. 97, pp. 2569–2577, 1998.

[124] S. H. Kim, M. J. Misner, T. Xu, M. Kimura, and T. P. Russell, “Highly oriented and ordered arrays from block copolymers via solvent evaporation,” *Adv. Mater.*, vol. 16, no. 3, pp. 226–231, 2004.

[125] D. A. Rider, K. Liu, J. Eloi, L. Vanderark, L. Yang, J. Wang, D. Grozea, Z. Lu, Ќ. T. P. Russell, and I. Manners, “Nanostructured Magnetic Thin Films,” *ACS Nano*, vol. 2, no. 2, pp. 263–270, 2008.

[126] J. G. Son, J. Gwyther, J. B. Chang, K. K. Berggren, I. Manners, and C. A. Ross, “Highly ordered square arrays from a templated ABC triblock terpolymer,” *Nano Lett.*, vol. 11, no. 7, pp. 2849–2855, 2011.

[127] S. O. Kim, H. H. Solak, M. P. Stoykovich, N. J. Ferrier, J. J. De Pablo, and P. F. Nealey, “Epitaxial self-assembly of block copolymers on lithographically defined nanopatterned substrates.,” *Nature*, vol. 424, no. 6947, pp. 411–414, 2003.

[128] J. Bodycomb, Y. Funaki, K. Kimishima, and T. Hashimoto, “Single-grain lamellar microdomain from a diblock copolymer,” *Macromolecules*, vol. 32, no. 6, pp. 2075–2077, 1999.

[129] D. E. Angelescu, J. H. Waller, D. H. Adamson, P. Deshpande, S. Y. Chou, R. A. Register, and P. M. Chaikin, “Macroscopic orientation of block copolymer cylinders in single-layer films by shearing,” *Adv. Mater.*, vol. 16, no. 19, pp. 1736–1740, 2004.

[130] G. Singh, K. G. Yager, B. Berry, H. C. Kim, and A. Karim, “Dynamic thermal field-induced gradient soft-shear for highly oriented block copolymer thin films,” *ACS Nano*, vol. 6, no. 11, pp. 10335–10342, 2012.

[131] Z. Qiang, L. Zhang, G. E. Stein, K. A. Cavicchi, and B. D. Vogt, “Unidirectional

Alignment of Block Copolymer Films Induced by Expansion of a Permeable Elastomer during Solvent Vapor Annealing," *Macromolecules*, vol. 47, no. 3, pp. 1109–1116, 2014.

[132] R. L. Davis, P. M. Chaikin, and R. A. Register, "Cylinder orientation and shear alignment in thin films of polystyrene-poly(n-hexyl methacrylate) diblock copolymers," *Macromolecules*, vol. 47, no. 15, pp. 5277–5285, 2014.

[133] R. L. Davis, B. T. Michal, P. M. Chaikin, and R. A. Register, "Progression of Alignment in Thin Films of Cylinder-Forming Block Copolymers upon Shearing," *Macromolecules*, vol. 48, no. 15, pp. 5339–5347, 2015.

[134] J. R. Felts, M. S. Onses, J. a Rogers, and W. P. King, "Nanometer scale alignment of block-copolymer domains by means of a scanning probe tip.," *Adv. Mater.*, vol. 26, no. 19, pp. 2999–3002, 2014.

[135] O. M. Leung and M. C. Goh, "Orientational Ordering of Polymers by Atomic Force Microscope Tip-Surface Interaction," *Science (80-.).*, vol. 255, no. 5040, pp. 64–66, 1992.

[136] L. G. Alharbe, R. A. Register, and J. K. Hobbs, "Orientation Control and Crystallization in a Soft Confined Phase Separated Block Copolymer," *Macromolecules*, vol. 50, no. 3, pp. 987–996, 2017.

[137] D. J. Quiram, R. A. Register, G. R. Marchand, and D. H. Adamson, "Chain Orientation in Block Copolymers Exhibiting Cylindrically Confined Crystallization," vol. 9297, no. 97, pp. 4891–4898, 1998.

[138] D. J. Quiram, R. A. Register, and G. R. Marchand, "Crystallization of Asymmetric Diblock Copolymers from Microphase-Separated Melts," vol. 9297, no. 96, pp. 4551–4558, 1997.

[139] R. Krishnamoortit, W. W. Graessley, N. P. Balsarat, and D. J. Lohse, "Structural Origin of Thermodynamic Interactions in Blends of Saturated Hydrocarbon Polymers," *Macromolecules*, vol. 27, no. 11, pp. 3073–3081, 1994.

[140] W. W. Graessley, R. Krishnamoortij, G. C. Reichart, N. P. Balsara, L. J. Fetters, and D. J. Lohse, "Regular and Irregular Mixing in Blends of Saturated Hydrocarbon Polymers," *Macromolecules*, vol. 28, no. 4, pp. 1260–1270, 1996.

[141] J. P. Cleveland, B. Anczykowski, A. E. Schmid, and V. B. Elings, “Energy dissipation in tapping-mode atomic force microscopy,” *Appl. Phys. Lett.*, vol. 72, no. 20, p. 2613, 1998.

[142] T. Xu, a. V. Zvelindovsky, G. J. a. Sevink, K. S. Lyakhova, H. Jinnai, and T. P. Russell, “Electric Field Alignment of Asymmetric Diblock Copolymer Thin Films,” *Macromolecules*, vol. 38, no. 26, pp. 10788–10798, 2005.

[143] N. P. Balsara and H. J. Dai, “A transition from shear-induced order to shear-induced disorder in block copolymers,” *J. Chem. Phys.*, vol. 105, no. 7, pp. 2942–2945, 1996.

[144] Y. Loo, R. Register, and A. Ryan, “Polymer Crystallization in 25-nm Spheres,” *Phys. Rev. Lett.*, vol. 84, no. 18, pp. 4120–3, May 2000.

[145] L. Zhu, Y. Chen, A. Q. Zhang, B. H. Calhoun, M. S. Chun, R. P. Quirk, S. Z. D. Cheng, B. S. Hsiao, F. J. Yeh, and T. Hashimoto, “Phase structures and morphologies determined by competitions among self-organization, crystallization, and vitrification in a disordered poly(ethylene oxide)-b-polystyrene diblock copolymer,” *Phys. Rev. B*, vol. 60, no. 14, pp. 10022–10031, 1999.

[146] L. Zhu, S. Z. D. Cheng, B. H. Calhoun, Q. Ge, R. P. Quirk, E. L. Thomas, B. S. Hsiao, F. Yeh, and B. Lotz, “Crystallization temperature-dependent crystal orientations within nanoscale confined lamellae of a self-assembled crystalline - Amorphous diblock copolymer,” *J. Am. Chem. Soc.*, vol. 122, no. 25, pp. 5957–5967, 2000.

[147] P. Huang, L. Zhu, S. Z. D. Cheng, Q. Ge, R. P. Quirk, E. L. Thomas, B. Lotz, B. S. Hsiao, L. Liu, and F. Yeh, “Crystal Orientation Changes in Two-Dimensionally Confined Nanocylinders in a Poly (ethylene oxide) - b - polystyrene / Polystyrene Blend,” *Macromolecules*, vol. 34, no. 19, pp. 6649–6657, 2001.

[148] R. Opitz, D. M. Lambreva, and W. H. De Jeu, “Confined crystallization of ethylene oxide-butadiene diblock copolymers in lamellar films,” *Macromolecules*, vol. 35, no. 18, pp. 6930–6936, 2002.

[149] W.-P. Gao, Y. Bai, E.-Q. Chen, and Q.-F. Zhou, “Crystallization and melting of poly(ethylene oxide) confined in nanostructured particles with cross-linked shells of polybutadiene,” *Chinese J. Polym. Sci.*, vol. 23, no. 3, pp. 275–284, 2005.

[150] L. Zhu, B. R. Mimnaugh, Q. Ge, R. P. Quirk, S. Z. . Cheng, E. L. Thomas, B. Lotz, B. S. Hsiao, F. Yeh, and L. Liu, “Hard and soft confinement effects on polymer crystallization in microphase separated cylinder-forming PEO-b-PS/PS blends,” *Polymer (Guildf).*, vol. 42, no. 21, pp. 9121–9131, 2001.

[151] J.-T. Xu, Y.-Q. Zhao, G.-D. Liang, and Z.-Q. Fan, “Melting–Recrystallization of Block Copolymer Crystals in Confined Environments,” *Polym. J.*, vol. 37, no. 1, pp. 43–46, 2005.

[152] Y. L. Loo, R. A. Register, A. J. Ryan, and G. T. Dee, “Polymer crystallization confined in one, two, or three dimensions,” *Macromolecules*, vol. 34, no. 26, pp. 8968–8977, 2001.

[153] I. W. Hamley, J. P. A. Fairclough, A. J. Ryan, F. S. Bates, and E. Towns-Andrews, “Crystallization of nanoscale-confined diblock copolymer chains,” *Polymer (Guildf).*, vol. 37, no. 19, pp. 4425–4429, 1996.

[154] L. Zha and W. Hu, “Molecular simulations of confined crystallization in the microdomains of diblock copolymers,” *Prog. Polym. Sci.*, vol. 54–55, pp. 232–258, 2016.

[155] P. Rangarajan, R. A. Register, L. J. Fetters, W. Bras, S. Naylor, and A. J. Ryan, “Crystallization of a Weakly Segregated Polyolefin Diblock Copolymer,” *Macromolecules*, vol. 28, no. 14, pp. 4932–4938, 1995.

[156] L. Zhu, Y. Chen, A. Zhang, B. Calhoun, M. Chun, R. Quirk, S. Cheng, B. Hsiao, F. Yeh, and T. Hashimoto, “Phase structures and morphologies determined by competitions among self-organization, crystallization, and vitrification in a disordered poly(ethylene oxide)-b-polystyrene diblock copolymer,” *Phys. Rev. B*, vol. 60, no. 14, pp. 10022–10031, 1999.

[157] G. Reiter, G. Castelein, J.-U. Sommer, A. Röttele, and T. Thurn-Albrecht, “Direct Visualization of Random Crystallization and Melting in Arrays of Nanometer-Size Polymer Crystals,” *Phys. Rev. Lett.*, vol. 87, no. 22, p. 226101,

2001.

[158] C. Harrison, “Mechanisms of Ordering in Striped Patterns,” *Science (80-.).*, vol. 290, no. 5496, pp. 1558–1560, 2000.

[159] M. R. Mackley and a Keller, “Flow induced crystallization of polyethylene melts orifices,” *Polymer (Guildf).*, vol. 14, no. 1, pp. 16–20, 1973.

[160] B. S. Hsiao, L. Yang, R. H. Somani, C. a. Avila-Orta, and L. Zhu, “Unexpected Shish-Kebab structure in a sheared polyethylene melt,” *Phys. Rev. Lett.*, vol. 94, no. 11, pp. 1–4, 2005.

[161] M. J. Miles and A. Keller, “Conformational relaxation time in polymer solutions by elongational flow experiments: 2. Preliminaries of further developments: chain retraction; identification of molecular weight fractions in a mixture,” *Polymer (Guildf).*, vol. 21, no. 11, pp. 1295–1298, 1980.

[162] R. H. Somani, B. S. Hsiao, A. Nogales, H. Fruitwala, S. Srinivas, and A. H. Tsou, “Structure Development during Shear Flow Induced Crystallization of i-PP: In Situ Wide-Angle X-ray Diffraction Study,” *Macromolecules*, vol. 34, no. 17, pp. 5902–5909, 2001.

[163] H. Huo, Y. Meng, H. Li, S. Jiang, and L. An, “Influence of shear on polypropylene crystallization kinetics,” *Eur. Phys. J. E*, vol. 15, no. 2, pp. 167–175, 2004.

[164] G. Kumaraswamy, “Crystallization of polymers from stressed melts,” *J. Macromol. Sci. Part C*, vol. C45, no. 4, pp. 375–397, 2005.

[165] O. Lee and M. R. Kamal, “Experimental study of post-shear crystallization of polypropylene melts,” *Polym. Eng. Sci.*, vol. 39, no. 2, pp. 236–248, 1999.

[166] G. Matsuba, S. Sakamoto, Y. Ogino, K. Nishida, and T. Kanaya, “Crystallization of Polyethylene Blends under Shear Flow . Effects of Crystallization Temperature and Ultrahigh Molecular Weight Component,” vol. 190, pp. 7270–7275, 2007.

[167] R. H. Somani, L. Yang, L. Zhu, and B. S. Hsiao, “Flow-induced shish-kebab precursor structures in entangled polymer melts,” *Polymer (Guildf).*, vol. 46, no. 20, pp. 8587–8623, 2005.

[168] E. Cappelaere, J. F. Berret, J. P. Decruppe, R. Cressely, and P. Lindner, "Rheology, birefringence, and small-angle neutron scattering in a charged micellar system: Evidence of a shear-induced phase transition," *Phys. Rev. E*, vol. 56, no. 2, pp. 1869–1878, 1997.

[169] J. A. Kornfield, G. Kumaraswamy, and A. M. Issaian, "Recent advances in understanding flow effects on polymer crystallization," *Ind. Eng. Chem. Res.*, vol. 41, no. 25, pp. 6383–6392, 2002.

[170] M. Seki, D. W. Thurman, J. P. Oberhauser, and J. A. Kornfield, "Shear-mediated crystallization of isotactic polypropylene: The role of long chain-long chain overlap," *Macromolecules*, vol. 35, no. 7, pp. 2583–2594, 2002.

[171] M. Nakae, H. Uehara, T. Kanamoto, A. E. Zachariades, and R. S. Porter, "Structure development upon melt drawing of ultrahigh molecular weight polyethylene: Effect of prior thermal history," *Macromolecules*, vol. 33, no. 7, pp. 2632–2641, 2000.

[172] Y. Koike and M. Cakmak, "Atomic force microscopy observations of the structural development during the uniaxial stretching of crosslinked low-density polyethylene in partial and fully molten states," *J. Polym. Sci. Part B Polym. Phys.*, vol. 42, no. 12, pp. 2228–2237, 2004.

[173] O. O. Mykhaylyk, P. Chambon, C. Impradice, J. P. A. Fairclough, N. J. Terrill, and A. J. Ryan, "Control of structural morphology in shear-induced crystallization of polymers," *Macromolecules*, vol. 43, no. 5, pp. 2389–2405, 2010.

[174] O. O. Mykhaylyk, "Time-resolved polarized light imaging of sheared materials: application to polymer crystallization," *Soft Matter*, vol. 6, no. 18, p. 4430, 2010.

[175] M. Dhaese, O. O. Mykhaylyk, and P. Van Puyvelde, "On the onset of oriented structures in flow-induced crystallization of polymers: A comparison of experimental techniques," *Macromolecules*, vol. 44, no. 7, pp. 1783–1787, 2011.

[176] O. O. Mykhaylyk, P. Chambon, R. S. Graham, J. P. A. Fairclough, P. D. Olmsted, and A. J. Ryan, "The specific work of flow as a criterion for orientation in polymer crystallization," *Macromolecules*, vol. 41, no. 6, pp. 1901–1904,

2008.

[177] Bruker, “MultiMode Heater / Cooler.” p. 18, 2011.

[178] H. Janeschitz-Kriegl, E. Ratajski, and M. Stadlbauer, “Flow as an effective promotor of nucleation in polymer melts: A quantitative evaluation,” *Rheol. Acta*, vol. 42, no. 4, pp. 355–364, 2003.

[179] S. Moreno-Flores and J. L. Toca-Herrera, *Hybridizing Surface Probe Microscopies: Toward a Full Description of the Meso- and Nanoworlds: Scanning Probe Microscopy to Measure Surface Interactions: The Nano Push-Puller*, vol. 8. 2013.

[180] W. L. Peticolas and J. M. Watkins, “The Molecular Structure of Polyethylene. VII. Melt Viscosity and the Effect of Molecular Weight and Branching1,” *J. Am. Chem. Soc.*, vol. 79, no. 19, pp. 5083–5085, 1957.

[181] Y. Kikkawa, H. Abe, T. Iwata, Y. Inoue, and Y. Doi, “In situ observation of crystal growth for Poly[(S)-lactide] by temperature-controlled atomic force microscopy,” *Biomacromolecules*, vol. 2, no. 3, pp. 940–945, 2001.

[182] N. Basu, A. Osichow, S. Mecking, and G. Reiter, “Morphological changes during annealing of polyethylene nanocrystals.,” *Eur. Phys. J. E*, vol. 35, no. 3, pp. 1–12, 2012.

[183] A. Toda, M. Okamura, M. Hikosaka, and Y. Nakagawa, “Three-dimensional shape of polyethylene single crystals grown from dilute solutions and from the melt,” *Polymer (Guildf).*, vol. 46, no. 20, pp. 8708–8716, 2005.

[184] A. Toda, “Growth of polyethylene single crystals from the melt: change in lateral habit and regime I-II transition,” *Colloid Polym. Sci.*, vol. 270, no. 7, pp. 667–681, 1992.

[185] A. Toda, “Growth Mode and Curved Lateral Habits of Polyethylene Single Crystals,” *Faraday Discuss*, vol. 95, pp. 129–143, 1993.

[186] K. Yamada, H. Kajioka, K. Nozaki, and A. Toda, “Morphology and Growth of Single Crystals of Isotactic Polypropylene from the Melt,” *J. Macromol. Sci. Part B*, vol. 50, no. 2, pp. 236–247, 2011.

[187] G. Kortaberria, C. Marieta, A. Jimeno, P. Arruti, and I. Mondragon, "Crystallization of poly(L-lactid acid) monitored by dielectric relaxation spectroscopy and atomic force microscopy," *J. Microsc.*, vol. 224, no. 3, pp. 277–289, 2006.

[188] H. Xiong, C. K. Chen, K. Lee, R. M. Van Horn, Z. Liu, B. Ren, R. P. Quirk, E. L. Thomas, B. Lotz, R. M. Ho, W. Bin Zhang, and S. Z. D. Cheng, "Scrolled polymer single crystals driven by unbalanced surface stresses: Rational design and experimental evidence," *Macromolecules*, vol. 44, no. 19, pp. 7758–7766, 2011.

[189] O. E. Farrance and J. K. Hobbs, "In-situ studies of polymer surface crystallization," The Univeristy of Sheffield, 2009.

[190] M. Fujita, Y. Takikawa, H. Sakuma, S. Teramachi, Y. Kikkawa, and Y. Doi, "Real-time observations of oriented crystallization of poly(ε-caprolactone) thin film, induced by an AFM tip," *Macromol. Chem. Phys.*, vol. 208, no. 17, pp. 1862–1870, 2007.

[191] L. G. M. Beekmans, R. Vallée, and G. J. Vancso, "Nucleation and Growth of Poly (ε-caprolactone) on Poly (tetrafluoroethylene) by in-Situ AFM," *Macromolecules*, vol. 35, pp. 9383–9390, 2002.